

# GOING WITH THE FLOW: TIDAL EVOLUTION IN ECCENTRIC SYSTEMS

A Dissertation

Presented to the Faculty of the Graduate School

of Cornell University

in Partial Fulfillment of the Requirements for the Degree of

Doctor of Philosophy

by

Michelle Lorraine Vick

August 2020

© 2020 Michelle Lorraine Vick

ALL RIGHTS RESERVED

# GOING WITH THE FLOW: TIDAL EVOLUTION IN ECCENTRIC SYSTEMS

Michelle Lorraine Vick, Ph.D.

Cornell University 2020

Eccentric binary systems are ubiquitous. They appear in many astrophysical contexts, ranging from migrating giant planets to coalescing neutron star (NS) binaries. In a highly eccentric binary, the separation between the two bodies can vary greatly over the course of an orbit. Yet any binary with a small minimum separation (even if it lasts a scant fraction of an orbit) can be shaped dramatically by the tidal distortion and heating of one or both bodies. Tides are commonly treated in a parameterized way for convenience. In truth, a body's efficiency at dissipating energy depends strongly on its structure and orbit.

This dissertation explores how the nuances of tidal physics can dramatically alter the expected orbital evolution of many types of binary systems. In Chapter 2, I demonstrate that a white dwarf (WD) on an eccentric orbit around a massive black hole (MBH) can experience significant tidal heating, long before it is torn apart by the tidal force of the BH. The WD-MBH pairing is especially interesting because the inevitable outcome — the tidal disruption of the WD — will be visible at cosmological distances, but only if the BH mass is  $\lesssim 10^5 M_\odot$ . These events could constrain the mass function of intermediate mass to massive BHs. In Chapter 3, I develop a simple model that captures the coupled evolution of a binary orbit and tidally excited oscillations in one (or both) of its components. I derive the conditions under which the oscillations can grow chaotically over successive orbits, and explore how the damping of these oscillations affects long-term orbital evolution. Chapter 4 applies the model from

Chapter 3 to the high-eccentricity migration of giant planets. I study how, when a giant planet is excited onto a highly eccentric orbit, chaotic tides can rapidly drain energy from the orbit and shrink the semi-major axis. I demonstrate that chaotic tides can resolve many of the difficulties facing the high-eccentricity migration theory of hot Jupiter formation. In Chapter 5, I analyze the role of tides in the coalescence of an eccentric neutron star binary. Measuring the tidal response of neutron stars would help to unveil their equation of state. Lastly, in Chapters 6 and 7, I develop a treatment for tidal dissipation via turbulent viscosity in a star with a convective envelope in an eccentric orbit and apply this formalism to pre-common envelope binaries with massive stars. As the massive star evolves off of the main sequence and develops a deep convective envelope, viscous dissipation in the star circularizes and shrinks the binary. However, I find that, in many cases, tidal dissipation cannot circularize the orbit before the binary reaches Roche-lobe overflow.

## BIOGRAPHICAL SKETCH

Michelle Vick grew up in Sammamish, Washington. As a young student, her favorite subject was math, and in highschool she became interested in physics. She completed her undergraduate degree at Harvey Mudd College and earned a B.S. in Physics in 2014. Michelle took her first astronomy course in college, and became very interested in the subject when she realized that it was just a grab bag of physics applied to space. While at Harvey Mudd, Michelle wrote an undergraduate thesis under Dr. Ann Esin on microlensing with a binary lens. In August 2014, Michelle moved to Ithaca NY to pursue a PhD in Astronomy, working with Professor Dong Lai on tides in eccentric binaries. In September 2020, Michelle will begin a position as a CIERA Postdoctoral Fellow at Northwestern University. Besides astrophysics, Michelle enjoys singing and origami.

To my Mom and Dad for encouraging me to set ambitious goals and for their  
boundless love and support.

## ACKNOWLEDGEMENTS

First and foremost, I would like to thank my advisor, Dong Lai. Dong has been an inspiring mentor who is passionate about research and dedicated to the success of his students. I have benefited enormously from seeing his methodical and insightful approach to science up close.

Next, I thank my thesis committee for their support of my research and career aspirations and for their time and feedback.

I have been fortunate to work with some very talented and generous scientists in the completion of my dissertation. I would like to thank Morgan MacLeod, Kassandra Anderson, Jean Teyssandier, and Jim Fuller for their time and hard work as collaborators. I am also grateful to many members of Dong's research group for stimulating discussions, including Diego Muñoz, Bin Liu, Jean Teyssandier, Ryan Miranda, J.J. Zanazzi, Kassandra Anderson, Bonan Pu, Yubo Su, Jiaru Li, and Chris O'Connor.

I gratefully acknowledge support from the NASA Earth and Space Sciences Fellowship for funding three years of my thesis work.

I thank my family for their unwavering support, and my friends in Ithaca who have made the last six years feel like six months. I'm especially grateful to Paul, Kassandra, Maryame, Ryan, Tyler, Jean, Cody, and Abhinav.

Lastly, I thank Millie for some quality cuddles and play time, and my husband, Sam for his love and for the many ways that he has helped me throughout graduate school. I never expected to meet my best friend and lifelong partner in graduate school, and I'm so happy I found you.

## TABLE OF CONTENTS

Biographical Sketch . . . . .	iii
Dedication . . . . .	iv
Acknowledgements . . . . .	v
Table of Contents . . . . .	vi
List of Tables . . . . .	ix
List of Figures . . . . .	x
<b>1 Introduction</b>	<b>1</b>
<b>2 Tidal Dissipation and Evolution of White Dwarfs Around Massive Black Holes: An Eccentric Path to Tidal Disruption</b>	<b>8</b>
2.1 Introduction . . . . .	8
2.2 Basic Scalings and Timescales . . . . .	11
2.3 WD Model and Physics of Tidal Dissipation . . . . .	15
2.4 Tidal Dissipation in an Eccentric Orbit . . . . .	20
2.5 Results for Tidal Energy and Angular Momentum Transfer Rates	27
2.6 Tidal Heating . . . . .	33
2.7 Summary and Discussion . . . . .	40
<b>3 Dynamical Tides in Highly Eccentric Binaries: Chaos, Dissipation and Quasi-Steady State</b>	<b>44</b>
3.1 Introduction . . . . .	44
3.2 Iterative Map for Mode Amplitudes . . . . .	47
3.3 Mode Energy Evolution without Dissipation . . . . .	50
3.3.1 Oscillatory Behaviour . . . . .	53
3.3.2 Resonance . . . . .	55
3.3.3 Chaotic Growth . . . . .	56
3.4 Mode Energy Evolution with Dissipation . . . . .	58
3.4.1 Quasi-Steady State . . . . .	60
3.4.2 Passing Through Resonances . . . . .	61
3.4.3 Tamed Chaos . . . . .	63
3.5 Systems with Multiple Modes . . . . .	65
3.6 Summary and Discussion . . . . .	68
<b>4 Chaotic Tides in Migrating Gas Giants: Forming Hot and Transient Warm Jupiters via Lidov-Kozai Migration</b>	<b>73</b>
4.1 Introduction . . . . .	73
4.2 Chaotic Dynamical Tides in Giant Planets in Eccentric Orbits . . . . .	78
4.2.1 Hydrodynamics of Tidally Forced Oscillations & Iterative Map . . . . .	79
4.2.2 Planetary Oscillation Modes . . . . .	85
4.2.3 Conditions for Chaotic Tides . . . . .	88

4.2.4	Conditions for Chaotic Tides When $E_{\alpha,0} > 0$ . . . . .	93
4.2.5	Conditions for Continued Chaotic Behaviour . . . . .	97
4.3	Lidov-Kozai migration with chaotic tides . . . . .	98
4.3.1	Description of the Model . . . . .	101
4.3.2	Examples of the Model . . . . .	108
4.4	Key Features of Chaotic Tidal Migration: Analytical Understanding	110
4.4.1	Condition for Chaotic Tidal Migration . . . . .	110
4.4.2	Evading Tidal Disruption . . . . .	112
4.4.3	Eccentric Warm Jupiter Formation . . . . .	116
4.4.4	Fast Long-Term Orbital Decay and Hot Jupiter Formation	118
4.4.5	Spin-Orbit Misalignment and Final Planet-Binary Inclination . . . . .	118
4.5	Population Synthesis . . . . .	121
4.5.1	Set-up and Method . . . . .	122
4.5.2	Migration and WJ/HJ Formation Fractions . . . . .	125
4.5.3	Parameter Space for WJ Formation . . . . .	126
4.5.4	Properties of WJs Formed by Chaotic Tidal Evolution . . . . .	128
4.5.5	Hot Jupiter Properties . . . . .	131
4.6	Analytical Calculation of WJ Formation Fraction . . . . .	133
4.7	Summary and Discussion . . . . .	137
4.7.1	Summary of Key Results . . . . .	137
4.7.2	Discussion . . . . .	142
<b>5</b>	<b>Tidal Effects in Eccentric Coalescing Neutron Star Binaries</b>	<b>145</b>
5.1	Introduction . . . . .	145
5.2	Equations of Motion Including Dynamical Tides and GR Effects .	148
5.3	Orbit and Mode Evolution without GR . . . . .	152
5.4	Orbit and Mode Evolution Including GR . . . . .	156
5.5	Discussion . . . . .	166
<b>6</b>	<b>Tidal Evolution of Eccentric Binaries Driven by Convective Turbulent Viscosity</b>	<b>168</b>
6.1	Introduction . . . . .	168
6.2	Tides and Dissipation in Eccentric Binaries: General Formalism .	171
6.2.1	The Slow-Rotation and Weak Friction Limits . . . . .	176
6.2.2	Orbital Evolution . . . . .	178
6.3	Viscous Dissipation in Convective Envelopes and Stellar Models .	180
6.4	Sample Results . . . . .	183
6.5	High-Eccentricity Limit: Alternative Calculation of Tidal Evolution	186
6.6	Summary and Discussion . . . . .	196
<b>7</b>	<b>Tidal Dissipation Impact on the Eccentric Onset of Common Envelope Phases in Massive Binary Star Systems</b>	<b>200</b>
7.1	Introduction . . . . .	200

7.2	Theory of Tidal Dissipation in Eccentric Binaries . . . . .	204
7.2.1	Stellar Models . . . . .	205
7.2.2	Calculation of the Tidal Dissipation Rate in a Giant Star . .	206
7.2.3	Coupling the Stellar and Orbital Evolution . . . . .	211
7.3	Results . . . . .	213
7.3.1	Tidal Dissipation Rate as a Function of Stellar Evolution .	213
7.3.2	Tidal Circularization Timescale and the Binary Orbit . . .	214
7.3.3	Outcomes of Coupled Stellar and Orbital Evolution . . . .	219
7.3.4	Tidal Circularization and the Eccentricity Distribution of pre-Common Envelope Stellar Binaries . . . . .	223
7.4	Discussion . . . . .	226
7.4.1	Possible Limitations . . . . .	226
7.4.2	Implications for Common Envelope Phases . . . . .	229
7.4.3	Implications for the Formation of Gravitational-Wave Mergers . . . . .	232
7.5	Summary & Conclusion . . . . .	235
<b>8</b>	<b>Future Work</b>	<b>239</b>
<b>A</b>	<b>Appendix for Chapter 2</b>	<b>242</b>
<b>B</b>	<b>Appendix for Chapter 3</b>	<b>244</b>
B.1	Physical Justification for the Iterative Map . . . . .	244
B.2	Non-dissipative Systems . . . . .	247
B.2.1	Maximum Mode Energy for Non-Chaotic Systems . . . .	247
B.2.2	Resonant Timescale . . . . .	249
B.2.3	Maximum Mode Energy for Chaotic Systems . . . . .	250
B.3	G-mode Properties of Stellar Models . . . . .	252
<b>C</b>	<b>Appendix for Chapter 5</b>	<b>257</b>
C.1	Orbital decay through f-mode resonances . . . . .	257
<b>D</b>	<b>Appendix for Chapter 6</b>	<b>261</b>
D.1	The Relationship between Damping Rates . . . . .	261

## LIST OF TABLES

4.1	Polytrope Oscillation Mode Properties . . . . .	85
4.2	Formation Fractions from Chaotic Tidal Migration . . . . .	122

## LIST OF FIGURES

2.1	White Dwarf Orbital Evolution Timescales . . . . .	12
2.2	White Dwarf Propagation Diagram . . . . .	16
2.3	White Dwarf Temperature, Density and Composition Profile . . . . .	17
2.4	The Dynamical Tide in a White Dwarf Model . . . . .	19
2.5	The Tidal Torque on a White Dwarf as a Function of Forcing Frequency . . . . .	21
2.6	Frequency Decomposition of the White Dwarf Tidal Torque: Large Separations . . . . .	27
2.7	Frequency Decomposition of the White Dwarf Tidal Torque: Small Separations . . . . .	28
2.8	White Dwarf Dimensionless Tidal Transfer Rates . . . . .	29
2.9	Tidal Transfer Paramters vs. Eccentricity: Model 1 . . . . .	30
2.10	Tidal Transfer Paramters vs. White Dwarf Spin Rate: Model 1 . . . . .	31
2.11	Tidal Transfer Paramters vs. Eccentricity: Model 2 . . . . .	32
2.12	Tidal Transfer Paramters vs. White Dwarf Spin Rate: Model 2 . . . . .	33
2.13	White Dwarf Dimensionless Tidal Transfer Rates: Small Separations . . . . .	34
2.14	White Dwarf Temperature and Orbital Evolution: Model 1 . . . . .	35
2.15	White Dwarf Temperature and Orbital Evolution: Model 2 . . . . .	36
2.16	White Dwarf Thermal Timescales . . . . .	38
2.17	Heated White Dwarf Temperature Profile . . . . .	39
3.1	Maximum Mode Energy as a Function of Period and Phase Shift	51
3.2	Maximum Mode Energy as a Function of Pericentre and Eccentricity . . . . .	52
3.3	Three Behaviours of Mode Energy Evolution . . . . .	54
3.4	Lyaponov Exponent of Chaotic Mode Evolution . . . . .	57
3.5	Chaotic Mode Energy Evolution . . . . .	59
3.6	Quasi-Steady State Mode Energy Evolution . . . . .	61
3.7	Resonant Mode Energy Evolution . . . . .	62
3.8	Chaotic Mode Evolution with Damping . . . . .	66
3.9	Resonant Energy Evolution for Multiple Modes . . . . .	67
3.10	Chaotic Energy Evolution for Multiple Modes . . . . .	68
3.11	Maximum Mode Energy as a Function of Period and Phase Shift: Multiple Modes . . . . .	69
4.1	Phase Shift Comparison for Different Modes . . . . .	86
4.2	Three Types of Mode Energy Evolution . . . . .	89
4.3	Maximum Mode Energy as a Function of Orbital Parameters . . . . .	91
4.4	Maximum Mode Energy for Different Initial Mode Energies . . . . .	94
4.5	Maximum Mode Energy as a Function of Orbital Parameters: Different Initial Mode Energies . . . . .	94

4.6	Lidov Kozai Migration with Chaotic Dynamical Tides . . . . .	99
4.7	Chaotic Evolution: Different $E_{\max}$ . . . . .	104
4.8	Chaotic Evolution: Different $E_{\text{resid}}$ . . . . .	105
4.9	Lidov Kozai Migration with Chaotic Tides: Multiple High Eccentricity Phases . . . . .	107
4.10	Outcomes of LK migration with Chaotic Tides as a Function of Initial Orbital Paramters . . . . .	113
4.11	Example of a System Saved from Disruption by Chaotic Tides . .	115
4.12	Predicted semi-major axis and Pericentre Distance of Warm Jupiters Formed via Chaotic Tidal Migration . . . . .	116
4.13	Obliquity Evolution throughout Chatoic Tidal Migration . . . .	119
4.14	The Parameter Space that Yields Warm Jupiters via Chaotic Tidal Migration . . . . .	123
4.15	Outcomes of Chaotic Tidal Migration as a Function of Initial Orbital Parameters . . . . .	127
4.16	Orbital Properties of Warm Jupiters formed via Chaotic Tidal Mi- gration . . . . .	128
4.17	Distribution of Orbital Parameters of Transient Warm Jupiters fromed via Chaotic Tidal Migratiton . . . . .	129
4.18	Warm Jupiter Orbit: Population Synthesis Compared with Theory	134
4.19	Distribution of Orbital Parameters of Hot Jupiters fromed via Chaotic Tidal Migratiton . . . . .	135
4.20	HJ Formation fraction as a Function of Planet Mass and Radius .	138
5.1	Neutron Star Mode and Orbital Energy: Low Amplitude Oscil- lations . . . . .	152
5.2	Neutron Star Mode and Orbital Energy: Resonant Behaviour .	153
5.3	Neutron Star Mode and Orbital Energy: Chaotic Behaviour . .	153
5.4	Neutron Star Binary Orbital Evolution with General Relativity and Dynamical Tides . . . . .	157
5.5	Eccentric Neutron Star Binary Gravitational Waveform . . . .	158
5.6	Cumulative Time Shift in a Neutron Star Binary Gravitational Wave Signal . . . . .	159
5.7	Cumulative Gravitaional Wave Phase shift due to Dynamical Tides as a function of Initial Eccentricity . . . . .	160
5.8	Examples of the Gravitational Wave Phase Shift . . . . .	161
6.1	Viscosity Profile in Giant Branch and Solar-Type Stellar Models .	181
6.2	The Stellar Viscous Damping Rate vs. Forcing Frequency . . . .	183
6.3	Dimensionless Tidal Torque vs. Stellar Rotation Rate: Giant Branch Star . . . . .	187
6.4	Dimensionless Tidal Torque vs. Stellar Rotation Rate: Solar-Type Star . . . . .	188
6.5	Dimensionless Tidal Energy Transfer Rate vs. Pericentre Distance	189

6.6	Dimensionless Tidal Energy Transfer Rate vs. Pericentre Distance: Fast Rotation . . . . .	190
6.7	Dimensionless Tidal Energy Transfer Rate vs. Pericentre Distance: Solar-Type Star . . . . .	191
6.8	Mode Energy Evolution at Small Pericentre vs. Large Pericentre . . . . .	194
6.9	Energy Dissipation at Pericentre and Over an Orbit . . . . .	195
6.10	Dimensionless Tidal Energy Transfer Rate High-Eccentricity Expression: Giant Branch Star . . . . .	197
6.11	Dimensionless Tidal Energy Transfer Rate High-Eccentricity Expression: Solar-Type Star . . . . .	198
7.1	Stellar Model Evolution . . . . .	215
7.2	Stellar Model Evolution: Giant Branch . . . . .	215
7.3	Circularization Timescale as Function of Eccentricity . . . . .	217
7.4	Circularization Timescale Throughout Stellar Evolution . . . . .	218
7.5	Orital and Spin Evolution of a Binary with a Massive Star . . . . .	220
7.6	Orbital Eccentricity and Stellar Rotation Rate at the Roche Radius for $10M_{\odot}$ star . . . . .	225
7.7	Orbital Eccentricity Stellar Rotation Rate at the Roche Radius for a $15M_{\odot}$ star . . . . .	225
7.8	The Cumulative Distribution Function of Binary Eccentricities at the Roche Limit . . . . .	226
7.9	Distribution of Stellar Spin Rates in Circularized Binaries at the Roche Limit . . . . .	227
8.1	Hydrodynamic Simulation of Tidally Excited Modes . . . . .	240
A.1	Hansen Coefficient Approximation . . . . .	243
B.1	Maximum Mode Energy During Chaotic Behaviour: Function of Period . . . . .	251
B.2	Maximum Mode Energy During Chaotic Behaviour: Function of Phase Shift . . . . .	252
B.3	Stellar Model $g$ -mode Frequencies . . . . .	254
B.4	Stellar Model Pericentre Energy Transfer . . . . .	255
B.5	Pericentre Energy Transfer vs. Binary Separation . . . . .	256
C.1	The Gravitational Wave Phase Shift due to Encountering a Mode-Orbit Resonance . . . . .	258

## CHAPTER 1

### INTRODUCTION

Tides sculpt a wide range of astrophysical two-body systems. Tidal forces can cause an orbit to circularize, shrink or expand, and stars and planets to spin up or down. In a strongly interacting binary, such as a giant planet closely orbiting its host star (a hot Jupiter) or a coalescing compact binary, tides can dramatically affect the orbit and cause significant heating in the binary components. Despite the importance and prevalence of tidal interactions, tidal dissipation is poorly understood in many types of astrophysical systems.

When a star or giant planet experiences the quadrupole gravitational potential of a companion, its shape is distorted. This deformation involves fluid motion, and generally results in tidal energy dissipation. In a binary, the end state of this interaction is two bodies in a circular orbit, both rotating synchronously with the orbital period. Observations of giant planet orbits and stellar binaries support this general picture and give some insight into the tidal dissipation rate of different astrophysical bodies. In some cases, for instance that of the hot Jupiter WASP-12b, it is possible to directly observe tidally driven decay of the planet's orbit [Yee et al., 2020, Patra et al., 2020]. Another way to infer the tidal dissipation rate of stars and planets is to look at the orbital properties of a population. A two-body system with a small enough semi-major axis (or equivalently a short enough orbital period) tends to be circular and have synchronously rotating components. The separation at which a transition between circular and eccentric orbits or synchronous and asynchronous rotation occurs can be used to place constraints on the tidal quality factors of different types of stars and planets [e.g. Abt and Boonyarak, 2004, Abt, 2005, 2006, Hansen, 2010, Socrates

et al., 2012, Lurie et al., 2017, O'Connor and Hansen, 2018].

However, reconciling inferred tidal dissipation rates with theoretical predictions remains challenging in many cases. One of the simplest and most widely used descriptions of tidal physics is the weak friction approximation [Alexander, 1973, Hut, 1981]. This treatment focuses on the equilibrium tide, the tidal bulge induced by the gravitational potential of a companion. As the equilibrium tide moves to follow the axis connecting the two bodies, the tide is damped by the viscosity associated with fluid motion. In giant planets and stars without a large convective envelope, the timescale for orbital circularization from this framework can be orders of magnitude longer than those inferred from the orbital parameters of stellar binaries and known reference points, such as the tidal quality factor of Jupiter [e.g. Zahn, 1975, Wu, 2005].

In this thesis, I explore the implications of a more nuanced description of tidal physics for a variety of astronomical binaries. Much of this work is focused on the dynamical tide in a body in an eccentric binary<sup>1</sup>. When the tidal forcing frequency (twice the orbital frequency in a circular orbit) is faster than the dynamical frequency of a star or planet, the response of the body is not accurately characterized by a hydrostatic bulge. The non-hydrostatic response is termed the ‘dynamical tide.’ It takes the form of tidally excited waves that propagate throughout the fluid body. In some cases, a tidally excited wave will grow in amplitude as it propagates until the height of the wave is comparable to its wavelength. When this occurs, non-linear effects such as wave-breaking are expected to quickly dissipate the energy and angular momentum carried by the traveling wave [Goodman and Dickson, 1998, Barker and Ogilvie, 2010, 2011,

---

<sup>1</sup>In convective bodies, inertial waves that are restored by the Coriolis force can also contribute significantly to tidal dissipation, but are not investigated in this dissertation.

Chernov et al., 2013, Ivanov et al., 2013, Bolmont and Mathis, 2016, Weinberg et al., 2017, Sun et al., 2018].

In other situations, the damping time for a tidally excited wave is longer than the time the wave takes to traverse a propagation cavity. In this case the wave is reflected off of the boundaries of the cavity and forms a standing wave pattern or normal oscillation mode. If the oscillations are restored by the buoyant force, or gravity, they are classified as g-modes. If pressure is the restoring force, they are p-modes. While the amplitude of these oscillations is small relative to the wavelength, they can be treated as linear perturbations to a spherical star or planet. The coupled system of the oscillation modes and the binary orbit can be described by a set of ordinary differential equations [Zahn, 1977, Goldreich and Nicholson, 1989, Lai, 1996a, 1997, Witte and Savonije, 1999, Goodman and Dickson, 1998, Barker and Ogilvie, 2010]. However, the long-term behavior of the system is surprisingly rich [Mardling, 1995a,b, Ivanov and Papaloizou, 2004a].

When a tidal forcing frequency is resonant with a natural oscillation mode of a fluid body (i.e. the mode frequency is an integer multiple of the orbital frequency) the oscillation amplitude and the tidal dissipation rate can be orders of magnitude larger than when the oscillation is driven off-resonance. In general the tidal response of a star or planet is highly frequency dependent, a reality that is ignored in the weak friction approximation. The gravitational potential experienced by a star or planet in an eccentric orbit can be expressed as a superposition of many tidal forcing frequencies. Much of this thesis is devoted to understanding how the combination of a frequency-dependent tidal response and the many forcing frequencies of an eccentric orbit combine to tell an intri-

cate story of tidal evolution in a variety of eccentric astrophysical binaries.

In Chapter 2, I study a white dwarf (WD) captured into a high-eccentricity orbit around a massive black hole (MBH). In some cases, the WD may undergo many pericentre passages before tidal disruption. During these passages, the tidal potential of the MBH excites internal oscillations or waves in the WD, and the dissipation of these oscillations can significantly influence the physical properties of the WD prior to its disruption. I calculate the amplitude of the tidally excited gravity waves in the WD as a function of the pericentre distance and eccentricity for realistic WD models, under the assumption that these outgoing gravity waves are efficiently dissipated in the outer layers of the WD by non-linear effects or radiative damping. I find that the dynamical tide is much weaker than gravitational radiation in driving the orbital decay of the WD-MBH binary. However, tidal heating can lead to appreciable brightening of the WD and may induce runaway fusion in the hydrogen envelope well before the WD undergoes tidal disruption.

In Chapter 3, I explore the case where the dynamical tide takes the form of tidally excited oscillation modes in one of the components of a highly eccentric binary. When these oscillations are excited at pericentre, the result is energy exchange between the modes and the binary orbit. These modes exhibit one of three behaviours over multiple passages: low-amplitude oscillations, large amplitude oscillations corresponding to a resonance between the orbital frequency and the mode frequency, and chaotic growth, with the mode energy reaching a level comparable to the orbital binding energy. I study these phenomena with an iterative map that includes mode dissipation, fully exploring how the mode evolution depends on the orbital and mode properties of the system. The dis-

sipation of mode energy drives the system toward a quasi-steady state, with gradual orbital decay punctuated by resonances. I quantify the quasi-steady state and the long-term evolution of the system.

Next, in Chapter 4, I apply the map developed in Chapter 3 to giant planet high-eccentricity migration. High-eccentricity migration is an important channel for the formation of hot Jupiters (HJs). In particular, Lidov-Kozai (LK) oscillations of orbital eccentricity/inclination induced by a distant planetary or stellar companion, combined with tidal friction, have been shown to produce HJs on Gyr timescales, provided that efficient tidal dissipation operates in the planet. I re-examine this scenario with the inclusion of chaotic dynamical tides. When the planet’s orbit is in a high-eccentricity phase, the tidal force from the star excites oscillatory f-modes and i-modes (fundamental modes and inertial modes) in the planet. For sufficiently large eccentricity and small pericentre distance, the modes can grow chaotically over multiple pericentre passages and eventually dissipate non-linearly, drawing energy from the orbit and rapidly shrinking the semi-major axis. I study the effect of such chaotic tides on the planet’s orbital evolution. I find that this pathway produces very eccentric ( $e \gtrsim 0.9$ ) warm Jupiters (WJs) on short timescales (a few to 100 Myrs). These WJs efficiently circularize to become HJs due to their persistently small pericentre distances. Chaotic tides can also save some planets from tidal disruption by truncating LK eccentricity oscillations, significantly increasing the HJ formation fraction for a range of planet masses and radii. Using a population synthesis calculation, I determine the characteristics of WJs and HJs produced in this scenario, including the final period distribution, orbital inclinations and stellar obliquities. Chaotic tides endow LK migration with several favourable features to explain observations of HJs. We expect that chaotic tides are also important

in other flavours of high- $e$  migration.

In Chapter 5, I explore a very different application of the coupled evolution of oscillation modes and a binary orbit. Dynamically formed compact object binaries may still be eccentric while in the LIGO/Virgo band. For a neutron star (NS) in an eccentric binary, the fundamental modes (f-modes) are excited at pericenter, transferring energy from the orbit to oscillations in the NS. I model this system by coupling the evolution of the NS f-modes to the orbital evolution of the binary as it circularizes and moves toward coalescence. NS f-mode excitation generally speeds up the orbital decay and advances the phase of the gravitational wave signal from the system. I calculate how this effect changes the timing of pericenter passages and examine how the cumulative phase shift before merger depends on the initial eccentricity of the system. This phase shift can be much larger for highly eccentric mergers than for circular mergers, and can be used to probe the NS equation of state.

In Chapters 6 and 7, I study how tidal dissipation in the convective regions of stars plays an important role in shaping the orbit of pre-common envelope systems. Such systems are possible sources of a variety of transients and of close compact binary systems that will eventually merge and produce detectable gravitational wave signals. In general, the effective viscosity in a convective stellar envelope depends on the tidal forcing frequency  $\omega_{\text{tide}}$ ; when  $\omega_{\text{tide}}$  is larger than the turnover frequency of convective eddies, the viscosity is reduced. Previous work has focused on binaries in nearly circular orbits. However, for eccentric orbits, the tidal potential has many forcing frequencies. In Chapter 6, I develop a formalism for computing tidal dissipation that captures the effect of frequency-dependent turbulent viscosity and is valid for arbitrary

binary eccentricities. I also present an alternative simpler formulation that is suitable for very high eccentricities. I find that tidal decay and circularization due to turbulent viscosity can be a few orders of magnitude faster than predicted by weak tidal friction in giant branch stars on eccentric, small pericentre orbits. In Chapter 7, I couple numerical models of the post main sequence stellar evolution of massive stars with the theory developed in Chapter 6. I find that, in many cases, tidal dissipation does not circularize the orbit before the onset of Roche-lobe overflow. These results demonstrate that some of the possible precursors to double neutron star systems are likely eccentric at the Roche radius, and the effects of pre-common envelope eccentricity on the resulting compact binary merit further study.

In Chapter 8, I discuss a possible avenue for future work.

# CHAPTER 2

## TIDAL DISSIPATION AND EVOLUTION OF WHITE DWARFS AROUND MASSIVE BLACK HOLES: AN ECCENTRIC PATH TO TIDAL DISRUPTION

Originally published in:

M. Vick, D.Lai, and J. Fuller. Tidal Dissipation and Evolution of White Dwarfs Around Massive Black Holes: An Eccentric Path to Tidal Disruption. *MNRAS* **468**, pp. 2296-2310, 2017. doi: 10.1093/mnras/sty225

### 2.1 Introduction

A tidal disruption event (TDE) occurs when a star passes close to a black hole (BH) and is torn apart by tidal forces. Debris from the star produces an accretion flare as it falls back onto an accretion disk around the BH. Tidal disruption events and the corresponding accretion flares were first predicted by Hills [1975] and Rees [1988] respectively. Over the last decade, dozens of TDE candidates have been discovered, and the detection of various exotic transients has renewed interest in theoretical models of TDEs. Some of the most unusual candidate events could be explained as the tidal disruption of a white dwarf (WD) by a moderately massive black hole (MBH) [Shcherbakov et al., 2013]. In particular, it has been suggested that WD-TDEs could be a source of a recently discovered population of ultra long gamma ray bursts [Levan et al., 2014, MacLeod et al., 2014, Ioka et al., 2016].

The possibility of detecting WD-TDEs is especially intriguing because the

disruption of a WD is only visible if the mass of the BH,  $M_{\text{bh}}$ , is less than about  $10^5 M_{\odot}$  or perhaps  $10^6 M_{\odot}$  depending on the BH spin [MacLeod et al., 2014, Tejeda et al., 2017]. For a more massive BH, the WD is “swallowed whole” without disruption. We expect these disruption events to be very luminous as a portion of the accretion power likely channels into a relativistic jet [Gianinos and Metzger, 2011, Krolik and Piran, 2012, De Colle et al., 2012]. There are now a few cases in which hard x-ray emission from launching a relativistic jet was observed following a flare from stellar disruption [Bloom et al., 2011, Burrows et al., 2011, van Velzen et al., 2016]. An otherwise quiet MBH would show bright, beamed emission after the disruption of a WD. Therefore detecting (or not detecting) signals from the tidal disruptions of WDs could place constraints on the MBH population.

Recognizing the signal from a WD-TDE requires a solid theoretical understanding of all pathways leading to the tidal disruption of WDs. The predicted signal from WD tidal disruption varies greatly with orbital parameters. A “normal” TDE occurs when the pericentre distance ( $r_p$ ) between the star and the BH is of the same order, but less than the tidal radius ( $r_{\text{tide}}$ ), leading to a one time shredding of the star. In an extreme case, where  $r_p$  is much smaller than  $r_{\text{tide}}$ , tidal compression of the WD could lead to a thermonuclear explosion, which would produce a distinctive signal [Luminet and Pichon, 1989, Rosswog et al., 2008a,b, 2009, MacLeod et al., 2016]. If, on the other hand,  $r_p$  is a few times larger than  $r_{\text{tide}}$ , the WD could undergo repeated tidal encounters with the BH, and may experience “gentle” tidal stripping, producing a signal that is periodic with the orbit [Zalamea et al., 2010, MacLeod et al., 2014]. This last case is especially intriguing because if the WD is able to complete many orbits, the system may be a source of gravitational waves, detectable by a space-based interferom-

eter [Sesana et al., 2008, Zalamea et al., 2010, Cheng and Evans, 2013, East, 2014, Cheng and Bogdanović, 2014, MacLeod et al., 2014].

In this paper, we consider the scenario that a WD is captured into an eccentric orbit with a pericentre distance that is too large for the WD to suffer immediate disruption or partial mass transfer. In this case, the WD continues on its orbit relatively intact and experiences multiple passages before disruption. When the WD passes close to the BH at pericentre, the tidal force from the BH excites oscillations and waves in the WD, transferring energy and angular momentum between the WD and its orbit. The dissipation of the excited oscillations can heat up the WD and influence its structural evolution.

A major goal of this paper is to determine the tidal energy and angular momentum transfer rates for a WD in a high-eccentricity orbit around a MBH. To this end, we examine the tidal excitation of gravity (buoyancy) waves, in the radiative envelope of the WD. As these waves propagate toward the stellar surface, they grow in amplitude, become non-linear and damp efficiently (Section 2.3). In this scenario, waves do not reflect from the WD surface, so there are no standing waves. We calculate the energy and angular momentum deposition near the surface of the WD by imposing outgoing boundary conditions on the fluid perturbation equations. Fuller and Lai [2012b] studied this scenario for binary WDs in circular orbits. In Section 2.4, we generalize the method to calculate tidal energy and angular momentum transfer to a WD in an eccentric orbit around a MBH using realistic WD models generated with MESA [Paxton et al., 2011]. These results are presented in Section 2.5. Lastly, in Section 2.6 we study the structural evolution of a WD experiencing tidal heating as the orbit evolves due to gravitational radiation.

## 2.2 Basic Scalings and Timescales

Before undertaking detailed calculations, we first consider the characteristic timescales for various physical processes associated with an eccentric WD-MBH binary. The rate of angular momentum loss due to gravitational radiation is well-known [Peters, 1964]:

$$\dot{J}_{\text{grav}} = -\frac{32}{5} \frac{M^2 M_{\text{bh}}^2 M_{\text{t}}^{1/2}}{c^5 a^{7/2} (1 - e^2)^2} \left(1 + \frac{7}{8} e^2\right), \quad (2.1)$$

where  $M$  is the mass of the WD,  $M_{\text{bh}} \gg M$  is the mass of the BH, and  $M_{\text{t}} = M_{\text{bh}} + M \simeq M_{\text{bh}}$  is the total mass. The semi-major axis and eccentricity of the orbit are  $a$  and  $e$  respectively. The orbital angular momentum is given by

$$J = \mu \sqrt{GM_{\text{t}}a(1 - e^2)}, \quad (2.2)$$

where  $\mu$  is the reduced mass of the system. We define

$$r_{\text{t}} \equiv R \left(\frac{M_{\text{t}}}{M}\right)^{1/3}, \quad (2.3)$$

where  $R$  is the WD radius, so that the tidal radius for stellar disruption is a few times  $r_{\text{t}}$ . It is convenient to define the dimensionless pericentre distance<sup>1</sup>

$$\eta \equiv \frac{r_{\text{p}}}{r_{\text{t}}} = (1 - e) \left(\frac{\Omega_*}{\Omega}\right)^{2/3} \quad (2.4)$$

where  $\Omega = \sqrt{GM_{\text{bh}}/a^3}$  is the orbital angular frequency and  $\Omega_* = \sqrt{GM/R^3}$ . Note that tidal disruption occurs when  $\eta \lesssim 3$ .

Throughout the paper, we assume that disruption occurs outside of the Schwarzschild radius, so  $r_{\text{t}} \gtrsim 2GM_{\text{t}}/c^2$  or

$$\frac{M_{\text{t}}}{M} \lesssim 3.2 \times 10^5 \left(\frac{R}{0.012R_{\odot}}\right)^{3/2} \left(\frac{M}{0.6M_{\odot}}\right)^{-3/2}. \quad (2.5)$$

---

<sup>1</sup>Note that this is a different notation from, e.g., Press and Teukolsky [1977], where  $\eta_{\text{PT}} \equiv (r_{\text{p}}/r_{\text{t}})^{3/2}$

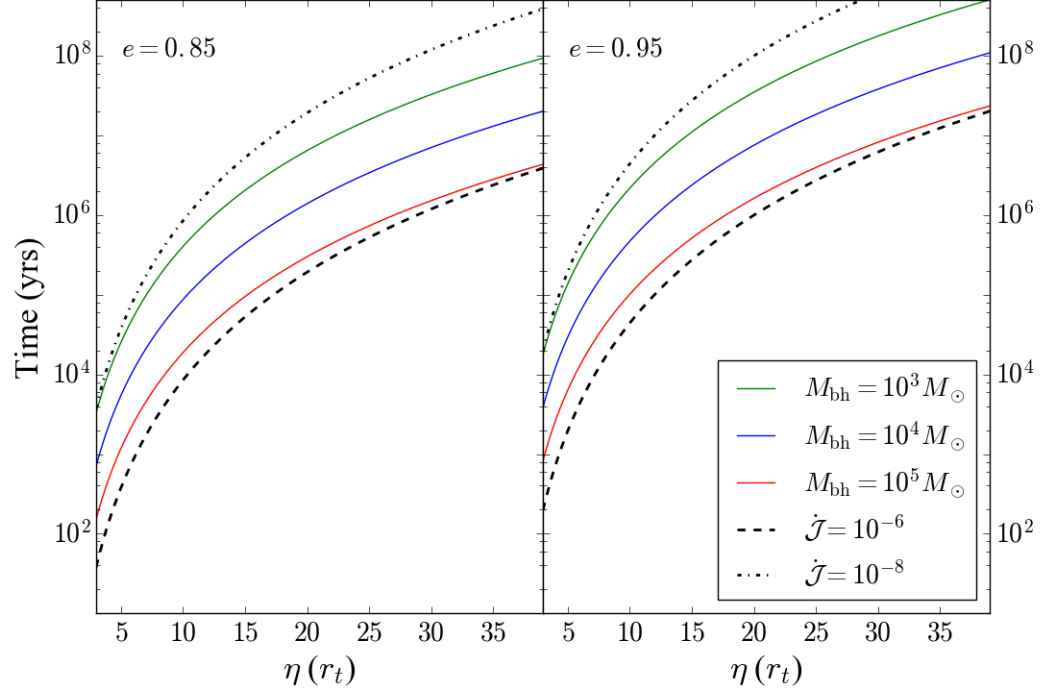


Figure 2.1: The orbital evolution timescales from equation (2.7) for gravitational radiation (solid coloured lines) for three different BH masses. The synchronization timescales (dotted lines) are also shown for two values of  $\dot{\mathcal{J}}$ . Note that the synchronization time [see equation (2.17)] is independent of  $M_{\text{bh}}$  when plotted vs.  $\eta$ . The WD mass is  $M = 0.6M_{\odot}$  and its radius is  $R = 0.012R_{\odot}$ . The left and right panels display results for  $e = 0.85$  and  $e = 0.95$  respectively.

In terms of  $\eta$ , the orbital evolution timescale due to gravitational radiation is (for  $M_{\text{bh}} \gg M$ )

$$t_{\text{grav}} = \frac{J}{|\dot{J}_{\text{grav}}|} = \frac{5}{32} \frac{c^5 R^4 \eta^4}{G^3 M^{7/3} M_{\text{bh}}^{2/3} (1-e)^{3/2}} \frac{(1+e)^{5/2}}{(1+7e^2/8)}. \quad (2.6)$$

Aside from the factor of  $(1-e)^{-3/2}$ ,  $t_{\text{grav}}$  depends rather weakly on  $e$ . Around  $e = 0.95$ , we have

$$\begin{aligned} t_{\text{grav}} = & 1.01 \times 10^5 \text{ yrs} \left( \frac{\eta}{10} \right)^4 \left( \frac{R}{0.012R_{\odot}} \right)^4 \\ & \times \left( \frac{M}{0.6M_{\odot}} \right)^{-7/3} \left( \frac{M_{\text{bh}}}{10^5 M_{\odot}} \right)^{-2/3} \left( \frac{1-e}{0.05} \right)^{-3/2}. \end{aligned} \quad (2.7)$$

The timescale for gravitational radiation is shown as a function of  $\eta$  in Fig. 2.1.

To estimate the timescale associated with tidal dissipation, we must know the rates of energy and angular momentum transfer via tides. In Sections 2.3 and 2.4, we present our calculations of these rates. A simple parametrization of the energy and angular momentum transfer rate can be obtained as follows. For a highly eccentric orbit, tidal torque on the WD mainly occurs near pericentre, and is of order

$$T_p \sim \frac{GM_{bh}^2 R^5}{r_p^6} \delta_p, \quad (2.8)$$

where  $\delta_p$  is the tidal lag angle (of order the inverse of the tidal quality factor,  $Q$ ). To obtain the orbit-averaged torque  $\langle T \rangle$ , we scale  $T_p$  by the ratio of  $\Omega$  to the orbital angular velocity at pericentre

$$\Omega_p = \frac{\Omega}{(1-e)^{3/2}} = \left(\frac{GM_{bh}}{a^3}\right)^{1/2} \frac{1}{(1-e)^{3/2}}. \quad (2.9)$$

Thus,

$$\langle T \rangle \sim \frac{GM_{bh}^2 R^5}{r_p^6} \delta_p \left(\frac{\Omega}{\Omega_p}\right). \quad (2.10)$$

Motivated by this expression, we define the dimensionless tidal angular momentum transfer rate,  $\dot{\mathcal{J}}$ , via

$$\langle T \rangle \equiv J_{tide} = \frac{GM_{bh}^2 R^5}{r_p^6} (1-e)^{3/2} \dot{\mathcal{J}}. \quad (2.11)$$

Similarly, we define the dimensionless tidal energy transfer rate in the inertial frame,  $\dot{\mathcal{E}}_{in}$ , via

$$\dot{E}_{tide,in} = \frac{GM_{bh}^2 R^5}{r_p^6} \Omega \dot{\mathcal{E}}_{in}. \quad (2.12)$$

When the WD has a finite rotation rate  $\Omega_s$ , we will also calculate the tidal energy transfer rate in the rotating frame,

$$\dot{E}_{tide,rot} = \dot{E}_{tide,in} - \Omega_s J_{tide} = \frac{GM_{bh}^2 R^5}{r_p^6} \Omega \dot{\mathcal{E}}_{rot}. \quad (2.13)$$

Our calculations in Sections 2.3 and 2.4 suggest that  $\dot{\mathcal{J}}$  ranges from  $\lesssim 10^{-8}$  for  $\eta \gtrsim 10$  to  $10^{-6}$  for  $\eta \sim$  a few.

The timescale for orbital evolution due to dynamical tides (for  $M_{\text{bh}} \gg M$ ) is given by

$$t_{\text{tide}} = \frac{J}{|\dot{J}_{\text{tide}}|} = \frac{M_{\text{bh}}^{2/3} R^{3/2} \eta^{13/2}}{G^{1/2} M^{7/6} \dot{\mathcal{J}}} \frac{(1+e)^{1/2}}{(1-e)^{3/2}}. \quad (2.14)$$

For an eccentricity of  $e = 0.95$ , we have

$$\begin{aligned} t_{\text{tide}} \simeq & 1.03 \times 10^{11} \text{ yrs} \left( \frac{\eta}{10} \right)^{13/2} \left( \frac{R}{0.012 R_{\odot}} \right)^{3/2} \left( \frac{M}{0.6 M_{\odot}} \right)^{-7/6} \\ & \times \left( \frac{M_{\text{bh}}}{10^5 M_{\odot}} \right)^{2/3} \left( \frac{\dot{\mathcal{J}}}{10^{-6}} \right)^{-1} \left( \frac{1-e}{0.05} \right)^{-3/2}. \end{aligned} \quad (2.15)$$

Comparing  $t_{\text{grav}}$  and  $t_{\text{tide}}$  shows that gravitational radiation dominates the orbital evolution. For an intermediate to massive BH, the gravitational radiation timescale is always much shorter than the tidal dissipation timescale, even for small pericentre distances of  $\eta \sim 3$ .

The tidal torque can also affect the rotation rate of the WD, driving it toward pseudo-synchronization, such that the WD rotation rate  $\Omega_s$  approaches a value comparable to the orbital frequency at pericentre  $\Omega_p$ . The tidal synchronization timescale can be estimated by

$$t_{\text{synch}} = \frac{I \Omega_p}{|\dot{J}_{\text{tide}}|} = \left( \frac{GM}{R^3} \right)^{-1/2} \frac{k \eta^{9/2}}{(1-e)^{3/2} \dot{\mathcal{J}}}, \quad (2.16)$$

where  $I = kMR^2$  is the moment of inertia of the WD. Note that the synchronization timescale is independent of the BH mass when written in terms of  $\eta$ . For  $k = 0.17$ , we have

$$t_{\text{synch}} = 4.1 \times 10^4 \text{ yrs} \left( \frac{\eta}{10} \right)^{9/2} \left( \frac{R}{0.012 R_{\odot}} \right)^{3/2} \times \left( \frac{M}{0.6 M_{\odot}} \right)^{-1/2} \left( \frac{\dot{\mathcal{J}}}{10^{-6}} \right)^{-1} \left( \frac{1-e}{0.05} \right)^{-3/2}. \quad (2.17)$$

For  $\dot{\mathcal{J}} = 10^{-6}$ , the synchronization timescale is shorter than the gravitational radiation timescale. In this case, the WD would be rotating at a rate  $\Omega_s \sim \Omega_p$  before tidal disruption, and rotation must be included in calculations of tidal

dissipation. However, if  $\dot{\mathcal{J}}$  is smaller by even a factor of 100, the WD will not synchronize before disruption (see Fig. 2.1). Results in Section 2.5 show that, at large separations,  $\dot{\mathcal{J}}$  can be as small as  $10^{-10}$ , implying that  $t_{\text{synch}} \gg t_{\text{grav}}$ . In this situation, the WD will rotate with its rotation rate at capture until its eventual disruption. For a captured isolated WD, we expect  $\Omega_s \ll \Omega_p$ , thus rotation has a small effect on dynamical tides. A WD that originated in a binary may still be rotating rapidly after capture, in which case the rotational effect can be significant.

### 2.3 WD Model and Physics of Tidal Dissipation

Tidal dissipation in WDs arises from the excitation of gravity waves in the deeper envelope of the WD and their dissipation in the outer envelope [Fuller and Lai, 2012c, 2013]. These processes depend on the detailed properties of the WD, in particular, properties of the envelope. In this paper, we consider two CO WD models consisting of a CO core with a He-H envelope. The models are constructed using the MESA stellar evolution code [Paxton et al., 2011]. Both WD models have mass  $M = 0.61M_\odot$ . One model has effective temperature  $T_{\text{eff}} = 9,000$  K. The other was allowed to evolve for a longer time and is therefore cooler with  $T_{\text{eff}} = 5,200$  K.

Fig. 2.2 displays the profiles for density  $\rho$ , Lamb (acoustic cut-off) frequency  $L_2$ , and the Brünt-Väisälä frequency  $N$  for the two WD models. The Lamb fre-

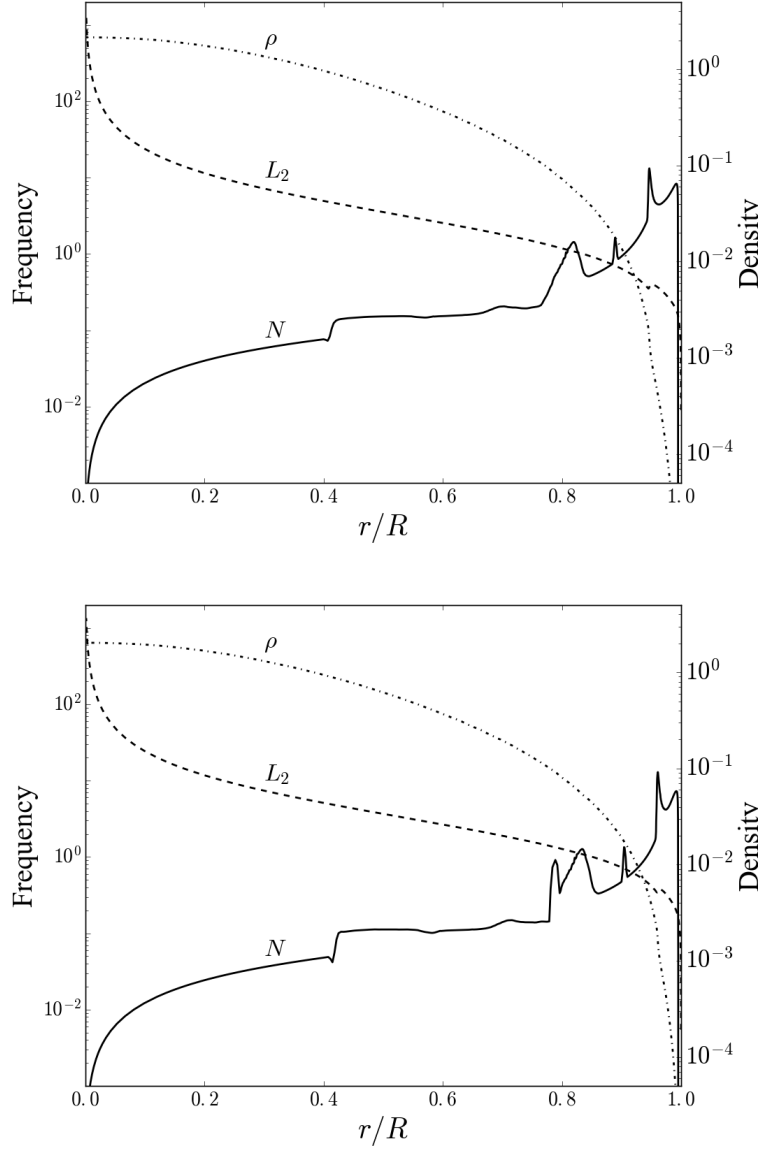


Figure 2.2: Propagation diagrams for MESA-generated WD models with mass  $M = 0.61M_{\odot}$  and radius  $R = 0.012R_{\odot}$ . The WD model in the upper plot has  $T_{\text{eff}} = 9,000$  K. The model in the lower plot has  $T_{\text{eff}} = 5,200$  K. The diagram includes the Brünt-Väisälä frequency  $N$  (solid line), the Lamb frequency  $L_2$  (dashed line) and the density  $\rho$  (dot-dashed line). Frequencies are in units of  $(GM/R^3)^{1/2}$ , and densities in units of  $(M/R^3)$ . The peaks in  $N$  generally correspond to compositional transitions from O to C, C to He, and He to H.

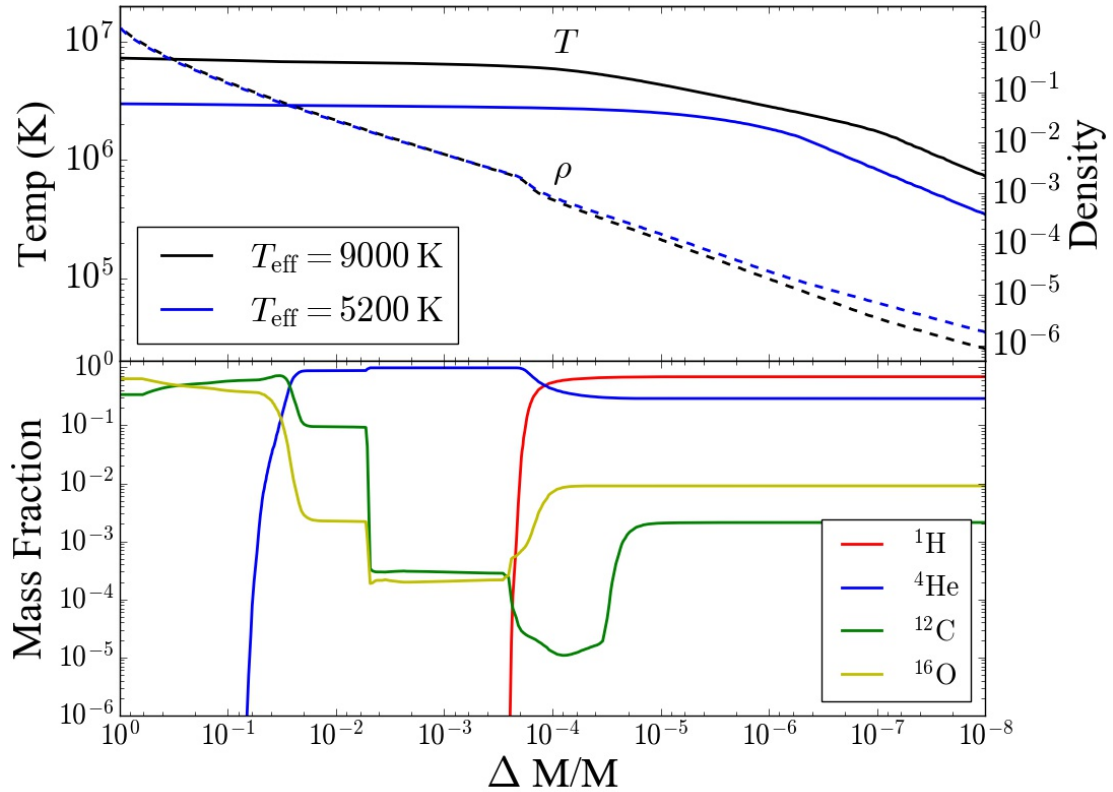


Figure 2.3: The upper panel displays the temperature  $T$  (solid lines) and density  $\rho$  (dashed lines) in units of  $(M/R^3)$  of two MESA-generated WD models as a function of the envelope depth by mass  $\Delta M$ . The bottom panel shows the composition of the WD with  $T_{\text{eff}} = 9,000$  K. The two models have very similar compositions. The transition from He to H occurs near  $\Delta M \sim 10^{-4}$ .

frequency  $L_l$  is given by

$$L_l^2 = \frac{l(l+1)a_s^2}{r^2}, \quad (2.18)$$

where  $a_s$  is the sound speed. The Brünt-Väisälä frequency is given by

$$N^2 = -g \left( \frac{1}{\rho} \frac{d\rho}{dr} + \frac{g}{a_s^2} \right), \quad (2.19)$$

where  $g$  is gravitational acceleration. Gravity waves propagate in regions where  $\omega < N$  and  $\omega < L_l$ , and become evanescent elsewhere. We see from Fig. 2.2 that the propagation diagrams for both WD models exhibit peaks in the  $N$ -profile that are associated with composition changes from CO to He and He to H. Fig.

2.3 shows the composition profile of the younger WD model. Peaks in  $N$  occur in similar locations in the two models but have somewhat different structures.

Fuller and Lai [2012b] studied dynamical tides in WD binaries. They showed that the binary companion excites a continuous train of outgoing gravity waves, primarily around the CO/He transition region. As the waves propagate toward the stellar surface, their amplitudes grow with decreasing density. Eventually, the waves dissipate through a combination of non-linear processes, radiative damping, and absorption at a critical layer[Zahn, 1975, Goldreich and Nicholson, 1989, Fuller and Lai, 2013]. For a circular orbit, the tidal potential acting on the WD can be written as

$$U(\mathbf{r}, t) = U(r)[Y_{22}(\theta, \phi)e^{-i\omega t} + c.c.], \quad (2.20)$$

with

$$U(r) = -\frac{GM_{\text{bh}}W_{22}r^2}{a^3}, \quad (2.21)$$

where  $W_{22} = (3\pi/10)^{1/2}$  and  $\omega = 2\Omega$  is the tidal forcing frequency for a non-rotating WD ( $\Omega_s = 0$ ). Using the method developed in Fuller and Lai [2012b] (similar in nature to the treatment of gravity wave damping in the centre of solar-type stars from Goodman and Dickson [1998], Ogilvie and Lin [2007], Barker and Ogilvie [2010], and Barker and Ogilvie [2011]) we calculate the amplitude of outgoing gravity waves excited by the potential in equation (2.20) as a function of  $\omega$  for the two WD models depicted in Fig. 2.2. The angular momentum flux carried by the waves is

$$\dot{J}(r) = 2m\omega^2\rho r^3\text{Re}(i\xi_r^*\xi_\perp), \quad (2.22)$$

where  $m$  is the azimuthal wave number ( $m = 2$  for circular binaries), and  $\xi_r(r)$  and  $\xi_\perp(r)$  are the radial and transverse Lagrangian displacements of the wave.

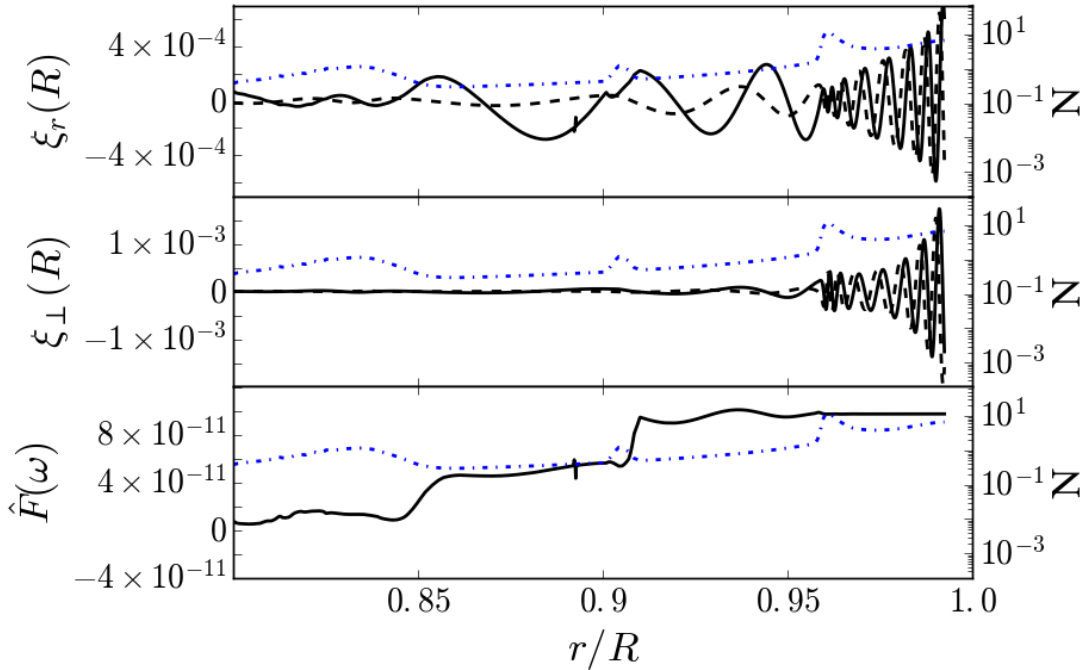


Figure 2.4: Dynamical tide in a realistic MESA-generated WD model produced by a companion in a circular orbit. The WD has mass  $M = 0.61M_{\odot}$  and radius  $R = 0.012M_{\odot}$  with  $T_{\text{eff}} = 5,200$  K. Tides are excited by a companion with mass  $M_{\text{bh}} = 10^5M_{\odot}$  at the frequency  $\omega = 0.01(GM/R^3)^{1/2}$ . The real parts of the radial and transverse Lagrangian displacements,  $\xi_r$  and  $\xi_{\perp}$ , are shown with solid black lines, and imaginary parts are shown with dotted black lines. The Brünt-Väisälä frequency in units of  $(GM/R^3)^{1/2}$  is overlaid in blue. Peaks correspond to compositional transitions. The dimensionless tidal torque  $\hat{F}(\omega)$  begins to rise at the C/He transition and settles to a constant value near the stellar surface.

Fig. 2.4 shows an example of the numerical result for  $\omega = 0.01 (GM/R^3)^{1/2}$ . We see that  $j(r)$  oscillates around zero in the WD interior but jumps to a constant value with the excitation of outgoing waves at compositional changes. The constant value of  $j(r)$  evaluated in the outermost region corresponds to the tidal torque acting on the WD.

Fuller and Lai [2012b] introduce a dimensionless function  $\hat{F}(\omega)$  to characterize how the tidal torque depends on the tidal forcing frequency:

$$j = G \left( \frac{M_{\text{bh}}}{a^3} \right)^2 R^5 \frac{|m|}{2} \hat{F}(\omega). \quad (2.23)$$

Similarly, the tidal energy transfer rate is given by

$$\dot{E} = G \left( \frac{M_{\text{bh}}}{a^3} \right)^2 R^5 \Omega \hat{F}(\omega). \quad (2.24)$$

Fig. 2.5 shows our numerical results for  $\hat{F}(\omega)$  for the two WD models. The  $\omega$  dependence of  $\hat{F}(\omega)$  can be roughly understood with a simplified WD model with two regions. The outer region has a much larger Brünt-Väisälä frequency than the inner region. The inner region is like a resonance cavity. While both ingoing and outgoing waves can propagate in the inner region, the outer region has only outgoing waves. In this model, a maximum tidal torque scales as  $\hat{F}_{\max}(\omega) \propto \omega^5$ . Our numerical results roughly agree with this scaling.

## 2.4 Tidal Dissipation in an Eccentric Orbit

We extend the method of the previous section to study dynamical tides in a WD in an eccentric orbit around a MBH. In this case, the quadrupolar tidal potential can be written as

$$U = \sum_m U_{2m}(\mathbf{r}_i, t), \quad (2.25)$$

with

$$U_{2m}(\mathbf{r}_i, t) = -\frac{GM_{\text{bh}}W_{2m}r_i^2}{D(t)^3} e^{-im\Phi(t)} Y_{2m}(\theta, \phi_i), \quad (2.26)$$

where  $D(t)$  is the binary separation,  $\Phi$  is the orbital phase (true anomaly),  $W_{2\pm 2} = \sqrt{3\pi/10}$ ,  $W_{20} = \sqrt{\pi/5}$  and  $W_{2\pm 1} = 0$ . The vector  $\mathbf{r}_i = (r, \theta, \phi_i = \phi + \Omega_s t)$ , is the position relative to the WD centre, with the azimuthal angle  $\phi_i$  measured in the inertial frame ( $\Omega_s$  is the rotation rate of the WD, and  $\phi$  is measured in the rotating frame). Each component of the potential can be decomposed into an infinite sum over

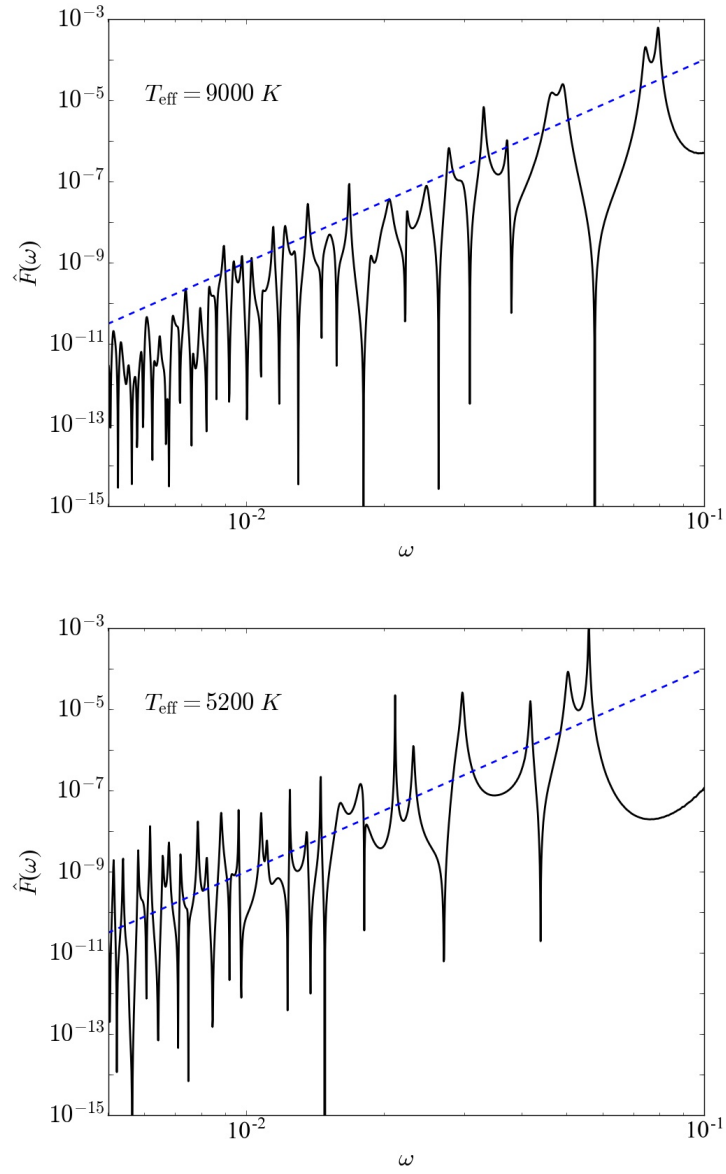


Figure 2.5: Dimensionless tidal torque  $\hat{F}(\omega)$  as a function of the tidal forcing frequency  $\omega$  in units of  $(GM/R^3)^{1/2}$  (solid lines). The left panel is for the WD model with  $M = 0.61M_\odot$ ,  $R = 0.012M_\odot$ , and  $T_{\text{eff}} = 9,000 \text{ K}$ . The blue dotted line shows  $10 \omega^5$ , which roughly follows the maximum of  $\hat{F}(\omega)$ . The right panel is for a similar WD model with effective temperature  $T_{\text{eff}} = 5,200 \text{ K}$ . The blue dotted line shows  $150 \omega^5$ .

forcing frequencies.

$$U_{2m} = -\frac{GM_{\text{bh}}W_{2m}r_i^2}{a^3}Y_{2m}(\theta, \phi_i) \sum_{N=-\infty}^{\infty} F_{Nm}e^{-iN\Omega t}, \quad (2.27)$$

where  $F_{Nm}$  is the Hansen coefficient [Murray and Dermott, 2000]

$$F_{Nm} = \frac{1}{\pi} \int_{-\pi}^{\pi} d\Psi \frac{\cos[N(\Psi - e \sin \Psi) - m\Phi(t)]}{(1 - e \cos \Psi)^2}, \quad (2.28)$$

with  $\Psi$  the eccentric anomaly.

The total energy and angular momentum transfer rates can be expressed as a sum of the responses due to each frequency term in the external potential.

First, consider the time-varying  $m = 0$  terms in the external potential,

$$U_{20} = -\frac{GM_{\text{bh}}W_{20}r^2}{a^3} \sum_{N=1}^{\infty} F_{N0}[Y_{20}(\theta, \phi_i)e^{-iN\Omega t} + c.c.]. \quad (2.29)$$

We have taken advantage of the fact that  $F_{N0} = F_{-N0}$ . Each term in equation (2.29) has the same form as equation (2.20), and contributes to the energy transfer rate as in equation (2.24):

$$\dot{E}_{m=0} = \frac{GM_{\text{bh}}^2R^5}{a^6} \left( \frac{W_{20}}{W_{22}} \right)^2 \sum_{N=1}^{\infty} N\Omega F_{N0}^2 \hat{F}(\omega = |N\Omega|). \quad (2.30)$$

The factor  $(W_{20}/W_{22})^2$  arises because  $\hat{F}(\omega)$  includes  $(W_{22})^2$ . The  $m = 0$  potential does not contribute to angular momentum transfer because it is axisymmetric.

We can determine the energy transfer rate due to  $m = \pm 2$  components of the potential using similar procedures. In the rotating frame of the WD,

$$U_{22} = -\frac{GM_{\text{bh}}W_{22}r^2}{a^3} \sum_{N=1}^{\infty} [F_{N2}Y_{22}(\theta, \phi)e^{-i(N\Omega-2\Omega_s)t} + F_{-N2}Y_{22}(\theta, \phi)e^{i(N\Omega+2\Omega_s)t}], \quad (2.31)$$

$$U_{2-2} = -\frac{GM_{\text{bh}}W_{22}r^2}{a^3} \sum_{N=1}^{\infty} [F_{-N2}Y_{2-2}(\theta, \phi)e^{-i(N\Omega+2\Omega_s)t} + F_{N2}Y_{2-2}(\theta, \phi)e^{i(N\Omega-2\Omega_s)t}]. \quad (2.32)$$

Using symmetries of the spherical harmonics, the sum of the  $m = 2$  and  $m = -2$  potentials reduces to

$$U_{22} + U_{-2} = -\frac{GM_{\text{bh}}W_{22}r^2}{a^3} \sum_{N=-\infty}^{\infty} [F_{N2}Y_{22}(\theta, \phi)e^{-i(N\Omega - 2\Omega_s)t} + c.c.] . \quad (2.33)$$

As with the  $m = 0$  terms of the potential, we can translate each term into an energy transfer rate of the same form as equation (2.24). However, equation (2.33) differs from equation (2.29) in that it includes both negative and positive  $\omega$ , so we must interpret the physical meaning of the contributions from the negative frequency terms. In a frame that rotates with the WD, positive  $\omega$  corresponds to the BH orbiting the WD in an anti-clockwise direction. Negative  $\omega$  corresponds to a clockwise orbit. Therefore, changing the sign of  $\omega$  reverses the sign of the angular momentum transfer rate, but does not affect the sign of the energy transfer rate (in the rotating frame).

Combining contributions from  $m = 0, -2$  and  $2$  gives the following expressions for angular momentum and energy transfer

$$\dot{J}_{\text{tide}} = T_0 \sum_{-\infty}^{\infty} F_{N2}^2 \text{sgn}(N\Omega - 2\Omega_s) \hat{F}(\omega = |N\Omega - 2\Omega_s|), \quad (2.34)$$

$$\begin{aligned} \dot{E}_{\text{tide,in}} = & T_0 \left[ \left( \frac{W_{20}}{W_{22}} \right)^2 \sum_{N=1}^{\infty} N\Omega F_{N0}^2 \hat{F}(\omega = |N\Omega|) \right. \\ & \left. + \frac{1}{2} \sum_{-\infty}^{\infty} N\Omega F_{N2}^2 \text{sgn}(N\Omega - 2\Omega_s) \hat{F}(\omega = |N\Omega - 2\Omega_s|) \right], \end{aligned} \quad (2.35)$$

$$\begin{aligned} \dot{E}_{\text{tide,rot}} = & T_0 \left[ \left( \frac{W_{20}}{W_{22}} \right)^2 \sum_{N=1}^{\infty} N\Omega F_{N0}^2 \hat{F}(\omega = |N\Omega|) \right. \\ & \left. + \frac{1}{2} \sum_{-\infty}^{\infty} F_{N2}^2 |N\Omega - 2\Omega_s| \hat{F}(\omega = |N\Omega - 2\Omega_s|) \right], \end{aligned} \quad (2.36)$$

with

$$T_0 \equiv \frac{GM_{\text{bh}}^2 R^5}{a^6}. \quad (2.37)$$

Note that the energy transfer rate in the inertial frame ( $\dot{E}_{\text{tide,in}}$ ) is related to that in the rotating frame through equation (2.13).

We can determine the dimensionless quantities  $\dot{\mathcal{J}}$ ,  $\dot{\mathcal{E}}_{\text{in}}$ , and  $\dot{\mathcal{E}}_{\text{rot}}$  from equations (2.11)-(2.13).

$$\dot{\mathcal{J}} = (1 - e)^{9/2} \sum_{-\infty}^{\infty} F_{N2}^2 \operatorname{sgn}(N\Omega - 2\Omega_s) \hat{F}(\omega = |N\Omega - 2\Omega_s|). \quad (2.38)$$

$$\begin{aligned} \dot{\mathcal{E}}_{\text{in}} = & (1 - e)^6 \left[ \left( \frac{W_{20}}{W_{22}} \right)^2 \sum_{N=1}^{\infty} N F_{N0}^2 \hat{F}(\omega = |N\Omega|) \right. \\ & \left. + \frac{1}{2} \sum_{-\infty}^{\infty} N F_{N2}^2 \operatorname{sgn}(N\Omega - 2\Omega_s) \hat{F}(\omega = |N\Omega - 2\Omega_s|) \right], \end{aligned} \quad (2.39)$$

$$\begin{aligned} \dot{\mathcal{E}}_{\text{rot}} = & (1 - e)^6 \left[ \left( \frac{W_{20}}{W_{22}} \right)^2 \sum_{N=1}^{\infty} N F_{N0}^2 \hat{F}(\omega = |N\Omega|) \right. \\ & \left. + \frac{1}{2} \sum_{-\infty}^{\infty} \hat{F}_{N2}^2 \left| N - 2 \frac{\Omega_s}{\Omega} \right| \hat{F}(\omega = |N\Omega - 2\Omega_s|) \right]. \end{aligned} \quad (2.40)$$

When calculating transfer rates, we used two conditions to truncate the sums in equations (2.38)-(2.40). The first is the physical condition that gravity waves with frequencies larger than  $\omega \sim 0.1 (GM/R^3)^{1/2}$  cannot propagate near the surface. This can be seen in the propagation diagrams for our two numerical WD models (see Fig. 2.2). Larger frequencies do not satisfy the conditions  $\omega < N$  and  $\omega < L_2$  in the outer envelope of the WD. Additionally, the WKB approximation used to calculate  $\hat{F}(\omega)$  becomes less reliable for  $\omega \sim 0.1 \gtrsim (GM/R^3)^{1/2}$ . We therefore assume that terms in the tidal potential with these frequencies do not contribute to the tidal transfer rates. Physically, this assumption is reasonable because high-frequency gravity waves either reflect from the stellar surface or do not suffer non-linear breaking, reducing their ability to contribute to tidal energy dissipation. Nevertheless, for small pericentre separations, this cut-off can significantly limit the number of allowed terms in equations (2.38)-(2.40), perhaps limiting the reliability of the calculated transfer rates.

The second truncation condition accounts for the fact that the Hansen coefficients fall off for large values of  $N$ . Terms with  $N \gtrsim 100$   $\Omega_p/\Omega$  do not contribute significantly to the transfer rates and are not included in the sums. Even with this cut-off, some values of  $F_{Nm}$  for large  $e$  and  $N$  cannot be efficiently calculated by numerically integrating equation (2.28). This is handled by approximating  $F_{Nm}$  for large  $N$  as a function of the form  $F_m(N) = \alpha N^\beta \exp(-\gamma N)$  where  $\alpha, \beta$ , and  $\gamma$  are determined by fitting  $F_m(N)$  for smaller  $N$ . The approximation is described in fuller detail in Appendix A.

To better understand which frequencies dominate the tidal transfer rates, we can examine individual components of the sum

$$\dot{\mathcal{J}} = \sum_N \dot{\mathcal{J}}_N. \quad (2.41)$$

Each value of  $N$  corresponds to an  $\omega$  via the relationship  $\omega = N\Omega - 2\Omega_s$ . In units of  $(GM/R^3)^{1/2}$ ,

$$\omega = \left(\frac{1}{\eta}\right)^{3/2} \left[ N(1-e)^{3/2} - 2\frac{\Omega_s}{\Omega_p} \right]. \quad (2.42)$$

Figs. 2.6 and 2.7 show examples of the individual terms that contribute to  $\dot{\mathcal{J}}$  for systems with different  $e$  and  $\eta$ . These figures display a few trends that are discussed further in Section 2.5. First, for  $\eta \gtrsim 10$ , increasing  $\eta$  lowers both the transfer rates and the dominant frequency in the sums (the frequency corresponding to the largest  $\dot{\mathcal{J}}_N$ ). Second, increasing  $e$  and  $\eta$  significantly increases the number of terms in the sums. This tends to smooth out the erratic dependence of  $\hat{F}(\omega)$  on  $\omega$ . Third, increasing  $\Omega_s$  tends to lower the transfer rates. Lastly, for  $\eta \lesssim 10$  and  $\Omega_s \sim \Omega_p$ , negative frequencies can contribute significantly to the sums.

There are a few limitations to the calculations of  $\dot{\mathcal{J}}$ ,  $\dot{\mathcal{E}}_{in}$ , and  $\dot{\mathcal{E}}_{rot}$  as presented in equations (2.38)-(2.40). First, the Coriolis force is not included in the com-

putation of  $\hat{F}(\omega)$ . The effects of rotation are handled solely by modifying the external potential. For the scenarios considered in this paper we do not expect a full treatment of rotation to significantly alter our results. Fuller and Lai [2014] demonstrated that increasing  $\Omega_s/\omega$  has little effect on  $\hat{F}(\omega)$  for a subsynchronous CO WD in which prograde g-waves contribute most to the tidal torque. However, the most dependable terms in the tidal transfer rate sums satisfy  $\omega \gtrsim \Omega_s$  or

$$N(1 - e)^{3/2} \gtrsim 3. \quad (2.43)$$

For a system with smaller  $\eta$ , few (if any) of the terms that satisfy this condition will also satisfy  $\omega < 0.1 (GM/R^3)^{1/2}$ . Furthermore, systems with small  $\eta$  are more likely to have large  $\Omega_s$  as they have shorter synchronization timescales. The calculated transfer rates may be less reliable for small  $\eta$  and large  $\Omega_s$ . Calculations for  $\eta \gtrsim 10$  are unaffected by this problem.

Another limitation is that (as noted above) the WKB approximation used to compute  $\hat{F}(\omega)$  breaks down for  $\omega \gtrsim 0.1 (GM/R^3)^{1/2}$ . Once again, only smaller values of  $\eta$  are affected by this limitation. Recall that  $\hat{F}(\omega)$  tends to increase steeply with  $\omega$ . Unless the Hansen coefficients,  $F_{Nm}$ , that correspond to large  $N\Omega$  are very small, the highest frequency terms dominate the tidal transfer rate sums. The Hansen coefficients fall off rapidly with increasing  $N$ , so the lower  $\Omega$ , the lower the dominant forcing frequency and the more reliable the calculated transfer rates. In general, results from systems with large  $\eta$  and small  $\Omega_s$  are the most reliable.

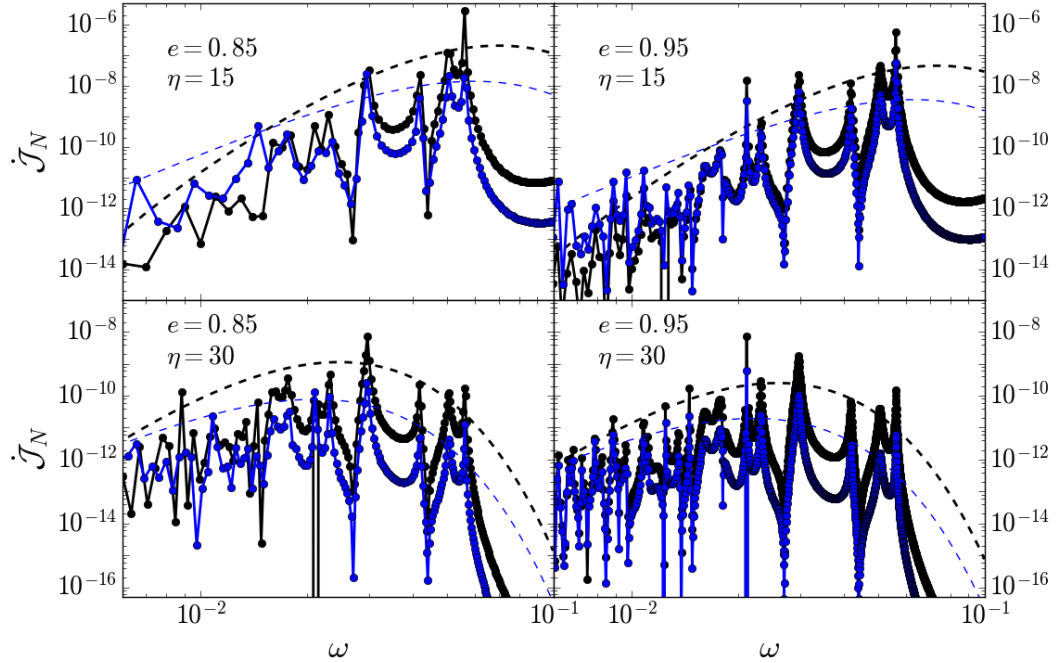


Figure 2.6: The individual terms  $\dot{\mathcal{J}}_N$  that sum to  $\dot{\mathcal{J}}$  as a function of frequency  $\omega$  in units of  $(GM/R^3)^{1/2}$  for the cooler WD model. Frequency is related to  $N$  by equation (2.42). The dotted lines show the same calculations using  $\hat{F}(\omega) = 150 \omega^5$ . The black lines show results for  $\Omega_s = 0$ . The blue lines show results for  $\Omega_s = \Omega_p$ , and roughly correspond to a system with a pseudo-synchronously rotating WD. For the bottom row with  $\eta = 30$ , the largest peak corresponds to a lower  $\omega$  than in the upper panels. Negative frequency terms are not included because their contributions are relatively small for large  $\eta$ .

## 2.5 Results for Tidal Energy and Angular Momentum Transfer Rates

Using the procedure and assumptions described in Section 2.4, we calculate the dimensionless tidal transfer rates  $\dot{\mathcal{E}}_{\text{in}}$ ,  $\dot{\mathcal{E}}_{\text{rot}}$  and  $\dot{\mathcal{J}}$  for both WD models for a variety of  $\eta$ ,  $e$  and  $\Omega_s$ . To discuss the results, we will consider two different regimes — the far regime, where  $\eta \gtrsim 10$  (the pericentre distance is more than 10 times the tidal radius), and the close regime, where  $\eta \lesssim 10$ .

Fig. 2.8 shows some numerical results of  $\dot{\mathcal{E}}_{\text{in}}$ ,  $\dot{\mathcal{E}}_{\text{rot}}$ , and  $\dot{\mathcal{J}}$  in the far regime.

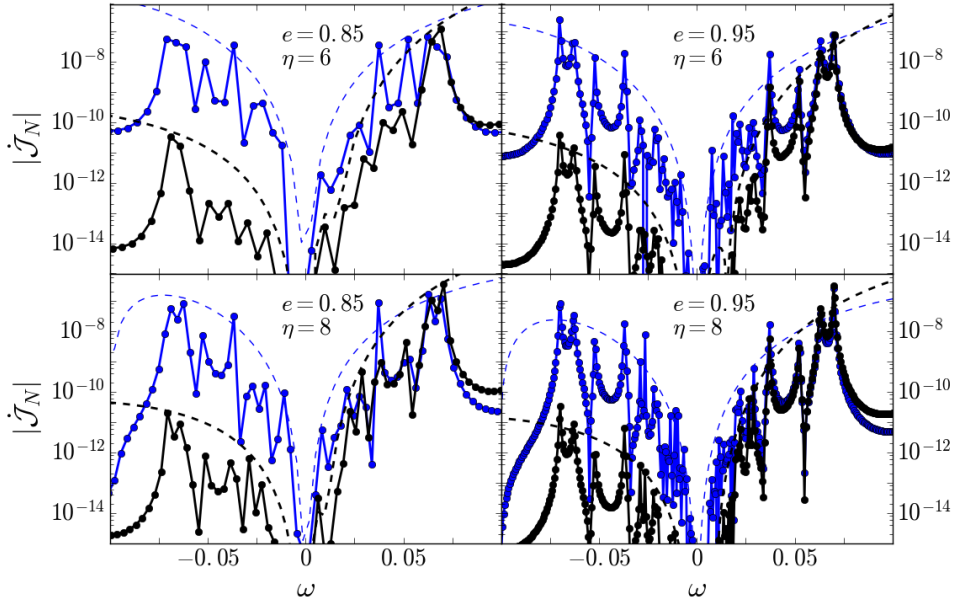


Figure 2.7: Similar to Fig. 2.6, but for smaller values of  $\eta$  and with negative frequency terms included. Negative frequency terms are most important for systems with rotating WDs and smaller values of  $\eta$ . Because calculations of  $\hat{F}(\omega)$  do not include the Coriolis force, terms with  $\Omega_s > |\omega|$  may be less reliable. Unfortunately, this stringently limits the number of reliable terms for small  $\eta$  and large  $\Omega_s$ . In the top panels,  $\Omega_s = 0.068 (GM/R^3)^{1/2}$ , and none of the plotted terms meet the above criterion. In the bottom panels,  $\Omega_s = 0.044 (GM/R^3)^{1/2}$ .

In general, the transfer rates decrease with increasing  $\eta$ . This occurs because increasing  $\eta$  decreases the orbital angular velocity  $\Omega$ , so a term in equations (2.38)–(2.40) with a given  $N$  will correspond to a lower frequency. Because  $\hat{F}(\omega)$  is generally smaller for smaller frequencies, the overall tidal transfer rates are lower.

The dependence of the transfer rates on  $\eta$  is stronger for lower eccentricities. This is because the Hansen coefficients  $F_{Nm}$  fall off more quickly with  $N$  for smaller values of  $e$ . As a result, fewer terms of the sums in equations (2.38)–(2.40) contribute significantly to the transfer rates. So as the eccentricity decreases,  $\dot{\mathcal{E}}_{\text{in}}(\eta)$ ,  $\dot{\mathcal{E}}_{\text{rot}}(\eta)$ , and  $\dot{\mathcal{J}}(\eta)$  exhibit more of the irregular variations of the dimensionless tidal torque,  $\hat{F}(\omega)$ .

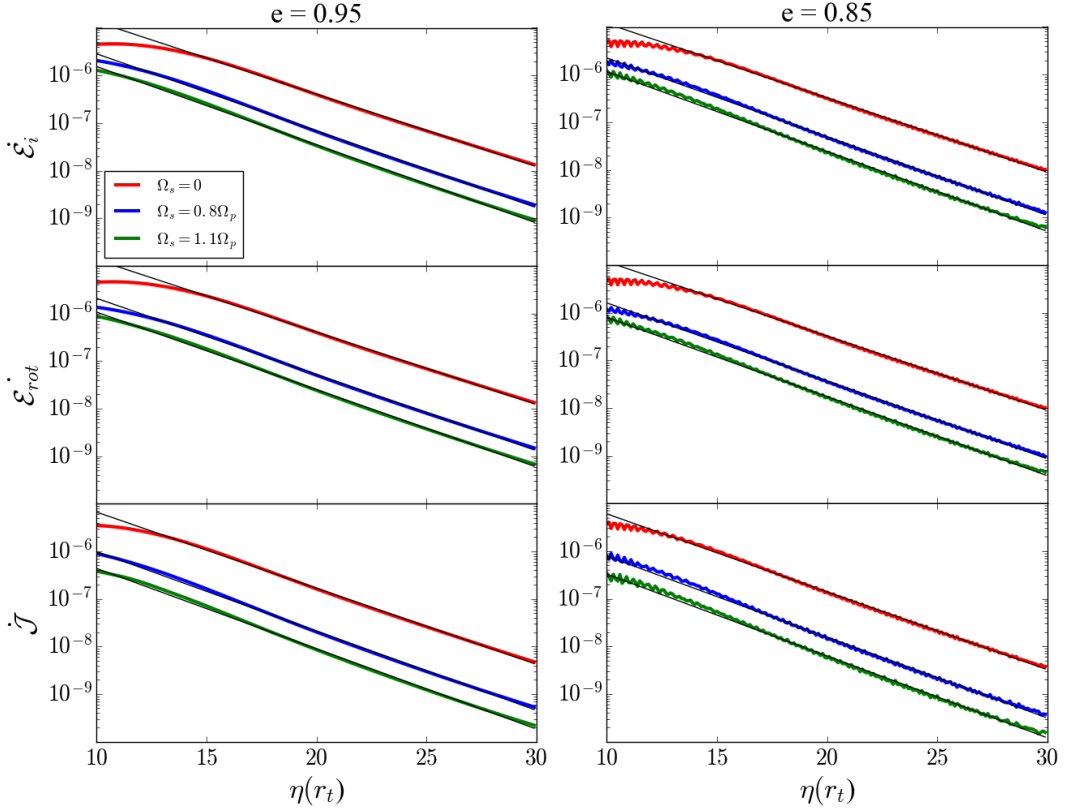


Figure 2.8: The dimensionless transfer rates  $\dot{\mathcal{E}}_{in}$  (on top),  $\dot{\mathcal{E}}_{rot}$  (in the middle), and  $\dot{\mathcal{J}}$  (on the bottom) as a function of  $\eta$  for eccentricities of  $e = 0.95$  (on the left) and  $e = 0.85$  (on the right). These results are for the WD model with  $T_{\text{eff}} = 9,000$  K. Results from the older, cooler WD are qualitatively similar. The three colours in each panel show calculations for three values of  $\Omega_s$  —  $\Omega_s = 0$ , and two values near  $\Omega_s = \Omega_p$ ,  $\Omega_s = 0.8 \Omega_p$  and  $1.1 \Omega_p$ . Simple power law fits for  $\eta \geq 15$  [see equations (2.44)-(2.46)] are plotted in black over the numerical results. For smaller values of  $\eta$ , the power law fits deviate from the results.

The tidal transfer rates decrease with increasing  $\Omega_s$ . The physical reason for this is especially clear for angular momentum transfer. As the WD is spun up to a pseudo-synchronous state, the angular momentum transfer rate goes to zero. If the WD rotation rate is larger than the pseudo-synchronous rate, the transfer rate is negative (i.e., angular momentum is transferred from the WD to the orbit). The primary mathematical reason why the dimensionless transfer rates decrease with increasing  $\Omega_s$  is that the tidal forcing frequency is

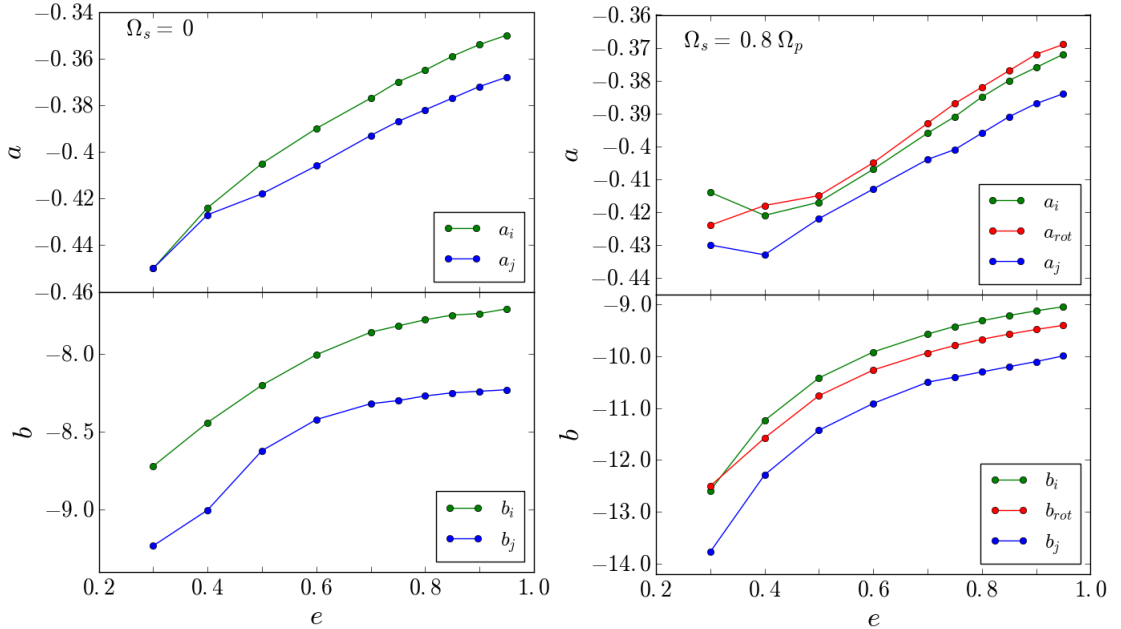


Figure 2.9: The parameters  $a$  and  $b$  found by fitting  $\dot{\mathcal{E}}_{\text{in}}(\eta)$ ,  $\dot{\mathcal{E}}_{\text{rot}}(\eta)$  and  $\dot{\mathcal{J}}(\eta)$  with equations (2.44)–(2.46) for  $\Omega_s = 0$  (on the left) and  $\Omega_s = 0.8 \Omega_p$  (on the right) and a variety of eccentricities  $e$ . Both  $a$  and  $b$  tend to increase with increasing  $e$ . These results are for the WD model with  $T_{\text{eff}} = 9,000$  K.

$\omega = N\Omega - 2\Omega_s$ . The  $2\Omega_s$  shift generally results in lower values of  $\hat{F}(\omega)$  for a given  $N$ , decreasing the overall sums in equations (2.38)–(2.40).

Recall that the synchronization timescale, equation (2.17), depends inversely on  $\dot{\mathcal{J}}$ . Examining Fig. 2.1 suggests that, for large  $\eta$ , the synchronization timescale will be orders of magnitude longer than the timescale for orbital evolution due to gravitational radiation. For a WD-MBH system with a large pericentre distance, it is reasonable to approximate the WD as non-rotating. In our study of the effects of tidal heating on the WD we assume a non-rotating WD.

Over the range  $15 \leq \eta \leq 30$ , the tidal transfer rates depend on  $\eta$  in a simple

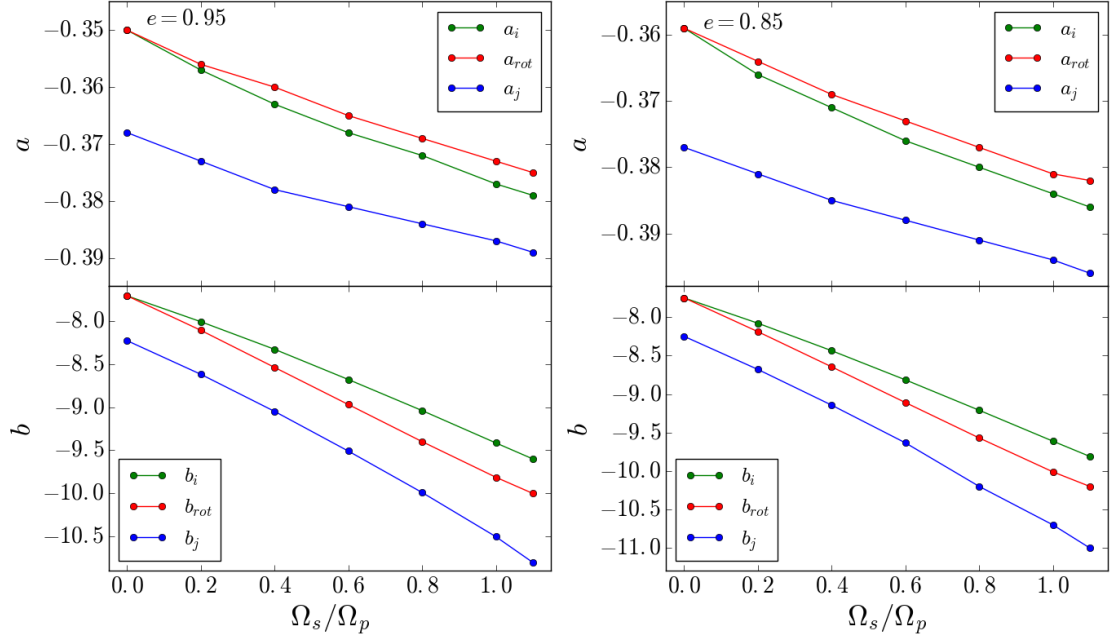


Figure 2.10: The parameters  $a$  and  $b$  found by fitting  $\dot{\mathcal{E}}_{\text{in}}(\eta)$ ,  $\dot{\mathcal{E}}_{\text{rot}}(\eta)$  and  $\dot{\mathcal{J}}(\eta)$  with equations (2.44)-(2.46) for  $e = 0.95$  (on the left) and  $e = 0.85$  (on the right) and a variety of  $\Omega_s$ . Both  $a$  and  $b$  tend to decrease with increasing  $\Omega_s$ . These results are for the WD model with  $T_{\text{eff}} = 9,000$  K.

way, and can be fitted in the form

$$\dot{\mathcal{E}}_{\text{in}}(\eta) = \exp(a_i \eta + b_i), \quad (2.44)$$

$$\dot{\mathcal{E}}_{\text{rot}}(\eta) = \exp(a_{\text{rot}} \eta + b_{\text{rot}}), \quad (2.45)$$

$$\dot{\mathcal{J}}(\eta) = \exp(a_j \eta + b_j). \quad (2.46)$$

In the above equations, the  $a$ 's and  $b$ 's depend on  $e$ ,  $\Omega_s$  and the WD models. Figs. 2.9-2.12 show the results of fittings for multiple combinations of  $e$  and  $\Omega_s$ . Both  $a$ 's and  $b$ 's tend to increase with  $e$  and decrease with  $\Omega_s$  over some small range. The smaller the eccentricity, the more variable the transfer rates, so fittings are less certain for  $e \lesssim 0.5$ . In the next section, we will ignore any  $\Omega_s$  dependence, assuming that a WD at  $\eta \gtrsim 10$  is far from synchronization and was very slowly rotating when captured.

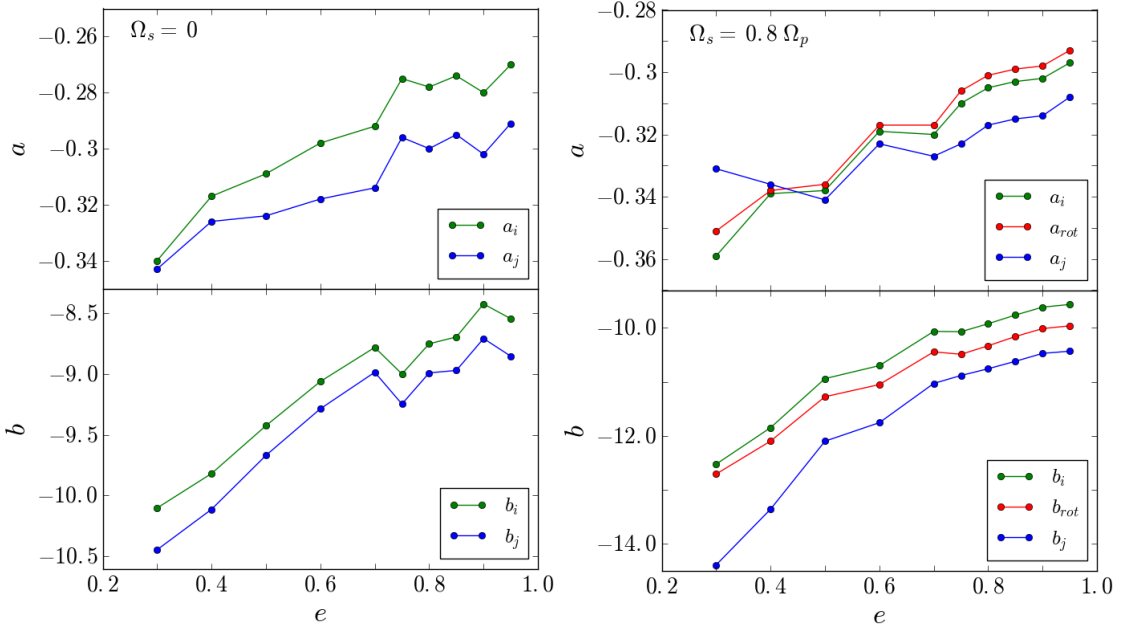


Figure 2.11: The parameters  $a$  and  $b$  found by fitting  $\dot{\mathcal{E}}_{\text{in}}(\eta)$ ,  $\dot{\mathcal{E}}_{\text{rot}}(\eta)$  and  $\dot{\mathcal{J}}(\eta)$  with equations (2.44)-(2.46) for  $\Omega_s = 0$  (on the left) and  $\Omega_s = 0.8 \Omega_p$  (on the right) and a variety of eccentricities  $e$ . Both  $a$  and  $b$  tend to increase with increasing  $e$ . These results are for the WD model with  $T_{\text{eff}} = 5,200$  K.

The tidal transfer rates for  $\eta \leq 10$  are shown in Fig. 2.13. These results can be understood qualitatively. For the same reasons as in the far regime, the transfer rates decrease with increased  $\Omega_s$  and vary more for lower values of  $e$ . Unlike in the far regime, the transfer rates do not decrease with  $\eta$ . They only vary within a factor of a few. This is because, for small values of  $\eta$ , setting a maximum frequency of  $0.1 (GM/R^3)^{1/2}$  significantly reduces the number of frequency terms that contribute to the transfer rates. For small  $\eta$ , imposing the maximum frequency when  $\Omega_s$  is comparable to  $\Omega_p$  can limit the number of positive frequency terms in equations (2.38) and (2.39) so that  $\dot{\mathcal{J}}$  and  $\dot{\mathcal{E}}_{\text{in}}$  are negative (see Fig. 2.13). As  $\eta$  increases, more terms fall within the allowed frequency range, increasing the value of the sum. This increase is counteracted by the decrease of  $\hat{F}(\omega)$  with decreasing  $\omega$ . Calculations in this regime are less reliable than those for large  $\eta$  due to a number of reasons discussed in Section 2.4. Additionally, calcula-

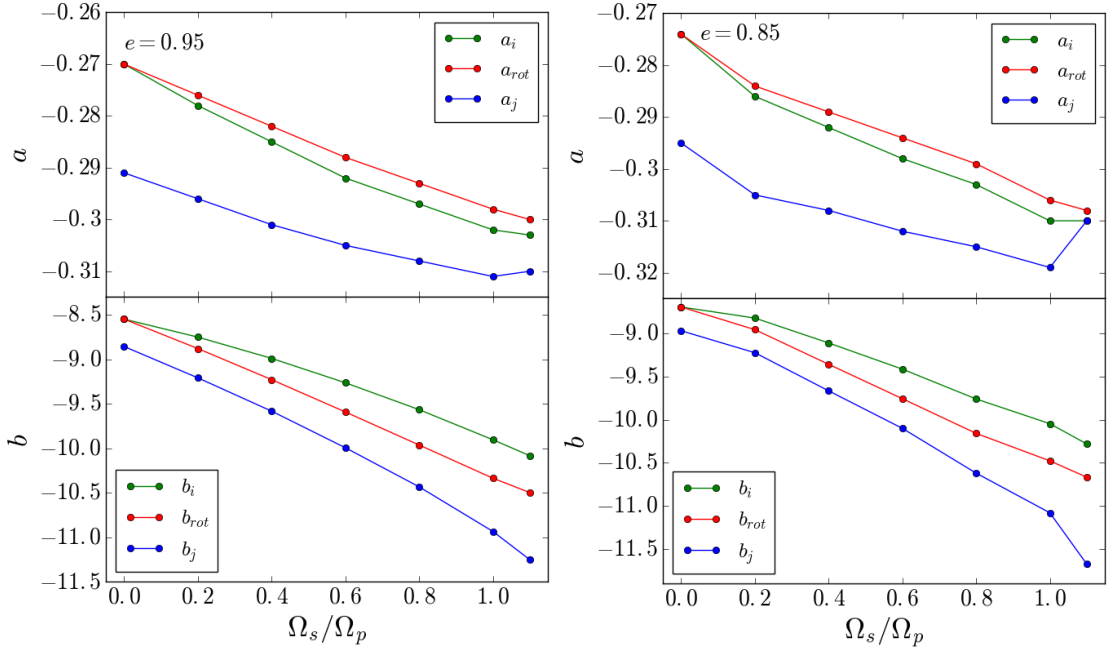


Figure 2.12: The parameters  $a$  and  $b$  found by fitting  $\dot{\mathcal{E}}_{\text{in}}(\eta)$ ,  $\dot{\mathcal{E}}_{\text{rot}}(\eta)$  and  $\dot{\mathcal{J}}(\eta)$  with equations (2.44)-(2.46) for  $e = 0.95$  (on the left) and  $e = 0.85$  (on the right) and a variety of  $\Omega_s$ . Both  $a$  and  $b$  tend to decrease with increasing  $\Omega_s$ . These results are for the WD model with  $T_{\text{eff}} = 5,200$  K.

tions for low  $\eta$  are more influenced by terms with  $\omega < \Omega_s$ , where it would be necessary to consider the Coriolis force for a realistic calculation of the transfer rates.

## 2.6 Tidal Heating

Though tidal dissipation has little impact on the WD's orbital evolution, tidal heating can still affect the structure of the WD. In Section 2.5, we showed that for  $\eta \gtrsim 15$ , the tidal energy transfer rates have a simple dependence on  $\eta$  [see equations (2.44)-(2.46)]. In particular,  $\dot{\mathcal{E}}_{\text{rot}}$  corresponds to the tidal heating rate of the WD. This allows for a first attempt at calculating the effects of tidal heating

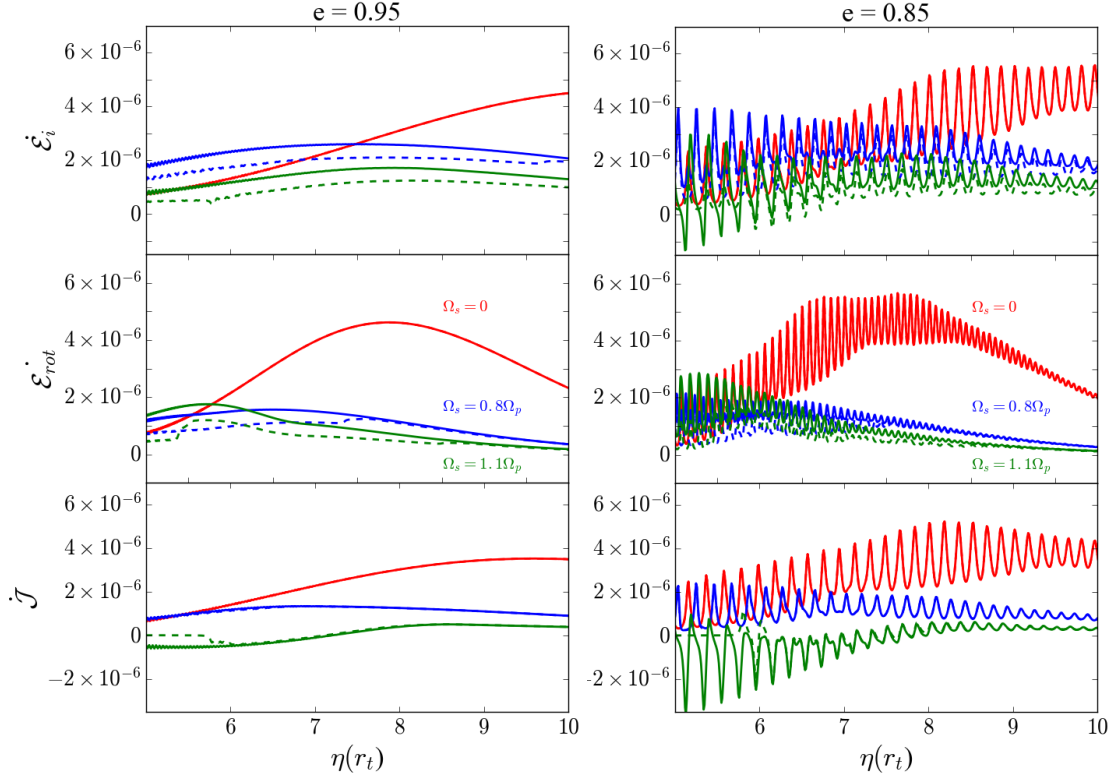


Figure 2.13: The dimensionless transfer rates  $\dot{\mathcal{E}}_{\text{in}}$  (on top),  $\dot{\mathcal{E}}_{\text{rot}}$  (in the middle), and  $\dot{\mathcal{J}}$  (on the bottom) as a function of  $\eta$  for the WD model with  $T_{\text{eff}} = 9,000$  K. The left and right panels show different eccentricities. The three colours in each panel show calculations for three values of  $\Omega_s$ . The dotted lines show the result of excluding terms with  $\omega < \Omega_s$  from each sum. Note that the transfer rates only vary by factors of a few. In addition,  $\dot{\mathcal{J}}$  is negative for small values of  $\eta$ .

on the WD throughout orbital decay.

We study the thermal evolution of the two MESA-generated WD models (described in Section 2.3). This calculation combines orbital evolution due to gravitational radiation and tidal heating as a function of orbital parameters  $\eta$  and  $e$ . We approximate the WD as non-rotating, which is supported by the fact that the synchronization timescale is many times longer than the timescale for orbital evolution. When  $\dot{\mathcal{E}}_{\text{rot}}$  is known, the energy transfer rate is given by

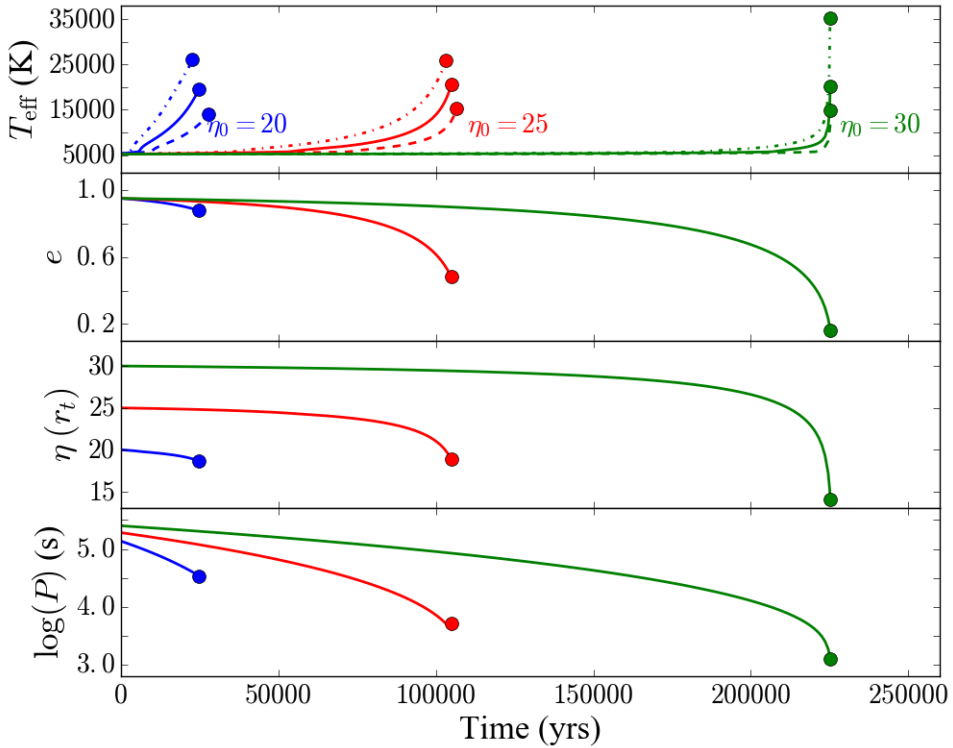


Figure 2.14: Evolution of the effective temperature of a MESA WD model with initial  $T_{\text{eff}} = 5,200$  K orbiting a  $10^5 M_{\odot}$  BH due to tidal heating as the orbit decays. The WD radius remains roughly constant throughout heating. The lower three panels show the evolution of  $e$ ,  $\eta$  and the orbital period  $P$  (in seconds). The different colours represent different initial separations between the BH and WD. All systems start evolution with  $e = 0.95$ . The solid, dashed and dotted lines show results for the envelope thicknesses  $\Delta M = 10^{-4}M$ ,  $2 \times 10^{-4}M$ , and  $5 \times 10^{-5}M$  respectively. The circles indicate the onset of hydrogen burning in the outer envelope of the WD.

equation (2.13). In terms of standard values,

$$\begin{aligned} \dot{E}_{\text{tide,rot}} = & 1.4 \times 10^{34} \text{ erg s}^{-1} \left( \frac{M}{0.6M_{\odot}} \right)^{5/2} \left( \frac{R}{0.012R_{\odot}} \right)^{-5/2} \\ & \times \left( \frac{\eta}{10} \right)^{-15/2} \left( \frac{\dot{E}_{\text{rot}}}{10^{-6}} \right) \left( \frac{1-e}{0.05} \right)^{3/2}. \end{aligned} \quad (2.47)$$

Heat is deposited in the outer envelope of the WD as waves break via non-linear processes. For simplicity, we assume uniform heat deposition in a shell with  $\Delta M \sim 10^{-4}M$ . This depth corresponds to the transition from He to H in the WD (see Fig. 2.3), which is approximately where non-linear wave breaking

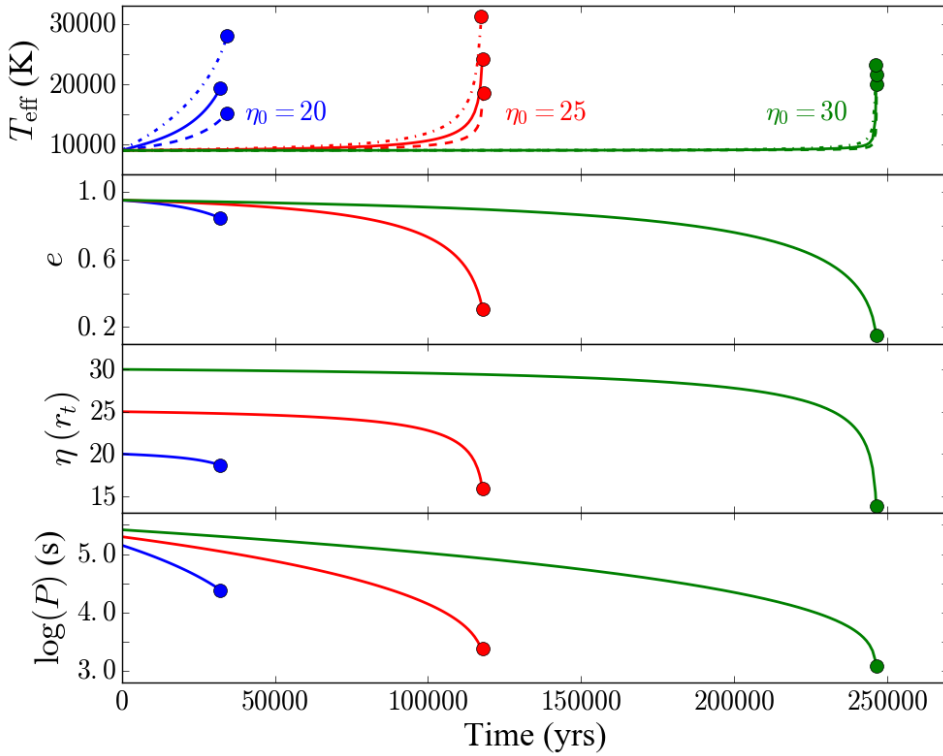


Figure 2.15: Same as above for a MESA WD model with initial  $T_{\text{eff}} = 9,000$  K.

occurs [Fuller and Lai, 2012c]. We inject tidal heat into the WD model and use MESA to track the profile and global properties of the WD as its orbit undergoes decay and circularization due to gravitational radiation.

In more detail, at each timestep of orbital evolution,

- the orbital parameters  $e$  and  $\eta$  are integrated forward in time;
- new values for  $a_{\text{rot}}$ ,  $a_j$ ,  $b_{\text{rot}}$ , and  $b_j$  are approximated by interpolating between results in Figs. 2.9-2.11;
- $\dot{\mathcal{E}}_{\text{rot}}$  is determined using equation (2.45). This value is always within a factor of a few of results from Section 2.5;
- the heating rate is calculated using equation (2.47) and the assumption that heat is uniformly deposited into an envelope of depth  $\Delta M$ ;

- the WD structure is evolved with the new heating rate until the next timestep using MESA.

Using this procedure, we can track the structural evolution of a WD that is captured into orbit around a BH at some initial pericentre distance  $\eta_0$  and eccentricity  $e_0$ . The results of these calculations are shown in Figs. 2.14 and 2.15. We used initial eccentricity  $e_0 = 0.95$  and a variety of initial pericentre distances  $\eta_0$ , focusing on the evolution of systems with  $15 < \eta_0 < 35$ . We have the cleanest prescription for  $\dot{E}_{\text{tide,rot}}(e, \eta)$  when  $\eta \gtrsim 15$ . When  $\eta_0 \gtrsim 35$ , the orbit will nearly circularize before  $\eta$  is small enough for the WD to experience significant heating. As the eccentricity falls below  $e \sim 0.5$ , our technique for calculating tidal heating becomes less reliable. Tidal dissipation in a WD in a circular orbit is studied in detail in Fuller and Lai [2012b,c].

As the WD orbit shrinks, the heating rate increases more and more rapidly. We find that, for both WD models, the amount of heating from tides excited by a  $10^5 M_\odot$  BH is enough to trigger fusion in the semi-degenerate hydrogen layer well before gravitational radiation shrinks the orbit to  $\sim 3r_t$ . While the WD undergoes tidal heating, the radius remains constant within a few percent. The maximum luminosity before envelope ignition varies from  $\sim 10^{-2} L_\odot$  for  $\Delta M = 2 \times 10^{-4}$  to  $\sim 0.4 L_\odot$  for  $\Delta M = 5 \times 10^{-3}$ . Tidally induced novae were also suggested to occur in merging WD binaries [Fuller and Lai, 2012c] but have not been examined in the context of eccentric WD-MBH binaries.

To understand why tidal heating induces nuclear runaway, it is useful to compare the timescale for extra heat to escape the WD with the timescale for injecting heat. The first of these is the thermal timescale  $t_{\text{therm}}$ , which

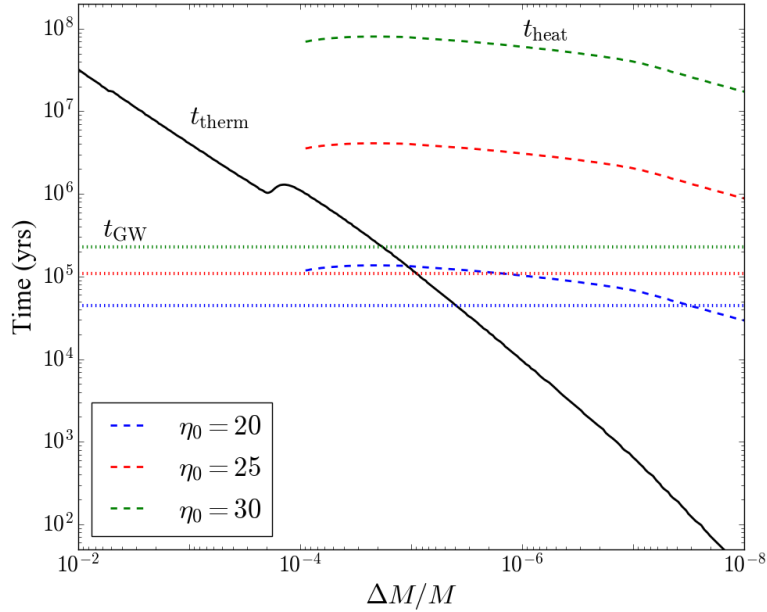


Figure 2.16: A comparison of timescales for the WD model with  $T_{\text{eff}} = 9,000 \text{ K}$  before tidal heating occurs. Envelope depth is plotted on the x-axis. The thermal timescale (solid line) characterizes the time for added heat to diffuse to the surface [see equation (2.48)]. The heating timescales (dashed lines) characterize the time for material at a given depth to heat up [see equation (2.49)]. The heating timescale is shown for heating rates at  $\eta_0 = 20, 25$  and  $30$ . The timescale for falling into a  $10^5 M_\odot$  BH (dotted lines) is also shown for  $\eta_0 = 20, 25$  and  $30$ .

characterizes the amount of time for heat to diffuse to the WD surface as a function of radius. This timescale is determined by the WD structure and given by

$$t_{\text{therm}}(r) = \frac{pc_p T}{gF}, \quad (2.48)$$

where  $c_p$  is the specific heat capacity at constant pressure,  $p$  is pressure,  $g$  is gravitational acceleration, and  $F$  is energy flux. Note that  $t_{\text{therm}}$  varies by many orders of magnitude between the core and surface. Heat deposited in the core may take billions of years to diffuse, while heat deposited very close to the surface can exit the WD in a fraction of a year.

The heating timescale measures how long it takes for a given energy trans-

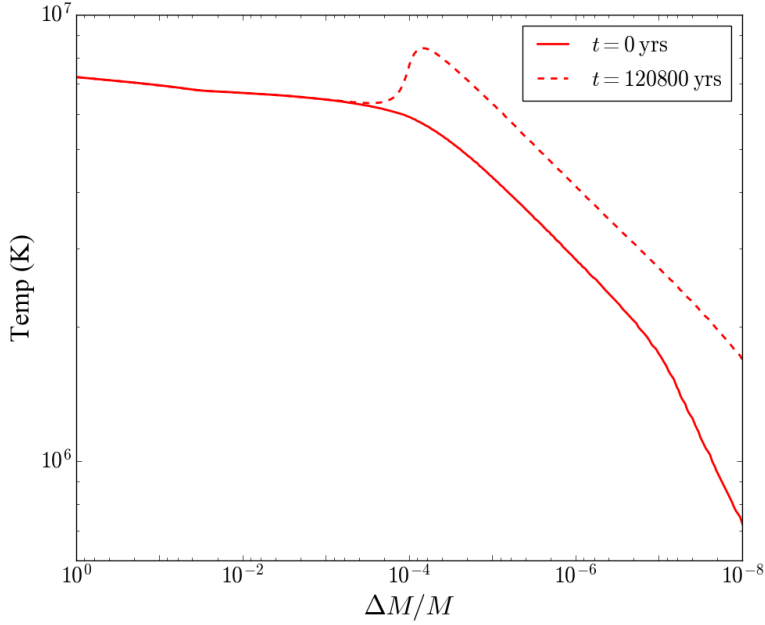


Figure 2.17: The temperature profile of the WD model with  $T_{\text{eff}} = 9,000 \text{ K}$  shown at two different times. At  $t = 0$  (solid line), the WD is in an orbit with  $e_0 = 0.95$  and  $\eta_0 = 25$ . After 120,800 yrs of evolution (dashed line), the hydrogen envelope is close to ignition.

fer rate to heat up of layer of material.

$$t_{\text{heat}}(r) = \frac{c_p T}{\dot{\epsilon}}, \quad (2.49)$$

where  $\dot{\epsilon}$  is  $\dot{E}_{\text{tide,rot}}/\Delta M$ . Note that this timescale depends on the assumed envelope mass. A thinner envelope will both heat and cool much more quickly. The heating timescale only varies by a factor of a few across the outer envelope. When  $t_{\text{heat}} \gtrsim t_{\text{therm}}$ , the additional heat diffuses very quickly and in layers closest to the surface. This is the case when the WD is far away from the BH and  $\dot{E}_{\text{rot}}$  is relatively small (see Fig. 2.16). However, as the WD orbit evolves, eventually  $t_{\text{heat}} \lesssim t_{\text{therm}}$  at the base of the outer envelope. Then heat is trapped and the shell heats up. This is clear from examining the temperature profile of the WD just before the onset of runaway fusion (see Fig. 2.17). Heating of the degenerate hydrogen layer can

lead to runaway fusion because the pressure of this layer is independent of the temperature. For a WD captured at  $\eta_0 = 20$ , the base of the heating envelope already meets the criterion  $t_{\text{heat}} < t_{\text{therm}}$  before gravitational radiation shrinks the orbit. In this case, the hydrogen layer quickly heats up and ignites within a few thousand years, well before gravitational radiation drives the WD toward tidal disruption. For a WD with the same envelope captured at  $\eta_0 = 30$ ,  $t_{\text{heat}} > t_{\text{therm}}$  for a substantial fraction of the gravitational radiation timescale. In this case, heat is only trapped after the orbit has evolved long enough that  $\eta$  is about half of its original value.

We caution that the non-linear breaking depth which determines  $\Delta M$  is somewhat uncertain, as is the formation of critical layers which can absorb wave energy [Fuller and Lai, 2012c, Burkart et al., 2012]. If heat deposition is limited to the outermost layers (where non-linear breaking is most assured)  $t_{\text{therm}} \ll t_{\text{heat}}$ , so the heat will diffuse out before creating a thermonuclear run away. If heat is distributed deeper in the WD, throughout the He layer, it may have little effect on the structural evolution of the WD. Assuming that non-linear breaking occurs at a critical layer of depth  $\Delta M \sim 10^{-4}M$ , we expect that a CO WD on the path to disruption will lose its hydrogen envelope due to a tidally induced nova before arrival.

## 2.7 Summary and Discussion

We have studied the effects of dynamical tides on the orbital and structural evolution of a WD in a high-eccentricity orbit around a massive BH. For such WD-MBH binaries, dynamical tides involve the tidal excitation of outgoing gravity waves in the deeper envelope (around the transition re-

gion between the CO core and He layer) and their dissipation in the outer envelope of the WD. We find that these dynamical tides have a negligible impact on the orbital evolution in comparison to gravitational radiation (GR). Additionally, the timescale for spinning up the WD via dynamical tides is generally longer than the GR-timescale. However, tidal dissipation can dramatically alter the WD structure.

We have calculated the rates of energy and angular momentum transfer due to tides as a function of the dimensionless pericentre distance  $\eta = r_p/r_t$  [see equation (2.4)] for various orbital eccentricities  $e$  and stellar rotation rates  $\Omega_s$ . These calculations assume that the tidally excited gravity waves are efficiently dissipated via non-linear effects or radiative damping as they propagate to the outer envelope of the WD. We have extended the method of Fuller and Lai [2012b], who considered WDs in circular orbits, to eccentric orbits by decomposing the tidal potential into a sum of multiple components with different forcing frequencies and studying the WD response to each component. We have applied this method to two MESA-generated CO WD models with  $T_{\text{eff}} = 9,000$  and  $5,200$  K. We found that the dimensionless energy and angular momentum transfer rates,  $\dot{\mathcal{E}}_{\text{in}}(\eta)$ ,  $\dot{\mathcal{E}}_{\text{rot}}(\eta)$ , and  $\dot{\mathcal{J}}(\eta)$  [see equations (2.11)-(2.13)], are relatively constant for  $\eta \lesssim 10$ , varying only by a factor of a few (see Fig. 2.13). The tidal transfer rates for  $\eta \gtrsim 15$  decrease exponentially with increasing  $\eta$  (see Fig. 2.8). For both models, increasing the stellar rotation rate  $\Omega_s$  decreases the transfer rates while increasing the eccentricity  $e$  smooths  $\dot{\mathcal{E}}_{\text{in}}(\eta)$ ,  $\dot{\mathcal{E}}_{\text{rot}}(\eta)$ , and  $\dot{\mathcal{J}}(\eta)$ .

We have used MESA to model the structural evolution of the WD due to tidal heating while the orbit shrinks due to gravitational radiation. We found that the hydrogen layer of the CO WD always heats up and ignites

long before the orbit evolves to the point of disruption. We therefore expect that a CO WD captured into an eccentric orbit may lose its hydrogen envelope before it is torn apart by tidal forces, provided a substantial fraction of the tidal heat is deposited near the base of the hydrogen envelope.

This paper is a first study on how dynamical tides affect a WD in an eccentric orbit around a MBH. Several caveats of our study are worth mentioning. First, the effect of rotation is treated approximately, without including the Coriolis force. In many cases, the WD is slowly rotating and will not synchronize before disruption, so this approximation is well founded. However, a WD captured from a binary could still have a significant rotation rate. Second, we assume that the outgoing gravity waves damp efficiently near the surface. This may not be true for all tidal frequencies, in which case, our calculations overestimate tidal heating. Finally, the location of tidal heat deposition is estimated crudely and our implementation of the heating rate is approximate (especially for small  $\eta$ 's).

Our work poses the question of what happens to a WD in an eccentric orbit around a BH that has already lost its hydrogen envelope in a runaway fusion event. The absence of a hydrogen envelope will change the behaviour of gravity waves near the surface of the WD and may reduce tidal dissipation. It is likely that the WD will only experience one tidal nova before disruption. However, as the WD continues to inspiral, the tidal heating rate will increase steeply as a function of decreasing  $\eta$  [see equation (2.47)]. This strong dependence presents the possibility of multiple novae before disruption, which may produce a distinctive observational signature. Future work is needed to understand how the absence of

the hydrogen envelope would change the tidal effect at smaller pericentre distances.

Our study of tidal dissipation in eccentric WD-MBH binaries can be easily adapted to other problems. For instance, WD-WD binaries with extreme eccentricities may be produced in triple systems, which could lead to direct WD-WD collisions and Type Ia supernovae ([Katz and Dong, 2012], [Kushnir et al., 2013]). In such WD-WD binaries, the physics of tidal dissipation studied in this paper can be directly applied, and equations (2.11)-(2.13) remain valid. In fact, the BH mass scales out if one expresses the pericentre distance in terms of the dimensionless parameter  $\eta$  [see equation (2.47)]. The only difference is that the orbital evolution timescale due to gravitational radiation becomes longer [see equation (2.7)] and therefore tidal dissipation may contribute to the orbital evolution.

CHAPTER 3

**DYNAMICAL TIDES IN HIGHLY ECCENTRIC BINARIES: CHAOS,  
DISSIPATION AND QUASI-STEADY STATE**

Originally published in:

M. Vick and D.Lai. Dynamical Tides in Highly Eccentric Binaries: Chaos, Dissipation and Quasi-Steady State. *MNRAS* **476**, pp. 482-495, 2018. doi: 10.1093/mnras/stx539

### 3.1 Introduction

Highly eccentric binaries appear in a variety of astrophysical contexts. In dense stellar clusters, two stars can be captured into a bound orbit with each other if a close encounter transfers enough energy into stellar oscillations [Fabian et al., 1975, Press and Teukolsky, 1977, Lee and Ostriker, 1986]. Such tidally captured binaries are highly eccentric and often involve compact objects (black holes and neutron stars). Massive black holes in nuclear star clusters may tidally capture normal stars, and could build up significant masses through successive captures [Stone et al., 2017]. Indeed, stars on highly eccentric orbits around massive black holes could be precursors of tidal disruption events [Rees, 1988], dozens of which have already been observed, e.g. Stone and Metzger [2016], Guillochon [2016]. Heating from tidal dissipation may affect the structure of stars moving toward disruption and potentially alter the observational signal of these events [Vick et al., 2017, MacLeod et al., 2014]. In exoplanetary systems, hot and warm Jupiters may be formed through high-eccentricity migration, in which a giant planet is pushed into a highly eccentric orbit by the

gravitational perturbation from a distant companion (a star or planet); at periastron, tidal dissipation in the planet reduces the orbital energy, leading to inward migration and circularization of the planet’s orbit [Wu and Murray, 2003, Fabrycky and Tremaine, 2007, Nagasawa et al., 2008, Petrovich, 2015a, Anderson et al., 2016, Muñoz et al., 2016]. Finally, the *Kepler* spacecraft has revealed a class of high-eccentricity stellar binaries with short orbital periods, whose light curves are shaped by tidal distortion and reflection at periastron [Thompson et al., 2012, Beck et al., 2014, Kirk et al., 2016]; many of these “heartbeat stars” also exhibit signatures of tidally induced stellar oscillations [Welsh et al., 2011, Fuller and Lai, 2012a, Burkart et al., 2012, Fuller, 2017].

In a highly eccentric binary, dynamical tidal interaction occurs mainly near pericentre and manifests as repeated tidal excitations of stellar oscillation modes. Since tidal excitation depends on the oscillation phase, the magnitude and direction of the energy transfer between the orbit and the modes may vary from one pericentre passage to the next [Kochanek, 1992]. Earlier works in the context of tidal-capture binaries have shown that for some combinations of orbital parameters, the energy in stellar modes may behave chaotically and grow to very large values. Mardling [1995a,b] first uncovered this phenomenon in numerical integrations of forced stellar oscillations and orbital evolution and explored the conditions for chaotic behaviour via Lyapunov analysis. In a later work, Mardling and Aarseth [2001] presented an empirical fitting formula for the location of a “chaos boundary,” beyond which tighter and more eccentric binaries exhibit chaotic orbital evolution. The possibility of chaotic growth of mode energy was also explored analytically in Ivanov and Pa-

paloizou [2004a, 2007a, 2011] in the context of giant planets on eccentric orbits. On the other hand, it is also expected that the long-term evolution of the binary depends on how effectively the binary components can dissipate energy [Kumar and Goodman, 1996]. Indeed, in the presence of dissipation, the system may reach a quasi-steady state in which the orbit-averaged mode energy remains constant [Lai, 1996a, 1997, Fuller and Lai, 2012a]. Numerical results from Mardling [1995b] have shown that chaotically evolving systems will eventually settle into a quiescent state of orbital evolution when modes are allowed to dissipate. The properties of this quasi-steady state that emerges from a chaotic dynamical system are unclear.

Given the important role played by dynamical tides in various eccentric stellar/planetary binary systems, a clear understanding of the dynamics of repeated tidal excitations of oscillation modes and the related tidal dissipation is desirable. In this paper, we develop an iterative map (Section 3.2) that accurately captures the dynamics and dissipation of the coupled “eccentric orbit + oscillation modes” system. Using this map, we aim to (i) characterize the classes of behaviours exhibited by eccentric binaries due to dynamical tides, (ii) explore the orbital parameters that lead to these behaviours, and (iii) study how the inclusion of mode damping affects the evolution of the system. As we shall see, the coupled “eccentric orbit + oscillation modes” system exhibits a richer sets of behaviours (see Section 3.3) than recognized in the previous works by Mardling [1995a,b] and Ivanov and Papaloizou [2004a]. In particular, the regime of chaotic mode growth (assuming a single mode) is determined by two dimensionless parameters (see Fig. 3.1 below), not one. Resonances between the oscillation

mode and orbital motion can significantly influence the chaotic boundary for mode growth. In the presence of mode dissipation, we show that even a chaotic system eventually reaches a quasi-steady state (Section 3.4); we quantify the properties of the quasi-steady state and the long-term evolution of the system. In Section 3.5, we generalize our analysis to multi-mode systems.

The results of this study are applicable to a variety of systems mentioned at the beginning of this section. Some of these applications are briefly discussed in Section 3.6. Of particular interest is the possibility that, in the high-eccentricity migration scenario of hot Jupiter formation, chaotic mode growth, combined with non-linear damping, may lead to efficient formation of warm Jupiters and hot Jupiters.

### 3.2 Iterative Map for Mode Amplitudes

Consider a binary system consisting of a primary body  $M$  (a star or planet) on an eccentric orbit with a companion  $M'$  (treated as a point mass). Near pericentre, the tidal force from  $M'$  excites oscillations in  $M$ . When the oscillation amplitudes are sufficiently small, we can follow the evolution of the modes and the orbit using linear hydrodynamics. For highly eccentric orbits ( $1 - e \ll 1$ ), the orbital trajectory around the pericentre remains almost unchanged even for large changes in the binary semi-major axis. Under these conditions, the full hydrodynamical solution of the system can be reduced to an iterative map (see Appendix B.1). We present the following map for a single-mode system and will discuss later the effects of multiple modes.

We define the dimensionless mode energy and binary orbital energy in units of  $|E_{B,0}|$  (the initial binary orbital energy), i.e.,  $\tilde{E} = E/|E_{B,0}|$ . Consider a single mode of the star with frequency  $\omega$  and (linear) damping rate  $\gamma$ . Let  $a_{k-1}$  be the mode amplitude just before the  $k$ -th pericentre passage. Immediately after the  $k$ -th passage, the mode amplitude becomes

$$a_{k-} = a_{k-1} + \Delta a, \quad (3.1)$$

where  $\Delta a$  (real) is the mode amplitude change in the “first” passage (i.e., when there is no pre-existing oscillation). We normalize  $a_k$  such that the (dimensionless) mode energy just after  $k$ -th passage is  $\tilde{E}_{k-} = |a_{k-}|^2$ . Thus the energy transfer to the mode in the  $k$ -th passage is

$$\Delta\tilde{E}_k = |a_{k-}|^2 - |a_{k-1}|^2 = |a_{k-1} + \Delta a|^2 - |a_{k-1}|^2. \quad (3.2)$$

In physical units, the energy transfer in the “first” passage is given by  $\Delta E_1 = (\Delta a)^2 |E_{B,0}|$ . The binary orbital energy ( $\tilde{E}_{B,k}$ ) immediately after the  $k$ -th passage is given by

$$\tilde{E}_{B,k} = \tilde{E}_{B,k-1} - \Delta\tilde{E}_k = \tilde{E}_{B,0} - \sum_{j=1}^k \Delta\tilde{E}_j, \quad (3.3)$$

and the corresponding orbital period is

$$\frac{P_k}{P_0} = \left( \frac{\tilde{E}_{B,0}}{\tilde{E}_{B,k}} \right)^{3/2}, \quad (3.4)$$

where  $\tilde{E}_{B,0} = -1$ . The mode amplitude just before the  $(k+1)$ -th passage is

$$a_k = a_{k-} e^{-(i\omega+\gamma)P_k} = (a_{k-1} + \Delta a) e^{-(i+\hat{\gamma})\hat{P}_k}, \quad (3.5)$$

where we have defined the dimensionless damping rate and orbital period

$$\hat{\gamma} = \frac{\gamma}{\omega}, \quad \hat{P}_k = \omega P_k. \quad (3.6)$$

Equations (3.1)-(3.5) complete the map from one orbit to the next, starting from the initial condition  $a_0 = 0$ ,  $\tilde{E}_0 = 0$ ,  $\tilde{E}_{B,0} = -1$ . In the absence of dissipation, this map reduces to that of Ivanov and Papaloizou [2004a]. The map depends on three parameters:

$$\hat{P}_0 \equiv \omega P_0, \quad (3.7)$$

$$|\Delta\hat{P}_1| \equiv \omega|\Delta P_1| \simeq \frac{3}{2}\hat{P}_0(\Delta a)^2 = \frac{3}{2}\hat{P}_0\left(\frac{\Delta E_1}{|E_{B,0}|}\right), \quad (3.8)$$

$$\hat{\gamma} = \frac{\gamma}{\omega} = \frac{\gamma P_0}{\hat{P}_0} = \frac{1}{\hat{P}_0}\left(\frac{P_0}{t_{\text{damp}}}\right). \quad (3.9)$$

To relate  $\hat{P}_0$  and  $|\Delta\hat{P}_1|$  to the physical parameters of the system, we scale the mode frequency  $\omega$  to  $\Omega_{\text{peri}} \equiv (GM_t/r_{\text{peri}}^3)^{1/2}$  (where  $M_t = M + M'$ , and  $r_{\text{peri}}$  is the pericentre distance), and find

$$\hat{P}_0 = \frac{2\pi(\omega/\Omega_{\text{peri}})}{(1-e)^{3/2}}. \quad (3.10)$$

The parameter  $|\Delta\hat{P}_1|$  is related to the energy transfer in the “first” pericentre passage via  $|\Delta\hat{P}_1|/\hat{P}_0 = (3/2)|\Delta E_1/E_{B,0}|$ . If we scale  $r_{\text{peri}}$  by the tidal radius  $r_{\text{tide}} = R(M_t/M)^{1/3}$  (where  $R$  is the stellar radius), i.e.,  $\eta = r_{\text{peri}}/r_{\text{tide}}$ , we have, for  $l = 2$ ,

$$\Delta E_1 = -\frac{GM'^2R^5}{r_{\text{peri}}^6} T(\eta, \omega/\Omega_{\text{peri}}, e), \quad (3.11)$$

where  $T$  is a dimensionless function of  $\eta$ ,  $\omega/\Omega_{\text{peri}}$ , and  $e$  (though  $T$  becomes independent of  $e$  as  $e$  approaches unity). The exact form of  $T(\eta, \omega/\Omega_{\text{peri}}, e)$  is provided in Appendix B.1. Then,

$$|\Delta\hat{P}_1| = \frac{6\pi(\omega/\Omega_{\text{peri}})}{(1-e)^{5/2}} \left(\frac{M'}{M}\right) \left(\frac{M}{M_t}\right)^{5/3} \eta^{-5} T(\eta, \omega/\Omega_{\text{peri}}, e). \quad (3.12)$$

In general,  $|\Delta\hat{P}_1|$  falls off steeply with  $\eta$ . However, even when  $\eta$  is large (weak tidal encounter),  $|\Delta\hat{P}_1|$  can be significant for highly eccentric systems (with  $1 - e \ll 1$ ).

The map (3.1)-(3.5) assumes that (i) energy transfer occurs instantaneously at pericentre; (ii) at each pericentre passage, the change in mode amplitude,  $a_{k-} - a_{k-1}$ , is the same; and (iii) the mode energy is always much less than the binding energy of the star. The first condition is satisfied when  $1 - e \ll 1$ . Eccentric systems that exhibit oscillatory behaviour (see Section 3.3) easily satisfy this condition over many orbits. Chaotic systems (see Section 3.3) can evolve through a larger range of mode energies and orbital eccentricities. For this condition to hold throughout evolution, they must begin with very large eccentricities. The second condition requires that the pericentre distance remains constant, which in turn requires that the fractional change in orbital angular momentum,  $\Delta L/L$ , remain small throughout orbital evolution. Using  $\Delta L \sim \Delta E_B/\Omega_{\text{peri}}$  as an estimate, we find that the condition  $\Delta L/L \ll 1$  becomes

$$\frac{\Delta L}{L} \sim \frac{1}{2\sqrt{2}} \Delta \tilde{E}_B (1 - e) \ll 1. \quad (3.13)$$

Thus, for sufficiently eccentric orbits,  $r_{\text{peri}}$  is roughly constant even when the orbital energy changes by  $\Delta \tilde{E}_B \sim 10$ . The third condition,  $E_k \ll GM^2/R$ , yields the expression

$$\frac{\tilde{E}_k(1 - e)}{2\eta} \left( \frac{M'}{M} \right) \left( \frac{M_t}{M} \right)^{-1/3} \ll 1. \quad (3.14)$$

Again, this is easiest to satisfy for very eccentric orbits.

### 3.3 Mode Energy Evolution without Dissipation

We first study the dynamics of the “eccentric orbit + mode” system without dissipation ( $\hat{\gamma} = 0$ ). The iterative map described in equations (3.1)-(3.5) displays a variety of behaviours depending on  $\hat{P}_0$  and  $|\Delta \hat{P}_1|$ . We can gain

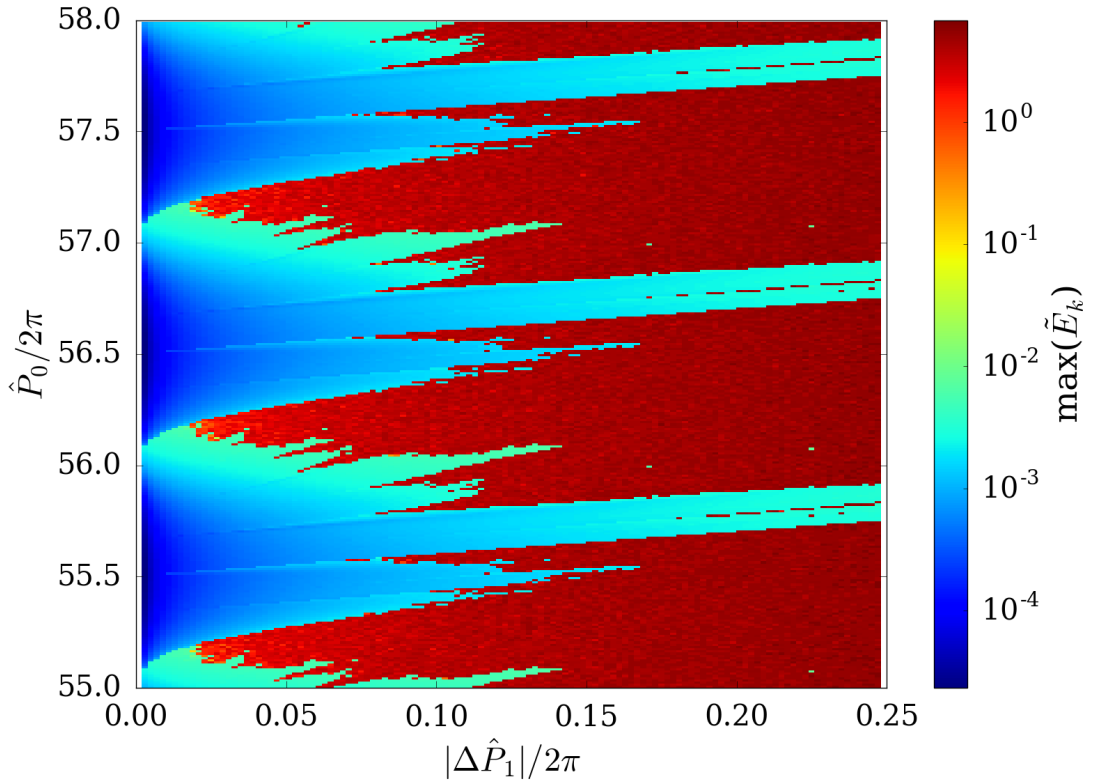


Figure 3.1: The maximum mode energy reached in  $10^4$  orbits as a function of  $|\Delta\hat{P}_1|/2\pi$  and  $\hat{P}_0/2\pi$ . The energy is normalized to the initial orbital energy of the binary. In the dark blue regions, the mode exhibits low-energy oscillations. In the light green regions, the mode exhibits high-amplitude oscillations corresponding to a resonance. The red regions indicate chaotic mode evolution.

insight into the evolution of the system by recording  $\tilde{E}_{\max}$ , the maximum mode energy reached over many orbits; this quantity reveals whether energy transfer to stellar modes is relatively small or whether the orbit can change substantially by transferring large amounts of energy. Figure 3.1 shows  $\tilde{E}_{\max}$  after  $10^4$  orbits for systems with a range of  $\hat{P}_0$  and  $|\Delta\hat{P}_1|$ . Similarly, Fig. 3.2 displays  $\tilde{E}_{\max}$  as a function of  $r_{\text{peri}}$  and  $e$  for an  $n = 1.5$  polytrope stellar model in a binary with mass ratio  $M'/M = 1$ . The relationship between the physical parameters  $r_{\text{peri}}$  and  $e$  and the mapping parameters  $\hat{P}_0$  and  $|\Delta\hat{P}_1|$  is given by equations (3.10) and (3.12) (see Appendix B.1 for

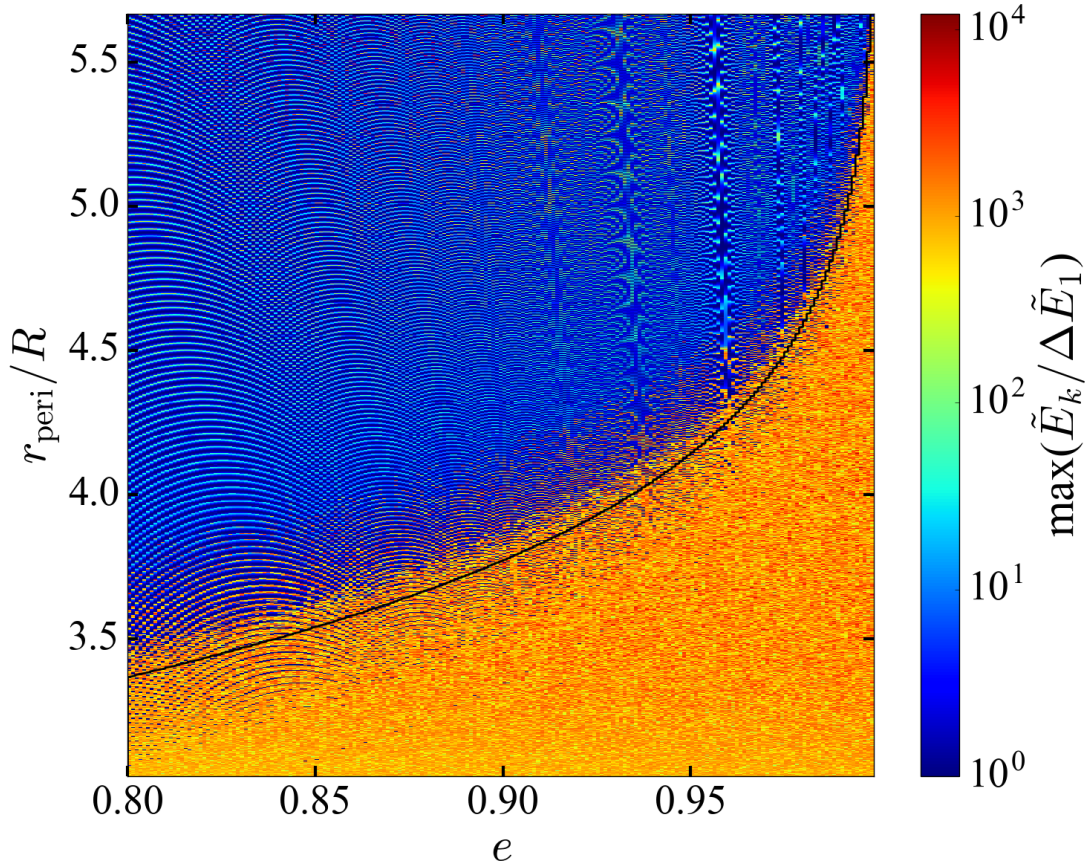


Figure 3.2: The maximum mode energy reached in  $10^4$  orbits as a function of the pericentre distance,  $r_{\text{peri}}$ , and  $e$  for the  $l = 2$  f-mode of an  $n = 1.5$  polytrope in a binary with mass ratio  $M'/M = 1$ . The energy is normalized to the energy transferred in the first pericentre passage,  $\Delta \tilde{E}_1$ . In the dark blue region, the mode exhibits low-amplitude oscillations. The light blue “fingerprint” ridges correspond to resonances. The yellow/orange region displays chaotic mode evolution. The black line indicates  $|\Delta \hat{P}_1| = 1$ . Note that, in this figure, the mode energy of the chaotic systems may not have attained the true “theoretical” maximum [see equation (3.26)] in  $10^4$  orbits; the energy may continue to climb to a large value if the system is allowed to continue evolving.

more detail).

The system evolution has a complex dependence on  $\hat{P}_0$  and  $|\Delta \hat{P}_1|$ . In general, the mode energy exhibits oscillatory behaviour for small  $|\Delta \hat{P}_1|$  and chaotic growth for large  $|\Delta \hat{P}_1|$ . However, Fig. 3.1 shows exceptions to this

trend. The figure also suggests that the response to  $\hat{P}_0$  is periodic and the mode amplitude is larger in magnitude near resonances where the orbital frequency is commensurate with the mode frequency. The map displays three primary types of behaviours — low-amplitude oscillation, resonant oscillation, and chaotic evolution. Transitions between the three regimes are complicated. However, within each regime,  $\tilde{E}_{\max}$  exhibits simple dependence on  $\hat{P}_0$  and  $|\Delta\hat{P}_1|$ . We now discuss the three types of behaviour in detail.

### 3.3.1 Oscillatory Behaviour

When  $|\Delta\hat{P}_1|/(2\pi) \lesssim 0.05$  and  $\hat{P}_0/(2\pi)$  is not close to an integer, the mode exhibits low-amplitude oscillations, shown in the top panels of Fig. 3.3. In this regime, the orbital period is nearly constant ( $\hat{P}_k \simeq \hat{P}_0$ ), and the map from equations (3.1)-(3.5) can be written simply as

$$a_k \simeq (a_{k-1} + \Delta a) e^{-i\hat{P}_0}. \quad (3.15)$$

This can be solved with the initial condition  $a_0 = 0$ , yielding

$$a_k \simeq \frac{\Delta a}{e^{i\hat{P}_0} - 1} \left( 1 - e^{-i\hat{P}_0 k} \right). \quad (3.16)$$

Note that, in the complex plane, this solution has the form of a circle of radius  $|1/(e^{i\hat{P}_0} - 1)|$  centred on  $1/(e^{i\hat{P}_0} - 1)$ , as shown in Fig. 3.3 [a result previously seen in Ivanov and Papaloizou [2004a]]. From equation (3.16), the maximum mode energy in this regime is

$$\tilde{E}_{\max} \simeq \frac{2(\Delta a)^2}{1 - \cos \hat{P}_0}. \quad (3.17)$$

This result demonstrates that our assumption of  $\hat{P}_k \simeq \hat{P}_0$  performs well when  $(\Delta a)^2 \ll 1$  and  $\hat{P}_0$  is not too close to an integer multiple of  $2\pi$ . Un-

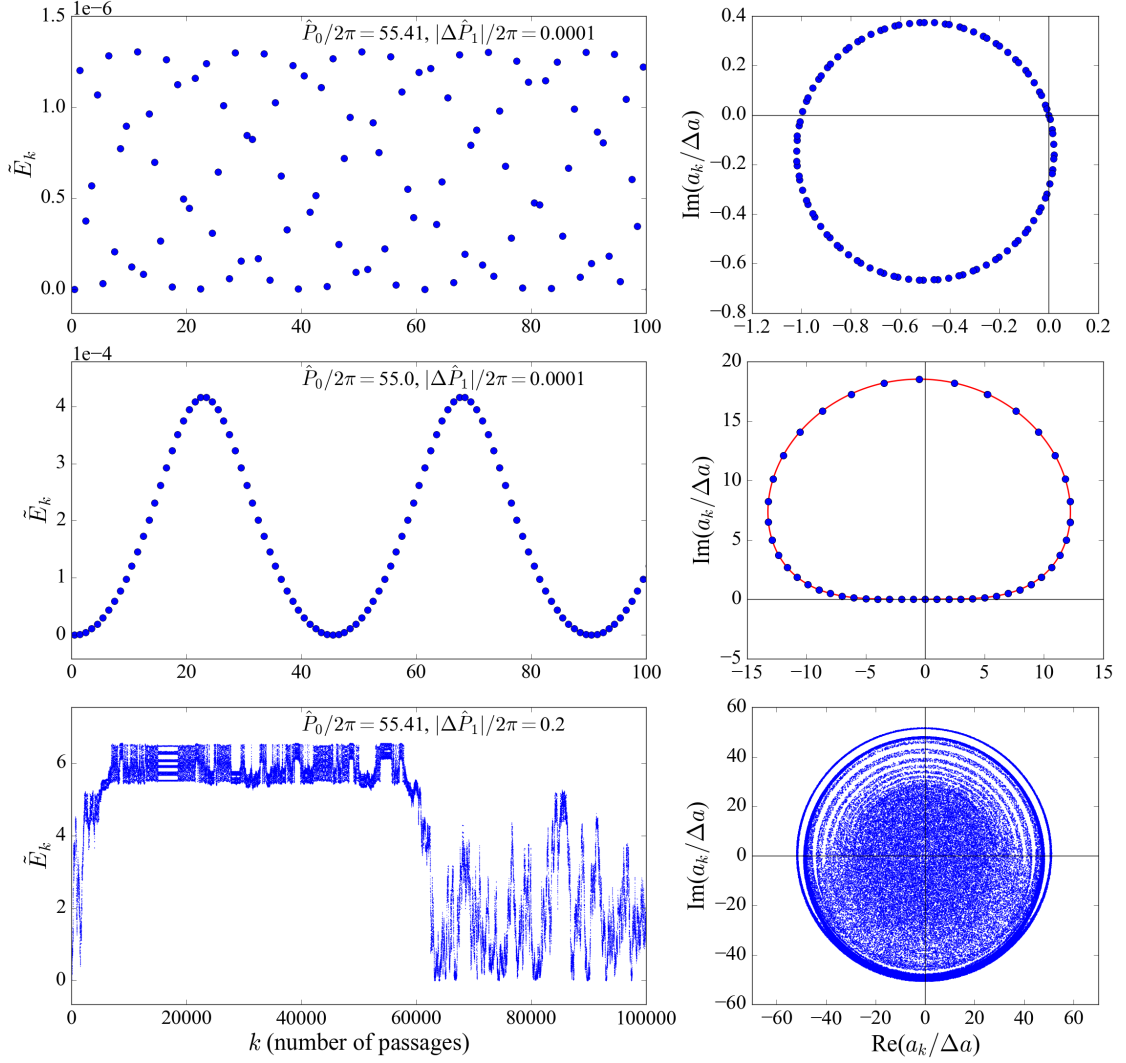


Figure 3.3: Left Column: The evolution of the mode energy over multiple pericentre passages. Right Column: The complex mode amplitude  $a_k$  (normalized to  $\Delta a$ , the change in mode amplitude during the first pericentre passage). From top to bottom, the three rows correspond to different types of behaviours — low-amplitude oscillations, resonant behaviour, and chaotic evolution. The red line is from equation (B.30) in Appendix B.2.1.

der these conditions, the mode energy remains of order  $(\Delta a)^2 = \Delta \tilde{E}_1$ , the energy transfer in the “first” pericentre passage.

### 3.3.2 Resonance

Figure 3.1 indicates that the stellar mode exhibits large-amplitude oscillations for  $\hat{P}_0 \simeq 2\pi N$  (with  $N = \text{integer}$ ), i.e., when the orbital period  $P_0$  is nearly an integer multiple of the mode period  $2\pi/\omega$ . To understand this behaviour, we assume  $\tilde{E}_k = |a_k|^2 \ll 1$ , which holds true in the non-chaotic regime. With no dissipation, equation (3.4) is replaced by

$$\hat{P}_k \simeq \hat{P}_0 \left( 1 - \frac{3}{2} |a_{k-}|^2 \right) = \hat{P}_0 - |\Delta \hat{P}_1| \|z_k\|^2, \quad (3.18)$$

where we have defined  $z_k \equiv a_{k-}/\Delta a$  and used equation (3.8). The map can then be written as

$$z_{k+1} = 1 + z_k e^{-i\hat{P}_k} \simeq 1 + z_k e^{-i\hat{P}_0 + i|\Delta \hat{P}_1| \|z_k\|^2}. \quad (3.19)$$

Near a resonance, with  $|\delta \hat{P}_0| = |\hat{P}_0 - 2\pi N| \ll 1$ , the above map can be further simplified to  $z_{k+1} - z_k \simeq 1 + z_k(-i\delta \hat{P}_0 + i|\Delta \hat{P}_1| \|z_k\|^2)$ . The maximum mode amplitude near resonance is determined by setting the non-linear term  $|\Delta \hat{P}_1| \|z_k\|^3 \sim 1$ , giving  $|z_{\text{res}}| \sim |\Delta \hat{P}_1|^{-1/3}$ . The corresponding mode energy is

$$\tilde{E}_{\text{res}} \sim \frac{(\Delta a)^2}{|\Delta \hat{P}_1|^{2/3}} \sim \frac{|\Delta \hat{P}_1|^{1/3}}{\hat{P}_0}. \quad (3.20)$$

Equation (3.20) is valid for  $|\delta \hat{P}_0| \lesssim |\Delta \hat{P}_1|^{1/3}$ , and agrees with our numerical result (see Appendix B.2.1 for more details).

### 3.3.3 Chaotic Growth

Chaotic growth of mode energy typically occurs when  $|\Delta\hat{P}_1| \gtrsim 1$ , i.e., when enough energy is transferred in a pericentre passage to change the orbital period and cause appreciable phase shift of the mode. In this regime, the mode amplitude fills a circle in the complex plane after the binary evolves for many orbits, as shown in the bottom panels of Fig. 3.3.

We can verify that the dynamical behaviour of systems with a large  $|\Delta\hat{P}_1|$  is chaotic by examining the difference between a trajectory and its shadow to estimate the Lyapunov exponent. The shadow trajectory is calculated with a slightly different initial value  $a_{0,\text{shadow}}$ , such that  $\delta a_0 \equiv |a_{0,\text{shadow}}| - |a_0| \ll 1$ . We follow the evolution of  $\delta a_k \equiv \|a_{k,\text{shadow}}| - |a_k\|$ . For chaotic behaviour, we expect

$$\delta a_k \approx \delta a_0 e^{\lambda k}, \quad (3.21)$$

where  $\lambda$  is the Lyapunov exponent.

Figure 3.4 suggests that systems with  $|\Delta\hat{P}_1| \sim 1$  indeed undergo chaotic evolution, with  $\delta a_k$  growing exponentially (but eventually saturating when  $\delta a_k \sim 0.1$ ). For the system depicted in Fig. 3.4,  $\lambda \approx 1.77$ . The exact value of  $\lambda$  can change slightly with the parameters  $\hat{P}_0$  and  $|\Delta\hat{P}_1|$ . Similar Lyapunov calculations were performed in Mardling [1995a,b] to determine numerically the boundary for chaotic behaviour in the  $r_{\text{peri}} - e$  plane [e.g. Fig. 13 in Mardling [1995a], which qualitatively agrees with our Fig. 3.2]. The condition  $|\Delta\hat{P}_1| \gtrsim 1$  for chaotic behaviour was first identified by Ivanov and Papaloizou [2004a].

While the Lyapunov saturation of  $\delta a_k$  occurs after 10's of orbits, the mode energy can continue to climb over much longer timescales (as in the bot-

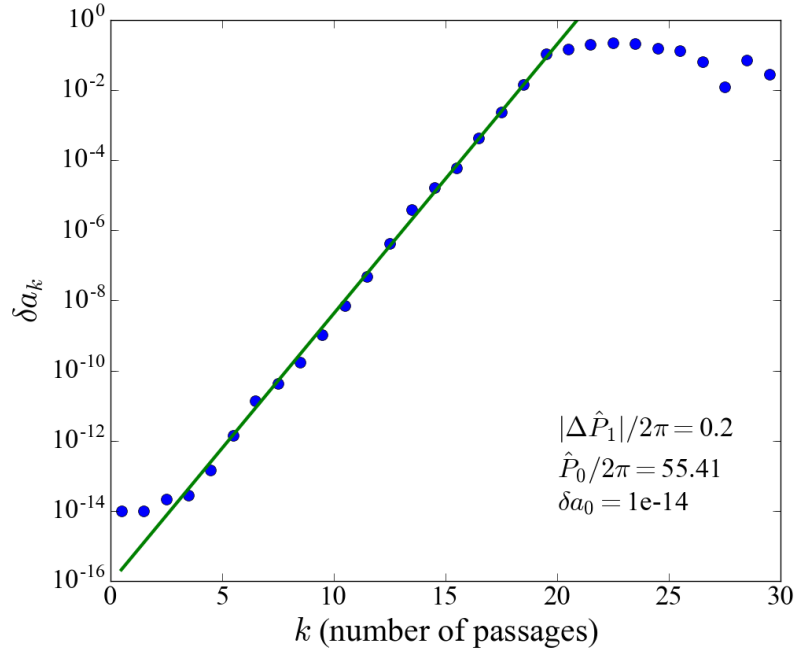


Figure 3.4: The blue dots show the difference between the mode amplitude of a trajectory and its shadow,  $\delta a_k$ , as a function of orbits. The green line shows a fit to the exponential rise with  $\lambda \approx 1.77$ , where  $\lambda$  is defined in equation (3.21). For  $k \gtrsim 20$ ,  $\delta a_k$  saturates around 0.1.

tom panel of Fig. 3.3). In the absence of dissipation, the mode amplitude map is simply

$$a_k = (a_{k-1} + \Delta a) e^{-i\hat{P}_k}, \quad \text{with } \hat{P}_k = \hat{P}_0 (1 + |a_k|^2)^{-3/2}. \quad (3.22)$$

When the change in orbital period between pericentre passages,  $\Delta\hat{P}_k = \hat{P}_k - \hat{P}_{k-1}$ , is much larger than unity,  $\hat{P}_k$  approximately takes on random phases. This random-phase model, previously studied in Mardling [1995a], Ivanov and Papaloizou [2004a], captures the key features of mode growth in the chaotic regime (see Fig. 3.5). The mode energy after the  $k$ -th passages can be written as

$$\tilde{E}_k = \sum_{j=1}^k \Delta \tilde{E}_j = \sum_{j=1}^k \left[ (\Delta a)^2 + 2(\Delta a) \operatorname{Re}(a_{j-1}) \right]. \quad (3.23)$$

If we assume that  $a_{j-1}$  exhibits random phases, then

$$\langle \tilde{E}_k \rangle \sim (\Delta a)^2 k, \quad (3.24)$$

a result previously obtained by Mardling [1995a] and Ivanov and Papaloizou [2004a]. This provides a crude description of the chaotic mode growth, shown in Fig. 3.5.

Although  $\tilde{E}_{\max}$  can become very large, Fig. 3.3 suggests that the mode energy cannot exceed a maximum value, a feature not captured by the random-phase model, but previously seen in some examples of numerical integrations of chaotic mode evolution [Mardling, 1995b]. This can be understood from the fact that as the mode energy increases, the the range of possible  $\Delta\hat{P}_k$  decreases. Indeed, from equation (3.22) we find

$$\Delta\hat{P}_k \equiv \hat{P}_k - \hat{P}_{k-1} \simeq -3\Delta a \hat{P}_0 \frac{\operatorname{Re}(a_{k-1})}{(1 + |a_{k-1}|^2)^{5/2}}. \quad (3.25)$$

Setting  $\Delta\hat{P}_k \sim 1$  leads to a maximum mode energy

$$\tilde{E}_{\max} = (|a_k|^2)_{\max} \sim (\hat{P}_0 \Delta a)^{1/2} \sim \left( |\Delta\hat{P}_1| \hat{P}_0 \right)^{1/4}. \quad (3.26)$$

More discussion on the maximum mode energy in the chaotic regime can be found in Appendix B.2.3. Note that  $\tilde{E}_{\max}$  of order a few can be easily reached for a large range of  $\hat{P}_0$  and  $|\Delta\hat{P}_1|$  (see Fig. 3.3). Such a large mode energy implies order unity change in the semi-major axis of the orbit, but for  $1 - e \ll 1$  it does not necessarily violate the requirements needed for the validity of the iterative map [see equations (3.13)-(3.14)].

### 3.4 Mode Energy Evolution with Dissipation

We now consider the effect of dissipation on the evolution of the system. In the presence of mode damping ( $\gamma \neq 0$ ), energy is preferentially trans-

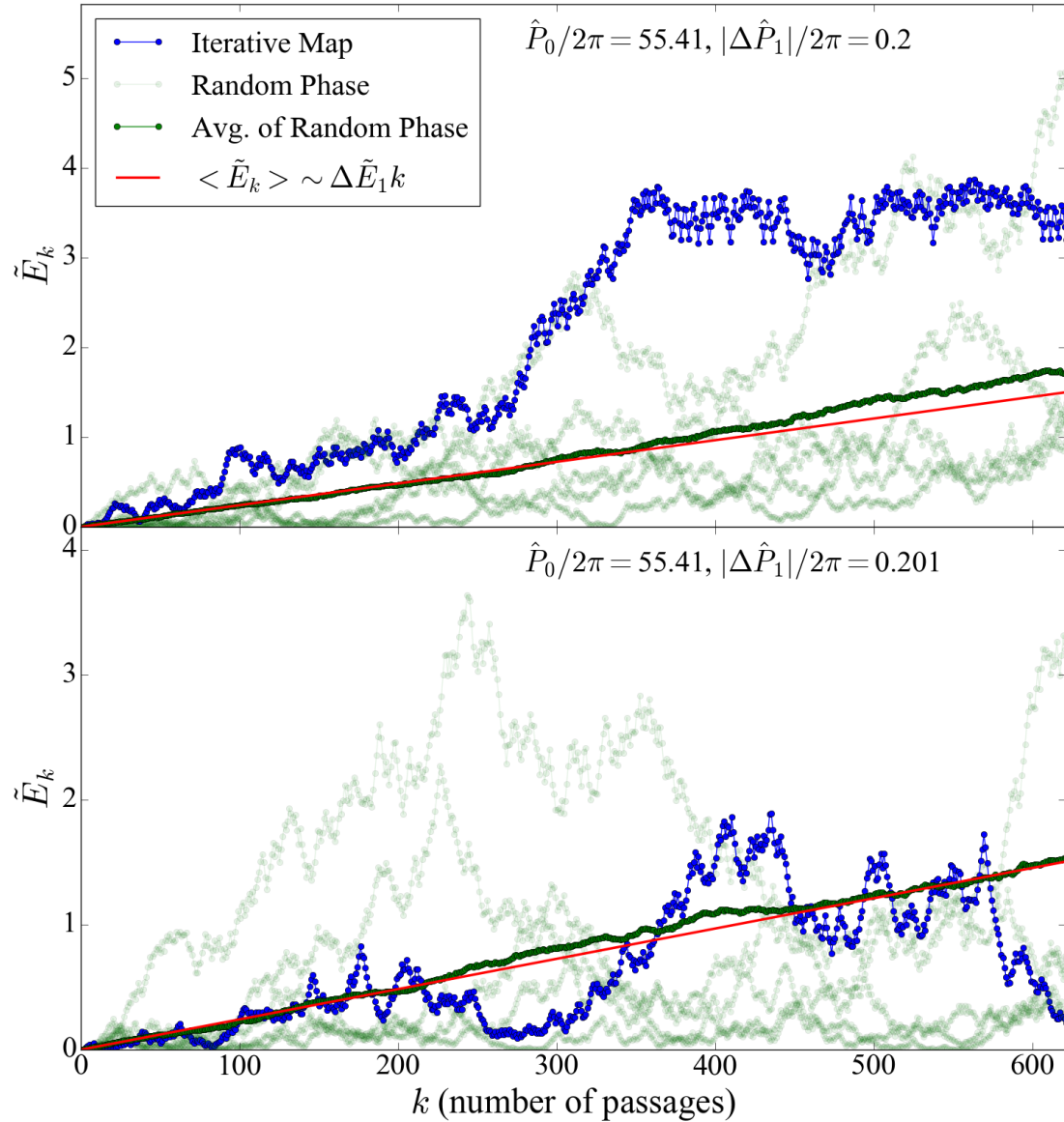


Figure 3.5: The mode energy evolution for two slightly different values of  $|\Delta \hat{P}_1|$ . The blue lines are the results from the iterative map; the light green lines show examples of the random phase model [where  $\hat{P}_k$  in equation (3.22) takes on random values between 0 and  $2\pi$ ]; the dark green is an average of 100 iterations of the random phase model; and the red lines show the expected average growth of the mode energy in the diffusion model.

ferred from the orbit to the stellar mode which then dissipates, causing long-term orbital decay. In the extreme case when the mode damping time  $t_{\text{damp}} = \gamma^{-1}$  is shorter than the orbital period  $P$ , the energy transfer in each pericentre passage  $\Delta E_1$  is dissipated, and the orbital energy  $E_B$  simply decays according to

$$\frac{dE_B}{dt} \simeq -\frac{\Delta E_1}{P}, \quad (\text{for } t_{\text{damp}} \lesssim P). \quad (3.27)$$

Below, we will consider the more realistic situation of  $t_{\text{damp}} \gg P$ .

### 3.4.1 Quasi-Steady State

Consider a system with  $|\Delta \hat{P}_1| \ll 1$  and an orbital period that is far from resonance. The mode energy will stay around  $\Delta E_1$ , and can attain a quasi-steady state after a few damping times (see Fig. 3.6). Indeed, since the orbital period  $P$  remains roughly constant over multiple damping times, the map simplifies to

$$a_k \simeq (a_{k-1} + \Delta a) e^{-(i+\hat{\gamma})\hat{P}}. \quad (3.28)$$

Assuming  $a_0 = 0$ , we find

$$a_k \simeq \frac{\Delta a}{e^{(i+\hat{\gamma})\hat{P}} - 1} \left[ 1 - e^{-(i+\hat{\gamma})\hat{P}k} \right]. \quad (3.29)$$

Clearly, the mode amplitude approaches a constant value after a few damping times ( $kP \gg \gamma^{-1}$ ), and the mode energy reaches the steady-state value [Lai, 1997]:

$$\tilde{E}_{\text{ss}} \simeq \frac{\Delta \tilde{E}_1 e^{-\hat{\gamma}\hat{P}}}{2(\cosh \hat{\gamma}\hat{P} - \cos \hat{P})} \simeq \frac{\Delta \tilde{E}_1}{4 \sin^2(\hat{P}/2) + (\hat{\gamma}\hat{P})^2}, \quad (3.30)$$

where the second equality assumes  $\hat{\gamma}\hat{P} = \gamma P \ll 1$ , or  $t_{\text{damp}} \gg P$ . The steady-state energy is of order  $\Delta \tilde{E}_1$ , provided that the system is not near a resonance. In the steady state, the star dissipates all the “additional” energy

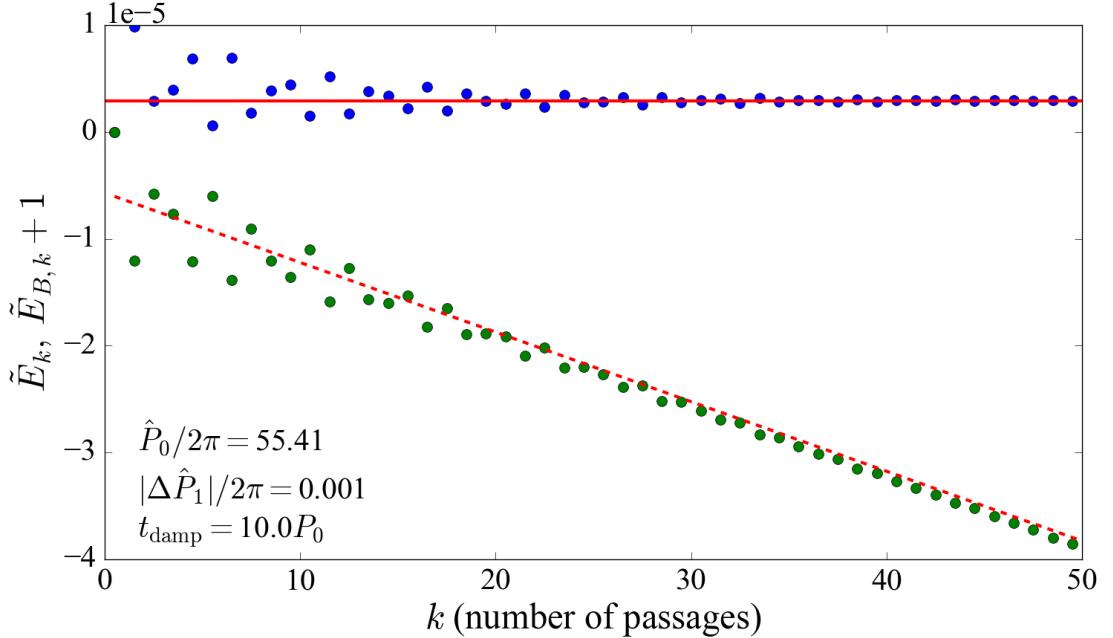


Figure 3.6: The stellar mode energy (blue dots) and the orbital energy (green dots; shifted for comparison) over 50 pericentre passages. Energy is normalized to the initial orbital energy of the binary. The solid red line shows the steady-state mode energy given by equation (3.30), and the dashed red line shows the orbital decay rate from equation (3.31).

gained at each pericentre passage, and thus the orbital energy decays according to

$$\frac{d\tilde{E}_B}{dt} \simeq -2\gamma\tilde{E}_{ss} \quad \text{or} \quad \frac{dE_B}{dt} \simeq -\frac{2E_{ss}}{t_{\text{damp}}}, \quad (\text{for } t_{\text{damp}} \gg P). \quad (3.31)$$

### 3.4.2 Passing Through Resonances

As the binary orbit experiences quasi-steady decay, it will encounter resonances with the stellar mode ( $\hat{P}/2\pi = \text{integer}$ ), during which rapid orbital decay occurs (see Fig. 3.7).

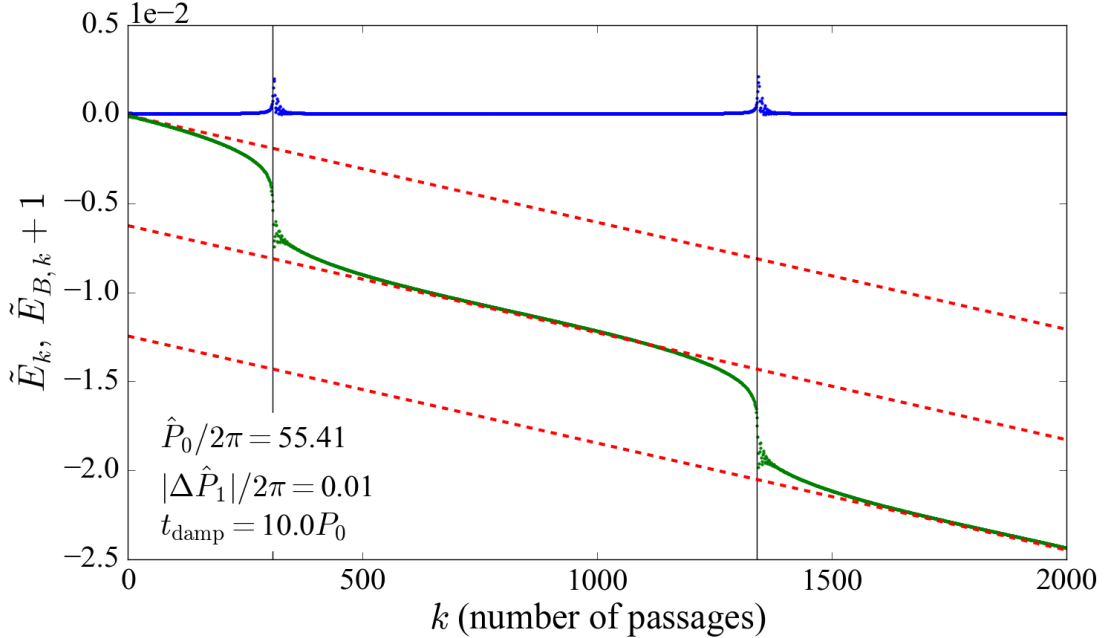


Figure 3.7: The mode energy (in blue) and the orbital energy (in green) over many pericentre passages. Energy is normalized to the initial orbital energy of the binary. The analytic orbital decay rate for the quasi-steady state is plotted in dashed red. The red lines are spaced by  $5.46\tilde{E}_{\text{res}}$  with  $\tilde{E}_{\text{res}}$  given by equation (3.20).

The change in orbital energy when a system moves through a resonance depends on how the resonance time  $t_{\text{res}}$  (the timescale for the mode energy of a system near resonance to reach  $\tilde{E}_{\text{res}}$ ) compares with  $t_{\text{damp}}$ . In most likely situations, the resonance time  $t_{\text{res}} \sim P/|\Delta\hat{P}_1|^{1/3}$  (see Appendix B.2.2) is much shorter than  $t_{\text{damp}}$ , so the orbital energy is quickly transferred to the stellar mode as the system approaches the resonance, and the mode energy reaches the maximum resonance value given by equation (3.20). All of this energy is dissipated within a few  $t_{\text{damp}}$ , resulting in a net change in the orbital energy during the resonance  $\Delta\tilde{E}_{B,\text{res}} \simeq \tilde{E}_{\text{res}} \sim |\Delta\hat{P}_1|^{1/3}/\hat{P}$ . By comparison, the quasi-steady orbital energy change between adjacent res-

onances [from  $\hat{P} = 2\pi N$  to  $\hat{P} = 2\pi(N - 1)$ ] is (assuming  $N \gg 1$ )

$$\Delta\tilde{E}_{B,ss} \simeq \frac{4\pi}{3\hat{P}}. \quad (3.32)$$

Thus  $\Delta\tilde{E}_{B,res}/\Delta\tilde{E}_{B,ss} \sim 0.2|\Delta\hat{P}_1|^{1/3}$ . In practice, systems that evolve into resonance rather than starting in resonance will reach a maximum mode energy of a few times equation (3.20), so  $\Delta\tilde{E}_{B,res}$  can be comparable to  $\Delta\tilde{E}_{B,ss}$ .

### 3.4.3 Tamed Chaos

In the presence of dissipation, even systems that experience chaotic mode growth eventually settle into a quasi-steady state. Figure 3.8 depicts an example. We see that initially the mode energy increases rapidly, accompanied by a large decrease in the orbital energy. This behaviour has been seen in numerical integrations of forced stellar oscillations and orbital evolution by Mardling [1995b], where the orbital eccentricity quickly decreases to a value dictated by the “chaos boundary” before settling into a state of gradual decay. With our exact “dissipative” map, we can predict the steady-state mode energy and orbital decay rate that emerge after a period of chaotic evolution. For systems with relatively large damping rates, the mode energy may not reach the full “chaotic maximum” given by equation (3.26). However, for systems with relatively small damping rates, the full maximum energy is attainable. In either case, the mode energy ultimately decays to a quasi-steady value of order  $\Delta E_1$  after a timescale of  $\sim t_{\text{damp}} \ln(E_{\max}/\Delta E_1)$ . The evolution of the system in quasi-steady state is well described by equations (3.30)-(3.31).

We can understand how an initially chaotic system (with  $|\Delta\hat{P}_1| \sim 1$ ) is brought into the “regular” regime by renormalizing various quantities

to their “post-chaotic” values (see the lower panel of Fig. 3.8). Recall that the key parameter that determines the dynamical state of the system is  $|\Delta\hat{P}| = \omega|\Delta P|$ , with  $\Delta P$  the change in the orbital period in a the first pericentre passage (i.e. when there is no prior oscillation). Since  $|\Delta P|/P \simeq 3\Delta E/(2|E_B|)$  and  $\Delta E$  is independent of the semi-major axis  $a$  (it depends only  $r_{\text{peri}}$ , which is almost unchanged), we find  $|\Delta\hat{P}| \propto a^{5/2} \propto (1-e)^{-5/2}$  [for  $r_{\text{peri}} = \text{constant}$ ; see equation (3.12)]. Thus, after significant orbital decay (with  $a$  decreased by a factor of a few),  $|\Delta\hat{P}|$  is reduced to a “non-chaotic” value, and the system settles into the regular quasi-steady state.

We can approximate the orbital parameters of a “tamed” chaotic system that has reached quasi-steady state from the evolution of the orbital energy,  $\tilde{E}_B$ . Our map assumes that angular momentum is conserved as the orbit evolves. Given this constraint, the orbital eccentricity just before the  $(k+1)$ -th pericentre passage is

$$e_k = \left[ 1 - |\tilde{E}_{B,k}|(1 - e_0^2) \right]^{1/2}. \quad (3.33)$$

As an example, a system with initial eccentricity  $e_0 = 0.99$  that settles to a quasi-steady state orbital energy  $\tilde{E}_B \approx -5$  would retain an eccentricity of  $e \approx 0.95$ . Note that less eccentric binaries (even  $e = 0.9$ ) can circularize substantially over the course of chaotic evolution and strain the assumptions of our map (see Section 3.2).

Our model assumes linear mode damping. In reality, modes that are excited to high amplitudes may experience non-linear damping. This will likely make the system evolve to the quasi-steady state more quickly. Other than this change of timescale, we expect that the various dynamical features revealed in our model remain valid. We note that a rapidly heated star/planet may undergo significant structural change depend-

ing on where heat is deposited. This may alter the frequencies of stellar modes. Our current model does not account for such feedback.

### 3.5 Systems with Multiple Modes

Our analysis can be easily generalized to systems with multiple modes (labelled by the index  $\alpha$ ). The total energy in modes just before the  $(k + 1)$ -th passage is  $\tilde{E}_k = \sum_{\alpha} |a_{\alpha,k}|^2$ . During a pericentre passage, the amplitude of each mode changes by  $\Delta a_{\alpha}$ . The total energy transferred to stellar modes in the  $k$ -th passage is

$$\Delta \tilde{E}_k = \sum_{\alpha} \left[ |a_{\alpha,k-1} + \Delta a_{\alpha}|^2 - |a_{\alpha,k-1}|^2 \right]. \quad (3.34)$$

As before, the orbital energy after the  $k$ -th passage is given by  $\tilde{E}_{B,k} = \tilde{E}_{B,0} - \sum_{j=1}^k \Delta \tilde{E}_j$ . The relationship between the orbital energy and the period is given by equation (3.4). The mode amplitude of each mode just before the  $(k + 1)$ -th passage is

$$a_{\alpha,k} = [a_{\alpha,k-1} + \Delta a_{\alpha}] e^{-(i+\hat{\gamma}_{\alpha})\hat{P}_{\alpha,k}} \quad (3.35)$$

where  $\hat{P}_{\alpha,k} \equiv \omega_{\alpha} P_k$ . Similarly, we define  $|\Delta \hat{P}_{\alpha,1}| \equiv \omega_{\alpha} |\Delta P_1|$ . The evolution of the system is completely determined by  $\hat{P}_{\alpha,0}$ ,  $|\Delta \hat{P}_{\alpha,1}|$  and  $\hat{\gamma}_{\alpha} = \gamma_{\alpha}/\omega_{\alpha}$ .

In general, systems with multiple modes exhibit the same types of behaviours seen in the single-mode system. Systems with small  $|\Delta \hat{P}_{\alpha,1}|$  pass through multiple resonances over many orbits. For systems with many modes, resonances play a significant role in the orbital evolution, as shown in Fig. 3.9. Multi-mode systems also exhibit chaotic growth that damps into a quasi-steady state (see Fig. 3.10).

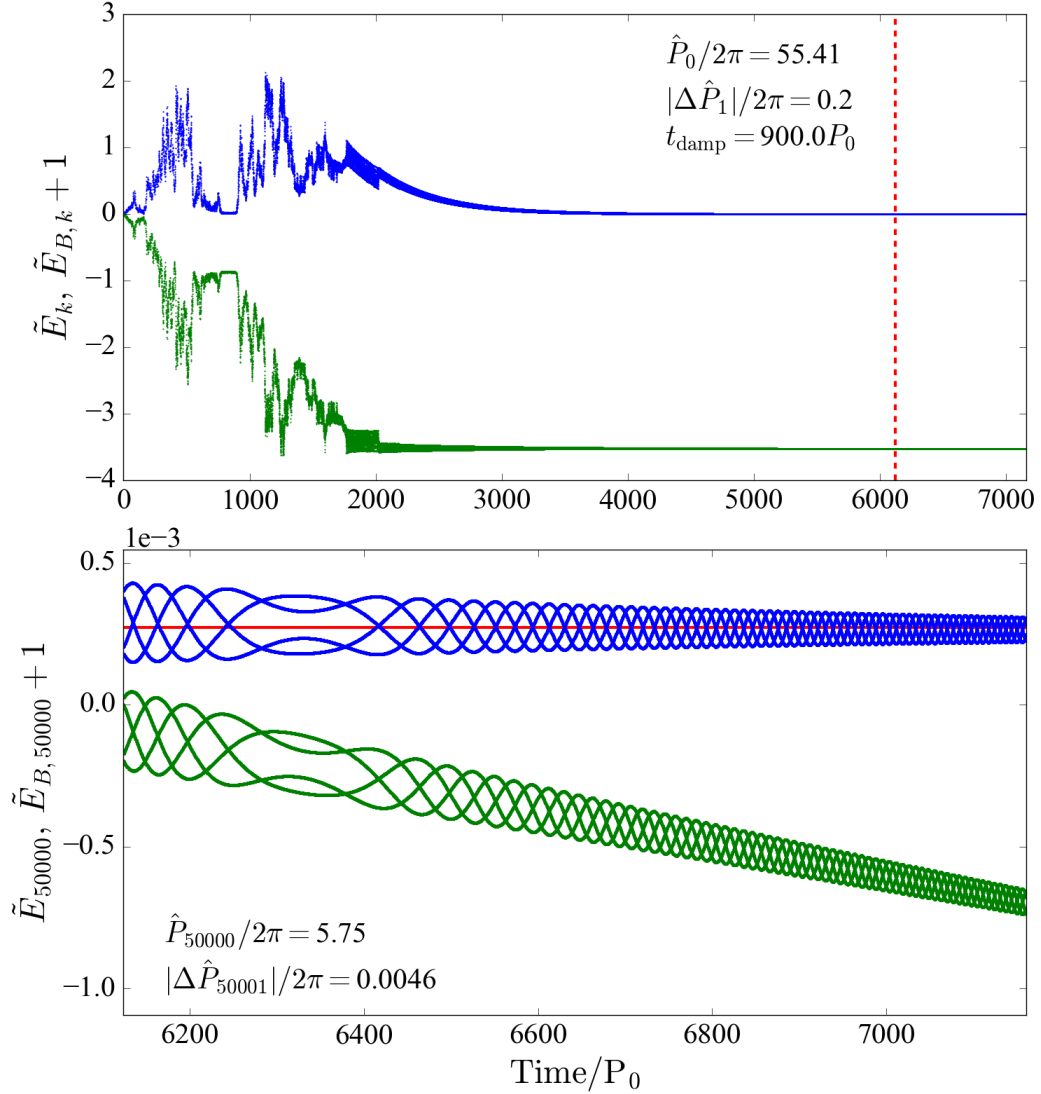


Figure 3.8: The mode energy (in blue) and the binary orbital energy (in green) over many pericentre passages. In the upper panel, the energy is normalized to the initial orbital energy of the binary. The mode energy undergoes chaotic evolution, and damps to a quasi-steady state after a few  $t_{\text{damp}}$ . The lower panel shows the later phase of the evolution (to the right of the dashed red line in the upper panel), with the energy re-normalized to the energy of the binary after 50,000 orbits. The predicted quasi-steady state mode energy is shown as a solid red line. The values of  $\hat{P}$  and  $|\Delta\hat{P}|$  at 50,000 orbits are indicated. Note that because of the significant orbital decay during chaotic evolution, we use time (in units of  $P_0$ ) rather than the number of orbits for the  $x$ -axis.

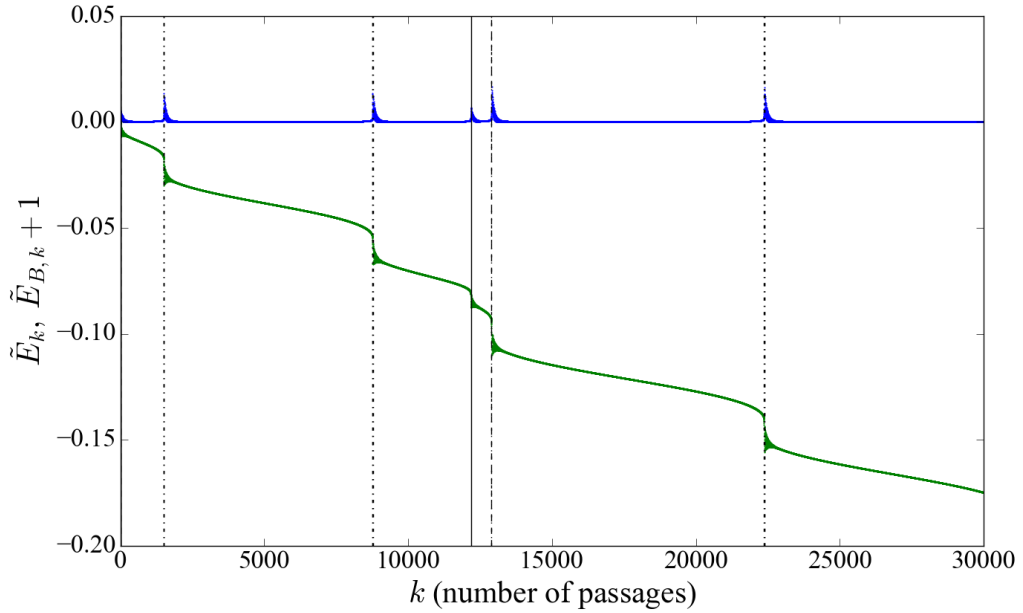


Figure 3.9: The total mode energy and orbital energy of a system with three modes that evolves through multiple resonances. The properties of the modes are discussed in detail in Appendix B.3. For this system, the parameters are  $\hat{P}_{\alpha,0}/2\pi = 123, 56.6, 50.4$  and  $|\Delta\hat{P}_{\alpha,1}|/2\pi = 0.1, 0.05, 0.04$ . The mode damping times are all of order  $t_{\text{damp}} \sim 100P_0$ . Resonances for different modes are shown with vertical solid, dashed, and dot-dashed lines.

Figure 3.11 shows two examples similar to Fig. 3.1 that explore the parameter space of systems with three modes — one with a dominant mode, and another with  $(\Delta a_\alpha)$  roughly equal for all modes. For application to stellar binaries, the example with a dominant mode is characteristic of a binary with  $M \sim (\text{a few})M_\odot$  and a small pericentre separation ( $\eta \sim 3$ ). For systems with larger  $\eta$ 's, the tidal potential tends to excite higher-order modes to similar amplitudes. Appendix B.3 provides more detail on the choice of mode properties, which are determined using MESA stellar models and the non-adiabatic GYRE pulsation code [Paxton et al., 2011, Townsend and Teitler, 2013]. In general, including multiple modes does not alter the classes of behaviours that the system exhibits. However, the multiple-

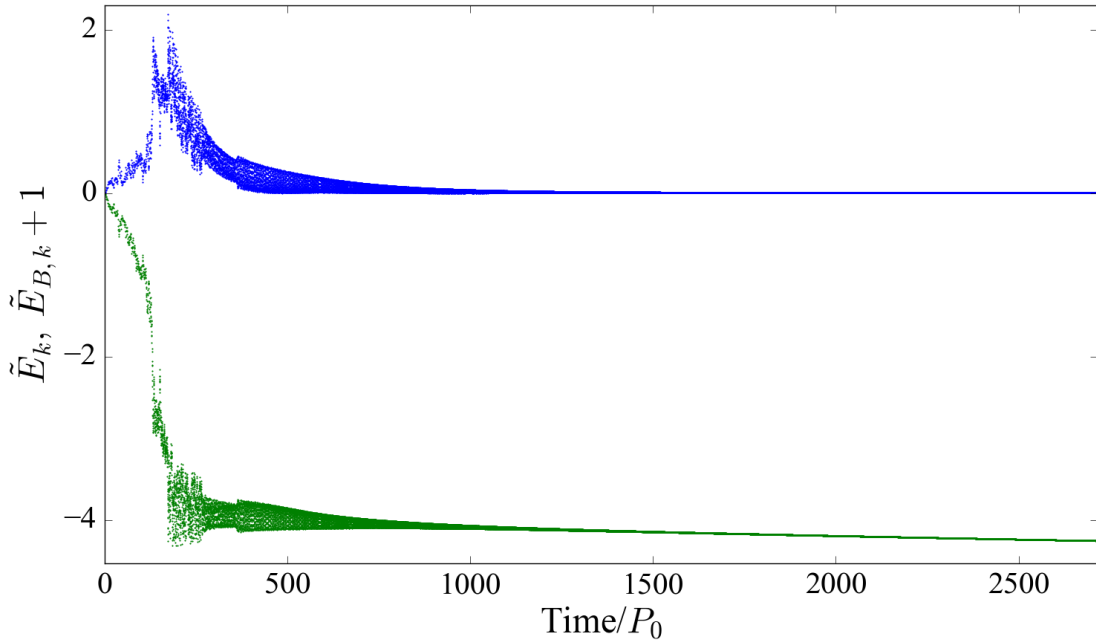


Figure 3.10: The total mode energy and orbital energy of a system with three modes that undergoes initial chaotic growth and eventually damps to a quasi-steady state. The properties of the modes are discussed in detail in Appendix B.3. For this system, the parameters are  $\hat{P}_{\alpha,0}/2\pi = 123, 137, 113$  and  $|\Delta\hat{P}_{\alpha,1}|/2\pi = 2.3, 2.5, 2.1$ . The mode damping times are all of order  $t_{\text{damp}} \sim 100P_0$ .

mode model is more prone to chaotic evolution. Additionally, all modes, even those with relatively small  $\Delta a_\alpha$  can guide the evolution of the system near resonance.

### 3.6 Summary and Discussion

We have developed a mathematically simple model that accurately captures the evolution of eccentric binary systems driven by dynamical tides. This model is exact for linear tidal oscillations in highly eccentric systems (see the last paragraph of Section 3.2 for the regime of validity of the model). The evolution of the “eccentric orbit + oscillation mode” system

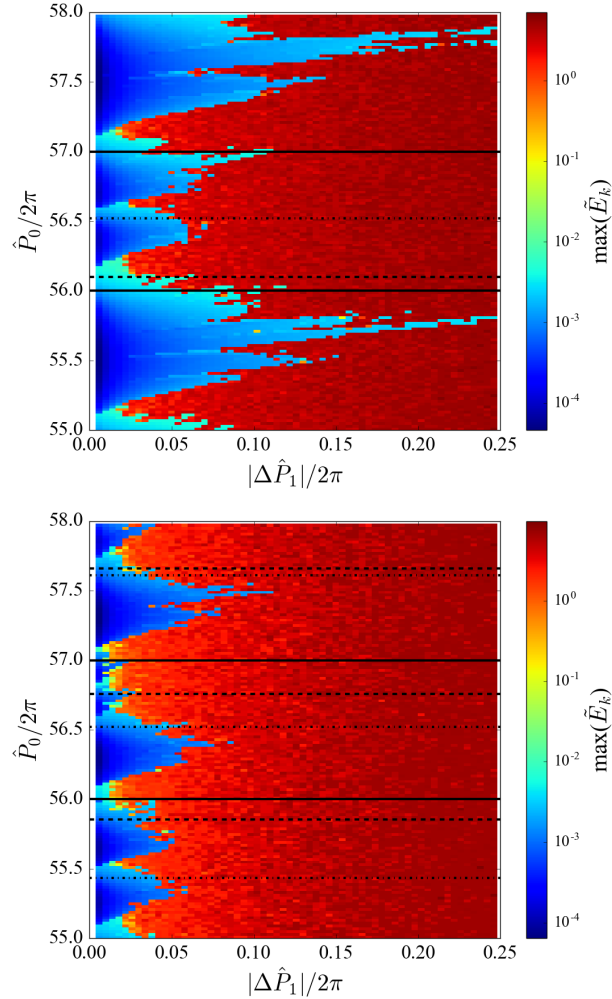


Figure 3.11: The maximum mode energy (summed over all modes) reached in 10,000 orbits as a function of  $\omega_1 |\Delta P_1|/2\pi$  and  $\omega_1 P_0/2\pi$ . In the dark blue regions, the modes exhibit low-energy oscillations, while in the dark red regions the modes grow chaotically to large amplitudes. The left panel shows a system with one dominant mode. The frequency ratios are  $\omega_2/\omega_1 = 0.41$  and  $\omega_3/\omega_1 = 0.46$ . The energy ratios are  $\Delta\tilde{E}_{2,1}/\Delta\tilde{E}_{1,1} = 0.04$  and  $\Delta\tilde{E}_{3,1}/\Delta\tilde{E}_{1,1} = 0.03$ . The dashed line corresponds to  $\omega_2\hat{P}_0/2\pi = 23$ , the dot-dashed line to  $\omega_3\hat{P}_0/2\pi = 26$ , and the solid lines to resonances for  $\omega_1$ . The right panel shows a system where all three modes are excited to similar energies. The frequency ratios are  $\omega_2/\omega_1 = 1.11$  and  $\omega_3/\omega_1 = 0.92$ . The energy ratios are  $\Delta\tilde{E}_{2,1}/\Delta\tilde{E}_{1,1} = 0.94$  and  $\Delta\tilde{E}_{3,1}/\Delta\tilde{E}_{1,1} = 0.58$ . The dashed lines corresponds to  $\omega_2\hat{P}_0/2\pi = 62, 63, 64$ , the dot-dashed lines to  $\omega_3\hat{P}_0/2\pi = 51, 52, 53$ , and the solid lines to resonances for  $\omega_1$ .

can be described by an iterative map, and depends on three parameters (for a single mode system):  $\hat{P}_0$ ,  $|\Delta\hat{P}_1|$  and  $\hat{\gamma}$  [see equations (3.7)-(3.9)], corresponding to the initial orbital period, the change in orbital period during the first pericentre passage, and the damping rate of an oscillation mode. Multiple modes can be easily incorporated.

The iterative map reveals the following key findings:

- For non-dissipative systems, the mode evolution exhibits three types of behaviours, depending on the values of  $|\Delta\hat{P}_1|$  and  $\hat{P}_0$  (see Figs. 3.1 and 3.3):
  - (i) For small  $|\Delta\hat{P}_1|$  and an orbital frequency far from resonance with the mode frequency (i.e.  $\hat{P}_0/2\pi$  not close to an integer), the mode experiences low-amplitude oscillations with a maximum mode energy given by equation (3.17).
  - (ii) For small  $|\Delta\hat{P}_1|$  and near resonance ( $\hat{P}_0/2\pi$  close to an integer), the mode exhibits larger-amplitude oscillations with a maximum energy given by equation (3.20).
  - (iii) For  $|\Delta\hat{P}_1| \gtrsim 1$ , the mode energy can grow chaotically (see Fig. 4), reaching a maximum of order the orbital binding energy [see equation (3.26)]. The chaotic mode growth can be approximately described by a diffusion model [equation (3.24)], although such a model would not contain the energy maximum.
- When mode dissipation is added, all systems, even those evolving chaotically, decay to a quasi-steady state (see Figs. 3.6-3.8), with the mode energy and orbital decay rate given by equations (3.30) and

(3.31), respectively. Continued orbital decay is punctuated by resonances (see Section 3.4.2).

These results are applicable to a variety of astrophysical systems mentioned in the introduction. In particular, a tidally captured star around a compact object in dense clusters [Mardling and Aarseth, 2001] or a massive black hole, [e.g. Li and Loeb, 2013] at the centre of galaxies may experience chaotic growth of mode amplitude during multiple pericentre passages, accompanied by significant orbital decay and tidal heating. A similar evolution may occur when a giant planet (“cold Jupiter”) is excited into a high-eccentricity orbit by an external companion (a distant star or a nearby planet) via the Lidov-Kozai mechanism [Wu and Murray, 2003, Fabrycky and Tremaine, 2007, Nagasawa et al., 2008, Petrovich, 2015a, Anderson et al., 2016, Muñoz et al., 2016]. We have found that a  $m_p \sim 1 M_J$  planet pushed into an orbit with pericentre distance  $\lesssim 0.015$  AU and  $e \gtrsim 0.95$  will enter the chaotic regime for the growth of f-modes. The planet can spend an appreciable time in the high- $e$  phase of the Lidov-Kozai cycle, allowing the mode energy to climb to a large value at which the mode becomes non-linear and suffers rapid decay. The consequence is that the planet’s orbit quickly shrinks (by a factor of a few), similar to the behaviour depicted in Fig. 3.8, and the system eventually enters a quasi-steady state with slow orbital decay. We suggest that this is a promising mechanism for forming eccentric warm Jupiters, whose origin remains poorly understood [Petrovich and Tremaine, 2016, Antonini et al., 2016, Huang et al., 2016, Anderson and Lai, 2017]. This mechanism also speeds up the formation of hot Jupiters through high-eccentricity migration channels.

Our study has revealed a rich variety of dynamical behaviours for highly eccentric binaries undergoing tidal interactions. Nevertheless, our model is still idealized. One effect we did not include is stellar (or planetary) rotation. The qualitative behaviours of systems that undergo low-amplitude oscillations or chaotic evolution are unlikely to change with the inclusion of rotation. However, tidal spin-up of the star (and tidal heating) can directly affect the mode frequencies, giving rise to the possibility of resonance locking under some conditions, which may extend the time frame over which the orbital energy rapidly decreases [Witte and Savonije, 1999, Fuller and Lai, 2012a, Burkart et al., 2012, Fuller, 2017]. In addition, as noted above, our assumption of linear damping may fail in the chaotic regime; non-linear damping could lead to even more rapid orbital evolution and significant structural changes in the excited star or planet. All of these issues deserve further study.

As this paper was under review, an independent work on dynamical tides in eccentric giant planets was submitted by Wu [2017]. She considers the effect of chaotic f-mode evolution (approximately diffusive evolution) on the orbits of gas giants undergoing high-eccentricity migration, assuming that the f-mode damps non-linearly when its amplitude becomes too large. Her conclusion that dynamical tides rapidly shrink the orbit, overtaking secular migration, agrees with our results and the discussion above.

CHAPTER 4

**CHAOTIC TIDES IN MIGRATING GAS GIANTS: FORMING HOT  
AND TRANSIENT WARM JUPITERS VIA LIDOV-KOZAI  
MIGRATION**

Originally published in:

M. Vick, D.Lai, and K.R. Anderson. Chaotic tides in migrating gas giants: forming hot and transient warm Jupiters via Lidov-Kozai migration. *MNRAS* **484**, pp. 5645–5668, 2019. doi: 10.1093/mnras/stz354

## 4.1 Introduction

Despite over two decades of observations, the origins of hot Jupiters (HJs, giant planets with orbital periods  $\lesssim 10$  days) remain puzzling [see Dawson and Johnson, 2018, for a review]. The materials and conditions necessary to form such massive planets are not thought to exist so close to a protostar. Some have suggested that HJs could form in-situ when a protoplanet migrates inward and accumulates a gas envelope [Boley et al., 2016, Batygin et al., 2016]. However, most theories propose that a fully formed gas giant migrated toward its host star either via interaction with the protoplanetary disk [e.g. Lin et al., 1996, Kley and Nelson, 2012] or through tidal decay and circularization of a high-eccentricity orbit, a process termed “high-eccentricity migration.” Equally puzzling is the origin of warm Jupiters (WJs), giant planets with periods between about 10 days and 200 days. Although these close-in giant planets (HJs and WJs) represent a relatively small population of exoplanetary systems compared to the more abundant super-earths, their dynamical history can potentially

shape the architecture of planetary systems.

High-eccentricity migration is an appealing avenue for HJ formation. In this scenario, a gas giant is excited into a highly eccentric orbit via interactions with other planets or with a distant stellar companion. Strong planet-planet scattering [Rasio and Ford, 1996, Chatterjee et al., 2008, Jurić and Tremaine, 2008], various forms of secular interactions [Wu and Lithwick, 2011, Hamers and Portegies Zwart, 2016, Petrovich, 2015b], or a combination of both [Nagasawa et al., 2008, Beaugé and Nesvorný, 2012], can produce very eccentric gas giants. A highly inclined stellar or planetary companion can excite “Lidov-Kozai” (LK) oscillations [Lidov, 1962, Kozai, 1962, Naoz, 2016, for a review], pushing the eccentricity of the giant planet to near unity [Wu and Murray, 2003, Fabrycky and Tremaine, 2007, Naoz et al., 2012, Correia et al., 2012, Petrovich, 2015a, Anderson et al., 2016]. In all cases, the orbit circularizes and decays to a period of few days due to the tidal dissipation within the planet.

High-eccentricity migration can account for several puzzling characteristics of observed HJs. For instance, tidal orbital decay produces the observed pile-up of HJs at an orbital period of  $\sim 3$  days [e.g. Santerne et al., 2016], corresponding to semi-major axes of a few times the Roche radii of the planets. Lidov-Kozai migration driven by an inclined stellar/planetary companion can naturally generate significant “spin-orbit” misalignments between the rotation axis of the host star and the orbital angular momentum axis of the planet, as observed in many HJ systems [Hébrard et al., 2008, Narita et al., 2009, Winn et al., 2009, Triaud et al., 2010, Albrecht et al., 2012, Winn and Fabrycky, 2015]; the chaotic evolution of the stellar spin axis driven by the changing planetary orbit may

play a dominant role in producing the observed stellar obliquities [Storch and Lai, 2014, Anderson et al., 2016, Storch et al., 2017]. Other flavors of high- $e$  migration can also produce appreciable spin-orbit misalignments [e.g. Lithwick and Wu, 2014, Petrovich, 2015b, Teyssandier et al., 2019]. In addition, direct RV and AO-imaging searches have shown that a large fraction of HJs have external massive planet companions at 5-20 au or distant stellar companions (50-2000 au) [Knutson et al., 2014, Ngo et al., 2015, Wang et al., 2015, Bryan et al., 2016], suggesting that dynamical interactions play a role in HJ formation. Huang et al. [2016] showed that most HJs do not have any detectable neighbors (while half of WJs are closely flanked by small neighbors), again suggesting that a significant fraction of HJs may have formed through a dynamically active process, such as high- $e$  migration.

A significant uncertainty in any high- $e$  migration scenario is tidal dissipation in the planet. Regardless of how the planet attains its high eccentricity, efficient tidal dissipation is necessary in order to circularize the planet's orbit and to bring it from a semi-major axis of several au's to  $\lesssim 0.05$  au. So far, almost all studies of high- $e$  migration have relied on the parameterized weak-friction theory of equilibrium tides [Alexander, 1973, Hut, 1981]. In order achieve tidal circularization within  $\sim 5$  Gyrs in high- $e$  migration scenarios, the giant planet generally should be more dissipative than Jupiter by more than an order of magnitude [e.g. Socrates et al., 2012, Petrovich, 2015a, Anderson et al., 2016].

The response of a fluid body (such as a giant planet) to tidal perturbation involves the excitation of internal waves and modes at different frequencies [see, e.g., Ogilvie, 2014]. For a body in a sufficiently eccentric orbit, os-

cillatory modes excited at pericentre by the star’s tidal potential can grow chaotically in amplitude, rapidly draining energy from the orbit over multiple close passages [Mardling, 1995a,b]. This effect is important for high-eccentricity migration because the same conditions that allow a planet to migrate quickly – small pericentre distance and large eccentricity – are those that result in chaotic tidal behaviour. Ivanov and Papaloizou [2004a] first studied the possibility that chaotic dynamical tides could speed up the circularization of eccentric gas giants. They developed an iterative algebraic map to simply follow f-mode evolution over many orbits from one pericentre passage to the next, and later extended that work to consider inertial mode or i-mode oscillations [Ivanov and Papaloizou, 2007b]. More recently, Vick and Lai [2018] used a similar map (generalized to include linear mode damping) to quantify the various dynamical behaviours of the “mode + eccentric orbit” system (see also Section 4.2 below); they suggested that chaotic tides could quickly produce eccentric warm Jupiters (WJs), with a semi-major axis between 0.1 and 1 au, that efficiently circularize to HJs. Wu [2018] also studied the orbital evolution of a planet experiencing chaotic tides, and uncovered some of the key features of high- $e$  migration with chaotic tides – we will examine these features in more detail in the later sections of this paper.

In this paper, we present a comprehensive study of high-eccentricity migration of giant planets, incorporating a detailed model of chaotic tidal evolution. We focus on migration via the LK effect with a stellar companion. Although this flavour of high- $e$  migration may only account for a fraction of the HJ population, it is most suitable for systematic study since the initial conditions (such as the orbital properties of the stellar perturber) are

reasonably well-justified, and it serves as a benchmark for other high- $e$  migration scenarios. Indeed, several aspects of our results presented in this paper can be applied to other flavours of high- $e$  migration [see Teyssandier et al., 2019, which studies chaotic dynamical tides in the “secular chaos” scenario]. By comparing to our previous study of LK migration with static tides [Anderson et al., 2016, Muñoz et al., 2016], we show that including chaotic tides leads to a number of “favourable” features for the formation of close-in giant planets: e.g., it naturally produces eccentric WJs on short timescales ( $\lesssim 10 - 100$  Myrs) and speeds up the formation of HJs; it generates a wider HJ period distribution; and it prevents some gas giants from undergoing tidal disruption, thereby increase the HJ formation fraction. Overall, chaotic tides make high- $e$  migration a more promising mechanism for producing HJs

The structure of the paper is as follows. In Section 4.2 we revisit the derivation of the iterative map for the evolution of planetary oscillation modes (dynamical tides), starting from hydrodynamical equations and including the effect of planetary rotation; we examine the different dynamical behaviours of the “modes + eccentric orbit” system and discuss the conditions for various modes in the planet to become chaotic. In Section 4.3 we describe our model for coupling LK oscillations with chaotic tides. Section 4.4 discusses the key features and signposts of LK migration with chaotic tides and includes a number of analytical results that characterize chaotic tidal migration. In Section 4.5 we present our population synthesis study for planets undergoing LK oscillations with chaotic tides. In Section 4.6 we give analytical calculations for the HJ formation and tidal disruption fractions from this migration mechanism and compare them

with our numerical results. We conclude in Section 7 with a summary of results and discussion of their implications.

## 4.2 Chaotic Dynamical Tides in Giant Planets in Eccentric Orbits

Consider a planet (mass  $M_p$  and radius  $R_p$ ) in a highly eccentric orbit around a star (mass  $M_*$ ). At each pericentre passage, the time-varying gravitational potential of the star excites oscillatory modes (e.g. f-modes and i-modes) in the planet. Over multiple pericentre passages, the orbit and the modes exchange energy and angular momentum. In general, this exchange can occur in either direction depending on the phase of the modes [Kochanek, 1992, Mardling, 1995a]. Provided the oscillation amplitudes are sufficiently small, one can determine the dynamical behaviour of the system using linear hydrodynamics [e.g. Mardling, 1995a,b, Lai, 1996a, Kumar and Goodman, 1996, Lai, 1997]. However, following the evolution of the system over many orbits can be challenging because of the short timescale associated with the pericentre passage. Fortunately, when the orbit is eccentric enough, such that the mode and the orbital evolution mainly occur at pericentre, the full hydrodynamic solution of the “eccentric orbit + oscillation modes” system can be expressed as an iterative map [Ivanov and Papaloizou, 2004a, Vick and Lai, 2018].

### 4.2.1 Hydrodynamics of Tidally Forced Oscillations & Iterative Map

In Vick and Lai [2018], we presented a simple iterative map to describe the long-term evolution of an “eccentric orbit + oscillation modes” system. Our map neglected the rotation of the planet and assumed that the change in the mode amplitude during each pericentre passage is constant throughout the orbital evolution. Giant planets can have substantial rotations, which affect their mode properties and introduce a few subtleties to the mapping. Also, during the long-term evolution of the planet’s orbit driven by an external companion (the Lidov-Kozai effect), the pericentre distance can change appreciably, which affects mode excitation. Here we present a general derivation of the iterative map from linear hydrodynamics, allowing for the planet to rotate and for the pericentre distance (and thus the change in mode amplitude at pericentre) to vary between passages.

The stellar gravitational potential that excites oscillations in the planet is given by

$$U(\mathbf{r}, t) = -GM_* \sum_{lm} \frac{W_{lm} r^l}{D^{l+1}} e^{-im\Phi(t)} Y_{lm}(\theta, \phi_i), \quad (4.1)$$

where  $\mathbf{r} = (r, \theta, \phi_i = \phi + \Omega_s t)$  is the position vector (in spherical coordinates) relative to the centre of mass of the planet (the azimuthal angle  $\phi$  is measured in the rotating frame of the planet, and  $\Omega_s$  is the rotation rate of the planet<sup>1</sup>). In equation (4.1),  $D(t)$  is the time-varying separation between the star and planet,  $\Phi(t)$  is the orbital true anomaly, and  $W_{lm}$  is a constant defined in Press and Teukolsky [1977]. The dominant (quadrupole) terms

---

<sup>1</sup>We assume the spin axis of the planet is aligned with the orbital angular momentum axis throughout this paper.

have  $l = |m| = 2$  with  $W_{2\pm 2} = \sqrt{3\pi/10}$ .

The linear, adiabatic response of the planet to tidal forcing is described by the Lagrangian displacement,  $\xi(\mathbf{r}, t)$ . A free oscillatory mode of frequency  $\omega_\alpha$  (in the rotating frame) has the form  $\xi_\alpha(\mathbf{r}, t) = \xi_\alpha(\mathbf{r}) e^{-i\omega_\alpha t} \propto e^{im\phi - i\omega_\alpha t}$ , where  $\alpha$  is the mode index. We expand  $\xi(\mathbf{r}, t)$  in terms of the eigenmodes in the phase space [Schenk et al., 2002]:

$$\begin{bmatrix} \xi \\ \partial\xi/\partial t \end{bmatrix} = \sum_\alpha b_\alpha(t) \begin{bmatrix} \xi_\alpha(\mathbf{r}) \\ -i\omega_\alpha \xi_\alpha(\mathbf{r}) \end{bmatrix}. \quad (4.2)$$

The linear fluid dynamics equations then reduce to a set of first-order differential equations [Lai and Wu, 2006],

$$\dot{b}_\alpha + i\omega_\alpha b_\alpha = \frac{iM_* W_{lm} Q_\alpha}{2\epsilon_\alpha D^{l+1}} e^{-im\Phi(t)+im\Omega_s t}, \quad (4.3)$$

where

$$Q_\alpha = \int d^3x \rho \xi_\alpha^\star \cdot \nabla(r^l Y_{lm}) \quad (4.4)$$

is the dimensionless tidal overlap integral (in units where  $G = M_p = R_p = 1$ ), and

$$\epsilon_\alpha = \omega_\alpha + \int d^3x \rho \xi_\alpha^\star \cdot (\mathbf{i}\Omega_s \times \xi_\alpha). \quad (4.5)$$

Note that in the slow rotation limit,  $\epsilon_\alpha$  is simply the mode frequency for a non-rotating planet,  $\omega_\alpha(0)$ . When  $\epsilon_\alpha \gg \Omega_s$ , the first-order correction to the mode frequency due to rotation is  $\omega_\alpha - \omega_\alpha(0) \approx -mC_\alpha\Omega_s = -\int d^3x \rho \xi_\alpha^\star \cdot (\mathbf{i}\Omega_s \times \xi_\alpha)$  [e.g. Unno et al., 1989]. In equations (4.3)-(4.5), the eigenmode is normalized according to

$$\int d^3x \rho(\mathbf{r}) |\xi_\alpha(\mathbf{r})|^2 = 1. \quad (4.6)$$

The general solution to equation (4.3) is

$$b_\alpha(t) = e^{-i\omega_\alpha t} \int_{t_0}^t \frac{iM_* W_{lm} Q_\alpha}{2\epsilon_\alpha D^{l+1}} e^{i\sigma_\alpha t' - im\Phi(t')} dt' + b_\alpha(t_0), \quad (4.7)$$

where

$$\sigma_\alpha = \omega_\alpha + m\Omega_s \quad (4.8)$$

is the mode frequency in the inertial frame.

For a highly eccentric orbit, we can assume that any energy transfer between a mode and the orbit occurs at pericentre. We can then manipulate equation (4.7) into a discrete form by defining  $t_k$  as the time at apocentre after the  $k$ -th pericentre passage, i.e.

$$t_k = t_{k-1} + \frac{1}{2} (P_{k-1} + P_k), \quad (4.9)$$

where  $P_k$  is the orbital period after the  $k$ -th pericentre passage. We also define

$$\Delta b_{\alpha,k} = \int_{-P_{k-1}/2}^{P_k/2} \frac{iM_* W_{lm} Q_\alpha}{2\epsilon_\alpha D(t')^{l+1}} e^{i\sigma_\alpha t' - im\Phi(t')} dt'. \quad (4.10)$$

Physically, this is the real change in mode amplitude during the  $k$ -th pericentre passage. Equation (4.7) becomes

$$b_\alpha = b_{\alpha,0} + e^{-i\omega_\alpha t_k} \sum_{j=1}^k e^{i\sigma_\alpha(t_{j-1}+P_{j-1}/2)} \Delta b_{\alpha,j}. \quad (4.11)$$

We assume the initial condition  $b_{\alpha,0} = 0$ . Equation (4.11) can be rewritten in an iterative form:

$$b_{\alpha,k} = b_{\alpha,k-1} e^{-i\omega_\alpha(P_{k-1}+P_k)/2} + \Delta b_{\alpha,k} e^{i(m\Omega_s t_k - \sigma_\alpha P_k/2)}. \quad (4.12)$$

We now define the mode amplitude in the inertial frame and shift the index  $k$  to count pericentre passages using

$$c_{\alpha,k} \equiv b_{\alpha,k} e^{-i(m\Omega_s t_k + \sigma_\alpha P_k/2)}. \quad (4.13)$$

Physically,  $c_{\alpha,k}$  is the mode amplitude just before the  $(k+1)$ -th pericentre passage. Equation (4.12) then becomes

$$c_{\alpha,k} = (c_{\alpha,k-1} + \Delta c_{\alpha,k}) e^{-i\sigma_\alpha P_k}, \quad (4.14)$$

where  $\Delta c_{\alpha,k} = \Delta b_{\alpha,k}$ . Equation (4.14) has a straight-forward physical interpretation: when the planet passes through pericentre (the  $k$ -th passage), the mode amplitude changes by  $\Delta c_{\alpha,k}$ , and the orbital period changes to  $P_k$ ; as the planet completes its orbit, the phase of the mode evolves due to the passage of time, and the complex mode amplitude gains a factor  $e^{-i\sigma_\alpha P_k}$ . Note that in general  $\Delta c_{\alpha,k}$  depends on the “current” parameters of the system. If the pericentre distance and the shape of the orbit near pericentre remain unchanged over many passages,  $\Delta c_{\alpha,k}$  is nearly constant from one passage to the next. In this case, equation (4.14) reduces to the result from Vick and Lai [2018] but without mode damping and with the phase evolution determined by the mode frequency in the inertial frame [see also Ivanov and Papaloizou, 2004a].

The mode amplitude is directly related to the mode energy via

$$E_{\alpha,k} = 2\sigma_\alpha \epsilon_\alpha |c_{\alpha,k}|^2, \quad (4.15)$$

where the factor of 2 arises because a mode with given  $m$  ( $> 0$ ), and  $\sigma_\alpha$  is physically identical to that with  $(-m)$  and  $(-\sigma_\alpha)$  — we treat them as the same mode. We define the dimensionless mode energy,  $\tilde{E}_{\alpha,k}$ , in units of the initial binary (planetary) orbital energy,  $|E_{B,0}| = GM_*M_p/(2a_0)$  (where  $a_0$  is the semi-major axis), and define the re-normalized mode amplitude  $\tilde{c}_{\alpha,k}$  such that

$$\tilde{E}_{\alpha,k} \equiv |\tilde{c}_{\alpha,k}|^2 \equiv \frac{E_{\alpha,k}}{|E_{B,0}|}. \quad (4.16)$$

The total energy transfer to modes in the  $k$ -th passage is therefore

$$\Delta \tilde{E}_k = \sum_\alpha \Delta \tilde{E}_{\alpha,k} = \sum_\alpha (|\tilde{c}_{\alpha,k-1} + \Delta \tilde{c}_\alpha|^2 - |\tilde{c}_{\alpha,k-1}|^2). \quad (4.17)$$

From energy conservation, the orbital energy ( $\tilde{E}_{B,k}$ ) immediately after the

$k$ -th passage is given by

$$\tilde{E}_{B,k} = \tilde{E}_{B,k-1} - \Delta\tilde{E}_k = \tilde{E}_{B,k-1} - \sum_{\alpha} \tilde{E}_{\alpha,k}, \quad (4.18)$$

and the corresponding orbital period is

$$\frac{P_k}{P_0} = \left( \frac{\tilde{E}_{B,0}}{\tilde{E}_{B,k}} \right)^{3/2}, \quad (4.19)$$

where  $\tilde{E}_{B,0} = -1$ , and  $P_0$  is the initial period.

Equations (4.14) and (4.17)-(4.19) complete the map. The required inputs are the initial mode energy,  $\tilde{E}_{\alpha,0} = |\tilde{c}_{\alpha,0}|^2$ , and  $\Delta\tilde{c}_{\alpha,k}$ , the change in mode amplitude during each pericentre passage. This map accurately determines the evolution of the orbit and mode energies provided that the orbit is highly eccentric and the modes remain linear (i.e., the sum of the mode energies is much less than the binding energy of the planet).

The dimensionless change in mode amplitude during a pericentre passage (suppressing the subscript ‘ $k$ ’),  $\Delta\tilde{c}_{\alpha}$ , depends on the orbital parameters (mainly the pericentre distance  $r_p$ ) and the mode properties. It is related to the energy transfer  $\Delta E_{\alpha}$  by

$$|\Delta\tilde{c}_{\alpha}|^2 = \frac{\Delta E_{\alpha}}{|E_{B,0}|}. \quad (4.20)$$

Note that in general the energy transfer to mode  $\alpha$  in a pericentre passage depends on the amplitude and phase of “pre-existing” oscillations [see equation (4.17)]. In equation (4.20),  $\Delta E_{\alpha}$  refers to the energy transfer when the mode has zero amplitude prior to the pericentre passage — in Vick and Lai [2018], we term this “the first passage.” The energy transfer  $\Delta E_{\alpha}$  for a parabolic encounter ( $e \rightarrow 1$ ) was first derived by Press and Teukolsky [1977]. This can be generalized to eccentric orbits and modified to include

the effect of rotation [Lai, 1997, Fuller and Lai, 2012a]. For a pericentre distance  $r_p$ ,  $\Delta E_\alpha$  can be written as (keeping only the  $l = 2$  terms)

$$\begin{aligned}\Delta E_\alpha &= \frac{GM_*^2}{r_p^6} R_p^5 T(\eta, \sigma_\alpha/\Omega_p, e) \\ &= \frac{GM_p^2}{R_p} \left( \frac{M_*}{M_{\text{tot}}} \right)^2 \eta^{-6} T(\eta, \sigma_\alpha/\Omega_p, e),\end{aligned}\quad (4.21)$$

where  $\eta$  is the ratio of  $r_p$  and the tidal radius  $r_{\text{tide}}$ , i.e.

$$\eta \equiv \frac{r_p}{r_{\text{tide}}}, \quad r_{\text{tide}} \equiv R_p \left( \frac{M_*}{M_p} \right)^{1/3}, \quad (4.22)$$

with  $M_{\text{tot}} = M_* + M_p \simeq M_*$ , and  $\Omega_p$  is the pericentre orbital frequency

$$\Omega_p \equiv \left( \frac{GM_{\text{tot}}}{r_p^3} \right)^{1/2} = \left( \frac{GM_p}{R_p^3} \right)^{1/2} \eta^{-3/2}. \quad (4.23)$$

Note that  $\sigma_\alpha/\Omega_p = \bar{\sigma}_\alpha \eta^{3/2}$ , with  $\bar{\sigma}_\alpha \equiv \sigma_\alpha (R_p^3/GM_p)^{1/2}$ . To avoid tidal disruption of the planet, we require [Guillochon et al., 2011]

$$r_p \geq r_{p,\text{dis}} = 2.7 r_{\text{tide}}, \quad \text{or} \quad \eta \geq 2.7. \quad (4.24)$$

The dimensionless function  $T$  is given by

$$T = 2\pi^2 \frac{\sigma_\alpha}{\epsilon_\alpha} (Q_\alpha K_{lm})^2, \quad (4.25)$$

where  $Q_\alpha$  is an overlap integral (see equation 4.4), and

$$K_{lm} = \frac{W_{lm}}{2\pi} \int_{-P/2}^{P/2} dt \left( \frac{r_p}{D(t)} \right)^{l+1} e^{i\sigma_\alpha t - im\Phi(t)}. \quad (4.26)$$

In equation (4.26), all quantities are in units where  $G = M_p = R_p = 1$  so that  $K_{lm}$  is dimensionless.

To follow the evolution of the system over many orbits, it is useful to be able to compute  $K_{lm}$  (and thus  $\Delta E_\alpha$ ) efficiently. For the dominant  $l = m = 2$  prograde mode ( $\sigma_\alpha > 0$ ), Lai [1997] derived an approximation for  $K_{22}$  that is accurate to within 2% for  $(1 - e) \ll 1$  and  $z \equiv \sqrt{2}\sigma_\alpha/\Omega_p \gtrsim$  a few:

$$K_{22} \simeq \frac{2z^{3/2} \exp(-2z/3)}{\sqrt{15}} \left( 1 - \frac{\sqrt{\pi}}{4\sqrt{z}} \right) \eta^{3/2}. \quad (4.27)$$

Table 4.1: Properties of  $l = m = 2$  f-modes and inertial modes for a  $\gamma = 2$  polytrope and a  $\gamma = 5/3$  polytrope. The mode frequencies  $\omega_\alpha$  (in the rotating frame),  $\epsilon_\alpha$  (equation 4.5), and  $\sigma_\alpha$  (in the inertial frame), and the planetary rotation rate  $\Omega_s$  are in units of  $(GM_p/R_p^3)^{1/2}$ , i.e.  $\omega_\alpha = \bar{\omega}_\alpha(GM_p/R_p^3)^{1/2}$ . The tidal overlap integral  $Q_\alpha$  is defined by equation (4.4).

Model Type	Mode	$\bar{\omega}_\alpha$	$\bar{\epsilon}_\alpha$	$\bar{\sigma}_\alpha$	$Q_\alpha$
$\gamma = 2$ polytrope	f-mode	$1.22 - \bar{\Omega}_s$	1.22	$1.22 + \bar{\Omega}_s$	0.56
	i-mode 1 ( $j = 3$ )	$0.56 \bar{\Omega}_s$	$0.28 \bar{\Omega}_s$	$2.56 \bar{\Omega}_s$	$0.015 \bar{\Omega}_s^2$
	i-mode 2 ( $j = 3$ )	$-1.1 \bar{\Omega}_s$	$-0.55 \bar{\Omega}_s$	$0.9 \bar{\Omega}_s$	$0.01 \bar{\Omega}_s^2$
$\gamma = 5/3$ polytrope	f-mode	$1.46 - \bar{\Omega}_s$	1.46	$1.46 + \bar{\Omega}_s$	0.49

As shown in Vick and Lai [2018], when the mode has no initial energy, i.e.  $\tilde{E}_{\alpha,0} = 0$ , the important quantity that determines the dynamical behaviour of the system is  $\Delta\hat{P}_\alpha = \sigma_\alpha\Delta P$ , where  $\Delta P = P_1 - P_0 \simeq -(3/2)P_0(\Delta E_\alpha/|E_{B,0}|)$  is the change in the initial orbital period ( $P_0$ ) due to the energy transfer  $\Delta E_\alpha$ . From equation (4.21), we have

$$\begin{aligned} |\Delta\hat{P}_\alpha| &= \sigma_\alpha\Delta P \simeq \frac{3}{2}\sigma_\alpha P_0 \frac{\Delta E_\alpha}{|E_{B,0}|} \\ &\simeq \frac{6\pi\sigma_\alpha/\Omega_p}{(1-e)^{5/2}} \left(\frac{M_p}{M_*}\right)^{2/3} \eta^{-5} T(\eta, \sigma_\alpha/\Omega_p, e). \end{aligned} \quad (4.28)$$

Physically,  $|\Delta\hat{P}_\alpha|$  is the phase change in the mode due to energy transfer at pericentre when there is no “pre-existing” mode energy.

## 4.2.2 Planetary Oscillation Modes

The gravitational potential of a star can excite many types of oscillation modes in the eccentric orbiting planet. Some of the modes will be more strongly excited than others and therefore more influential in long-term orbital evolution. The dominant modes are quadrupole, with  $l = |m| = 2$ . For the relevant values of  $r_p$ , we find that the quadrupole modes are at least 10 times more important for single passage pericentre energy transfer

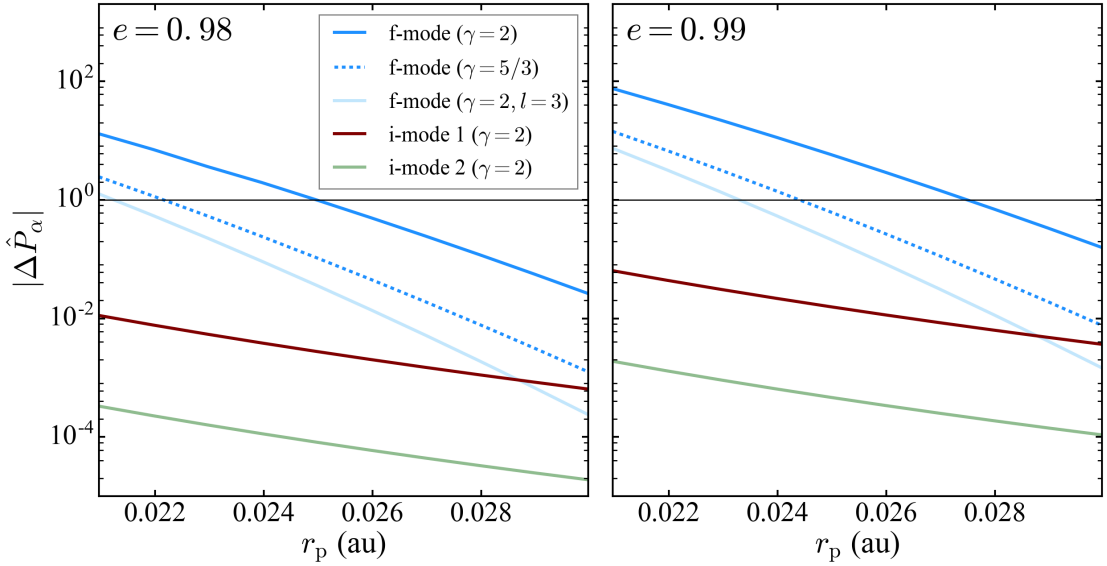


Figure 4.1: The dimensionless quantity  $|\Delta \hat{P}_\alpha|$  (see equation 4.28) as a function of the pericentre distance  $r_p$  for various planetary oscillation modes: the  $l = m = 2$  and  $l = m = 3$  f-modes and two i-modes of a  $\gamma = 2$  polytrope, and the  $l = m = 2$  f-mode of a  $\gamma = 5/3$  polytrope. The properties of these modes are provided in Table 4.1. The left and right panels show the results for two values of the orbital eccentricity ( $e = 0.98, 0.99$ ). For all models, we use  $R_p = 1.6 R_J$ ,  $q = M_*/M_p = 10^3$ . The black line marks  $\Delta \hat{P}_\alpha = 1$ .

than the higher degree  $l = |m| = 3$  modes (see Fig. 4.1). The  $m = 0$  modes generally are not strongly excited because  $K_{10}$  (equation 4.26) is small. In this paper, we adopt the convention  $m > 0$ , so a mode with  $\sigma_\alpha > 0$  ( $\sigma_\alpha < 0$ ) is prograde (retrograde) with respect to the rotation of the planet in the inertial frame. For the rest of this paper, we only consider modes with  $l = m = 2$ .

We adopt a simple giant planet model composed of a neutrally stratified fluid characterized by a  $\gamma = 2$  polytrope equation of state ( $P \propto \rho^2$ ). The f-mode (fundamental mode) has a frequency closest to the frequency of tidal forcing near pericentre, and the largest tidal overlap integral  $Q_\alpha$ . Higher order acoustic modes (p-modes) have higher frequencies and smaller tidal

overlaps, and are much less important than the f-mode for energy transfer. For a rotating planet, the stellar potential can also excite i-modes [i.e. inertial modes, with the restoring force being the Coriolis force; see Xu and Lai [2017] and references therein]. In a gas giant that has stratification, g-modes (driven by buoyancy) may also be excited [Fuller and Lai, 2014]. The presence of a large solid core also supports elastic modes which can “mix” with the f-mode [e.g. Fuller and Lai, 2013]. We do not consider such planet models in this paper because there are considerable uncertainties in the stratification and core size of giant planets [e.g. Guillot, 2005].

Table 4.1 lists the key properties of the  $l = m = 2$  f-modes and the first two inertial modes for the  $\gamma = 2$  polytropic planet model. For comparison, the f-mode properties of the  $\gamma = 5/3$  polytrope are also given. The f-modes are calculated using the slow-rotation approximation, which gives  $\omega_\alpha = \omega_\alpha(0) - mC_\alpha\Omega_s$ , and we find  $C_\alpha \approx 0.5$  for both the  $\gamma = 2$  and  $\gamma = 5/3$  models. The i-mode result is from Xu and Lai [2017] (see their Table IV), based on calculations using a non-perturbative spectral code. Note that for  $m = 2$ , the mode frequencies in the rotating frame ( $\omega_\alpha$ ) and in the inertial frame ( $\sigma_\alpha$ ) are related by  $\sigma_\alpha = \omega_\alpha + 2\Omega_s$ .

To determine which of these modes produces the strongest dynamical tides, we calculate  $|\Delta\hat{P}_\alpha|$  with equation (4.28) as a function of  $r_p$  for each of the modes (see Fig. 4.1). For definiteness, we assume that the planet rotates at the pseudo-synchronous rate  $\Omega_{ps}$  given by the weak friction theory of equilibrium tides [e.g. Hut, 1981], i.e.

$$\Omega_s = \Omega_{ps} \equiv \frac{f_2(e)}{(1 - e^2)^{3/2} f_5(e)} n, \quad (4.29)$$

where  $n = (GM_{\text{tot}}/a^3)^{1/2}$  is the mean motion of the planet and

$$f_2(e) = 1 + \frac{15}{2}e^2 + \frac{45}{8}e^4 + \frac{5}{16}e^6, \quad (4.30)$$

$$f_5(e) = 1 + 3e^2 + \frac{3}{8}e^4. \quad (4.31)$$

For  $(1 - e) \ll 1$ ,  $\bar{\Omega}_{\text{ps}} = \Omega_{\text{ps}}(GM_p/R_p^3)^{-1/2} \simeq 1.17/\eta^{3/2}$ , and the mode frequency in the inertial frame,  $\sigma_\alpha$ , is nearly independent of the orbital eccentricity. In this limit,  $T(\eta, \sigma_\alpha/\Omega_p, e)$  also has negligible eccentricity dependence, and  $|\Delta\hat{P}_\alpha| \propto (1 - e)^{-5/2}$  [see equation (4.28)]. The two panels of Fig. 4.1 shows that  $|\Delta\hat{P}_\alpha|$  indeed increases with  $e$  for all modes. We are most interested in systems where  $r_p$  is sufficiently small such that  $|\Delta\hat{P}_\alpha| \gtrsim 1$  (the criterion for chaotic mode growth; see Section 4.2.3). For such systems, it is clear that the  $l = m = 2$  f-mode is most strongly excited at pericentre passages. For the remainder of the paper, we focus on the prograde  $l = 2$  f-mode and neglect the contributions to energy transfer from other modes.

### 4.2.3 Conditions for Chaotic Tides

When the planetary orbit is sufficiently eccentric, the change in mode amplitude in a pericentre passage,  $\Delta c_\alpha$  (or equivalently the energy transfer in the “first” passage,  $\Delta E_\alpha$ , see equation 4.21), is constant over many pericentre passages.<sup>2</sup> In this case, if the mode has negligible dissipation, the dynamical behaviour of the iterative map depends on  $\hat{P}_{\alpha,0} = \sigma_\alpha P_0$ , the initial mode energy  $E_{\alpha,0}$ , and  $|\Delta\hat{P}_\alpha|$  (see equation 4.28), assuming that the initial mode energy  $E_{\alpha,0}$  is negligible (see Section 4.2.4). In particular, a

---

<sup>2</sup>This requires that the pericentre distance is constant, which in turn requires that the fractional change in the orbital angular momentum,  $\Delta L/L$ , remains small throughout orbital evolution. See equation (13) of Vick and Lai [2018].

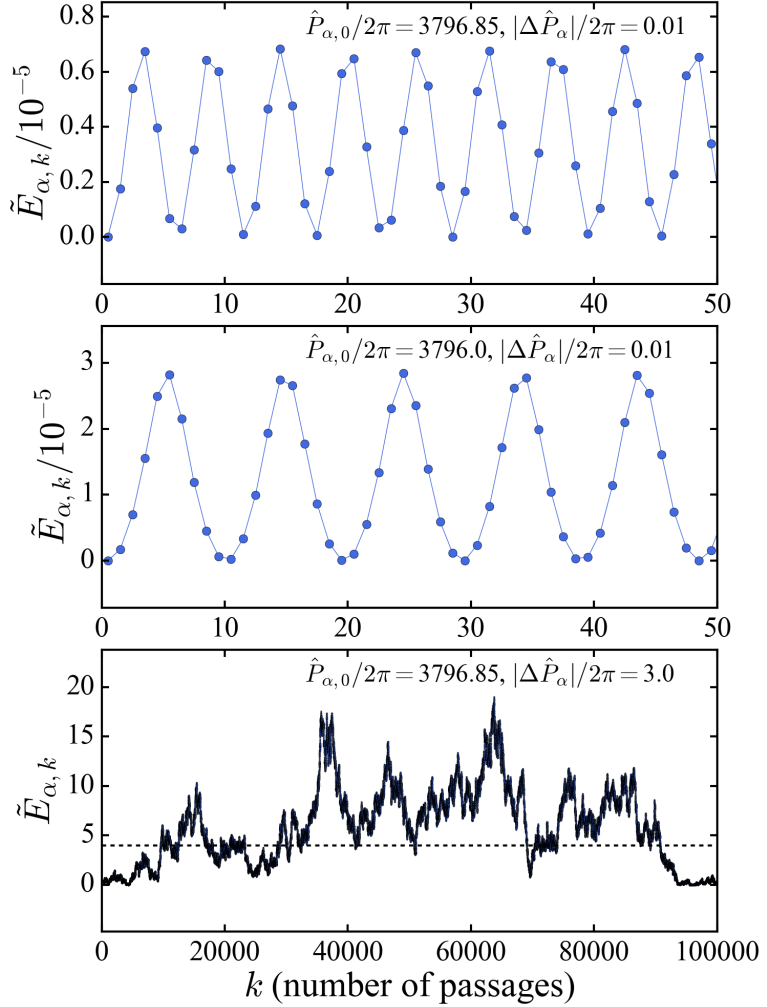


Figure 4.2: The evolution of the f-mode energy (scaled to the initial orbital energy  $|E_{B,0}|$ ) over multiple pericentre passages for star-planet systems with different values of  $\hat{P}_{\alpha,0}$  and  $|\Delta\hat{P}_\alpha|$ . Note that the top two panels have a different y-scale and x-axis range from the bottom panel. Top: An example of low-amplitude oscillations (with  $|\Delta\hat{P}_\alpha| \lesssim 1$ ). Middle: An example of resonant mode evolution (with  $\hat{P}_0/2\pi = \text{integer}$ ). Bottom: An example of chaotic mode growth (with  $|\Delta\hat{P}_\alpha| \gtrsim 1$ ). For a system with  $M_* = 1M_\odot$ ,  $M_p = 1M_J$ ,  $R_p = 1.6R_J$ , and the f-mode properties of a  $\gamma = 2$  polytrope, the three panels correspond to  $a \approx 1.5$  au and  $e \approx 0.98$  in the top two panels and  $e \approx 0.985$  in the bottom panel. This calculation does not include dissipation of the mode energy. In the bottom panel, the planet binding energy is shown with a dashed line; physically, the mode must dissipate energy well before  $\tilde{E}_{\alpha,k}$  climbs to this value.

system with  $|\Delta\hat{P}_\alpha|$  greater than a critical value,  $\Delta\hat{P}_{\text{crit}}$ , behaves very differently from systems with  $|\Delta\hat{P}_\alpha| \lesssim \Delta\hat{P}_{\text{crit}}$ . The exact value of  $\Delta\hat{P}_{\text{crit}}$  depends on the dimensionless orbital period,  $\hat{P}_{\alpha,0}$ . On average,  $\Delta\hat{P}_{\text{crit}} \sim 1$ . The map exhibits three classes of behaviour [Vick and Lai, 2018]:

- (i) When  $|\Delta\hat{P}_\alpha| \lesssim \Delta\hat{P}_{\text{crit}} \sim 1$ , the mode energy undergoes low-amplitude oscillations. A small amount of energy (of order  $\Delta E_\alpha$ ) is transferred back and forth between the mode and the orbit over multiple pericentre passages. An example of this behaviour is shown in the top panel of Fig. 4.2.
- (ii) When  $|\Delta\hat{P}_\alpha| \lesssim \Delta\hat{P}_{\text{crit}}$  and  $\hat{P}_{\alpha,0}/(2\pi)$  is close to an integer (i.e., when  $\sigma_\alpha$  is an integer multiple of the orbital frequency,  $2\pi/P_0$ ), the mode energy exhibits larger-amplitude oscillations with a mean mode energy  $\gg \Delta E_\alpha$  (see the middle panel of Fig. 4.2.)
- (iii) When  $|\Delta\hat{P}_\alpha| \gtrsim \Delta\hat{P}_{\text{crit}}$ , the mode amplitude evolves chaotically and can grow to very large values of order the initial orbital energy  $|E_{B,0}|$ ; meanwhile, the orbit experiences significant decay in the semi-major axis. The bottom panel of Fig. 4.2 provides an example. Note that in this example the binding energy of the planet is of order the initial orbital energy ( $GM_p^2/R_p = 2.6 |E_{B,0}|$  for an initial semi-major axis  $a_0 = 1$  au). For such chaotic systems, the mode energy will eventually grow to values comparable to the binding energy of the planet, at which point the linear treatment is no longer appropriate and the mode will dissipate energy due to non-linear effects. We will discuss the implications of non-linear dissipation in later sections.

These three different behaviours can be characterized by the maximum mode energy that is attained over many pericentre passages. The examples in Fig. 4.2 demonstrate that the mode energy remains a small fraction

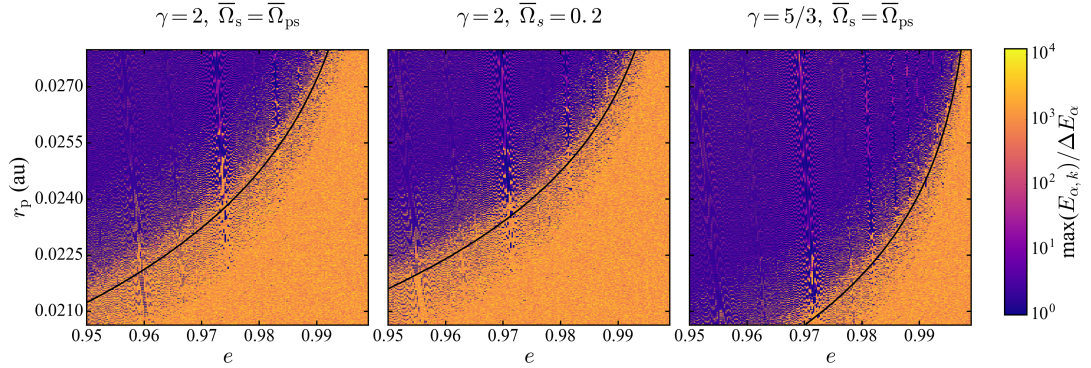


Figure 4.3: The maximum planet f-mode energy,  $\max(E_{\alpha,k})$  (in units of  $\Delta E_\alpha$ ), after  $10^3$  orbits for a system with  $M_* = 1M_\odot$ ,  $M_p = 1M_J$ ,  $R_p = 1.6 R_J$  and a polytropic planet model with either  $\gamma = 2$  or  $\gamma = 5/3$  as labelled. Planets below the minimum  $r_p = 0.0207$  au for the assumed star/planet parameters are expected to tidally disrupt; see equation (4.24). In the left and right panels, the planet is assumed to be rotating pseudo-synchronously (see equation 4.29). In the middle panel, the planet rotates at the rate  $\Omega_s = 0.2(GM_p/R_p^3)^{1/2}$ . Systems in the blue region display low-amplitude oscillations, while those in the orange region exhibit chaotic mode growth. The light purple ridges correspond to resonances between the mode frequency and the orbital frequency. The solid black lines correspond to  $|\Delta \hat{P}_\alpha| = 1$  (equations 4.28 and 4.32).

of the initial orbital energy for non-chaotic evolution. However, when the system behaves chaotically, the maximum mode energy,  $\max(E_{\alpha,k})$ , can be significant compared to  $|E_{B,0}|$ . Physically, the mode must dissipate energy before  $E_{\alpha,k}$  reaches a significant fraction of the planet binding energy.

In Fig. 4.3 we explore the boundary for chaotic behaviour in the  $r_p - e$  plane by recording  $\max(E_{\alpha,k})$  over  $10^3$  orbits for different planet models with  $M_p = 1M_J$  and  $R_p = 1.6 R_J$  (the stellar mass is fixed at  $M_* = 1M_\odot$ ). The left and right panels of Fig. 4.3 assume that  $\Omega_s$  is the pseudo-synchronous rate from equation (4.29) while the middle panel uses a constant value of  $\Omega_s = 0.2(GM_p/R_p^3)^{1/2}$ . Small changes in  $\Omega_s$  do not have a large effect on the chaotic boundary. The right panel of Fig. 4.3 uses a  $\gamma = 5/3$  polytropic planet model rather than our standard choice of  $\gamma = 2$ . A comparison

between the right panel and others suggests that changes in the structure of the planet can significantly shift the boundary for chaotic behaviour.

Figure 4.3 demonstrates that the condition  $|\Delta\hat{P}_\alpha| \gtrsim 1$  generally captures the boundary for chaotic behaviour. This boundary is somewhat fuzzy because the precise value of  $\Delta\hat{P}_{\text{crit}}$  spans a wide range, from  $< 0.1$  to  $> 1$ , depending on the value of  $\hat{P}_{\alpha,0}$  [see Fig. 1 of Vick and Lai, 2018]. In particular,  $\Delta\hat{P}_{\text{crit}} \ll 1$  when  $\hat{P}_{\alpha,0}/(2\pi)$  is close to an integer (resonance). Figure 4.3 confirms that  $\Delta\hat{P}_{\text{crit}} \sim 1$  on average. When  $|\Delta\hat{P}_\alpha| \gtrsim 1$ , the change in the mode phase is nearly a random number mod  $2\pi$ , and each pericentre “kick” to the mode occurs at a random phase. Under this condition, the mode energy grows in a diffusive manner [Mardling, 1995a, Ivanov and Papaloizou, 2004a, Wu, 2018]. Note that this “diffusion” is approximate; as explained in Vick and Lai [2018] (see their Fig. 3), there exists an upper limit to the mode energy even in the absence of dissipation. For this reason, we prefer to call the mode growth and dissipation in the regime  $|\Delta\hat{P}_\alpha| \gtrsim 1$  “chaotic tides.”

From equation (4.28), we see that  $|\Delta\hat{P}_\alpha|$  is larger for more eccentric orbits, and smaller  $\eta$  (i.e. smaller  $r_p$  and larger  $R_p$ ). A young gas giant that is pumped into a highly eccentric orbit can satisfy the condition for chaotic tidal evolution (see Fig. 4.3) and rapidly transfer orbital energy to the f-mode. This behaviour is most likely to occur for  $e \gtrsim 0.95$ . The critical condition for chaotic tides,  $|\Delta\hat{P}_\alpha| \simeq \Delta\hat{P}_{\text{crit}} \sim 1$ , can be written (using equation 4.28) as

$$(1 - e_{\text{crit}}) \simeq 0.11 \bar{\sigma}_\alpha^{2/5} \left( \frac{10^3 M_p}{M_*} \right)^{4/15} \left( \frac{\eta}{3} \right)^{-7/5} (\Delta\hat{P}_{\text{crit}} T)^{2/5}. \quad (4.32)$$

Note that  $T$  depends on  $\eta$  and  $\sigma_\alpha/\Omega_p = \bar{\sigma}_\alpha \eta^{3/2}$ , and is nearly independent of  $e$  for large eccentricities. Equation (4.32) gives the critical eccen-

tricity, for a given  $\sigma_\alpha$ , above which chaotic tides operate as a function of the dimensionless pericentre distance  $\eta$  (equation 4.22).<sup>3</sup> If we make further simplification for the function  $T$  by replacing  $K_{22}$  in equation (4.25) with the approximate fitting formula  $K_{22} \approx 1.79 \times 10^4 z^{-6} \eta^{3/2}$  [Wu, 2018], equation (4.32) can be inverted to yield

$$\eta_{\text{crit}} \simeq 4.25 \bar{\sigma}_\alpha^{-0.59} Q_\alpha^{0.11} \left( \frac{1-e}{0.02} \right)^{-0.135} \left( \frac{10^3 M_p}{M_*} \right)^{0.036} \left( \frac{\sigma_\alpha}{\epsilon_\alpha \Delta \hat{P}_{\text{crit}}} \right)^{0.054}, \quad (4.33)$$

or equivalently,

$$r_{p,\text{crit}} \simeq (0.0206 \text{ au}) \bar{\sigma}_\alpha^{-0.59} Q_\alpha^{0.11} \left( \frac{1-e}{0.02} \right)^{-0.135} \left( \frac{R_p}{R_J} \right) \left( \frac{10^3 M_p}{M_*} \right)^{-0.297} \left( \frac{\sigma_\alpha}{\epsilon_\alpha \Delta \hat{P}_{\text{crit}}} \right)^{0.054}. \quad (4.34)$$

Equation (4.34) gives the critical pericentre distance for chaotic tides to operate as a function of eccentricity.

#### 4.2.4 Conditions for Chaotic Tides When $E_{\alpha,0} > 0$

In Section 4.2.3, we have discussed the condition for the onset of chaotic mode growth for an “eccentric orbit + oscillatory modes” system where there is no initial energy in the mode ( $E_{\alpha,0} = 0$ ). When chaotic dynamical tides are the only influence on the planet’s orbital evolution, and when the total energy of the system is conserved (i.e. the modes do not dissipate),  $\hat{P}_{\alpha,0}$  and  $|\Delta \hat{P}_\alpha|$  completely determine the behaviour of the system. For instance, a system with  $\Delta \hat{P}_\alpha \lesssim \Delta \hat{P}_{\text{crit}} \sim 1$  will never undergo chaotic mode growth, and one with  $\Delta \hat{P}_\alpha \gtrsim \Delta \hat{P}_{\text{crit}}$  will always be chaotic. However, when non-tidal effects alter the planet’s orbit (e.g. LK eccentricity oscillations driven by an external companion), a system can transition in and

---

<sup>3</sup>The mode frequency  $\sigma_\alpha$  depends on the planet rotation rate  $\Omega_s$ , which may depend on  $e$  if the equilibrium rotation rate depends on  $e$ . For pseudo-synchronous rotation, this dependence is very weak when  $(1-e) \ll 1$  (for which  $\Omega_s \simeq 1.17 \Omega_p$ ); see equation (4.29).

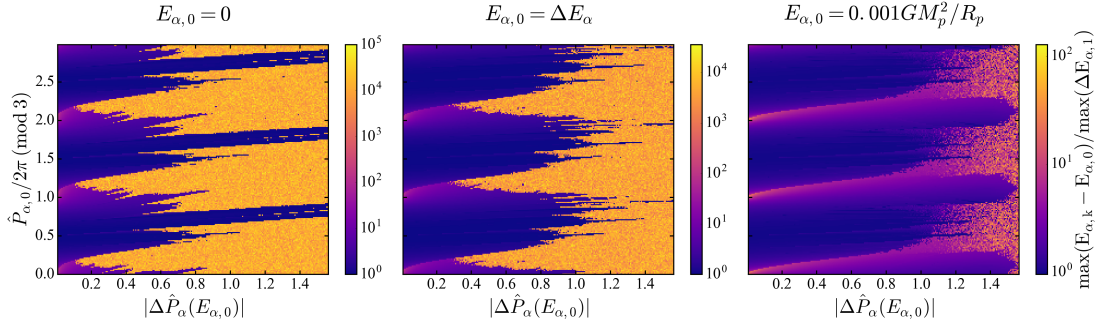


Figure 4.4: The maximum mode energy, shifted by the initial mode energy  $E_{\alpha,0}$  and scaled to  $\max(\Delta E_{\alpha,1})$  (see equation 4.36) for a range of  $\hat{P}_{\alpha,0}$  and  $|\Delta \hat{P}_{\alpha}(E_{\alpha,0})|$ . The dark purple regions exhibit low-amplitude oscillations, the pink regions exhibit resonant behaviour, and the orange regions correspond to chaotic mode growth. Each panel shows calculations for a different choice of  $E_{\alpha,0}$ . The left panel corresponds to no initial energy in the mode. The middle panel corresponds to a mode that is already undergoing low-amplitude oscillations with  $E_{\alpha,0} = \Delta E_{\alpha}$ . The right panel shows a mode with a significant amount of initial energy such that  $E_{\alpha,0} \gg \Delta E_{\alpha}$ . For the plotted range of  $\hat{P}_{\alpha,0}$ ,  $\Delta \tilde{E}_{\alpha} \simeq 2.5 \times 10^{-4}$  in the right panel. In general, the boundary for chaotic behaviour varies with  $\hat{P}_{\alpha,0}$  and shifts to larger  $|\Delta \hat{P}_{\alpha}(E_{\alpha,0})|$  for larger  $E_{\alpha,0}$ .

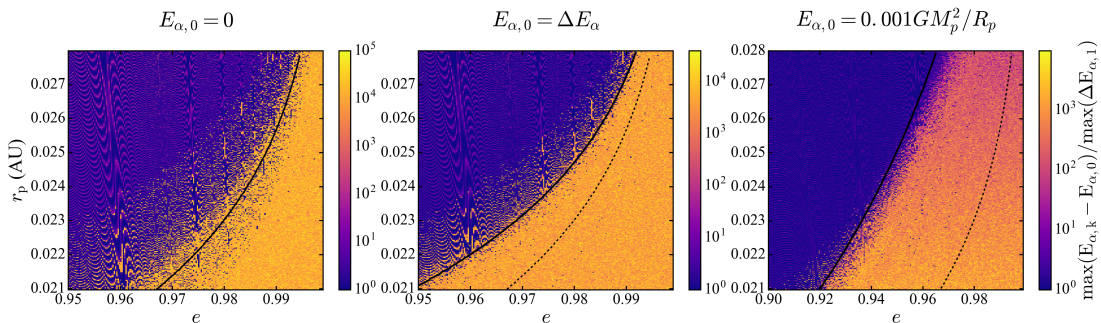


Figure 4.5: Similar to Fig. 4.3, but showing the effect of finite initial mode energy  $E_{\alpha,0}$  (see also Fig. 4.4). Each panel corresponds to a  $\gamma = 2$  polytrope and assumes that the planet spin,  $\Omega_s$ , is pseudo-synchronous (see equation 4.29). In general the boundary for chaotic behaviour shifts to larger  $r_p$  and lower  $e$  for larger  $E_{\alpha,0}$ . The solid black lines show  $|\Delta \hat{P}_{\alpha}(E_{\alpha,0})| = 1$  while the dashed lines show  $|\Delta \hat{P}_{\alpha}| = |\Delta \hat{P}_{\alpha}(E_{\alpha,0} = 0)| = 1$ ; in the left panel, the two lines coincide.

out of the chaotic regime as  $r_p$  is driven below and above  $r_{p,\text{crit}}$  [see equations (4.32)-(4.34) and Fig. 4.3]. Therefore, it is useful to know whether a system is “currently chaotic” when there is “pre-existing” energy in the mode ( $E_{\alpha,0} > 0$ ). Here, we generalize the criterion for the onset of chaotic tides to account for the “pre-existing” mode energy [see Mardling, 1995a, Wu, 2018].

As discussed in Section 4.2.3, the mode amplitude evolves chaotically when the mode phase at pericentre is nearly random from one passage to the next. This occurs when the phase-shift from pericentre energy transfer is of order unity. For a mode with no “pre-existing” energy, the pericentre phase shift is solely due to  $\Delta E_\alpha$ . When the mode already has energy  $E_{\alpha,0}$  prior to the first passage, the pericentre phase shift can reach a maximum value of

$$|\Delta \hat{P}_\alpha(E_{\alpha,0})| \equiv \sigma_\alpha \max(|P_1 - P_0|) \simeq \frac{3}{2} \hat{P}_{\alpha,0} \frac{\max(\Delta E_{\alpha,1})}{|E_{B,0}|}, \quad (4.35)$$

where  $\max(\Delta E_{\alpha,1})$  is the maximum possible energy transfer in the first pericentre passage given the initial mode energy  $E_{\alpha,0}$ , and is given by

$$\max(\Delta E_{\alpha,1}) = \Delta E_\alpha + 2 \sqrt{\Delta E_\alpha E_{\alpha,0}}. \quad (4.36)$$

The general condition for chaotic behaviour is that the maximum pericentre phase shift is sufficiently large that the mode phase is nearly random at pericentre, i.e.

$$|\Delta \hat{P}_\alpha(E_{\alpha,0})| \gtrsim \Delta \hat{P}_{\text{crit}} \sim 1. \quad (4.37)$$

Note that  $|\Delta \hat{P}_\alpha(E_{\alpha,0})|$  can be many times larger than  $|\Delta \hat{P}_\alpha| = |\Delta \hat{P}_\alpha(0)|$  if  $E_{\alpha,0} \gg \Delta E_\alpha$ ; in this case equation (4.37) reduces to equation (18) of Wu [2018].<sup>4</sup>

---

<sup>4</sup>Wu [2018] adopted  $\Delta \hat{P}_{\text{crit}} = 2/3$ . In reality,  $\Delta \hat{P}_{\text{crit}}$  depends strongly on  $\hat{P}_0$ ; see Fig. 4.4.

Figure 4.4 shows how the dynamical behaviour of the system depends on  $\hat{P}_{\alpha,0}$  and  $|\Delta\hat{P}_\alpha(E_{\alpha,0})|$  for  $E_{\alpha,0} = 0, \Delta E_\alpha$ , and  $0.001GM_p^2/R_p$ . The left panel is similar to Fig. 1 from Vick and Lai [2018]. The middle panel corresponds to a system where the planet has an initial energy  $E_{\alpha,0} = \Delta E_\alpha$ . This is likely the case by the time LK oscillations drive the planet’s orbital eccentricity to the regime for chaotic mode growth. In the right panel,  $E_{\alpha,0} \gg \Delta E_\alpha$ , which is relevant for determining whether a system undergoing chaotic mode growth will continue to behave chaotically (see Section 4.3.1). As in Fig. 4.3, the orange regions indicate chaotic tides. While the exact value of  $\Delta\hat{P}_{\text{crit}}$  depends on whether the mode frequency is near a resonance with the orbital frequency, in general a system with  $|\Delta\hat{P}_\alpha(E_{\alpha,0})| \gtrsim 1$  is more likely than not to experience chaotic tides. This criterion works best for  $\tilde{E}_{\alpha,0} \equiv E_{\alpha,0}/|E_{B,0}| \ll 1$ ; for larger  $\tilde{E}_{\alpha,0}$ ,  $\Delta\hat{P}_{\text{crit}}$  gradually moves to larger values, as suggested by the right panel of Fig. 4.4.

We can also test the generalized criterion for chaotic tides over the range of orbital parameters relevant to migrating gas giants. Figure 4.5 shows the similar results as Fig. 4.3, but for multiple values of  $E_{\alpha,0}$ . We see that the condition  $|\Delta\hat{P}_\alpha(E_{\alpha,0})| = 1$  (the solid black line) matches well with the boundary for chaotic tidal behaviour. The critical pericentre distance for chaotic tides (for a given eccentricity  $e$ ),  $r_{\text{p,crit}}$ , increases with  $E_{\alpha,0}$  while  $e_{\text{crit}}$  (for given  $r_{\text{p}}$ ) decreases.

In summary, chaotic tides are easier to achieve when planetary modes are already oscillating. The larger the mode energy, the more relaxed the conditions for chaotic tidal behaviour.

### 4.2.5 Conditions for Continued Chaotic Behaviour

As mentioned in Section 4.2.3, we expect the f-mode of a planet experiencing chaotic tides to dissipate a significant amount of energy when the mode amplitudes become non-linear. As a mode drains energy from the orbit, the orbit becomes more tightly bound and a larger amount of energy transfer is required to significantly alter the mode phase at pericentre. Eventually, a system undergoing chaotic tides can dissipate enough energy that the planetary mode enters a quasi-steady state. For dissipative systems, it is useful to know when the orbit is too tightly bound for the mode to continue chaotic behaviour.

To determine whether the system is chaotic after the  $k$ -th pericentre passage, we ask whether the current maximum pericentre phase shift,  $|\Delta\hat{P}_{\alpha,k}(E_{\alpha,k-1})|$  is sufficiently large ( $\gtrsim 1$ ). A natural way to think of this condition is to rescale  $\Delta\hat{P}_{\alpha}(\tilde{E}_{\alpha,0})$  to the current orbital energy and period,  $E_{B,k}$  and  $P_k$ . Similar to equation (4.35), we have

$$|\Delta\hat{P}_{\alpha,k}(E_{\alpha,k-1})| = \sigma_{\alpha,k-1} \max(|P_k - P_{k-1}|) \simeq \frac{3}{2} \sigma_{\alpha,k-1} P_{k-1} \frac{\max(\Delta E_{\alpha,k})}{|E_{B,k-1}|}, \quad (4.38)$$

where

$$\max(\Delta E_{\alpha,k}) = \Delta E_{\alpha} + 2 \sqrt{\Delta E_{\alpha} E_{\alpha,k-1}}. \quad (4.39)$$

When evaluating equations (4.38) and (4.39), one must use the “current” parameters of the system, e.g. the orbital period  $P_{k-1}$  and mode frequency  $\sigma_{\alpha,k-1}$  just before the  $k$ -th pericentre passage. Note that the mode frequency may change as the system evolves because it depends on the planet’s spin.

Equations (4.38) and (4.39) suggest that a system can escape the influence of chaotic tides in several ways. If a non-tidal effect is dominating the orbital evolution and  $r_p$  increases or  $e$  decreases,  $\Delta E_{\alpha}$  and  $\max(\Delta E_{\alpha,k})$  can

become too small for chaotic tides to continue operating; if the orbital evolution is dominated by chaotic tides,  $r_p$  and therefore  $\Delta E_\alpha$  are nearly constant, but the orbit can become too tightly bound (i.e.  $|E_{B,k-1}|$  is too large and  $P_{k-1}$  is too small), for the system to satisfy  $|\Delta \hat{P}_{\alpha,k}(E_{\alpha,k-1})| \gtrsim 1$ . Chaotic behaviour can also be suppressed if the mode suddenly dissipates a large amount of energy such that  $E_{\alpha,k} \ll E_{\alpha,k-1}$ .

### 4.3 Lidov-Kozai migration with chaotic tides

We now discuss our implementation of chaotic dynamical tides in giant planet migration driven by the Lidov-Kozai (LK) mechanism. In this scenario, an external stellar or planetary companion induces quasi-periodic oscillations in the eccentricity of the giant planet’s orbit; as the eccentricity attains a large value ( $\sim 1$ ), tidal dissipation in the planet at pericentre reduces the orbital energy, leading to circularization and decay of the planet’s orbit. As noted in Section 4.1, previous works on LK migration adopted the (parametrized) weak friction theory of static tides (ST). The grey curves of Fig. 4.6 give an example of this “standard” LK migration scenario.

The theory of LK migration with static tides involves two important timescales. The first is the timescale for quadrupole LK eccentricity oscillations,  $t_{\text{LK}}$ , given by

$$t_{\text{LK}} = \left( \frac{10^6}{2\pi} \text{yr} \right) \left( \frac{M_b}{M_\odot} \right)^{-1} \left( \frac{M_*}{M_\odot} \right)^{1/2} \left( \frac{a_0}{1 \text{ au}} \right)^{-3/2} \left( \frac{a_{\text{b,eff}}}{100 \text{ au}} \right)^3, \quad (4.40)$$

where  $a_0$  is the initial semi-major axis of the planet’s orbit,  $M_b$  is the mass of the (stellar) companion, and

$$a_{\text{b,eff}} \equiv a_{\text{b}}(1 - e_{\text{b}}^2)^{1/2}, \quad (4.41)$$

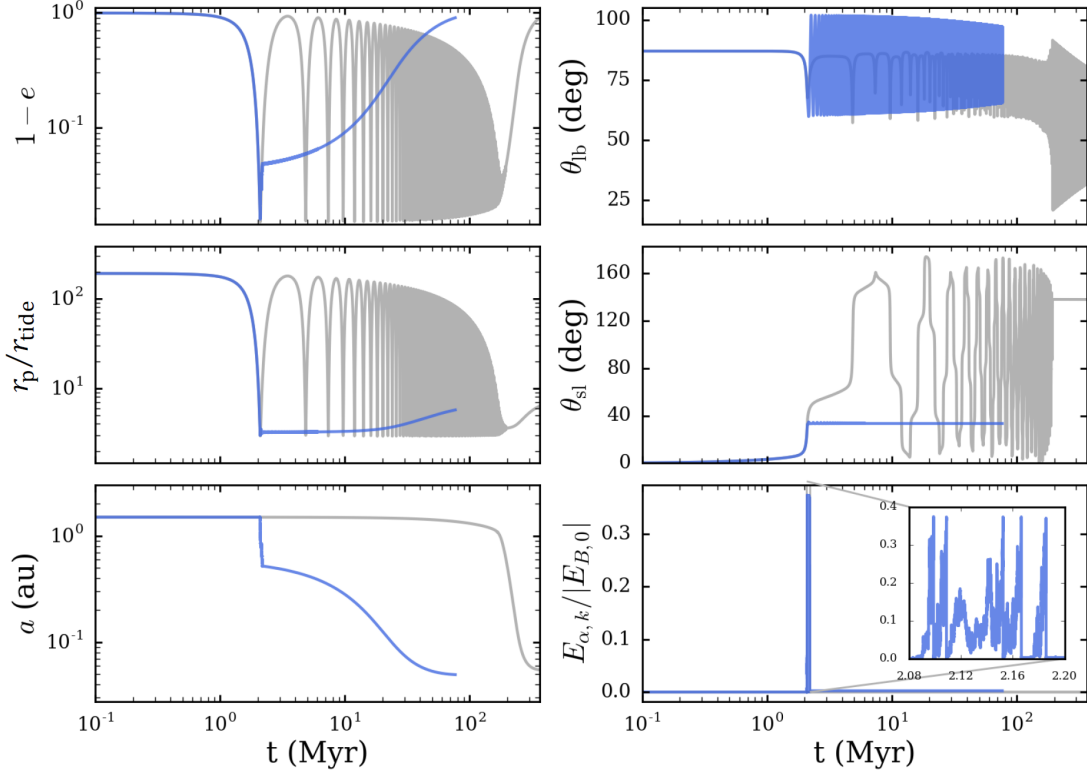


Figure 4.6: An example of LK migration of giant planets driven by binary companions, with and without chaotic tides. The parameters are  $a_b = 200$  au,  $e_b = 0$ ,  $M_p = M_J$ ,  $M_* = M_b = M_\odot$ , and  $R_p = 1.6 R_J$ . The initial semi-major axis and eccentricity for the planet are  $a_0 = 1.5$  au and  $e_0 = 0.01$ , inclination  $\theta_{lb,0} = 87^\circ$ , and the initial rotation period of the star is 2.3 days. The left panels show the orbital eccentricity, pericentre distance (in units of  $r_{\text{tide}} \equiv R_p(M_{\text{tot}}/M_p)^{1/3}$ ), and the semi-major axis. The right panels show  $\theta_{lb}$  (the inclination between the orbits of the planet and the binary companion),  $\theta_{sl}$  (the angle between the stellar spin vector and the planet's orbital angular momentum vector), and the mode energy  $E_{\alpha,k}$ . The grey lines show results without chaotic tides. The blue lines display the results that include chaotic tides for the same system, with an upper limit for the mode energy of  $E_{\text{max}} = 0.1GM_p^2/R_p$  and a residual energy after non-linear dissipation of  $E_{\text{resid}} = 0.01E_{\text{max}}$ . In both models, long-term orbital decay is due to weak tidal friction, with  $\Delta t_L = 1$  s. The inset in the bottom right panel shows a zoom-in of the high-eccentricity phase where chaotic tides operate.

with  $a_b$  and  $e_b$  the semi-major axis and eccentricity of the companion's orbit. The time that the planet spends near the maximum eccentricity,  $e_{\max}$ , is of order [e.g. Anderson et al., 2016]

$$\Delta t(e_{\max}) \sim (1 - e_{\max}^2)^{1/2} t_{\text{LK}}. \quad (4.42)$$

The second important timescale is that of orbital decay due to static tides given by [Alexander, 1973, Hut, 1981].

$$t_{\text{ST}}^{-1} = \left| \frac{\dot{a}}{a} \right|_{\text{ST}} = (6k_{2p}\Delta t_L) \frac{M_*}{M_p} \left( \frac{R_p}{a} \right)^5 \frac{n^2}{(1 - e^2)^{15/2}} \left[ f_1(e) - \frac{f_2^2(e)}{f_5(e)} \right], \quad (4.43)$$

where  $k_{2p}$  is the tidal Love number of the planet,  $\Delta t_L$  is the lag time,  $f_1(e) = 1 + 31e^2/2 + 255e^4/8 + 185e^6/16 + 25e^8/64$ , and  $f_2(e)$  and  $f_5(e)$  are given in equations (4.30) and (4.31). (We have assumed that the planet has a pseudo-synchronous spin rate.) Tidal dissipation is most efficient near the maximum eccentricity. Since the planet only spends a fraction ( $\sim \sqrt{1 - e_{\max}^2}$ ) of the time near  $e_{\max}$ , the effective orbital decay rate during LK migration is

$$\begin{aligned} t_{\text{ST,LK}}^{-1} &= \left( \left| \frac{\dot{a}}{a} \right|_{\text{ST}} \sqrt{1 - e^2} \right)_{e_{\max}} \\ &\approx \frac{1.27}{\text{Gyr}} \left( \frac{k_{2p}}{0.37} \right) \left( \frac{\Delta t_L}{1 \text{ s}} \right) \left( \frac{M_p}{M_\odot} \right)^2 \left( \frac{M_p}{M_J} \right)^{-1} \\ &\quad \times \left( \frac{R_p}{R_J} \right)^5 \left( \frac{a_0}{1 \text{ au}} \right)^{-1} \left( \frac{r_{\text{p,min}}}{0.025 \text{ au}} \right)^{-7} \end{aligned} \quad (4.44)$$

where  $r_{\text{p,min}} = a_0(1 - e_{\max})$  is the minimum pericentre distance (in the second of the above equalities, we have used  $e_{\max} = 0.96$ ). Successful migration within a few Gyrs requires  $r_{\text{p,min}} \lesssim 0.025 \text{ au}$ , corresponding to a final (circularized) planet semi-major axis  $a_F \lesssim 0.05 \text{ au}$ . A planet would need to be more dissipative than Jupiter (larger  $\Delta t_L$ )<sup>5</sup> to become a HJ with a larger  $a_F$ .

---

<sup>5</sup>For Jupiter,  $\Delta t_L \simeq 0.1 \text{ s}$ , corresponding to  $k_{2p}/Q_p \simeq 10^{-5}$  at a tidal forcing period of 0.5 hrs.

As we shall see, chaotic tides can change the standard LK migration scenario in several important aspects (see Fig. 4.6). Although the planet spends only a small fraction of time in the high-eccentricity phase of the LK oscillations, this time covers enough orbits to allow chaotic mode growth. Consider the example depicted in Fig. 4.6: the critical eccentricity (for  $a_0 = 1.5$  au) for chaotic mode growth to operate is  $e_{\text{crit}} \approx 0.985$  (see Fig. 4.3 and equation 4.32). So the time the planet spends around  $e \gtrsim e_{\text{crit}}$  is  $\sim \sqrt{1 - e_{\text{crit}}^2} t_{\text{LK}} \approx 0.17 t_{\text{LK}} \approx 0.23$  Myr, which is more than  $1.2 \times 10^5$  orbital periods. The planet's oscillation mode can grow to a large amplitude within this time frame, stealing orbital energy in the process and allowing the orbit to decay within one or a few LK cycles.

### 4.3.1 Description of the Model

We now describe our method for coupling the evolution of the oscillation mode (the  $l = m = 2$  f-mode) of a gas giant with the evolution of its orbit driven by an external binary companion (LK oscillations). The planet starts out with eccentricity  $e_0 \approx 0$  and zero mode amplitude ( $E_{\alpha,0} = 0$ ). The other planet and stellar properties as well as the initial values of  $e_b$ ,  $a_0$ ,  $a_b$ ,  $\theta_{lb,0}$  (the mutual inclination of the orbits) and  $\Omega_0$  (the longitude of the ascending node of the planet's orbit) are taken as input parameters. Apart from chaotic dynamical tides, we evolve the orbital angular momentum vector  $\mathbf{L}$  and eccentricity vector  $\mathbf{e}$  of the planet, and the spin angular momentum vector,  $\mathbf{S}_*$  of the host star in the same way as in Anderson et al.

[2016] (hereafter ASL16), i.e.

$$\frac{d\mathbf{L}}{dt} = \left. \frac{d\mathbf{L}}{dt} \right|_{LK} + \left. \frac{d\mathbf{L}}{dt} \right|_{SL} + \left. \frac{d\mathbf{L}}{dt} \right|_{ST}, \quad (4.45)$$

$$\frac{d\mathbf{e}}{dt} = \left. \frac{d\mathbf{e}}{dt} \right|_{LK} + \left. \frac{d\mathbf{e}}{dt} \right|_{SL} + \left. \frac{d\mathbf{e}}{dt} \right|_{SRF} + \left. \frac{d\mathbf{e}}{dt} \right|_{ST}, \quad (4.46)$$

$$\frac{d\mathbf{S}_*}{dt} = \left. \frac{d\mathbf{S}_*}{dt} \right|_{SL} + \left. \frac{d\mathbf{S}_*}{dt} \right|_{MB}. \quad (4.47)$$

Here the LK terms are contributions (to the octupole order) from the binary companion that give rise to LK oscillations [equations A1-A2 of ASL16; from Liu et al. [2015]]; the SL terms arise from the spin-orbit coupling between the host star spin,  $\mathbf{S}_*$ , and the planet's orbital angular momentum (equations 60-61 of ASL16); and the short-range force (SRF) terms account for periastron precession of the planet's orbit due to general relativity (GR) and tidal/rotational distortions of the planet (sections A3 and A4 of ASL16). The stellar spin evolution includes the spin-down torque due to magnetic braking (MS), i.e.

$$\left. \frac{d\mathbf{S}_*}{dt} \right|_{MB} = -\alpha_{MB} I_* \Omega_*^3 \hat{\mathbf{S}}_*, \quad (4.48)$$

where  $\alpha_{MB}$  is taken to be  $1.5 \times 10^{-14}$  yr to model a solar type star [Barker and Ogilvie, 2009],  $I_*$  is the moment of inertia of the star, and  $\Omega_*$  is its rotation rate. We assume an initial spin period of 2.3 days. We also evolve the angular momentum and eccentricity vectors of the outer orbit ( $\mathbf{L}_b$  and  $\mathbf{e}_b$ ) according to the octupole LK effect [equations 19 and 20 of Liu et al., 2015]; these changes in the outer orbit are small because  $M_p \ll M_b$ . Throughout evolution, we take the planet's rotation rate to be the pseudo-synchronous rotation rate given by equation (4.29)<sup>6</sup>. Equations (4.45)-(4.46) include contributions from the dissipation of static tides (ST); these are parametrized

---

<sup>6</sup>A full treatment of the planet's spin evolution would require including the retrograde  $m = -2$  mode in our calculations. See Lai [1997] and Ivanov and Papaloizou [2004a] for discussions of how dynamical tides affect the planet spin and ASL16 (Section 3.3) for analysis of the the planet spin evolution during LK oscillations.

by the tidal lag time  $\Delta t_L$ , and are distinct from the effects of chaotic dynamical tides.

In the presence of dynamical tides, we must supplement equations (4.45)-(4.47) with the evolution of the mode amplitude. This is based on the iterative map discussed in Section 4.2.1. Here, we provide a summary of the implementation of this procedure. At a certain time in the orbital evolution, just before the  $k$ -th pericentre passage, the orbital parameters are  $a_{k-1}$  and  $e_{k-1}$ , the planet spin rate is  $\Omega_{s,k-1}$ , and the mode amplitude is  $c_{\alpha,k-1}$ . To advance to the next orbit, we carry out the following steps:

- (i) Calculate  $\Delta E_\alpha$  from equations (4.21), (4.25), and (4.27) using mode parameters from Table 4.1 and the current orbital/planet parameters (i.e.  $a_{k-1}$ ,  $e_{k-1}$ ,  $\Omega_{s,k-1}$ , etc.) and obtain  $\Delta c_\alpha \propto \sqrt{\Delta E_\alpha}$ . In practice, we normalize mode energy by  $|E_{B,0}|$  (the initial orbital energy), and thus  $\Delta \tilde{c}_\alpha = \sqrt{\Delta \tilde{E}_\alpha} = \sqrt{\Delta E_\alpha / |E_{B,0}|}$ .
- (ii) Calculate the energy transfer in the  $k$ -th passage using  $\Delta E_{\alpha,k} = |E_{B,0}|(|\tilde{c}_{\alpha,k-1} + \Delta \tilde{c}_\alpha|^2 - |\tilde{c}_{\alpha,k-1}|)$  (see equation 4.17) and obtain the new orbital energy  $E_{B,k} = E_{B,k-1} - \Delta E_{\alpha,k}$ .
- (iii) Obtain the new orbital semi-major axis and eccentricity (after the  $k$ -th pericentre passage) according to

$$a_k = \frac{E_{B,k-1}}{E_{B,k}} a_{k-1} \quad (4.49)$$

$$e_k = \left[ 1 - \frac{E_{B,k}}{E_{B,k-1}} (1 - e_{k-1}^2) \right]^{1/2}, \quad (4.50)$$

where we have assumed that the orbital angular momentum is conserved during the passage.

- (iv) Evolve the (complex) mode amplitude over one orbit to obtain its value just before the  $(k+1)$ -th passage using  $c_{\alpha,k} = (c_{\alpha,k-1} + \Delta c_\alpha) e^{-i\sigma_{\alpha,k} P_k}$

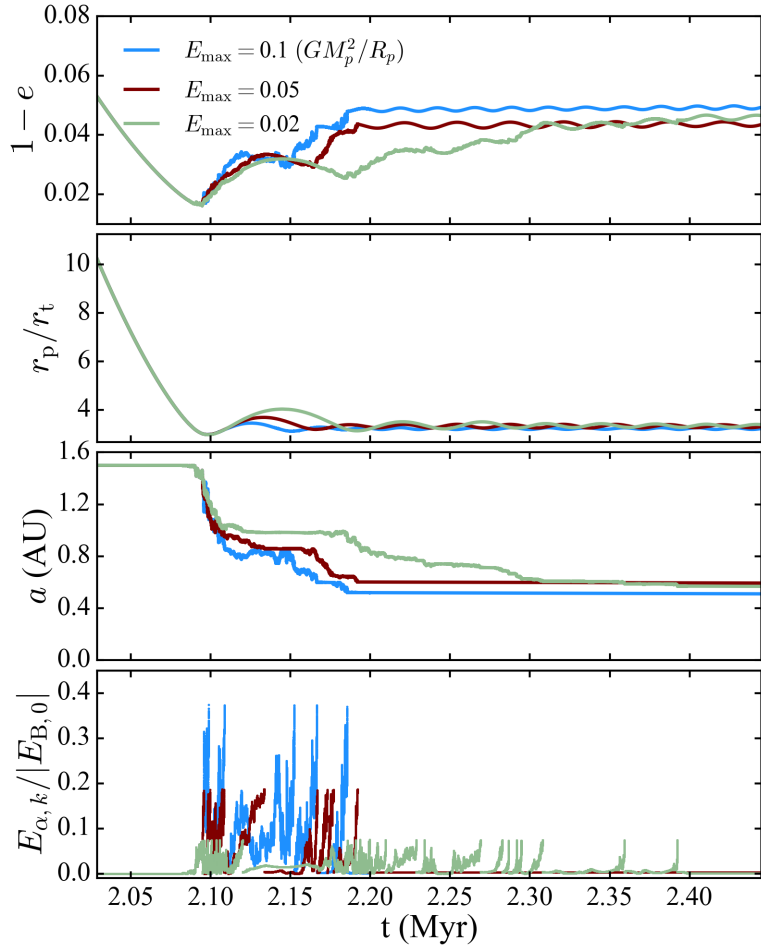


Figure 4.7: A zoom-in of the chaotic tidal evolution of the system depicted in Fig. 4.6 showing the effect of different choices of  $E_{\max}$  (the maximum mode energy at which non-linear dissipation occurs). In all three cases, the residual mode energy after non-linear dissipation is set to  $E_{\text{resid}} = 0.001GM_p^2/R_p$ . In general, the value of  $E_{\max}$  does not have a large effect on orbital parameters of the planet that result from chaotic tidal evolution.

(see equation 4.14), where  $P_k$  is the orbital period corresponding to  $a_k$  and  $\sigma_{a,k}$  is the mode frequency after the  $k$ -th passage (assuming a pseudo-synchronous rotation rate).

Left unchecked, the mode energy in this model can grow to unphysically large values (as in the bottom panel of Fig. 4.2). We therefore assume that, when the mode energy reaches a significant fraction of the planet's

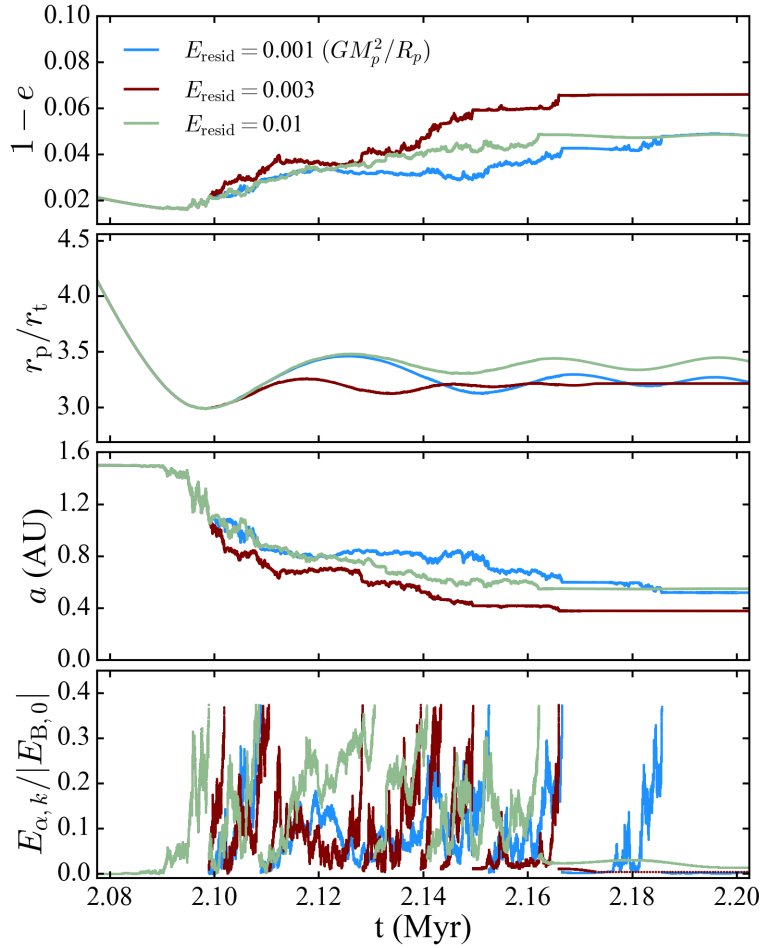


Figure 4.8: The same as Fig. 4.7 but showing the effect of different choices of  $E_{\text{resid}}$ . In all cases,  $E_{\text{max}}$  is set to  $0.1GM_p^2/R_p$ .

binding energy, non-linear effects dissipate nearly all of the mode energy within an orbital period. We parametrize the maximum energy that the mode can reach before non-linear effects become important,  $E_{\text{max}}$ , and the residual energy in the mode after an episode of non-linear mode dissipation and tidal heating,  $E_{\text{resid}}$ . Thus, when  $|\tilde{c}_{\alpha,k}|^2 > E_{\text{max}}/|E_{B,0}|$ , the mode amplitude is immediately changed to  $|\tilde{c}_{\alpha,k}|^2 = E_{\text{resid}}/|E_{B,0}|$ . This method for handling dissipation was used in Wu [2018]. The parameter  $E_{\text{max}}$  does not change the qualitative features of evolution due to chaotic tides (see

Fig. 4.7), but can alter the details. The quantity  $E_{\text{resid}}$  is more important because chaotic behaviour is easier to excite when the f-mode already has some energy, as discussed in Section 4.2.4, but still does not change the overall behaviour of the model (see Fig. 4.8). Unless stated otherwise, we use  $E_{\text{max}} = 0.1(GM_p^2/R_p)$  and  $E_{\text{resid}} = 0.01E_{\text{max}} = 10^{-3}(GM_p^2/R_p)$  in the results presented in this paper.

Since dynamical tides must be implemented on an orbit by orbit basis, it is not practical to evolve the whole system over many Myrs. Because chaotic dynamical tides are effective only during the high-e phase of the LK cycle, when chaotic mode growth occurs, we only need to evolve the modes when the eccentricity is sufficiently high and the pericentre distance is sufficiently small. As discussed in Section 4.2.5, chaotic tides operate when  $|\Delta\hat{P}_{\alpha,k}(E_{\alpha,k-1})| \gtrsim \Delta\hat{P}_{\text{crit}}$  (see equation 4.38). In our implementation, we turn on dynamical tides only when  $|\Delta\hat{P}_{\alpha,k}(E_{\alpha,k-1})| \gtrsim 0.01$ . As we see from Fig. 4.4, this is a conservative choice, allowing us to capture the onset of chaotic behaviour for all reasonable parameters regardless of resonances and the value of “pre-existing” mode energy.

After the orbit has decayed through chaotic tides, the system will eventually satisfy  $|\Delta\hat{P}_{\alpha,k}(E_{\alpha,k-1})| < \Delta\hat{P}_{\text{crit}} \sim 1$  (see the right panel of Fig. 4.4) while the orbital eccentricity is still large. This typically occurs just after the mode energy is dissipated non-linearly from  $E_{\text{max}}$  to  $E_{\text{resid}}$ . Thus, when the system satisfies

$$|\Delta\hat{P}_{\alpha,k}(E_{\alpha,k-1})| \simeq \frac{3\sqrt{\Delta E_\alpha E_{\alpha,k-1}}}{|E_{B,k}|} \sigma_{\alpha,k} P_k \lesssim 1, \quad (4.51)$$

(where we have assumed  $E_{\alpha,k-1} \sim E_{\text{resid}} \gg \Delta E_\alpha$ ) the f-mode will no longer behave chaotically and influence the orbital evolution. Instead, static tides drive the gradual decay and circularization of the planet’s orbit. To save

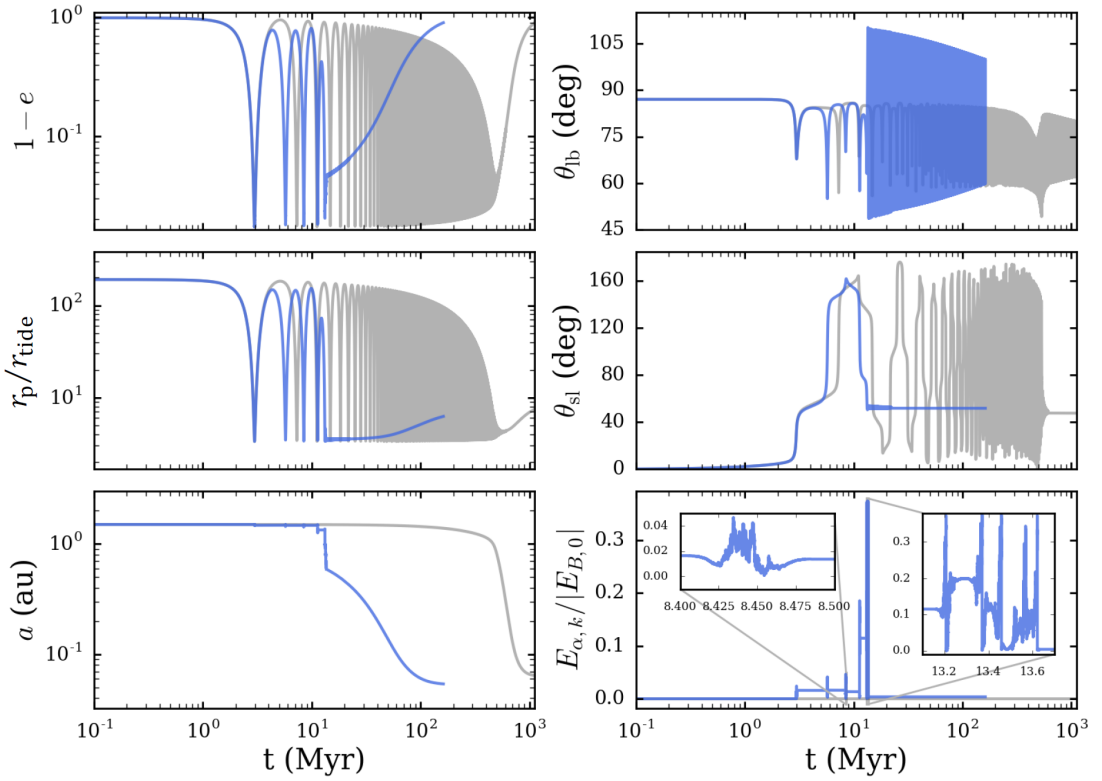


Figure 4.9: Same as Fig. 4.6, except for  $a_b = 225$  au. The insets in the bottom right panel show a closer look at two high-eccentricity phases. In the first inset, the mode energy does not dissipate. In the second inset, the planet undergoes multiple episodes of tidal dissipation.

computation time, when equation (4.51) is satisfied while the orbital eccentricity is large, we take note. If equation (4.51) is still satisfied in 30,000 orbits, we stop evolving the dynamical tides; if equation (4.51) is not satisfied after 30,000 orbits, we check again in another 30,000 orbits. The multiple checks are to account for the fact that  $\Delta\hat{P}_{\text{crit}}$  varies significantly depending on the orbital period and can be less than 1.

### 4.3.2 Examples of the Model

LK migration with chaotic tides proceeds in three steps (see the blue curves in Fig. 4.6). First, the external companion drives the planet's orbital eccentricity beyond  $e_{\text{crit}}$  (see equation 4.32), where chaotic tides set in and begin to take over orbital evolution, freezing  $r_p$  due to angular momentum conservation. The blue lines in Figs. 4.7 and 4.8 show a zoom-in view. We see that  $r_p$  decreases due to the LK effect until settling to an approximately constant value around 2.1 Myr while  $e$  and  $a$  start to wander chaotically. In the second stage, chaotic tides dominate orbital evolution and quickly shrink the orbit until it is too bound for such tides to continue operating. In Figs. 4.7 and 4.8, it is clear that the planet undergoes multiple episodes of non-linear dissipation (where the mode energy rapidly dissipates to a small residual value of  $E_{\text{resid}}$  after climbing to maximum energy  $E_{\text{max}}$ ) while subject to chaotic tides. The result is a very eccentric WJ. At this new semi-major axis, the planet is decoupled from the influence of the stellar companion, and no longer experiences significant eccentricity oscillations. Finally, weak tidal friction circularizes and shrinks the orbit to form a HJ on a Gyr timescale (depending on the dissipation rate of static tides in the planet).

In some cases, a system will undergo multiple high-eccentricity phases before chaotic tides reach the threshold  $E_{\text{max}}$  and the f-mode dissipates energy. An example is shown in the blue lines of Fig. 4.9, where the system has the same parameters and initial conditions as in Fig. 4.6 but with a slightly larger companion semi-major axis ( $a_b = 225$  au). We see that the planet's eccentricity undergoes five LK oscillations before the f-mode energy climbs to  $E_{\text{max}}$ . Before an episode of tidal dissipation, any energy

transferred from the orbit to the mode can easily pass back to the orbit. For example, in the third high-eccentricity phase of Fig. 4.9 (shown in an inset of the bottom right panel) the f-mode loses a small amount of energy and the semi-major axis increases slightly. Once the mode energy reaches  $E_{\max}$  and is dissipated, the orbit shrinks irreversibly and continues to rapidly decay until the orbit is too bound for chaotic tides to operate.

We can gain some insight into when a system requires multiple high-eccentricity phases to reach  $E_{\max}$  by studying the rate of chaotic orbital decay predicted by the iterative map from Section 4.2.1. While  $|\Delta\hat{P}_a| > 1$  (for  $E_{a,0} = 0$ ), the mode amplitude grows in an approximately diffusive manner [Fig. 5 of Vick and Lai [2018]; see also Mardling [1995a], Ivanov and Papaloizou [2004a], Wu [2018]], with the averaged mode energy

$$\langle E_{a,k} \rangle \simeq \Delta E_a k \quad (4.52)$$

For a sufficiently eccentric orbit,  $\Delta E_a$  is roughly constant over many pericentre passages. We can define a timescale for orbital decay from the energy transfer and dissipation,

$$t_{\text{decay}} \equiv \frac{P_0 |E_{B,0}|}{\Delta E_a}. \quad (4.53)$$

If we use the largest value of  $e$  attained by the system in Fig. 4.9, we find that  $t_{\text{decay}} = 0.31$  Myr and the timescale for the system to remain at high eccentricity is  $\Delta t(e = 0.983) = 0.13$  Myr (see equation 4.42). Because  $t_{\text{decay}} < \Delta t(e = 0.983)$ , the system must undergo multiple LK cycles for the mode energy to climb to  $E_{\max}$ . In contrast, the system in Fig. 4.6 reaches  $e = 0.989$ , for which  $t_{\text{decay}} = 3.9 \times 10^{-2}$  Myr and  $\Delta t(e = 0.989) = 0.15$  Myr. For this system, where the timescale for chaotic tides to alter the orbit is very short, the planet's orbit decays within one high-eccentricity phase.

## 4.4 Key Features of Chaotic Tidal Migration: Analytical Understanding

LK migration with chaotic tides has a few characteristic features. First, it can prevent some gas giants from undergoing tidal disruption. Second, it naturally produces very eccentric WJs. Lastly, this population of WJs circularizes relatively quickly, due to weak tidal friction because the planets are “detached” from the companions’ perturbations. In the following, we discuss the necessary conditions for LK chaotic tidal migration, hallmarks of this process, and predictions for the stellar obliquities of HJs formed via this mechanism.

### 4.4.1 Condition for Chaotic Tidal Migration

As discussed in Section 4.2.3, a planet must have  $e \gtrsim e_{\text{crit}}$  to initiate chaotic tides, where  $e_{\text{crit}}$  as a function of  $a_0$  (the initial semi-major axis of the planet) is implicitly given by equation (4.32). To reach such a high eccentricity, a system must have sufficiently large initial mutual inclination,  $\theta_{lb,0}$ . In the idealized case of quadrupole LK oscillations, the maximum eccentricity is  $e_{\max} = [1 - (5/3) \cos^2 \theta_{lb,0}]^{1/2}$ . Accordingly,  $e_{\max} \sim 1$  can be achieved only for  $\theta_{lb,0} \approx 90^\circ$ . Including octupole terms complicates the relationship between the initial mutual inclination and the maximum attainable eccentricity and broadens the inclination window for extreme eccentricity excitation. A realistic treatment of the LK effect must also account for the short-range forces (SRFs) that cause the planet’s pericentre to precess. These limit the maximum attainable eccentricity in LK cycles to a value  $e_{\text{lim}}$ , where  $e_{\text{lim}}$

is the maximum eccentricity achieved when  $\theta_{lb,0} = 90^\circ$  in the quadrupole limit. In the presence of the octupole potential, the eccentricity still cannot exceed  $e_{\text{lim}}$ , but this eccentricity can be realized for a wider range of initial inclinations [Liu et al., 2015]. The relevant SRFs for this problem are GR and the effect of static tides raised on the planet. When  $(1 - e_{\text{lim}}) \ll 1$ , the limiting eccentricity is given by

$$\frac{\epsilon_{\text{GR}}}{(1 - e_{\text{lim}}^2)^{1/2}} + \frac{7}{24} \frac{\epsilon_{\text{Tide}}}{(1 - e_{\text{lim}}^2)^{9/2}} \simeq \frac{9}{8}, \quad (4.54)$$

where  $\epsilon_{\text{GR}}$  and  $\epsilon_{\text{Tide}}$  measure the strengths of precession due to GR and the planet's tidal bulge relative to the quadrupole LK effect, respectively:

$$\epsilon_{\text{GR}} \equiv \frac{3GM_*^2 a_{b,\text{eff}}^3}{a_0^4 c^2 M_b}, \quad (4.55)$$

$$\epsilon_{\text{Tide}} \equiv \frac{15M_*^2 a_{b,\text{eff}}^3 k_{2p} R_p^5}{a_0^8 M_p M_b}. \quad (4.56)$$

For our “standard” system (shown in Fig. 4.6) with  $a_0 = 1.5$  au,  $a_b = 200$  au, and  $e_b = 0$ , we find  $e_{\text{lim}} \approx 0.998$  and  $e_{\text{crit}} \approx 0.985$ , so the planet can reach large enough eccentricities to experience chaotic tides, provided the initial mutual inclination angle,  $\theta_{lb,0}$ , is sufficiently large.

In general, the necessary condition for chaotic tidal migration is

$$e_{\text{lim}} \geq e_{\text{crit}}, \quad (4.57)$$

or equivalently  $r_{p,\text{lim}} \equiv a_0(1 - e_{\text{lim}}) \leq r_{p,\text{crit}}$ , where  $e_{\text{crit}}$  and  $r_{p,\text{crit}}$  are given by equation (4.32) (or more approximately by equation 4.34). Because  $e_{\text{lim}}$ , given by equation (4.54), depends on  $a_{b,\text{eff}}$ , the condition on  $e_{\text{lim}}$  translates to an upper limit on  $a_{b,\text{eff}}$  for chaotic migration to occur:

$$a_{b,\text{eff}} \leq \frac{3^{1/3}}{2^{5/6}} \frac{a_0^{7/6}}{R_p^{1/6}} \left( \frac{M_b M_p}{M_*^2} \right)^{1/3} \left[ \frac{GM_p}{R_p c^2} \left( \frac{R_p}{r_{p,\text{crit}}} \right)^{1/2} + \frac{35}{384} \frac{k_{2p}}{2^{9/2}} \left( \frac{R_p}{r_{p,\text{crit}}} \right)^{9/2} \right]^{-1/3}, \quad (4.58)$$

The upper limit in equation (4.58) is shown as a blue line in Fig. 4.10.

We can also derive the maximum  $r_p$  that allows for standard LK migration with static tides within a stellar lifetime. Using equation (4.44) and requiring that the planet migrate within  $t_{\text{mig}}$  (i.e.  $t_{\text{ST,LK}} \lesssim t_{\text{mig}}$ ), we find

$$r_p \lesssim r_{p,\text{ST}} \equiv (0.021 \text{ au}) \left( \frac{t_{\text{mig}}}{1 \text{ Gyr}} \right)^{1/7} \left( \frac{R_p}{R_J} \right)^{5/7} \left( \frac{M_p}{M_J} \right)^{-1/7} \\ \times \left( \frac{a_0}{1 \text{ au}} \right)^{-1/7} \left( \frac{k_{2p}}{0.37} \right)^{1/7} \left( \frac{M_*}{1 M_\odot} \right)^{2/7} \left( \frac{\Delta t_L}{1 \text{ s}} \right)^{1/7}, \quad (4.59)$$

[ $r_{p,\text{ST}}$  is called  $r_{p,\text{mig}}$  in Muñoz et al. [2016]]. Substituting  $r_{p,\text{ST}}$  for  $r_{p,\text{crit}}$  in equation (4.58) yields an approximate maximum  $a_{\text{b,eff}}$  for standard LK migration (without chaotic tides). The result is shown as the dashed line in Fig. 4.10. For a  $1M_J$ ,  $1.6R_J$  gas giant, the conditions for chaotic tidal migration are typically more generous than for standard LK migration. This suggests that LK migration with chaotic tides yields more HJs than LK migration with static tides.

#### 4.4.2 Evading Tidal Disruption

The planet can be tidally disrupted if its pericentre distance,  $r_p$ , is less than the tidal disruption limit from equation (4.24),

$$r_{p,\text{dis}} = (0.013 \text{ au}) \left( \frac{R_p}{R_J} \right) \left( \frac{M_*}{10^3 M_p} \right)^{1/3}. \quad (4.60)$$

Therefore, when  $r_{p,\text{lim}} < r_{p,\text{dis}}$ , the companion can induce tidal disruption of the planet if  $\theta_{\text{lb},0}$  is sufficiently large. Substituting  $r_{p,\text{dis}}$  for  $r_{p,\text{crit}}$  in equation (4.58) yields the maximum  $a_{\text{b,eff}}$  for tidal disruption to be possible. This is shown as the red line in Fig. 4.10.

In the standard LK migration scenario (with static tides), a large fraction of migrated giant planets are tidally disrupted because  $r_{p,\text{dis}}$  can be quite close

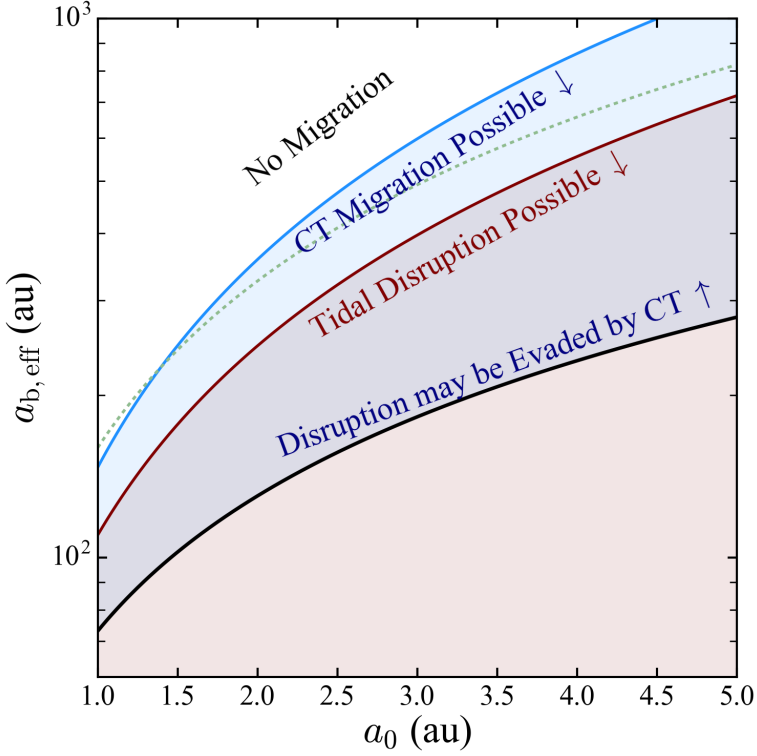


Figure 4.10: The effective outer companion semi-major axis  $a_{b,\text{eff}}$  (equation 4.41) vs. the initial semi-major axis of the planet, for  $M_p = 1M_J$ ,  $R_p = 1.6R_J$  and  $M_* = M_\odot$ . LK migration via chaotic tides (CT) is possible below the blue line, equation (4.58); tidal disruption becomes possible below the red line, equation (4.58) with  $r_{p,\text{dis}}$  in place of  $r_{p,\text{crit}}$ ; tidal disruption may be evaded by chaotic tides above the black line, equation (4.62). The dashed line corresponds to the maximum  $a_{b,\text{eff}}$  for standard LK migration (with static tides) to operate within  $10^9$  yrs, assuming  $\Delta t_L = 1$  s, see equation (4.59).

to  $r_{p,\text{ST}}$ ; moreover, Saturn-mass planets can rarely migrate successfully via LK oscillations and static tides because  $r_{p,\text{dis}} \gtrsim r_{p,\text{ST}}$  [ASL16, Muñoz et al., 2016]. In contrast, with chaotic tides, there is always a region of parameter space where chaotic tidal migration is possible without disruption ( $r_{p,\text{crit}} > r_{p,\text{dis}}$ ; see Fig. 4.3) for any reasonable values of  $M_p$  and  $R_p$  for giant planets.

In some cases, chaotic tides can shepherd to safety the planets that are otherwise destined for tidal disruption by acting to rapidly decrease  $e$  and increase  $r_p$ . This possibility was suggested in Wu [2018]. Figure 4.11

shows one such example. Before the planet is pushed to extreme eccentricity and tidal disruption by the octupole potential, it is frozen into a high-eccentricity orbit with a small semi-major axis and becomes decoupled from the companion. Without further interference from the LK effect, the eccentric WJ circularizes in orbit over a Gyr timescale to eventually become a HJ.

We can understand the condition for chaotic tides to save a planet from disruption using a simple time-scale argument. Tidal disruption occurs when  $r_p \leq r_{p,\text{dis}}$ . At high eccentricity, the timescale for a planet to remain below a given  $r_p$  is  $\Delta t(< r_p) \sim t_{\text{LK}} \sqrt{1 - e^2} \sim \sqrt{2} t_{\text{LK}} (r_p/a_0)^{1/2}$  (see equation 4.42), while the timescale for chaotic tides to decay the orbit is  $t_{\text{decay}}$ , given by equation (4.53). The planet reaches a minimum  $r_p$  when these timescales are roughly equal. For planets that are “just saved” from disruption, this minimum is nearly  $r_{p,\text{dis}}$ . A system that can be saved from disruption must satisfy  $t_{\text{decay}} \lesssim \Delta t(< r_{p,\text{dis}})$ , i.e.

$$\frac{P_0 |E_{B,0}|}{\Delta E_\alpha} \lesssim \sqrt{2} t_{\text{LK}} \left( \frac{r_{p,\text{dis}}}{a_0} \right)^{1/2}, \quad (4.61)$$

where  $\Delta E_\alpha$  is evaluated at  $r_p = r_{p,\text{dis}}$  (see equation 4.21). Recall that  $\Delta E_\alpha$  depends on  $T(\eta, \sigma_\alpha/\Omega_p, e)$ . When  $(1 - e) \ll 1$ ,  $T$  and the pseudo-synchronous spin rate,  $\Omega_{ps}$ , have negligible dependence on  $e$ . We can then evaluate  $T(\eta)$  by using equation (4.25) with the approximate  $K_{22}$  from equation (4.27) and taking  $\bar{\sigma}_\alpha \simeq \bar{\omega}_\alpha + 1.17/\eta^{3/2}$  for the mode frequency in the inertial frame. At  $r_{p,\text{dis}}$ ,  $T(\eta = 2.7) = 2.5 \times 10^{-2}$ .

By rearranging equation (4.61), we can find the minimum  $a_{b,\text{eff}}$  needed for chaotic tidal migration:

$$a_{b,\text{eff}} \gtrsim 27.7 a_0^{5/6} r_{\text{tide}}^{1/6} \left( \frac{M_*}{M_p} \right)^{2/9} \left( \frac{M_b}{M_*} \right)^{1/3}, \quad (4.62)$$

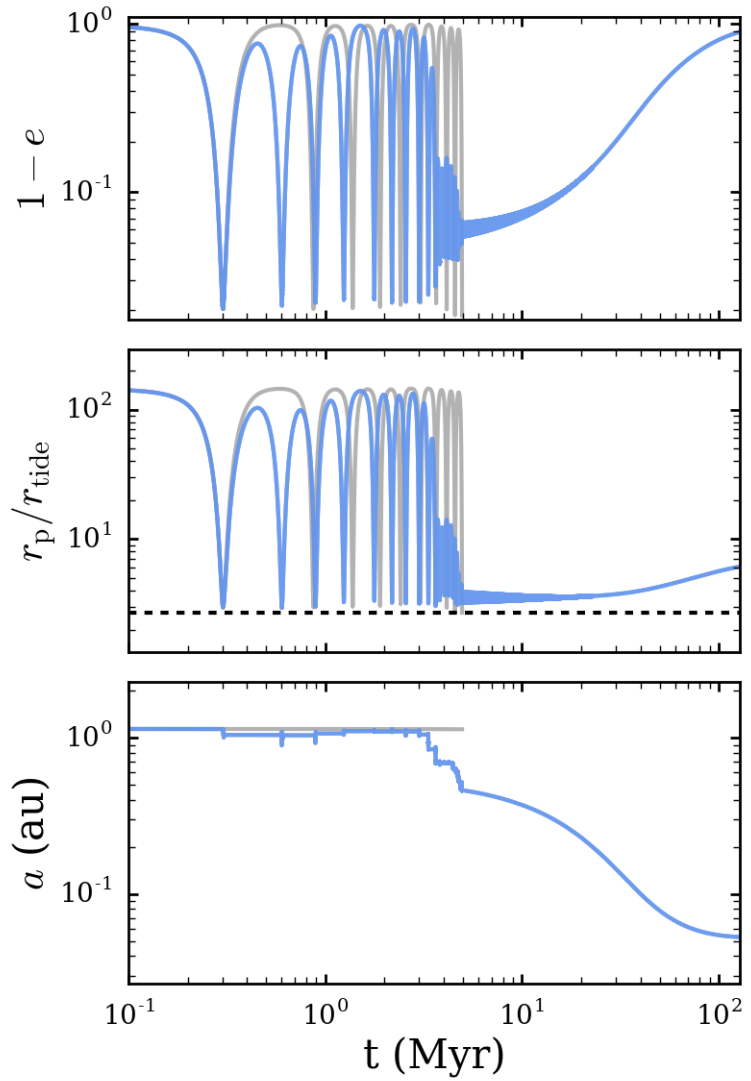


Figure 4.11: Evolution of a system that is spared disruption by chaotic tides. The blue lines include chaotic tides, and the grey lines do not. The initial conditions are  $a_0 = 1.14$  au,  $a_b = 102$  au,  $\theta_{lb,0} = 82^\circ$ ,  $e_b = 0.47$ , and  $\Omega_0 = 179^\circ$  (where  $\Omega_0$  is the longitude of the ascending node of the planet). The physical properties of the planet and stars are  $M_p = M_J$ ,  $M_* = M_b = M_\odot$ , and  $R_p = 1.6 R_J$ . The black dashed line is  $r_{p,\text{dis}}$  from equation (4.60).

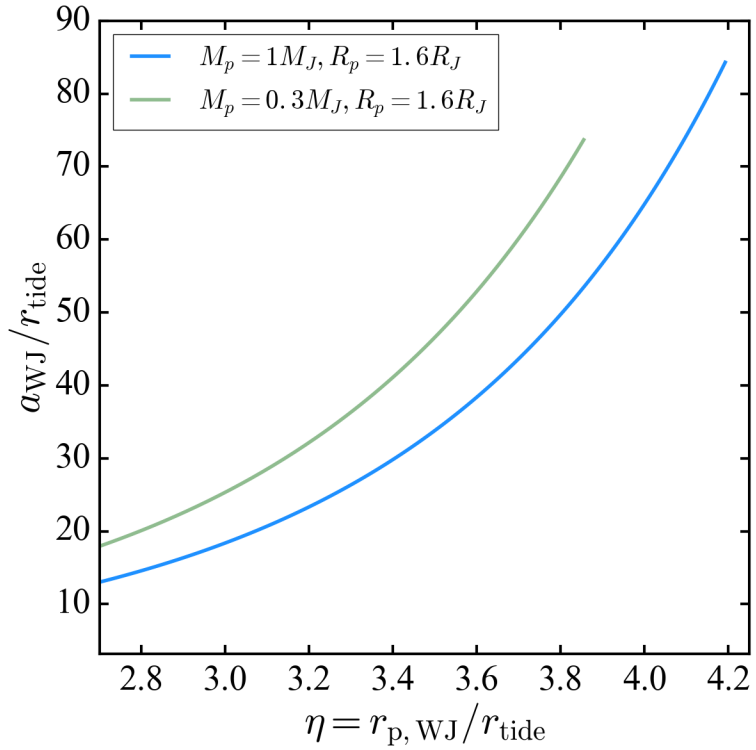


Figure 4.12: The predicted semi-major axis (see equation 4.64) of WJs that have undergone chaotic tidal migration as a function of the pericentre distance  $r_{p,WJ}$  for two different planet models. The minimum value of  $\eta$  is set by the criterion for tidal disruption (equation 4.60). The maximum value of  $\eta$  is set by the chaotic tides boundary [equation (4.33) with  $a_0 = 5$  au].

with  $r_{p,dis} = 2.7r_{tide}$ . The limit on  $a_{b,eff}$  is shown as a black line in Fig. 4.10.

#### 4.4.3 Eccentric Warm Jupiter Formation

A giant planet that undergoes chaotic orbital decay becomes an eccentric WJ after reaching a semi-major axis where both chaotic tides and the LK effect have little influence on the continued evolution of the planet's orbit. For example, in Figs. 4.6 - 4.8, all of the integrations produce a planet with a semi-major axis between 0.35 and 0.65 au and an eccentricity between 0.93 and 0.97. We can understand why this occurs by re-examining the

criterion for chaotic tides to stop affecting orbital evolution (see equation 4.51). Typically, chaotic tides end just after a dissipation episode, where  $E_{\alpha,k-1} \sim E_{\text{resid}}$ . Setting  $|\Delta\hat{P}_{\alpha,k}(E_{\text{resid}})| \sim 1$  with  $P_k \propto a_k^{3/2}$  and  $|E_{B,k}| \propto a_k^{-1}$ , we find

$$a_{\text{WJ}} \simeq a_0 \left[ (3\sigma_\alpha P_0)^2 \frac{\Delta E_\alpha E_{\text{resid}}}{|E_{B,0}|^2} \right]^{-1/5}, \quad (4.63)$$

where  $\Delta E_\alpha$  and  $\sigma_\alpha$  are evaluated at  $r_p = r_{p,\text{WJ}}$ , the pericentre distance of the planet when chaotic tides stop operating. The value of  $r_{p,\text{WJ}}$  varies erratically for small changes of initial conditions, but must fall between  $r_{p,\text{dis}}$  ( $\eta = 2.7$ ) and  $r_{p,\text{crit}}$  (very roughly  $\eta \sim 4$ ) for a system with  $a_0 < 5$  au. Equation (4.63) gives the relationship between  $a$  and  $r_p$  for WJs formed by chaotic tides. Parametrizing the residual mode energy by  $E_{\text{resid}} \equiv fGM_p^2/R_p$ , and using equation (4.21), we can write  $a_{\text{WJ}}$  in terms of the planet properties and  $\eta$ :

$$a_{\text{WJ}} \simeq r_{\text{tide}} \left( \frac{M_*}{M_p} \right)^{4/15} \left[ (6\pi\bar{\sigma}_\alpha)^2 f \frac{4T(\eta)}{\eta^6} \right]^{-1/5}. \quad (4.64)$$

Equation (4.64) is plotted in Fig. 4.12 for two different planet models. For values of  $\eta$  between 2.7 and 3.6, equation (4.64) yields semi-major axes in the range of 0.3 – 1.0 au (for  $R_p = 1.6R_J$  and  $M_*/M_p = 1000$ ). We can also find the eccentricity of the WJs via

$$\begin{aligned} (1 - e_{\text{WJ}}) &= \frac{\eta R_p}{a_{\text{WJ}}} \left( \frac{M_*}{M_p} \right)^{1/3} \\ &\simeq \left( \frac{M_p}{M_*} \right)^{4/15} \left[ (6\pi\bar{\sigma}_\alpha)^2 f \frac{4T(\eta)}{\eta} \right]^{1/5}. \end{aligned} \quad (4.65)$$

For  $\eta$  between 2.7 and 3.6,  $(1 - e_{\text{WJ}})$  is between 0.027 and 0.060 (again for  $R_p = 1.6R_J$  and  $M_*/M_p = 1000$ ).

Figures 4.6, 4.9, and 4.11 show that after the WJ forms through chaotic tides, the eccentricity freezes at a high value and the planet's orbit decouples from the companion. In general, LK eccentricity oscillations freeze

when  $\dot{\omega}_{\text{SRF}} t_{\text{LK}} \sqrt{1 - e^2} \gtrsim 1$ , where  $\dot{\omega}_{\text{SRF}}$  is the rate of precession due to SRFs. This is equivalent to  $\epsilon_{\text{GR}} / \sqrt{1 - e^2} \gtrsim 1$  or  $\epsilon_{\text{Tide}} / (1 - e^2)^{9/2} \gg 1$ . We find that tidal effects play a more important role than GR in the “freezing” of eccentricity oscillations of WJs.

#### 4.4.4 Fast Long-Term Orbital Decay and Hot Jupiter Formation

When the planet’s orbit is no longer strongly influenced by chaotic f-mode evolution and the LK effect, the orbit decays and eventually circularizes due to tidal friction from static tides raised on the planet. With enough time, the final result is a HJ. This is the same mechanism that has been used to explain HJ formation in previous studies of migration via the LK effect [ASL16; Petrovich, 2015a]. Here, the process occurs more quickly because the orbit is frozen into a small pericentre value rather than oscillating between high and low eccentricities. Figures 4.6 and 4.9 compare the long-term orbital evolution predicted by our model (in blue) with the standard calculation that does not include chaotic tides (in grey). In both cases, the orbit circularizes much more quickly when chaotic tides are included.

#### 4.4.5 Spin-Orbit Misalignment and Final Planet-Binary Inclination

Recent studies [ASL16 Storch and Lai, 2014, Storch et al., 2017] have shown that a giant planet undergoing LK migration can induce complex dynam-

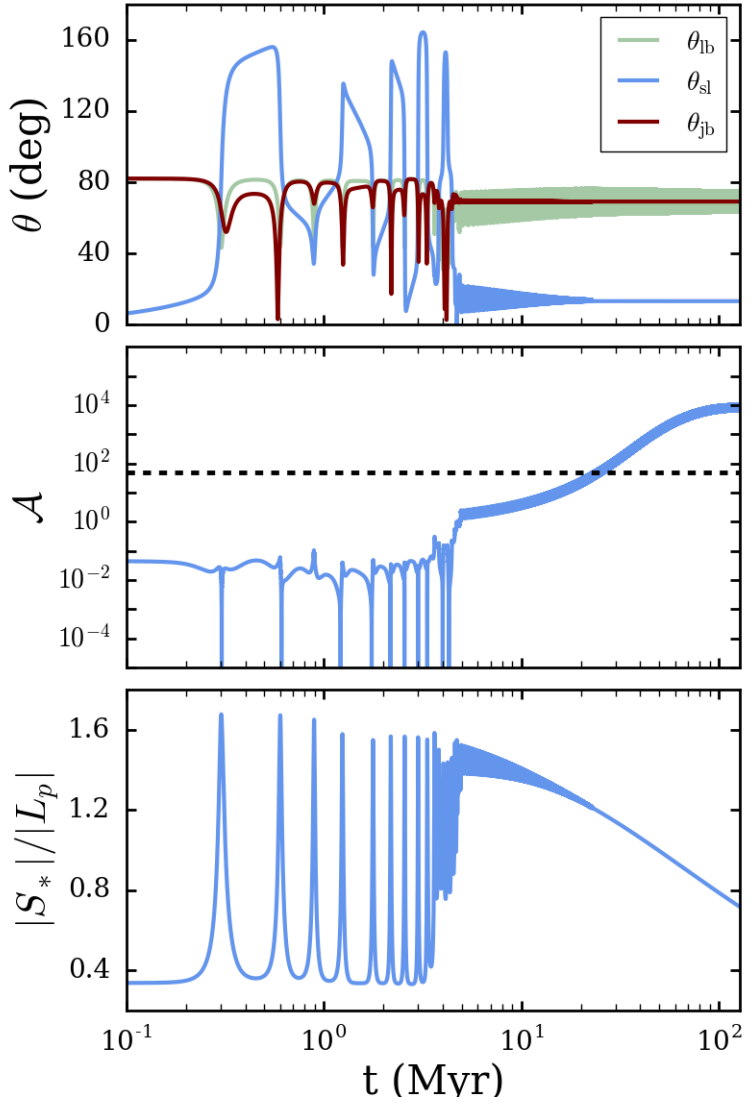


Figure 4.13: The same system as in Fig. 4.11 (with chaotic tides), but showing the evolution of various misalignment/inclination angles, the adiabaticity parameter  $\mathcal{A}$  (equation 4.66), and the ratio of the spin angular momentum of the star to the planet's orbital angular momentum. The stellar obliquity,  $\theta_{\text{sl}}$ , freezes when  $\mathcal{A} \gg 1$  (the dotted line in the second panel denotes  $\mathcal{A} = 50$ , the criterion used in our population synthesis).

ics in the spin axis of the oblate host star before the spin-orbit misalignment angle (stellar obliquity),  $\theta_{\text{sl}}$ , becomes frozen. This freezing occurs when the precession rate,  $\Omega_{p*}$ , of the stellar spin vector ( $S_*$ ) around  $\hat{\mathbf{L}}$  (the unit orbital angular momentum vector of the planet) becomes much faster than the precession rate ( $\Omega_L$ ) of  $\hat{\mathbf{L}}$  around the binary angular momentum axis  $\hat{\mathbf{L}}_b$ . The ratio of precession rates is

$$\mathcal{A} \equiv \left| \frac{\Omega_{p*}}{\Omega_L} \right|, \quad (4.66)$$

where

$$\Omega_L \equiv \left| \frac{d\hat{\mathbf{L}}}{dt} \right|_{\text{LK,quad}} \simeq \frac{3(1+4e^2)}{8t_{\text{LK}} \sqrt{1-e^2}} |\sin 2\theta_{\text{lb}}|, \quad (4.67)$$

and

$$\Omega_{p*} = -\frac{3}{2} \frac{k_{q*}}{k_*} \frac{M_p}{M_*} \left( \frac{R_*}{a} \right)^3 \frac{\Omega_*}{(1-e^2)^{3/2}} \cos \theta_{\text{sl}}, \quad (4.68)$$

with  $k_*$  as the stellar moment of inertia constant,  $k_{q*}$  as the stellar rotational distortion coefficient, and  $\Omega_*$  as the stellar spin rate (see ASL16). We take  $k_* = 0.1$  and  $k_{q*} = 0.05$ . We call  $\mathcal{A}$  the adiabaticity parameter. The spin-orbit angle freezes when  $\mathcal{A} \gg 1$ .

Figure 4.13 shows an example of the evolution of the spin-orbit misalignment angle  $\theta_{\text{sl}}$  during chaotic tidal migration. The stellar spin rate evolves according to the Skumanich law given in equation (4.48). When chaotic tides stop operating, around 4.5 Myr,  $\mathcal{A} \sim 1$ , and  $\theta_{\text{sl}}$  still oscillates with an amplitude of  $\sim 16^\circ$ . Because  $\mathcal{A}$  depends on the stellar spin rate and  $\theta_{\text{lb}}$ , the condition for the adiabatic “spin-orbit freeze” ( $\mathcal{A} \gg 1$ ) is generally different from the condition for “LK oscillations freeze” [ $\epsilon_{\text{Tide}}/(1-e^2)^{9/2} \gg 1$ ; see section 4.4.3]. Many of the planets that migrate via LK chaotic tides will not have a fixed  $\theta_{\text{sl}}$  when they become eccentric WJs.

The mutual inclination  $\theta_{\text{lb}}$  between the orbits of the planet and the stellar

companion is also of interest. We see from Fig. 4.13 that  $\theta_{lb}$  can oscillate even at the end of the evolution (when the planet has become a HJ). This variation of  $\theta_{lb}$  arises from the coupling between  $\mathbf{L}$  and  $\mathbf{S}_*$  (with  $|\mathbf{S}_*|$  non-negligible compared to  $|\mathbf{L}|$ ). We define

$$\mathbf{J} \equiv \mathbf{L} + \mathbf{S}_*. \quad (4.69)$$

We find that the angle between  $\mathbf{J}$  and  $\mathbf{L}_b$ ,  $\theta_{jb}$ , is constant when the planet's orbit is decoupled from the influence of the stellar companion. To understand this, consider the time evolution of the planet's orbital angular momentum axis  $\hat{\mathbf{L}}$  and the stellar spin axis  $\hat{\mathbf{S}}_*$ . Both are rapidly precessing around  $\mathbf{J}$ . An external torque acting on  $\mathbf{S}_*$  (from magnetic braking) or  $\mathbf{L}$  (from the binary companion) also acts on  $\mathbf{J}$ . But after averaging over the fast timescale  $2\pi/|\Omega_{p*}|$ , the net effect is that  $\mathbf{J}$  precesses around  $\mathbf{L}_B$ . As a result,  $\theta_{jb}$  is constant and  $\theta_{lb}$  oscillates around  $\theta_{jb}$  with amplitude  $\theta_{jl}$ , where

$$\tan \theta_{jl} = \frac{|\mathbf{S}_*|}{|\mathbf{L}|} \frac{\sin \theta_{sl}}{(1 + |\mathbf{S}_*|/|\mathbf{L}| \cos \theta_{sl})}. \quad (4.70)$$

The top panel of Fig. 4.13 illustrates this behaviour. As the star gradually spins down due to magnetic braking,  $\theta_{lb}$  asymptotes to  $\theta_{jb}$ .

## 4.5 Population Synthesis

In this section we carry out a population synthesis study of giant planets undergoing LK migration with chaotic tides. Our goal is to determine the production efficiencies of eccentric WJs and HJs, as well as their general properties as predicted by this scenario.

Table 4.2: Outcomes of LK migration with chaotic tides for three planet models. The fraction of systems that undergo chaotic evolution is denoted by  $\mathcal{F}_{\text{mig}}$ ; these planets are either tidally disrupted ( $\mathcal{F}_{\text{dis}}$ ) or exit chaotic tides as eccentric WJs ( $\mathcal{F}_{\text{WJ}} = \mathcal{F}_{\text{mig}} - \mathcal{F}_{\text{dis}}$ ). The fraction of planets that circularize to  $e = 0.1$  with 1 Gyr is  $\mathcal{F}_{\text{HJ}}$ . We compare our results with semi-analytical predictions using the method described in Section 4.6.

	$1 R_J, 1M_J$		$1.6 R_J, 1M_J$		$1.6 R_J, 0.3M_J$	
	Rate	Prediction	Rate	Prediction	Rate	Prediction
$\mathcal{F}_{\text{mig}}$	14.0 %	13.7 %	15.4 %	14.2 %	16.7 %	15.2%
$\mathcal{F}_{\text{dis}}$	10.1%	$\leq 11.9\%$	11.5 %	$\leq 11.9\%$	13.2 %	$\leq 13.1\%$
$\mathcal{F}_{\text{WJ}}$	3.9%	$\geq 1.8\%$	3.9%	$\geq 2.3\%$	3.6 %	$\geq 2.1\%$
$\mathcal{F}_{\text{HJ}}$	3.9%	—	3.8%	—	2.2 %	—

### 4.5.1 Set-up and Method

All of our population synthesis calculations use the same stellar and companion masses  $M_* = M_b = M_\odot$ . The initial rotational period of the host star is 2.3 days, and the star spins down according to the Skumanich law (equation 4.48). The planet model is a  $\gamma = 2$  polytrope. We consider two planet radii,  $R_p = R_J$  and  $R_p = 1.6R_J$ , and two planet masses  $M_p = 1M_J$  and  $M_p = 0.3M_J$ .

While some of our earlier examples have assumed that  $e_b = 0$  (so that the octupole terms vanish), in the population synthesis we consider a broad range of  $e_b$  and incorporate the octupole LK effect. The importance of the octupole effect (relative to the quadrupole effect) is encoded in the dimensionless parameter

$$\epsilon_{\text{oct}} = \frac{a}{a_b} \frac{e_b}{1 - e_b^2}. \quad (4.71)$$

We have explored a variety of initial conditions, uniformly spanning  $a_0 = [1, 5]$  au,  $a_b = [10^2, 10^3]$  (au) (uniformly sampled in  $\log a_b$ ),  $\cos(\theta_{lb,0}) = (-0.77, 0.77)$ ,  $e_b = [0, 0.8]$  and  $\Omega_0 = [0, 2\pi]$  (where  $\Omega_0$  is the initial longitude

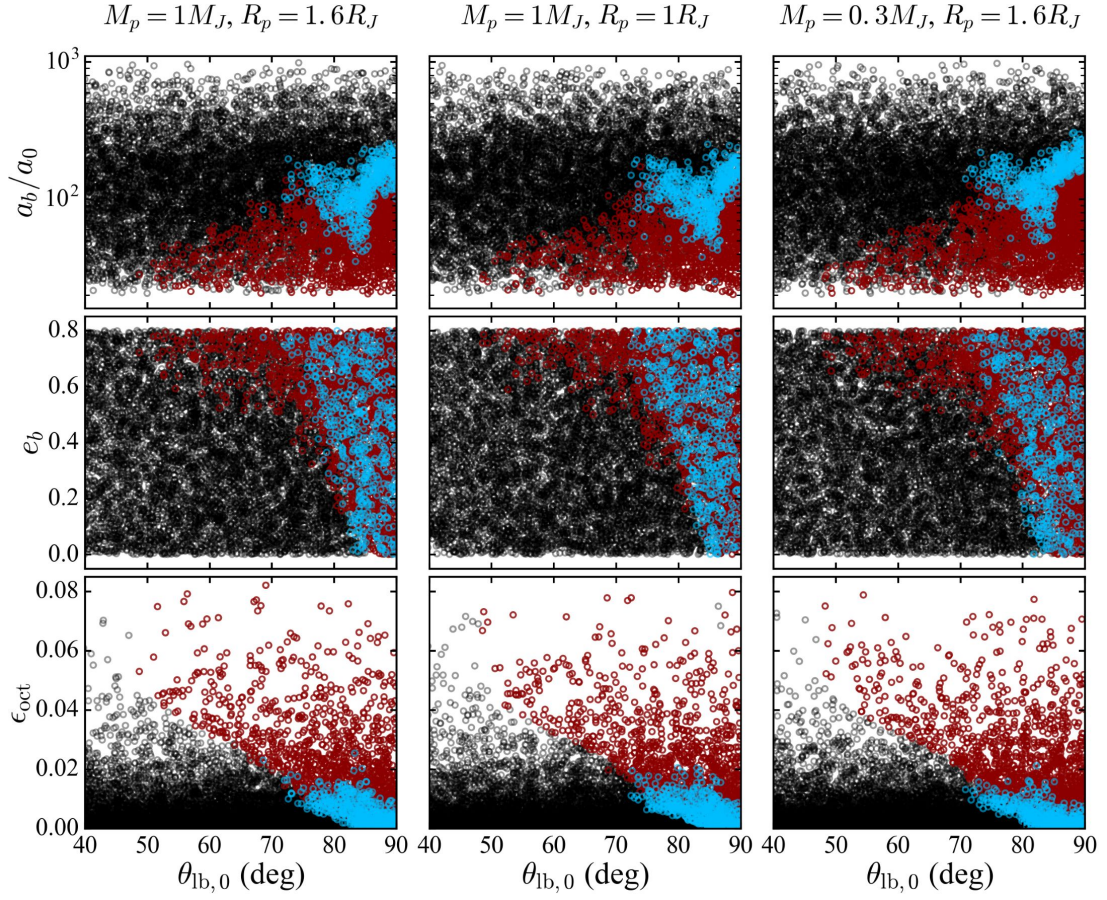


Figure 4.14: The parameter space that results in WJs formed by chaotic tidal migration (blue) and tidal disruption (red). Each point represents a calculation with different initial binary inclination  $\theta_{lb,0}$ , semi-major axes ( $a_b$  in units of  $a_0$ ), eccentricity  $e_b$  and octupole parameter  $\epsilon_{\text{oct}}$ . Systems with  $\theta_{lb,0} > 90^\circ$  are plotted as  $180 - \theta_{lb,0}$ . For most systems, the planetary f-mode never becomes chaotic (black points). WJs are produced for a narrow range of  $a_b/a_0$  and for  $\epsilon_{\text{oct}} \lesssim 0.02$ . The three columns show different combinations of planet mass and radius (as labelled).

of the ascending node of the planet's orbit). Our choice of initial mutual inclinations,  $\theta_{lb,0}$ , is limited to the range where the quadrupole LK effect can operate, i.e.  $\cos^2 \theta_{lb,0} < 3/5$ . Systems that do not obey the stability criterion [Mardling and Aarseth, 2001],

$$\frac{a_b}{a} > 2.8 \left(1 + \frac{M_b}{M_{\text{tot}}}\right)^{2/5} \frac{(1 + e_b)^{2/5}}{(1 - e_b)^{6/5}} \left[1 - 0.3 \frac{\theta_{lb,0}}{180^\circ}\right], \quad (4.72)$$

are discarded. Note that the range of initial conditions is identical to that of

ASL16 for straightforward comparison between the HJ formation fraction from LK migration with and without chaotic tides.

The details of how the evolution of the planetary f-mode is calculated in combination with the LK effect are discussed in Section 4.3.1. In all calculations, we use  $E_{\max} = 0.1GM_p^2/R_p$  and  $E_{\text{resid}} = 0.001GM_p^2/R_p$  to parametrize the maximum f-mode energy and the residual energy after an episode of non-linear tidal dissipation. The planet is assumed to be rotating at the pseudo-synchronous rate (equation 4.29). The effect of chaotic dynamical tides on the planet’s spin is not accounted for in this investigation, but could be incorporated into future studies that follow the evolution of multiple oscillatory modes in the planet.

Our study is structured to efficiently determine the likelihood of three possible outcomes: “No Chaotic Tidal Migration”, “Tidal Disruption”, and ‘Chaotic Tidal Migration’. Each calculation is stopped when the integration time reaches 1 Gyr or when one of the following conditions is met:

- (i) If  $|\Delta\hat{P}_{\alpha,k}(E_{\alpha,k-1})|$  (equation 4.38) has not reached 1 after  $\min(500t_{\text{LK}}, 5t_{\text{LK}}/\epsilon_{\text{oct}})$ , the calculation is terminated and the system is labelled as “No Chaotic Tidal Migration”. Note that a small percentage of such systems may migrate within 1 Gyr via standard LK migration without the assistance of chaotic tides. These are not identified as a separate outcome from planets that will not migrate at all.
- (ii) If the system has evolved for more than  $10^7$  planetary orbits in the chaotic phase (i.e. where the orbital evolution is coupled with the f-mode evolution, as discussed in Section 4.3.1) without reaching  $E_{\alpha,k} = E_{\max}$ , the integration is stopped and the system is classified as “No Chaotic Tidal Migration”.

- (iii) If, at any time, the pericentre distance is within the tidal disruption radius, i.e.  $r_p < r_{p,\text{dis}}$ , the outcome is classified as “Tidal Disruption”, and the integration is stopped.
- (iv) If the planet has experienced chaotic orbital evolution and its orbit has circularized to  $e = 0.1$  within 1 Gyr, the integration is stopped and the system is classified as having undergone “Chaotic Tidal Migration”.

For each system, we begin by integrating the full equations of motion and incorporating the evolution of the planet f-mode (as described in Section 4.3.1). However, at different points in the giant planet’s evolution, it is possible to “turn off” various effects without losing accuracy. As discussed in Section 4.3.1, the effect of chaotic dynamical tides is only accounted for when it can significantly affect orbital evolution. Additionally, when the semi-major axis is small, LK oscillations are suppressed. As the planet’s orbit shrinks and circularizes on a long time-scale due to static tides [see equation (4.43) with  $\Delta t_L = 1$  s], the eccentricity of the planet’s orbit precesses on a much shorter time-scale than that of tidal decay. Following this precession is computationally expensive and does not affect the final properties of the migrating planet. When the LK oscillations are “frozen” [ $\epsilon_{\text{Tide}}/(1 - e^2)^{9/2} > 30$ ] and the spin-orbit angle is safely adiabatic ( $\mathcal{A} > 50$ ), we continue the integration without LK and SRF terms.

### 4.5.2 Migration and WJ/HJ Formation Fractions

The results of our population synthesis are summarized in Table 4.2. For each combination of planetary mass and radius, we ran  $10^4$  calculations to determine the fraction of systems that undergo chaotic tidal migration

( $\mathcal{F}_{\text{mig}}$ ). These migrated planets are either tidally disrupted (fraction  $\mathcal{F}_{\text{dis}}$ ) or survive as eccentric WJs (fraction  $\mathcal{F}_{\text{WJ}} = \mathcal{F}_{\text{mig}} - \mathcal{F}_{\text{dis}}$ ) that undergo further orbital decay and circularization due to static tides, eventually becoming HJs. The fraction of systems that evolve into HJs within 1 Gyr is denoted by  $\mathcal{F}_{\text{HJ}}$ . Note that our population synthesis did not sample initial mutual inclinations with  $|\cos(\theta_{\text{lb},0})| > 0.77$ , as such planets do not experience large excursions in eccentricity. The migration, disruption, WJ, and HJ fractions are calculated assuming a uniform distribution in  $\cos(\theta_{\text{lb},0})$ , e.g.  $\mathcal{F}_{\text{mig}} = 0.77N_{\text{mig}}/N_{\text{run}}$  with  $N_{\text{mig}}$  the number of systems that displayed chaotic tidal migration and  $N_{\text{run}}$  the total number of runs. For  $1M_J$ ,  $1R_p$  planets, the HJ formation percentage from our population synthesis is larger than the value obtained for standard LK migration by a factor of  $\sim 1.6$  (3.9 % vs 2.4 %); see [ASL16; Muñoz et al., 2016].

### 4.5.3 Parameter Space for WJ Formation

We can learn about the parameter space that leads to eccentric WJ formation by examining how the outcome of orbital evolution depends on the initial conditions and the planet properties (see Fig. 4.14; see also Fig. 18 from ASL16 for comparison with the standard LK migration results). It is clear that smaller values of  $\theta_{\text{lb},0}$  do not yield migration. This is unsurprising as the eccentricities required for chaotic tides are very large, which necessitates large initial mutual inclinations. Another pronounced feature is that the systems that produce eccentric WJs are clustered in  $a_b/a_0$ . The reason for this is discussed in Section 4.4 (see Fig. 4.10). In essence, only a narrow window in  $a_b/a_0$  can produce systems that will reach large enough eccentricities to undergo chaotic tides (see equation 4.58), but not

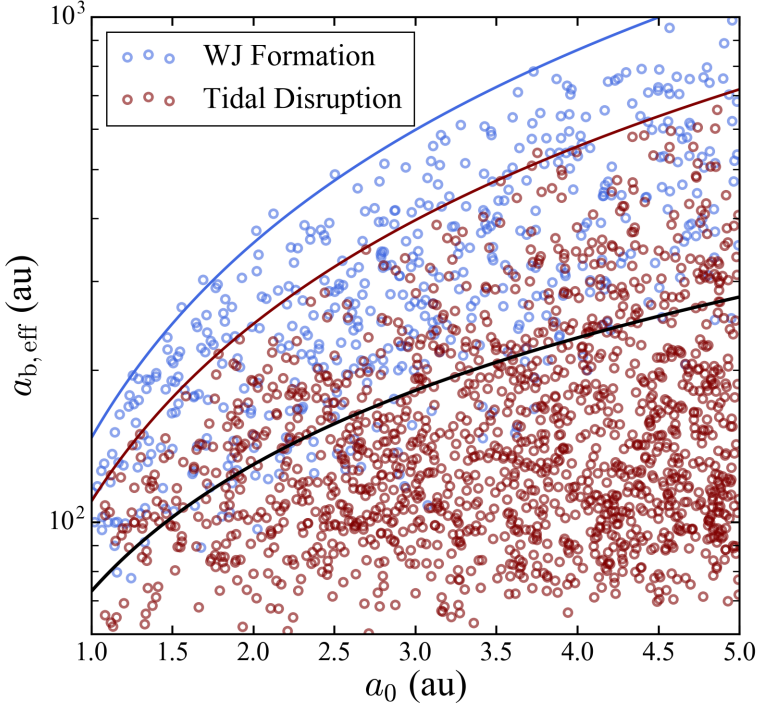


Figure 4.15: Initial conditions for LK migration with chaotic tides, coloured by the outcomes of the evolution, either the formation of an eccentric WJ (blue) or tidal disruption (red). The giant planet has  $M_p = 1M_J$  and  $R_p = 1.6R_J$ . The blue, red, and black lines are the same as in Fig. 4.10.

so large that the planets are tidally disrupted (see equation 4.62). Figure 4.15 demonstrates that the systems that produce surviving WJs indeed satisfy equations (4.58) and (4.62). The range of  $\epsilon_{\text{oct}}$  that can produce eccentric WJs is capped by the limit on  $a_b/a_0$  (see equation 4.71). Lastly, Fig. 4.14 shows that changing the properties of the gas giant has little effect on the parameter space that produces eccentric WJs. Unlike standard LK migration with static tides, where systems with  $M_p = 0.3M_J$  produce hot Saturns at a rate of 0.5% (assuming  $\Delta t_L = 1$  s) after evolving for 5 Gyr [see ASL16, Muñoz et al., 2016], chaotic tides allow low-mass planets to survive high-eccentricity migration without suffering tidal disruption, and produce hot Saturns at a rate of about 2.2% after only 1 Gyr.

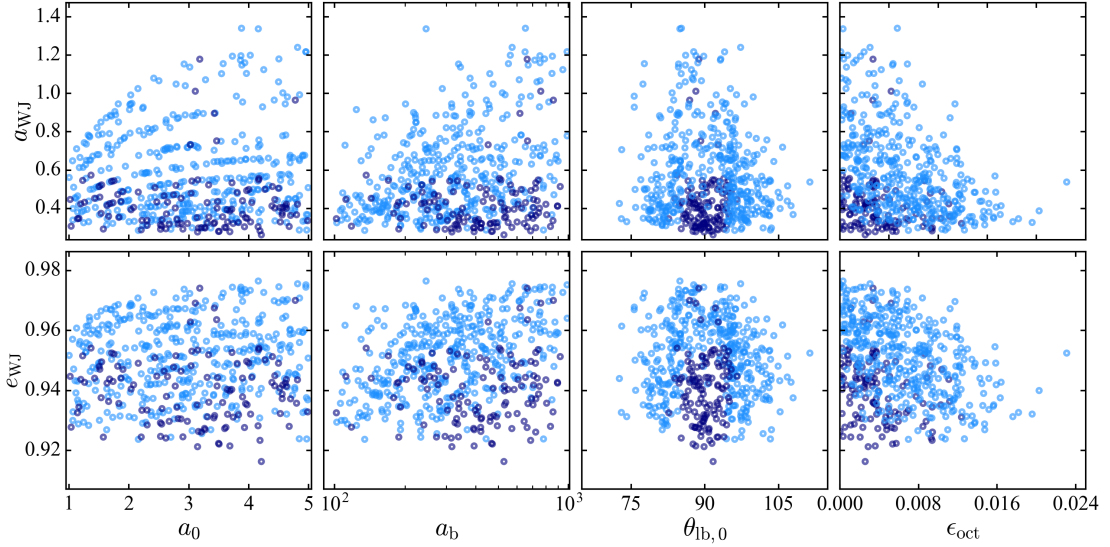


Figure 4.16: The orbital semi-major axis  $a_{\text{WJ}}$  (top row) and eccentricity  $e_{\text{WJ}}$  (second row) of WJs formed by chaotic tidal migration (for planets with  $M_p = 1M_J$ ,  $R_p = 1.6R_J$ ) as a function the initial  $a_0$  of the planet,  $a_b$  of binary, the initial binary inclination,  $\theta_{\text{lb},0}$ , and the octupole parameter  $\epsilon_{\text{oct}}$  [see equation (4.71)]. Systems that only experience one high-eccentricity phase are shown in dark blue, and those that undergo multiple LK cycles are shown in light blue.

#### 4.5.4 Properties of WJs Formed by Chaotic Tidal Evolution

We now examine the orbital properties of planets produced by chaotic tides. The scatter plots in Fig. 4.16 show an overview of the WJ eccentricities and semi-major axes ( $e_{\text{WJ}}$  and  $a_{\text{WJ}}$ ) for the  $M_p = 1M_J, R_p = 1.6R_J$  planet model after the planetary f-mode has settled into a quiescent state (but before weak tidal friction circularizes the orbit over a long time-scale). Most planets have  $a_{\text{WJ}}$  between 0.2 and 1 au and  $e_{\text{WJ}}$  between 0.91 and 0.97. Systems that have undergone multiple LK cycles tend to have larger  $a_{\text{WJ}}$  and  $e_{\text{WJ}}$ . This is expected because larger values of  $a_{\text{WJ}}$  and  $e_{\text{WJ}}$  correspond to systems that do not reach a small enough value of  $r_p$  for chaotic tides to significantly alter the orbit within the time-frame of a single high-eccentricity phase. In general,  $a_{\text{WJ}}$  and  $e_{\text{WJ}}$  increase with  $\eta = r_p/r_{\text{tide}}$  [see

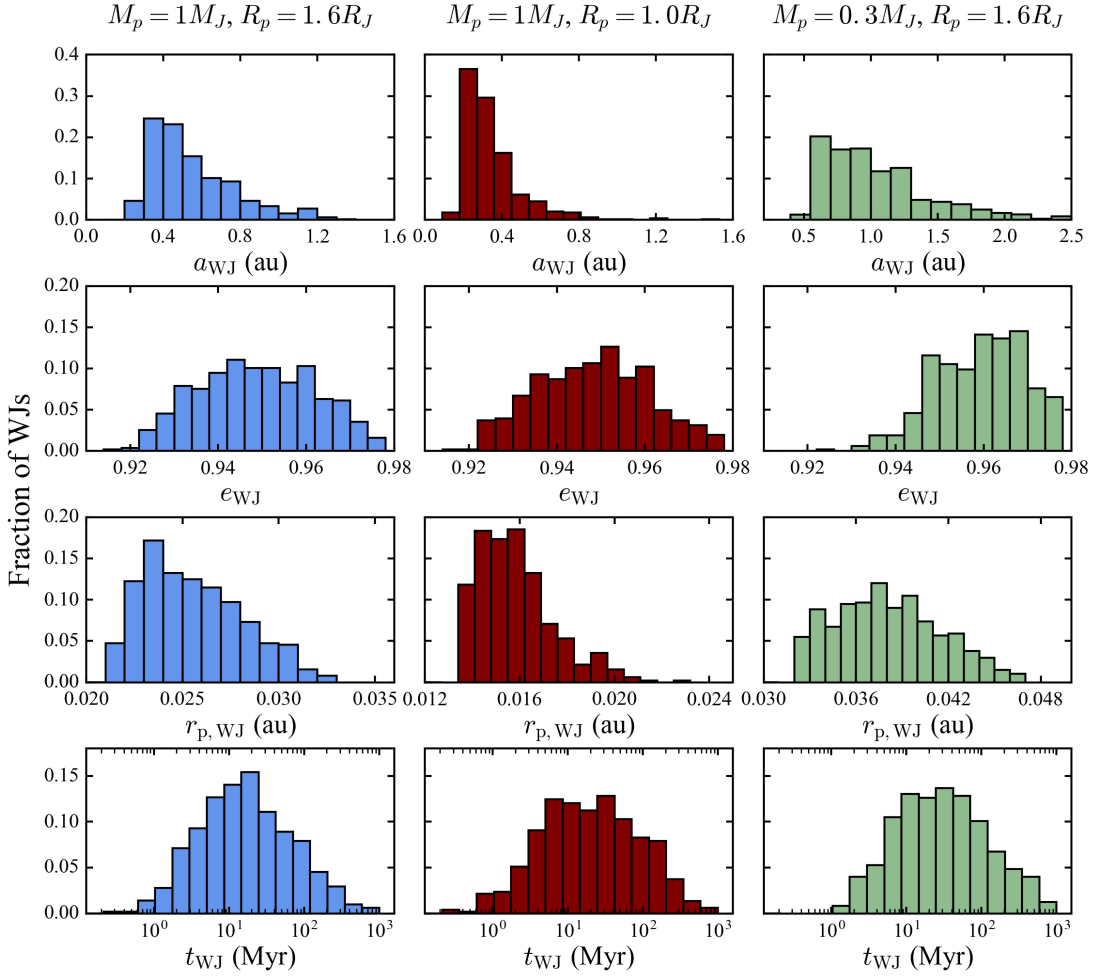


Figure 4.17: The distributions of  $a_{\text{WJ}}$ ,  $e_{\text{WJ}}$ ,  $r_{\text{p},\text{WJ}}$ , and  $t_{\text{WJ}}$  (the time at which chaotic evolution stops) for WJs produced by LK migration with chaotic tides for three different planet models. The ranges of  $a_{\text{WJ}}$  and  $e_{\text{p},\text{WJ}}$  are in agreement with equations (4.64) and (4.65), (see also Fig. 4.18). The peaks of the  $r_{\text{p},\text{WJ}}$  distributions occur near  $\eta \sim 3$  [see equation (4.22)] for all three planet models.

equations (4.64) and (4.65) and Fig. 4.12].

In the top left panel of Fig. 4.16, the values of  $a_{\text{WJ}}$  seem to fall on a set of  $a_{\text{WJ}} - a_0$  curves. This feature arises from our treatment of non-linear dissipation, where the f-mode rapidly dissipates energy after reaching  $E_{\max}$ . Each curve corresponds to some number  $N$  of non-linear dissipation episodes, after which the orbital energy becomes  $(E_{B,0} - NE_{\max})$ . The systems with

the most distant stellar companions can produce WJs with relatively large semi-major axes ( $\gtrsim 1$  au) after chaotic tidal evolution. This occurs because the minimum  $\eta$  required for chaotic tides to compete with the LK effect is larger for systems with larger  $a_{b,\text{eff}}$ . In Fig. 4.16, we can also see that most systems that exhibit chaotic behaviour have initial mutual inclinations around  $90^\circ$ , as expected. Lastly, as seen earlier in Fig. 4.14, large values of  $\epsilon_{\text{oct}}$  do not produce surviving WJs.

Figure 4.17 shows the histogram of the parameters of WJs produced by chaotic tidal migration. The distributions of planet properties are generally more sharply peaked for denser planets. The ranges of  $a_{\text{WJ}}$  and  $e_{p,\text{WJ}}$  are in agreement with equations (4.64) and (4.65), which predict that  $a_{\text{WJ}}$  scales linearly with  $R_p$  while  $e_{\text{WJ}}$  has no dependence on the planet radius and a weak dependence on the planet mass (for a given minimum  $\eta$  achieved during the orbital evolution). Combining equations (4.64) and (4.65), we can see that the distribution of  $r_{p,\text{WJ}} = a_{\text{WJ}}(1 - e_{\text{WJ}})$  should scale directly with  $r_{\text{tide}}$ . This would imply that the peak at 0.015 au in the  $r_{p,\text{WJ}}$  distribution for the  $M_p = 1M_J, R_p = 1 R_J$  planet model should appear near 0.024 au and 0.036 au in the  $M_p = 1M_J, R_p = 1.6 R_J$  and  $M_p = 0.3M_J, R_p = 1.6 R_J$  models, respectively, as is the case in Fig. 4.17. The timescale for chaotic evolution to shrink the orbit,  $t_{\text{WJ}}$ , peaks near 10 Myr for all planet models.

The range of  $r_{p,\text{WJ}}$  is narrow for all three planet models. The lower edge of this distribution is determined by the tidal disruption radius. A planet cannot survive if  $\eta < 2.7$ . The upper value of  $r_{p,\text{WJ}}$  is roughly set by the pericentre distance where the planet with the largest semi-major axis (in our simulation,  $a_0 = 5$  au) crosses the chaos boundary, generally near

$\eta \sim 4$ . Figure 4.18 shows the relationship between  $a_{\text{WJ}}$ ,  $e_{\text{WJ}}$  and  $r_{\text{p,WJ}}$  for planets that have undergone chaotic evolution. The solid lines show equation (4.65) for each planet model. Recall that equation (4.65) yields the eccentricity where  $|\Delta\hat{P}_\alpha(E_{\text{resid}})| = 1$  for a given  $r_p$ . Therefore, the restrictions on  $r_{\text{p,WJ}}$  determine the range in the distributions of  $a_{\text{WJ}}$  and  $e_{\text{WJ}}$ . This simple calculation explains the properties of planets that survive chaotic tidal evolution very well. The spread in the results from the population synthesis arises from the fuzziness in the chaotic tides boundary, i.e. variations in  $\Delta\hat{P}_{\text{crit}}$ . These variations are larger for smaller  $E_{\text{resid}}$  (see Fig. 4.4). On average, systems with smaller  $M_p$  and larger  $R_p$  have smaller  $E_{\text{resid}}$ . Accordingly, the spread in the results is largest for the  $M_p = 0.3M_J, R_p = 1.6 R_J$  model and smallest for the  $M_p = 1M_J, R_p = 1 R_J$  model.

### 4.5.5 Hot Jupiter Properties

The eccentric WJs formed by chaotic tidal migration continue to experience orbital decay and circularization due to static tides. As long as the static tide is sufficiently dissipative, the planet will circularize to

$$a_F = a_{\text{WJ}}(1 - e_{\text{WJ}}^2) \simeq 2r_{\text{p,WJ}} \quad (4.73)$$

For our population synthesis, most WJs circularize within 1 Gyr (assuming  $\Delta t_L = 1$  s) to become HJs (see Table 4.2). Those that do not are almost exclusively from the low-density planet model with the largest  $r_{\text{tide}}$ . The HJ period distributions for our population synthesis calculations are shown in Fig. 4.19. The peak lies between 3.5 and 4 days for our standard model with  $M_p = 1M_J, R_p = 1.6R_J$ ; this shifts to smaller periods for denser planets (with  $M_p = 1M_J, R_p = 1R_J$ ). As discussed in Section 4.5.4, the range of  $r_{\text{p,WJ}}$

is set by the pericentre distance requirements for tidal disruption and for chaotic tidal behaviour. Both of these conditions vary directly with  $r_{\text{tide}}$ , so the peak of the HJ period distribution scales as  $r_{\text{tide}}^{3/2}$ .

The final spin-orbit misalignments ( $\theta_{\text{sl}}$ ) are also shown in Fig. 4.19. For all three planet models, the distribution in  $\theta_{\text{sl}}$  is bimodal, peaking near  $30^\circ$  and  $140^\circ$ . These distributions are qualitatively similar to those obtained in ASL16 for standard LK migration with static tides. In general, the percentage of retrograde configurations ( $\theta_{\text{sl}} > 90^\circ$ ) is slightly larger for chaotic tidal migration than for standard LK migration. This may be due to the fact that, because chaotic tides dramatically speed up orbital decay, the star is rotating more rapidly when  $\theta_{\text{sl}}$  becomes “frozen,” and the feedback torque from the star on the orbit is larger. Nearly all of the retrograde configurations are produced by systems that experience multiple high eccentricity phases. A planetary orbit that only undergoes one LK oscillation remains more aligned with the stellar spin, likely because the planet does not have sufficient opportunity to change the spin-axis of the star.

We have also provided the final values of  $\theta_{\text{jb}}$ , the angle between  $\mathbf{J} = \mathbf{S}_* + \mathbf{L}$  and  $\mathbf{L}_B$ . In all of our calculations, the ratio  $|\mathbf{S}_*|/|\mathbf{L}|$  is still of order unity near  $t_{\text{HJ}}$  (the time when the planet’s orbit has circularized to  $e = 0.1$ ), so the mutual inclination of the inner and outer orbits,  $\theta_{\text{lb}}$ , is not fixed at  $t_{\text{HJ}}$ . As the star continues to spin down,  $\theta_{\text{lb}}$  will approach  $\theta_{\text{jb}}$ , as discussed in Section 4.4.5. The distributions of  $\theta_{\text{jb}}$  have two strong peaks around  $65^\circ$  and  $115^\circ$ .

Lastly, Fig. 4.19 shows the distribution of “arrival times” for HJs,  $t_{\text{HJ}}$ , when  $e = 0.1$ . For the  $M_p = 1M_J, R_p = 1R_J$  planet model, all orbits circularize to  $e = 0.1$  within 1 Gyr. For the  $M_p = 0.3M_J, R_p = 1.6R_J$  model, only 65%

of the WJs circularize within a Gyr time-frame, yet 97% can become HJs within 10 Gyr. In general, planets with larger  $r_{\text{tide}}$  finish chaotic evolution at larger  $r_{p,\text{WJ}}$  and take longer to circularize via static tides. Most planets that undergo chaotic tidal evolution can be expected to become HJs within the lifetimes of their host stars. As a result, the population of eccentric WJs formed by chaotic tides is transient.

The numerical results presented in this paper assume  $\Delta t_L = 1$  s. We can generalize our results by understanding the effect of changing  $\Delta t_L$  on the HJ formation rate. The time-scale for orbital decay and circularization via static tides is typically the longest time-scale in LK chaotic tidal migration. This time-scale depends linearly on  $\Delta t_L$  (see equation 4.43). A system that produces a HJ within 1 Gyr with  $\Delta t_L \gtrsim 1$  s can yield a HJ in 10 Gyr if  $\Delta t_L \gtrsim 0.1$  s. From Fig. 4.19, it is clear that the two planet models with  $M_p = M_J$  can produce HJs within 10 Gyr even if the planets are no more dissipative than Jupiter ( $\Delta t_L = 0.1$  s). However, for the  $M_p = 0.3M_J$  planet model, the choice of  $\Delta t_L$  influences the calculated HJ formation fraction.

## 4.6 Analytical Calculation of WJ Formation Fraction

Muñoz et al. [2016] developed an analytical method to calculate the HJ formation fraction in the standard LK migration (with static tides) scenario. In this section, we adapt this method to calculate the fractions of systems that experience chaotic tidal migration or tidal disruption. A system will become chaotic or suffer disruption when the planet's pericentre distance is smaller than a critical value — for chaotic behaviour,  $r_{p,\text{crit}}$  from equation (4.34), for disruption,  $r_{p,\text{dis}}$  from equation (4.60). We define  $\theta_{lb,\text{crit}}$  as the

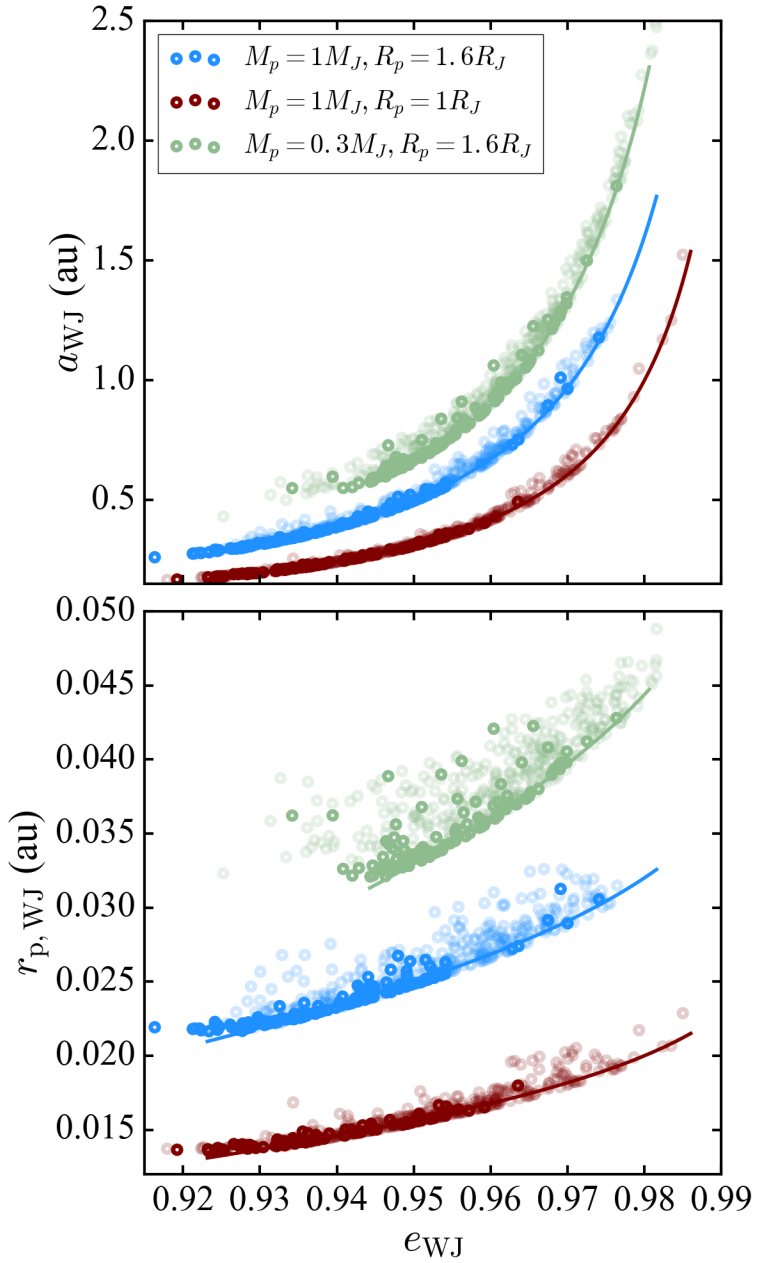


Figure 4.18: Semi-major axis ( $a_{\text{WJ}}$ ), pericentre distance ( $r_{p,\text{WJ}}$ ), and eccentricity ( $e_{\text{WJ}}$ ) correlations of WJs produced by chaotic tidal migration for three planet models. Dark points indicate systems that have only undergone one LK cycle, and light points show systems that have experienced multiple LK cycles. The solid lines denote  $|\Delta \hat{P}_a(\tilde{E}_{\text{resid}})| = 1.0$  for different planet properties calculated from equations (4.64) and (4.65).

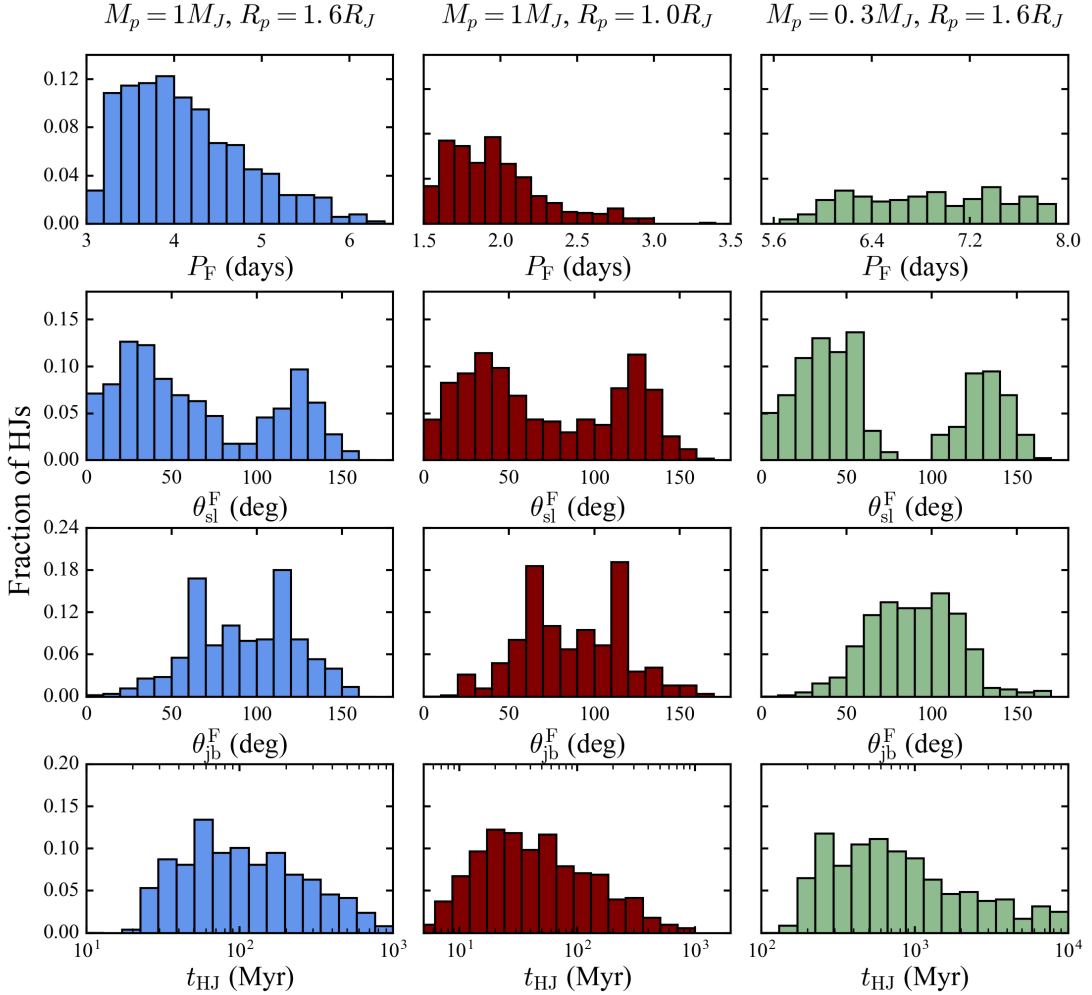


Figure 4.19: The distribution of the final orbital periods, spin-orbit misalignments ( $\theta_{\text{sl}}^{\text{F}}$ ), asymptotic mutual orbital inclinations ( $\theta_{\text{jb}}^{\text{F}}$ ; see Section 4.4.5), and circularization times (when  $e = 0.1$ ) for HJs that have formed in our population synthesis calculation. LK chaotic tidal migration can produce HJs with orbital periods in the range of 1.5-8 days depending on the planet mass and radius. This migration mechanism yields a bimodal distribution in  $\theta_{\text{sl}}^{\text{F}}$ . The final mutual orbital inclinations can span a large range of values from  $\theta_{\text{jb}}^{\text{F}} = 0^\circ$  to  $\sim 170^\circ$ . LK chaotic tidal migration can comfortably generate HJs within 10 Gyr time-scales.

minimum initial mutual inclination necessary for a system to reach  $r_{p,\text{crit}}$ , or equivalently  $e_{\text{crit}}$  (see equation 4.32). Assuming uniform distribution in  $\cos \theta_{lb,0}$ , the fraction of systems (for a given  $a_0$ ,  $a_b$ ,  $e_b$ ) that experience chaotic tidal behaviour is then

$$f_{\text{mig}}(a_0, a_b, e_b) = \cos \theta_{lb,\text{crit}}, \quad (4.74)$$

where  $\cos \theta_{lb,\text{crit}} = 0$  when  $e_{\text{lim}} < e_{\text{crit}}$ . We refer to Muñoz et al. [2016] for the calculation of  $\cos \theta_{lb,\text{crit}}$  given  $e_{\text{crit}}$ . By performing a Monte Carlo integration over  $a_0 = [1, 5]$  (au),  $a_b = [10^2, 10^3]$  (au) (uniformly sampled in  $\log a_b$ ), and  $e_b = [0, 0.8]$ , we can predict the fraction of systems in our population synthesis where the planet undergoes chaotic tidal migration ( $\mathcal{F}_{\text{mig}}$ ) and fraction of systems where the planet is tidally disrupted ( $\mathcal{F}_{\text{dis}}$ ). The fraction of systems that become chaotic but are not disrupted is given by

$$\mathcal{F}_{\text{WJ}} = \mathcal{F}_{\text{mig}} - \mathcal{F}_{\text{dis}}. \quad (4.75)$$

As discussed in Section 4.4.2, chaotic tides can compete with the LK effect and prevent planet tidal disruption. Our analytic calculations therefore provide an upper limit to the tidal disruption fraction ( $\mathcal{F}_{\text{dis}}$ ) and a lower bound on the fraction of WJs formed ( $\mathcal{F}_{\text{WJ}}$ ) in this scenario. Table 4.2 shows that our analytical results are in good agreement with the population synthesis results. Our analytical  $\mathcal{F}_{\text{mig}}$  is slightly smaller than the value obtained from population synthesis, likely because the boundary for chaotic tides is fuzzy and we have chosen a conservatively low value for  $r_{p,\text{crit}}$ .

In addition to calculating  $\mathcal{F}_{\text{mig}}$  and  $\mathcal{F}_{\text{dis}}$ , we can estimate the total migration fraction  $\mathcal{F}_{\text{mig}}^{\text{st+ct}}$  where the planet either migrates via chaotic tides or migrates within 1 Gyr due to weak tidal friction (the standard LK migra-

tion scenario). For a given  $a_0$ ,  $a_b$ , and  $e_b$ , this is

$$f_{\text{mig}}^{\text{st+ct}}(a_0, a_b, e_b) = \max(\cos \theta_{\text{lb,crit}}, \cos \theta_{\text{lb,st}}), \quad (4.76)$$

where  $\cos \theta_{\text{lb,st}}$  is the maximum value of  $\cos \theta_{\text{lb},0}$  for which a system can reach  $r_{\text{p,ST}}$ , given in equation (4.59). We can integrate  $f_{\text{mig}}^{\text{st+ct}}$  over orbital parameters  $a_0$ ,  $a_b$ , and  $e_b$  (as before) to find  $\mathcal{F}_{\text{mig}}^{\text{st+ct}}$ . Because  $r_{\text{p,ST}}$  is generally less than  $r_{\text{p,crit}}$ , the percentage of systems that are not chaotic but become HJs due to weak tidal friction is much less than 1%.

In our population synthesis calculations (Section 4.5) we have only considered planets with  $M_p = M_J$  and  $0.3M_J$  and radius  $R_p = R_J$  or  $1.6 R_J$ . With analytic calculations, we can easily predict the fractions of systems that survive chaotic tides or suffer disruption as a function of  $M_p$  and  $R_p$ . The results are shown in Fig. 4.20. The fraction of systems that undergo chaotic tidal migration is nearly independent of  $M_p$ ,  $R_p$  ( $\mathcal{F}_{\text{mig}} \sim 13 - 15\%$ ) for the considered range of planet parameters. The WJ formation fraction from LK chaotic tides is also insensitive to  $M_p$  and  $R_p$  because  $r_{\text{p,crit}}$  and  $r_{\text{p,dis}}$  have roughly the same scaling with  $M_p$  and  $R_p$ . This result differs from the standard picture of LK migration, where Saturn-mass planets that migrate are destined for tidal disruption (see ASL16).

## 4.7 Summary and Discussion

### 4.7.1 Summary of Key Results

In this paper, we have systematically studied the role of dynamical tides in high-eccentricity gas giant migration via the LK effect. Our investigation

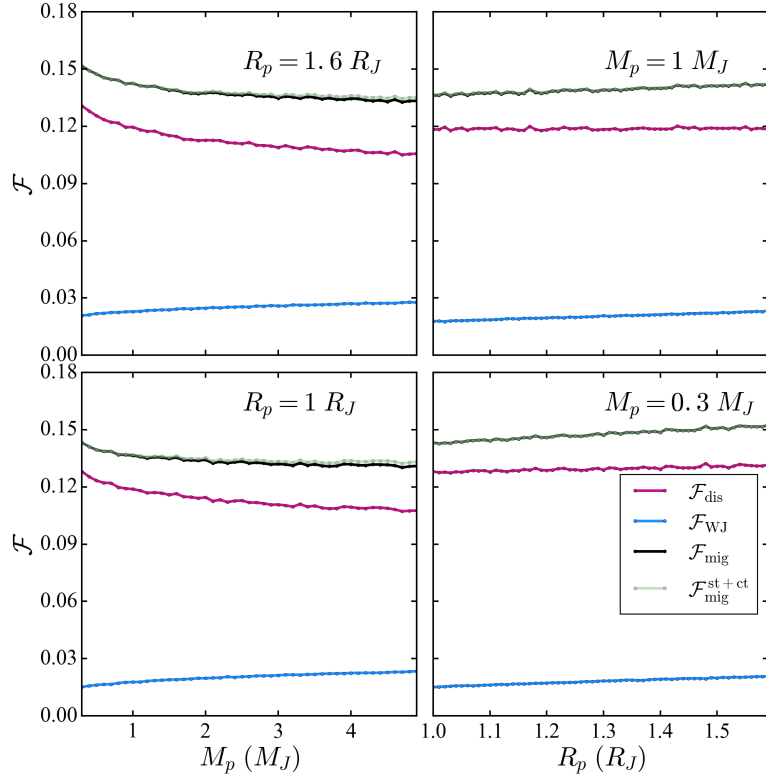


Figure 4.20: Analytical results for the planet migration/disruption fractions for various planet masses and radii (see Section 4.6).  $\mathcal{F}_{\text{mig}}$  gives the fraction of systems that experience chaotic tidal migration,  $\mathcal{F}_{\text{dis}}$  gives the upper bound on the fraction of systems that are tidally disrupted, and  $\mathcal{F}_{\text{WJ}} = \mathcal{F}_{\text{mig}} - \mathcal{F}_{\text{dis}}$  gives the lower bound on the fraction of eccentric WJs formed in this scenario.  $\mathcal{F}_{\text{mig}}^{\text{st+ct}}$  gives the fraction of systems that experience chaotic tidal migration or standard LK migration with static tides. Note that  $\mathcal{F}_{\text{mig}}^{\text{st+ct}} \approx \mathcal{F}_{\text{mig}}$  (the green line rests nearly on top of the black line). This suggests that almost all planets (with  $\Delta t_L = 1$  s) that could migrate via standard LK migration within 1 Gyr will experience chaotic tides.

has revealed (i) the conditions under which dynamical tides in the planet have a significant effect on migration, (ii) the characteristics of the planet population that results from LK migration with chaotic dynamical tides, and (iii) the expected HJ fraction from this formation path. The overall summary of the paper is already given in the abstract. Here we provide a guide to the key results of each section.

In Section 4.2, we explored the orbital parameters necessary for a gas giant to undergo chaotic tidal migration. When a planet’s orbit is very eccentric and its pericentre distance is sufficiently small, the tidal force from the host star can excite planetary oscillations at pericentre in such a way that these oscillations chaotically climb in amplitude over repeated close passages (an example is shown in the bottom panel of Fig. 4.2). We found that, for the  $\gamma = 2$  polytrope planetary model, the fundamental mode (f-mode) is more strongly excited than inertial modes, and is the most likely to experience chaotic growth over multiple orbits. The condition for these “chaotic tides” to operate is given by equation (4.32) and plotted in Fig. 4.3. In general, chaotic tides can occur in planets on highly eccentric orbits with small pericentre distances. We also explored (in Sections 4.2.4 and 4.2.5) how the conditions for chaotic tides become more generous when the f-mode already has some non-zero energy.

In Section 4.3, we developed a model to couple the LK migration with orbital changes due to chaotic dynamical tides. The model is fully described in Section 4.3.1, and can be readily adapted to other high-eccentricity migration mechanisms. Although the model is largely *ab initio*, there are two free parameters that characterize the (uncertain) non-linear mode dissipation:  $E_{\max}$  (the maximum energy the mode can reach before non-linear dissipation sets in) and  $E_{\text{resid}}$  (the residual energy in the mode after an episode of non-linear dissipation). We found that these parameters (with reasonable values) do not change the general features of evolution due to chaotic tides, but can alter the details (see Figs. 4.7-4.8).

In Sections 4.3.2 and 4.4, we presented example calculations of the LK chaotic tidal migration, and explained some key features of this migration

mechanism:

- Chaotic tidal migration leads to rapid formation of WJs (see Fig. 4.6 for an example) on timescales a few to 100 Myrs (see Fig. 4.17). These WJs have eccentricities in the range  $0.85 \lesssim e_{\text{WJ}} \lesssim 0.98$  and semi-major axes between 0.1 and 2 au (with lower values more likely), depending on the giant planet mass and radius (see Fig. 4.16).
- These eccentric WJs efficiently circularize to HJs via dissipation of static tides. This process is faster than standard LK migration because a planet that experiences chaotic tides quickly becomes decoupled from the influence of the perturber and the eccentricity oscillations are frozen (see Figs. 4.6, 4.9 and 4.11).
- Some giant planets that are otherwise fated for tidal disruption can be saved by chaotic tides (see Fig. 4.11). This occurs when the orbital decay timescale associated with chaotic tides is shorter than the timescale for the perturber to change the planet’s eccentricity (see Section 4.4.2).

In Section 4.5, we conducted a population synthesis study to determine the formation fractions and properties of eccentric WJs and HJs for a few combinations of planet mass and radius. Our study sampled the same range of initial orbital parameters as in Anderson et al. (2016) for the standard LK migration scenario. The calculated fractions for chaotic tidal migration ( $\mathcal{F}_{\text{mig}}$ ), tidal disruption ( $\mathcal{F}_{\text{dis}}$ ), WJ formation ( $\mathcal{F}_{\text{WJ}}$ ; note that  $\mathcal{F}_{\text{mig}} = \mathcal{F}_{\text{dis}} + \mathcal{F}_{\text{WJ}}$ ) and HJ formation within 1 Gyr ( $\mathcal{F}_{\text{HJ}}$ ), are provided in Table 4.2. For an  $M_p = 1M_J, R_p = 1R_J$  planet, LK chaotic tidal migration produces more HJs than standard LK migration ( $\mathcal{F}_{\text{HJ}}$  increases from 2.4% to 3.9%; see Table 3 in ASL16). More importantly, chaotic tides can produce hot giant planets

with a broad range of masses and radii. This is in stark contrast with the standard LK migration, which produces very few hot Saturns because of the severe tidal disruption experienced by such low-mass giants (ASL16; Munoz et al. 2016).

The orbital properties of planets from our population synthesis that survived chaotic tidal migration are shown in Figs. 4.17 and 4.19. The WJs that are produced directly by chaotic tidal dissipation have pericentre distributions that peak near  $r_{p,WJ} \sim 3r_{\text{tide}} = 3R_p(M_\star/M_p)^{1/3}$ . These pericentre values are smaller than those of observed high-eccentricity WJs such as HD80606 b [Hébrard et al., 2010]. This is expected as the eccentric WJs formed by chaotic tides are “transient” and should move quickly through the high-eccentricity phase. The HJs that form via LK chaotic tidal migration exhibit a pile-up around a 3 day orbital period, depending on the planet’s mass-radius relation and the assumed tidal disruption criterion. This is a feature of all tidal migration mechanisms. However, our predicted HJ period distribution for LK chaotic tidal migration differs from that for the standard LK migration, particularly for low-mass giant planets (compare Fig. 4.19 with the middle row of Fig. 23 from ASL16). Chaotic tidal migration can produce Saturn-mass planets at periods longer than 5 days and generates a wider period distribution for such planets. Finally, we found that chaotic tidal migration yields similar spin-orbit misalignments as the standard LK migration (compare Fig. 4.19 with Fig. 24 of ASL16). For all three planet models we considered, the distribution of final spin-orbit misalignments is bimodal with peaks at  $\theta_{\text{sl}}^{\text{F}} \sim 30^\circ$  and  $\theta_{\text{sl}}^{\text{F}} \sim 130^\circ$ .

In Section 4.6, we used an analytical method, developed in Muñoz et al. [2016], to understand how the HJ formation rate varies with planet mass

and radius. We calculated a lower-bound on the eccentric WJ formation rate (not accounting for planets that are spared from tidal disruption by chaotic tides). The predicted (analytical) rates are in agreement with the results from the population synthesis study (see Section 4.5) and are shown in Fig. 4.20. We confirmed that the WJ formation rate from LK chaotic tidal migration is constant over a reasonable range of giant planet masses and radii, as suggested by, e.g., Fig. 4.14 and Table 4.2.

### 4.7.2 Discussion

The results presented in this paper show that chaotic tides endow the LK migration scenario with a number of “favourable” features [see also Wu, 2018]. These not only reduce the theoretical uncertainties regarding tidal dissipation that are inherent in the theory, but also may help reconcile some of the discrepancies between observations and predictions of LK migration. Chaotic tides drastically reduce the amount of time that a gas giant spends at high eccentricity. This could explain the lack of observations of super-eccentric gas giants [Dawson et al., 2015]. In addition, chaotic tides quickly decouple a gas giant experiencing LK oscillations from the stellar perturber. This allows planets at larger pericentre distances to migrate within the lifetime of their host stars, provided the planets’ tidal lag times,  $\Delta t_L$ , are at least comparable to Jupiter’s. In this way, chaotic tidal migration naturally produces a period distribution with a longer tail. Indeed, HJs beyond the 3-day pile-up are observed but difficult to explain with standard high-e migration scenarios.

Although chaotic tides increase the HJ yield from LK migration in stellar

binaries, particularly for low-mass planets, we should not expect this particular formation channel to account for all HJs. The occurrence rate of HJs produced by this channel can be computed from

$$\mathcal{R}_{\text{HJ}} = \mathcal{F}_b \times \mathcal{F}_p \times \mathcal{F}_{\text{HJ}}, \quad (4.77)$$

where  $\mathcal{F}_b$  is the fraction of stars with a binary companion and  $\mathcal{F}_p$  is the fraction of solar-type stars with a giant planet at a few au. Assuming  $\mathcal{F}_b \sim 50\%$  [Raghavan et al., 2010, Ngo et al., 2015],  $\mathcal{F}_p \sim 10\%$  (as in ASL16), and  $\mathcal{F}_{\text{HJ}} \sim 4\%$  from our population synthesis calculation, we obtain an estimate of  $\mathcal{R}_{\text{HJ}} \sim 0.2\%$ , which is nearly an order of magnitude smaller than the observed occurrence rate of 1% [Marcy et al., 2005, Wright et al., 2012, Fressin et al., 2013]. Thus, LK chaotic tidal migration in stellar binaries can roughly account for 20 – 30% of the observed HJ population.

However, we expect that many of the “nice” features of chaotic tides may also apply to other flavours of high- $e$  migration scenarios, such as LK migration induced by planetary companions and secular chaos in multi-planet systems. The eccentricity and pericentre ranges of planets that are susceptible to chaotic tides are set by the boundary for chaotic f-mode behaviour (see Section 4.2), and do not depend on a specific high- $e$  migration scenario. Chaotic tides can save a planet from tidal disruption when the time-scale for energy transfer to the planet’s oscillation mode is shorter than the time-scale for driving and maintaining the planet’s high-eccentricity (see Section 4.4.2) – this condition can be satisfied by all secular eccentricity excitation mechanisms. Indeed, the recent work by Teyssandier et al. [2019] showed that chaotic tides significantly increase the HJ formation fraction in the secular-chaos high- $e$  migration scenario. Overall, chaotic tides boost the importance of high- $e$  migration for the for-

mation of HJs.

The story of chaotic tidal migration hinges upon the planet's ability to survive rapid tidal heating. There is reason to expect that the planet interior could survive this process [Wu, 2018] if most of the dissipated energy goes into the outer layers of the planet, which can quickly radiate heat. However, if the tidal energy is deposited at a larger depth, the planet's envelope may expand. Such changes in the structure of the planet would affect the f-mode frequency and could have a larger influence on the evolution of the planet's orbit. A sudden expansion of the planet's radius may also put the planet in danger of tidal disruption. Many of the planets that survive chaotic tidal migration come close to the tidal disruption radius. Expansion of the planet could easily lead to stripping of the outer layers and initiate mass transfer or mass loss. The effect of mode energy dissipation on the planetary structure is a very important problem for future study.

# CHAPTER 5

## TIDAL EFFECTS IN ECCENTRIC COALESCING NEUTRON STAR BINARIES

Originally published in:

M. Vick and D.Lai. Tidal Effects in Eccentric Coalescing Neutron Star Binaries.  
*Phys. Rev. D* **100**, pp. 063001, 2019. doi: 10.1103/PhysRevD.100.063001

### 5.1 Introduction

In its first and second observing runs, the LIGO/Virgo collaboration has detected 10 black hole (BH) binary mergers The LIGO Scientific Collaboration et al. [2018] and one neutron star (NS) binary merger Abbott et al. [2019]. As LIGO and Virgo improve in sensitivity, they are expected to detect many more NS binary merger events. The proposed formation channels for compact object (CO) binary mergers can be divided into two broad classes: isolated binary evolution and dynamical formation. In the first, an isolated stellar binary becomes tighter in separation due to drag forces in the common-envelope phase [e.g. Lipunov et al., 1997, 2017, Podsiadlowski et al., 2003, Belczynski et al., 2010, Dominik et al., 2012, 2013, 2015, Belczynski et al., 2016]. CO binaries that form via this pathway are expected to be circular while emitting gravitational waves (GWs) in the LIGO band. In the second class, CO binaries form dynamically through gravitational interactions between multiple stars and COs. For instance, BH binaries in dense star clusters can become bound and shrink in separation due to three-body encounters (e.g. an exchange interaction between a binary and a CO) and/or secular interactions [e.g. Portegies Zwart and

McMillan, 2000, Miller and Hamilton, 2002, Wen, 2003, O’Leary et al., 2009, Miller and Lauburg, 2009, Antonini and Perets, 2012, Rodriguez et al., 2015, Samsing, 2018]. Another type of dynamical formation occurs in the galactic field, where CO mergers are induced in hierarchical triple or quadruple systems Silsbee and Tremaine [2017], Antonini et al. [2017], Liu and Lai [2018, 2019], Liu et al. [2019]. Intriguingly, some fraction of dynamically assembled CO binaries may emit GWs within the LIGO band while their orbits are still highly eccentric. The formation rate for such binaries is uncertain, but detecting these eccentric systems by LIGO/Virgo would be of great interest.

The effects of tides on the gravitational waveform of coalescing NS binaries in circular orbits have been studied in many papers [e.g. Kochanek, 1992, Bildsten and Cutler, 1992, Lai et al., 1994b, Lai and Wiseman, 1996, Baumgarte et al., 1998, Binnington and Poisson, 2009, Damour and Nagar, 2009, Uryū et al., 2009, Penner et al., 2011, Ferrari et al., 2012]; (see Section I of Xu and Lai [2017] for a short review). Quasi-equilibrium tides (corresponding to the quadrupolar f-mode distortion of the NS) are important at high frequencies (near binary merger). An analytical expression for the GW phase shift associated with quasi-equilibrium tides was derived in Flanagan and Hinderer [2008] (see also Lai et al. [1994a]) and used to obtain constraints on NS tidal deformability from GW170817 Abbott et al. [2019]. Numerous papers have been written on the nuclear physics implications of such a constraint (see Tews et al. [2018]). On the other hand, resonant tides, which occur when the tidal forcing frequency (of order the orbital frequency) matches an intrinsic NS mode frequency, have also been explored. The general conclusion is that the phase shifts due to tidal

resonances are negligible for “canonical” NSs (mass  $1.4 M_{\odot}$  and radius 10 km), but can be important if the NS has a larger radius (e.g  $R \gtrsim 13$  km) Lai [1994], Shibata [1994], Reisenegger and Goldreich [1994], Ho and Lai [1999], Lai and Wu [2006], Yu and Weinberg [2017a,b], Andersson and Ho [2018], Xu and Lai [2017], Yang [2019] (see Xu and Lai [2017] for a review).

In this work, we study the effect of dynamical tides on the orbital decay and the resulting GW signal from an eccentric CO binary with a NS. We focus on the f-mode oscillation of the NS as other modes (g-modes and r-modes) couple rather weakly with the tidal potential and produce very small effects even in resonance with circular orbits (see Xu and Lai [2017] and references therein). By coupling the f-mode evolution to the post-Newtonian (PN) orbital evolution, we calculate the effect of tides on the GW signal as the binary evolves toward merger. Several recent papers have examined the energy transfer to the f-mode at pericenter passages, GWs from the excited f-mode, and the corresponding change in the binary trajectory with varying degree of approximations [Chirenti et al., 2017, Parisi and Sturani, 2018, Yang et al., 2018, Yang, 2019, see also the appendix of the present paper]. There have also been several numerical relativity simulations of the final stages of eccentric NS binary mergers Gold et al. [2012], East et al. [2012], Chaurasia et al. [2018], Papenfort et al. [2018]. Our paper instead focuses on how the energy exchange between the NS f-mode and the orbit affects the phase of the GW signal prior to binary merger (or NS tidal disruption). We evolve the amplitude of the NS f-mode as the binary decays and circularizes due to gravitational radiation from a highly eccentric orbit to one that is moderately eccentric or near circular. We specifically investigate how tides alter the phase and timing of

features in the GW signal of an eccentric coalescing NS binary. We study binaries with a range of initial pericenter separations and eccentricities to quantify how such dynamical tides affect orbital evolution as a function of eccentricity.

In Section 5.2, we present our model for evolving the NS f-mode and binary orbit. In Section 5.3 we discuss the behavior of the mode-orbit coupling in the absence of relativistic effects. In Section 5.4 we present results of our calculations for binaries with a range of initial pericenter separations and eccentricities, and we conclude in Section 5.5. The Appendix for this chapter contains an analytical assessment of the mode-orbit resonance effect, which we show generally produces a small GW phase shift.

## 5.2 Equations of Motion Including Dynamical Tides and GR Effects

The orbit of a NS binary evolves in response to the tides raised on the NS as well as general relativity (GR). For a binary with a NS (mass  $M_1$  and radius  $R_1$ ) and companion  $M_2$  (either another NS or a BH), the Newtonian gravitational potential produced on  $M_1$  by  $M_2$  is

$$U(\mathbf{r}, t) = -M_2 \sum_{lm} \frac{W_{lm} r^l}{D(t)^{(l+1)}} e^{-im\Phi(t)} Y_{lm}(\phi, \theta), \quad (5.1)$$

where  $\mathbf{r} = (r, \theta, \phi)$  is the position vector in spherical coordinates with respect to the center of mass of  $M_1$ ,  $D(t)$  and  $\Phi(t)$  are respectively the orbital separation and true anomaly, and

$$W_{lm} = (-1)^{(l+m)/2} \left[ \frac{4\pi}{2l+1} (l+m)!(l-m)! \right]^{1/2} \left[ 2^l \left( \frac{l+m}{2} \right)! \left( \frac{l-m}{2} \right)! \right]^{-1}. \quad (5.2)$$

We adopt units such that  $G = c = 1$  throughout the paper. We will focus on the dominant quadrupole tides ( $l = 2$ ), for which  $W_{2\pm 2} = \sqrt{3\pi/10}$ ,  $W_{2\pm 1} = 0$ , and  $W_{20} = \sqrt{\pi/5}$ .

The Lagrangian displacement vector  $\xi(\mathbf{r}, t)$  denotes the fluid perturbation on  $M_1$  driven by the tidal potential. We can decompose  $\xi(\mathbf{r}, t)$  into normal modes  $\xi_\alpha(\mathbf{r}) \propto e^{im\phi}$  of frequencies  $\omega_\alpha$ , where  $\alpha = \{n_r l m\}$  specifies the mode index:

$$\begin{bmatrix} \xi \\ \partial\xi/\partial t \end{bmatrix} = \sum_\alpha c_\alpha(t) \begin{bmatrix} \xi_\alpha(\mathbf{r}) \\ -i\omega_\alpha \xi_\alpha(\mathbf{r}) \end{bmatrix}. \quad (5.3)$$

A freely oscillating mode has  $\xi(\mathbf{r}, t) \propto e^{im\phi-i\omega_\alpha t}$ . This decomposition includes both positive and negative mode frequencies Schenk et al. [2002]. We neglect NS rotation and adopt the convention  $\omega_\alpha > 0$  such that  $m > 0$  corresponds to prograde modes and  $m < 0$  to retrograde modes. The mode amplitude  $c_\alpha(t)$  satisfies

$$\dot{c}_\alpha + i\omega_\alpha c_\alpha = \frac{iM_2 W_{lm} Q_\alpha}{2\omega_\alpha D^{l+1}} e^{-im\Phi}, \quad (5.4)$$

with

$$Q_\alpha \equiv \int d^3x \rho \xi_\alpha^* \cdot \nabla(r^l Y_{lm}). \quad (5.5)$$

In Eqs. (5.4) and (5.5),  $\xi_\alpha$  is normalized such that  $\langle \xi_\alpha, \xi_\alpha \rangle \equiv \int d^3x \rho \xi_\alpha^* \cdot \xi_\alpha = 1$ , and we have adopted the units  $G = M_1 = R_1 = 1$  in these equations, so that  $Q_\alpha$  is dimensionless Lai and Wu [2006], Fuller and Lai [2012a].

The general relativistic equations of motion of compact binaries in eccentric orbits are rather complicated, and even the notion of eccentricity is difficult to define in general relativity [e.g. Blanchet, 2014, Loutrel et al., 2019]. For the purpose of our study, we find it convenient to use the effective one-body PN equations of motion developed by Lincoln and Will [1990] (see also Kidder et al. [1993] for discussion). These equations of

motion contain all PN corrections through (Post)<sup>5/2</sup>-Newtonian order, including effects due to the radiation reaction. We incorporate the tidal effect in the same way as in Fuller and Lai [2011]. Thus, restricting to the  $l = 2$  modes, the orbital evolution equations are

$$\begin{aligned}\ddot{D} = & D\dot{\Phi}^2 - \sum_{\alpha} \frac{3M_t}{D^4} W_{2m} Q_{\alpha} \left( e^{im\Phi} c_{\alpha} + \text{c.c.} \right) \\ & - \frac{M_t}{D^2} \left( 1 + A_{\text{PN}} + A_{5/2} + B_{\text{PN}} \dot{D} + B_{5/2} \ddot{D} \right),\end{aligned}\quad (5.6)$$

$$\begin{aligned}\ddot{\Phi} = & - \frac{2\dot{D}\dot{\Phi}}{D} + \sum_{\alpha} im \frac{M_t}{D^5} W_{2m} Q_{\alpha} \left( e^{im\Phi} c_{\alpha} - \text{c.c.} \right) \\ & - \frac{M_t}{D^2} (B_{\text{PN}} + B_{5/2}) \dot{\Phi},\end{aligned}\quad (5.7)$$

where the sum over  $\alpha$  is restricted to positive mode frequencies (with  $m = \pm 2, 0$ ) and  $M_t = M_1 + M_2$  is the total mass. Throughout this paper, we use the values  $\omega_{\alpha} = 1.22 (M_1/R_1^3)^{1/2}$  and  $Q_{\alpha} = 0.56$ , which correspond the  $l = 2$  f-mode of a  $\Gamma = 2$  polytrope (i.e.  $P \propto \rho^{\Gamma}$ ). In Eqs. (5.6) and (5.7),  $A_{5/2}$  and  $B_{5/2}$  represent the leading-order gravitational radiation reaction forces, and the  $A_{\text{PN}}$  and  $B_{\text{PN}}$  terms are the non-dissipative first and second-

order PN corrections. These coefficients are given by

$$A_{5/2} = -\frac{8\mu}{5D}\dot{D}\left(18v^2 + \frac{2M_t}{3D} - 25\dot{D}^2\right), \quad (5.8)$$

$$B_{5/2} = \frac{8\mu}{5D}\left(6v^2 - \frac{2M_t}{D} - 15\dot{D}^2\right), \quad (5.9)$$

$$\begin{aligned} A_{\text{PN}} = & (1 + 3\eta)v^2 - 2(2 + \eta)\frac{M_t}{D} - \frac{3}{2}\eta\dot{D}^2 \\ & + \frac{3}{4}(12 + 29\eta)\left(\frac{M_t}{D}\right)^2 + \eta(3 - 4\eta)v^4 \\ & + \frac{15}{8}\eta(1 - 3\eta)\dot{D}^4 - \frac{3}{2}\eta(3 - 4\eta)v^2\dot{D}^2 \\ & - \frac{1}{2}\eta(13 - 4\eta)\frac{M_t}{D}v^2 - (2 + 25\eta + 2\eta^2)\frac{M_t}{D}\dot{D}^2, \end{aligned} \quad (5.10)$$

$$\begin{aligned} B_{\text{PN}} = & -2(2 - \eta)\dot{D} - \frac{1}{2}\dot{D}\left[\eta(15 + 4\eta)v^2 \right. \\ & \left. - (4 + 41\eta + 8\eta^2)\frac{M_t}{D} - 3\eta(3 + 2\eta)\dot{D}^2\right], \end{aligned} \quad (5.11)$$

with  $\mu = M_1M_2/M_t$  the reduced mass,  $\eta = \mu/M_t$ , and  $v^2 = \dot{D}^2 + (D\dot{\Phi})^2$ .

Note that while Eqs. (5.6) and (5.7) include gravitational radiation associated with the orbital motion, they do not include gravitational radiation due to the tidally excited oscillation modes. Incorporating the latter effect is complicated by the fact that the orbit and modes can radiate coherently (see Lai [1994] for the circular orbit case where this effect can be included in an approximate way), and is beyond the scope of this paper. Because of this, our results in Section 5.4 underestimate the influence of dynamical tides on the orbital evolution.

The total energy of the system is the sum of the energy in the oscillation modes and the orbital energy, including the interaction between the modes and the gravitational potential. The total energy in stellar oscillations is

$$E_{\text{mode}} = 2 \sum_{\alpha} \omega_{\alpha}^2 |c_{\alpha}|^2, \quad (5.12)$$

where the sum is again restricted to positive mode frequencies. The New-

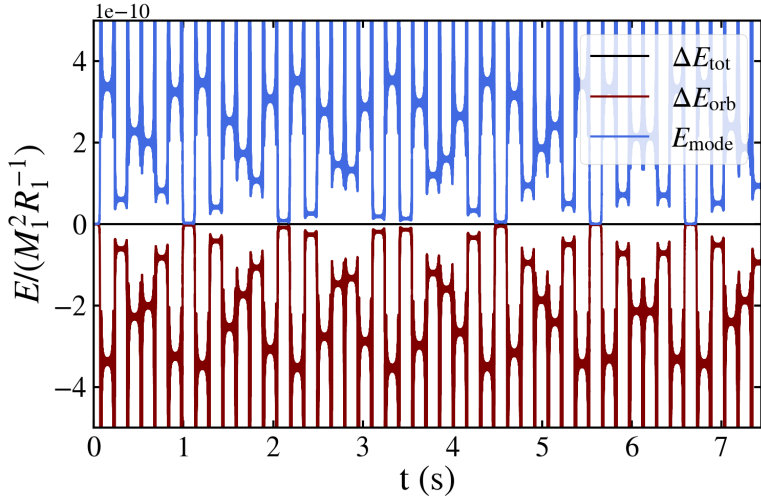


Figure 5.1: The evolution of the mode energy, Eq. (5.12), orbital energy ( $\Delta E_{\text{orb}} = E_{\text{orb}} - E_{\text{orb},0}$ ), Eq. (5.13), and total energy ( $\Delta E_{\text{tot}} = E_{\text{tot}} - E_{\text{tot},0} = E_{\text{mode}} + \Delta E_{\text{orb}}$ ) in units where  $G = M_1 = R_1 = 1$  for a binary with a single NS. We have used a  $\Gamma = 2$  polytrope to model the NS with  $\omega_\alpha = 1.22 (M_1/R_1^3)^{1/2}$  and  $Q_\alpha = 0.56$ . The initial pericenter and eccentricity are  $D_{\text{p},0} = 5.995R_1$  and  $e_0 = 0.9$ , corresponding to  $|\Delta\hat{P}_\alpha| = 1.6 \times 10^{-4}$  (see Eq. 5.15). This calculation does not include GR (i.e.  $A_{5/2} = B_{5/2} = A_{\text{PN}} = B_{\text{PN}} = 0$ ). The  $l = 2$ ,  $m = (2, 0, -2)$  f-modes are all accounted for in the integration. The peaks occur during pericenter passages. The mode energy away from pericenter undergoes small-amplitude oscillations over multiple orbits.

tonian expression for the orbital energy is

$$E_{\text{orb}} = -\frac{\mu M_t}{D} + \frac{\mu}{2} (\dot{D}^2 + D^2 \dot{\Phi}^2) - \mu M_t \sum_\alpha \frac{W_{2m} Q_\alpha}{D^3} (\text{e}^{im\Phi} c_\alpha + \text{c.c.}) \quad (5.13)$$

When GR effects are neglected (i.e.  $A_{\text{PN}} = B_{\text{PN}} = A_{5/2} = B_{5/2} = 0$ ), the total energy  $E_{\text{tot}} = E_{\text{orb}} + E_{\text{mode}}$  is conserved.

### 5.3 Orbit and Mode Evolution without GR

Before studying coalescing binaries using the full equations from Section 5.2, we consider in this section the “mode + orbit” problem without GR

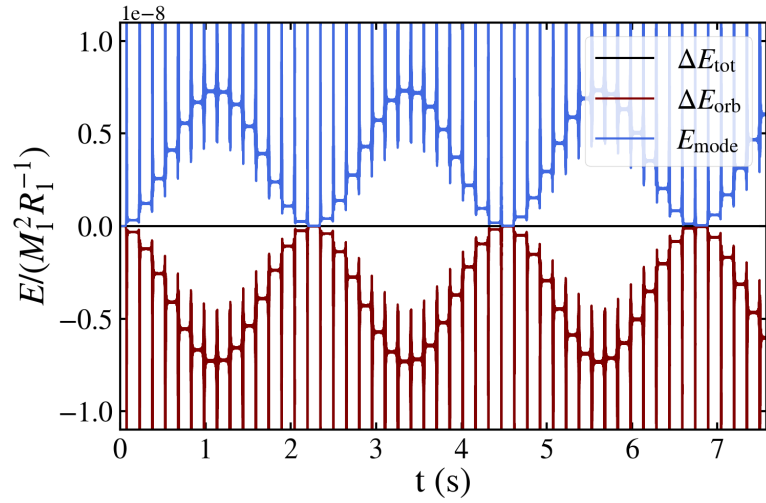


Figure 5.2: Same as Fig. 5.1, but with an initial pericenter distance of  $D_{p,0} = 6R_1$  and  $|\Delta\hat{P}_\alpha| = 1.5 \times 10^{-4}$ . The mode energy (away from the peaks at pericenter passages) can reach larger values than in Fig. 5.1 due to a resonance between the mode frequency and the orbital frequency ( $\omega_\alpha \simeq 401\Omega_{\text{orb}}$ ).

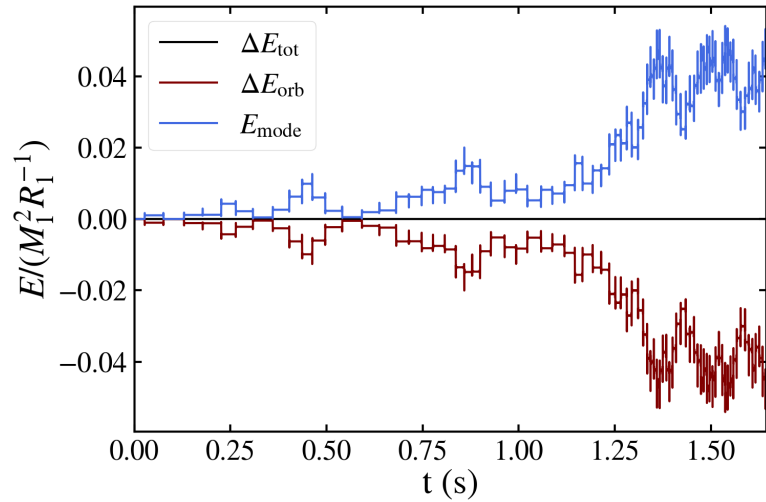


Figure 5.3: Same as Fig. 5.1, but with a smaller initial pericenter distance of  $D_{p,0} = 3R_1$  so that  $|\Delta\hat{P}_\alpha| = 82$ . The mode energy grows chaotically over many orbits.

(i.e. we set  $A_{\text{PN}} = B_{\text{PN}} = A_{5/2} = B_{5/2} = 0$ ). Previous studies of dynamical tides in a variety of astrophysical situations Mardling [1995a], Lai [1996b], Ivanov and Papaloizou [2004a], Vick and Lai [2018], Wu [2018], Vick and Lai [2019a] have demonstrated that the coupled evolution of the eccentric orbit and tidally driven oscillation modes can yield different behaviors depending on the binary orbital properties. We briefly discuss how the binary pericenter distance  $D_p$  and eccentricity  $e$  affect the interaction between the orbit and the oscillation modes. For a more thorough analysis, see Section 2 of Vick and Lai [2018].

For a NS in an eccentric binary, the  $l = 2$  f-mode is excited most strongly at pericenter, and the mode amplitude changes by the real quantity  $\Delta c_\alpha$  (see Eq. 10 of Vick and Lai [2018]) during each pericenter passage, transferring energy and angular momentum between the orbit and the NS f-mode. When the binary is highly eccentric, the shape of the NS orbit near pericenter is unchanged over many orbits, and  $\Delta c_\alpha$  remains constant over multiple pericenter passages. We can relate  $\Delta c_\alpha$  to a change in the mode energy in the “first” passage (i.e. when there is no pre-existing mode oscillation)

$$\Delta E_{\text{mode}} = 2 \sum_\alpha \omega_\alpha^2 (\Delta c_\alpha)^2. \quad (5.14)$$

As the mode energy changes, so too will the orbital energy, causing a slight adjustment,  $|\Delta P|$ , in the initial orbital period (initially  $P_0$ ). We define

$$|\Delta \hat{P}_\alpha| \equiv \omega_\alpha |\Delta P| \simeq \frac{3}{2} \omega_\alpha P_0 \left( \frac{\Delta E_{\text{mode}}}{|E_{\text{orb},0}|} \right), \quad (5.15)$$

where  $E_{\text{orb},0}$  is the initial orbital energy. Physically,  $|\Delta \hat{P}_\alpha|$  is the phase shift in the mode oscillation due to tidal energy transfer at pericenter. The phase shift is largest for binaries with strong tidal interactions (small  $D_p$ ) and large orbital periods (high  $e$ ).

In the absence of mode damping and GR, the properties  $|\Delta\hat{P}_\alpha|$  and  $\omega_\alpha P_0$  determine the behavior of the “mode + eccentric orbit” system over multiple orbits. The system exhibits three types of behavior:

1. When  $|\Delta\hat{P}_\alpha| \lesssim 1$ , the orbit and the f-mode oscillations gently trade a small amount of energy (of order  $\Delta E_{\text{mode}}$ ) back and forth, as shown in Fig. 5.1.
2. When  $|\Delta\hat{P}_\alpha| \lesssim 1$  and  $\omega_\alpha P_0 = 2\pi n$  (with integer  $n$ ), the mode exhibits resonant behavior, with the mode energy climbing to  $E_{\text{mode}} \gg \Delta E_{\text{mode}}$ , but still undergoing oscillations (see Fig. 5.2).
3. When  $|\Delta\hat{P}_\alpha| \gtrsim 1$ , the mode energy grows chaotically and can reach an appreciable fraction of the NS binding energy (see Fig. 5.3). This behavior occurs because the pericenter energy transfer changes the orbital period enough that the phase of the f-mode at pericenter is nearly random from one orbit to the next. The chaotic mode growth resembles a diffusive process, except there exists an “upper floor” that the mode energy can attain. Note that the linear mode treatment is no longer appropriate when the f-mode energy becomes too large.

A highly eccentric NS binary may pass through the regimes for all three behaviors — low-amplitude oscillations, resonance, and chaotic growth — as gravitational radiation shrinks the orbit. However, as we shall see in Section 5.4 (see also the Appendix), because of the rapid orbital decay, these behaviors may not manifest as prominently as in the case of non-dissipative systems.

## 5.4 Orbit and Mode Evolution Including GR

We have integrated Eqs. (5.4), (5.6), and (5.7) for coalescing NS binaries on initially eccentric orbits and compared the results with integrations that do not include tidal effects [ $c_\alpha(t) = 0$ ]. Our goal is to quantify how tides affect the orbital evolution of a coalescing NS binary and the resulting gravitational waveform.

A sample integration is shown in Fig. 5.4 for an equal mass  $M_1 = M_2 = 1.4M_\odot$ ,  $R_1 = R_2 = 10$  km NS binary with initial pericenter distance  $D_{\text{p},0} = 6R_1$  and initial eccentricity  $e_0 = 0.9$ . At time  $t = 0$ , the NSs are at apocenter with separation  $D_0 = D_{\text{p},0}(1 + e_0)/(1 - e_0)$ , and  $E_\alpha = 0$  for both NSs, i.e., there is no energy in the f-mode. We define  $e_0$  in terms of the ratio of the initial angular velocity,  $\dot{\Phi}_0$ , to  $\dot{\Phi}_{\text{circ},0}$ , the angular velocity required to maintain a circular orbit with radius  $D_0$  (in the absence of tidal effects and gravitational radiation) such that

$$\sqrt{1 - e_0} \equiv \frac{\dot{\Phi}_0}{\dot{\Phi}_{\text{circ},0}}. \quad (5.16)$$

We obtain  $\dot{\Phi}_{\text{circ},0}$  by solving Eq. (5.6) for  $\dot{\Phi}(t = 0)$  using  $D(0) = D_0$  and  $\dot{D}(0) = \ddot{D}(0) = c_\alpha(0) = 0$ . The GW frequency at the initial pericenter passage is

$$f_{\text{p},0} = \frac{1}{\pi} \sqrt{\frac{M_t(1 + e_0)}{a_0(1 - e_0)^3}}. \quad (5.17)$$

For our sample system,  $f_{\text{p},0} = 575$  Hz. We stop the integration when the binary separation  $D(t)$  becomes smaller than  $2.5R_1$ . The time when a system reaches this criterion is labeled  $t_{\text{merg}}$ .

Comparison of the calculations with and without tides reveals that tides typically speed up the binary coalescence (see Fig. 5.4). The difference in

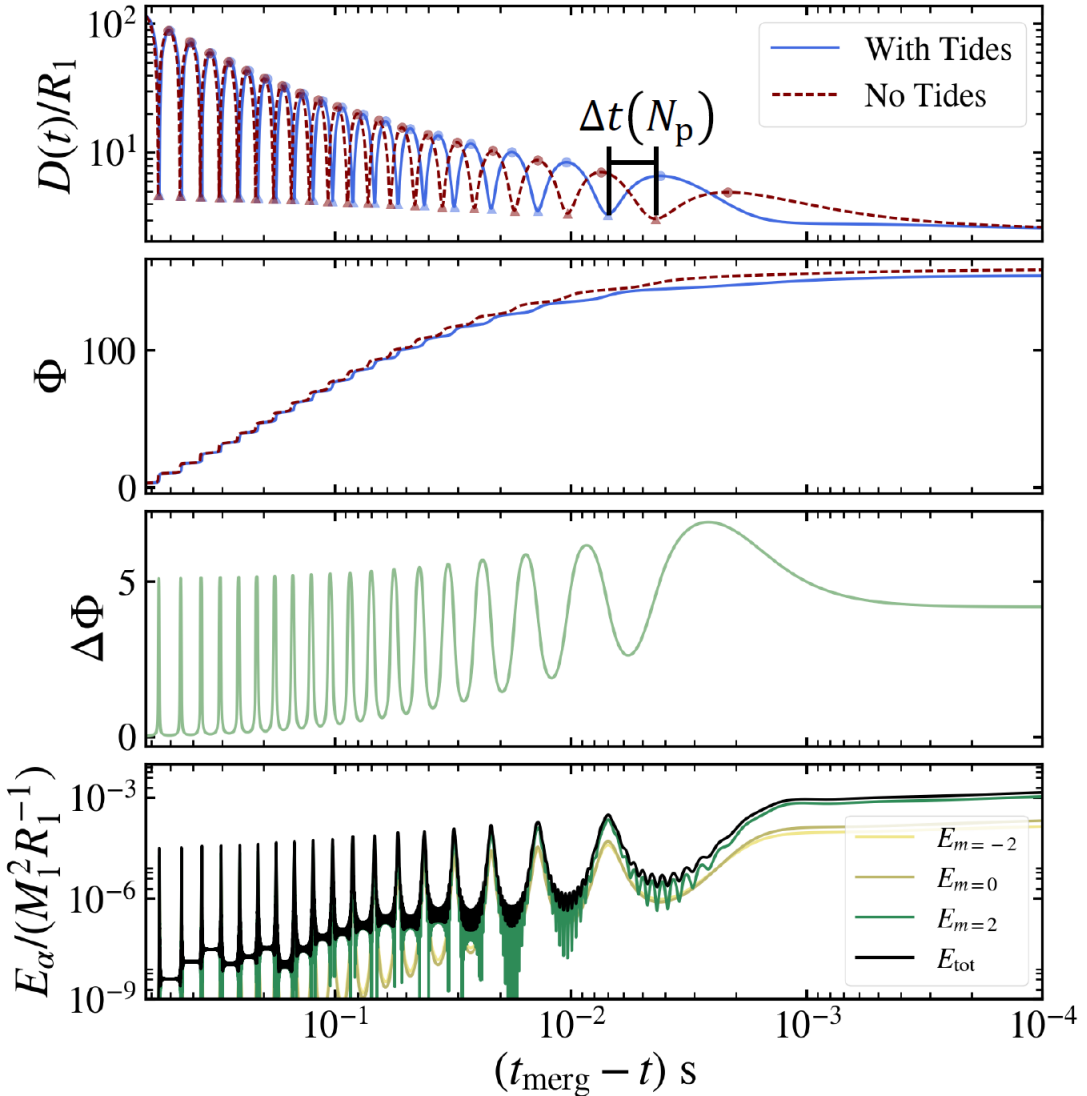


Figure 5.4: An example of how f-mode oscillations alter the orbital evolution of a coalescing, eccentric NS binary with  $M_1 = M_2 = 1.4M_\odot$  and  $R_1 = R_2 = 10$  km. The NSs are modeled as  $\Gamma = 2$  polytropes. This system has initial eccentricity  $e_0 = 0.9$  and pericenter distance  $D_{p,0} = 6R_1$ , corresponding to a GW pericenter frequency of  $f_{p,0} = 575$  Hz. The solid blue lines in the top two panels show the binary separation and orbital phase (true anomaly) including tidal effects, while the dashed red lines show the same without tides. The blue (red) circles and triangles mark the times of apocenter and pericenter. The quantity  $\Delta t(N_p)$  is defined as the difference in the timing of a pericenter passage for calculations with and without tides, where  $N_p$  is the number of pericenter passages prior to merger, i.e. the example in the top panel shows  $\Delta t(N_p = 1)$ . The third panel shows  $\Delta\Phi$ , the difference in the orbital phase for calculations with and without dynamical tides (see Eq. 5.18). The bottom panel shows the evolution of the mode energies; the  $m = 2$  (prograde) mode dominates.

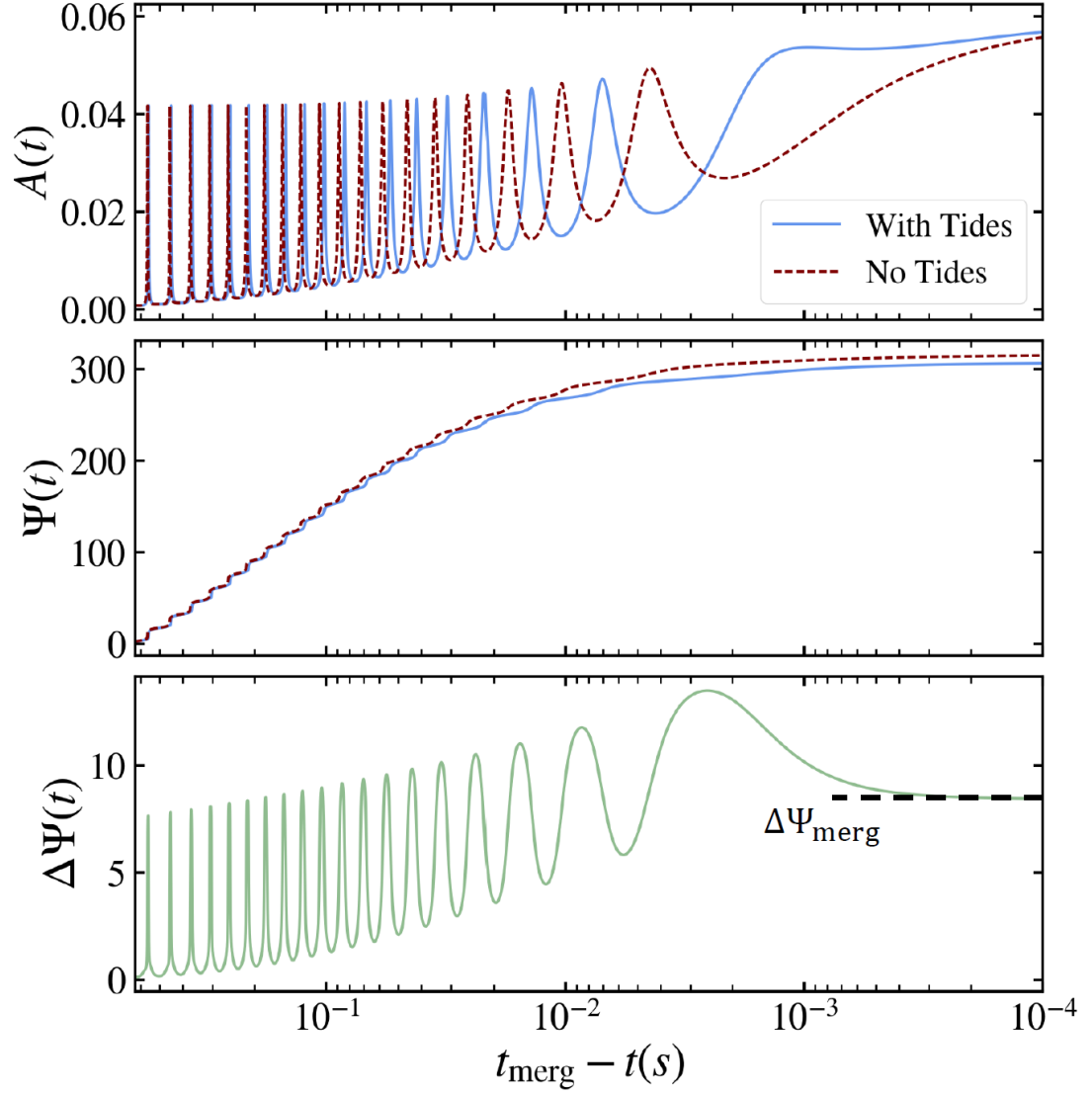


Figure 5.5: The gravitational waveform (Eq. 5.23) that corresponds to the orbital evolution shown in Fig. 5.4. The amplitude is scaled by  $(R_1/d)$ , with  $d$  the distance to the system. The bottom panel shows the difference in the phase of the GWs,  $\Delta\Psi(t)$ , for a calculation with dynamical tides and one without (Eq. 5.24).

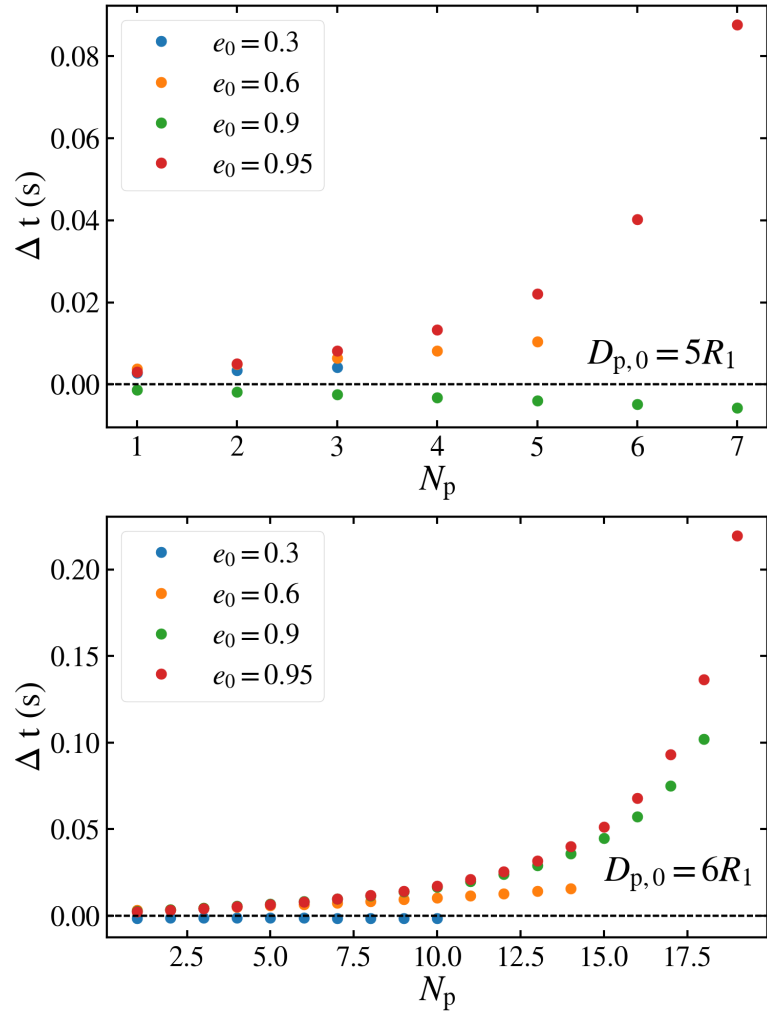


Figure 5.6: Cumulative time advance due to dynamical tides [see the top panel of Fig. 5.4 for the definition of  $\Delta t(N_p)$ , where  $N_p$  is the number of pericenter passages prior to merger] as a function of the number of orbits for equal mass NS binaries with an initial pericenter distance of  $D_{p,0} = 5R_1$  in the left panel and  $D_{p,0} = 6R_1$  in the right panel.

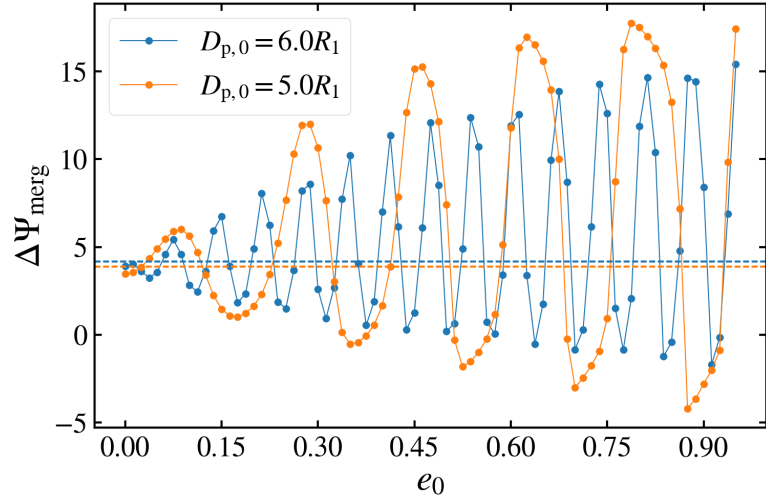


Figure 5.7: Cumulative GW phase difference between a calculation with dynamical tides and without at  $t_{\text{merg}}$  (the time when  $D = 2.5R_1$ ) as a function of initial eccentricity  $e_0$  for two different values of the initial pericenter distance (see Fig. 5.5). The two dashed lines show the result for circular orbits (see Eq. 5.26).

phase traversed before merger (related to the number of orbits completed between  $t = 0$  and  $t = t_{\text{merg}}$ ) is

$$\Delta\Phi(t) = \Phi_{\text{Ntide}}(t) - \Phi_{\text{tide}}(t), \quad (5.18)$$

where  $\Phi_{\text{tide}}(t)$  [ $\Phi_{\text{Ntide}}$ ] is the orbital phase at time  $t$  for a calculation that includes [does not include] tidal effects. For the example depicted in Fig. 5.4, we see that  $\Delta\Phi$  reaches 4 radians, mostly accumulated in the last  $\sim 10$  ms prior to merger. The mode energy (Eq. 5.12) approaches  $\sim 10^{-3}$  of the NS binding energy ( $M_1^2/R_1$ ) and is dominated by the  $m = 2$  prograde mode.

To understand how tidal effects influence the GW signal, we calculate the waveform assuming that the binary is “face-on.” The components of the strain,  $h_+$  and  $h_\times$ , are given by

$$h_+ = \frac{1}{d}(\ddot{I}_{xx} - \ddot{I}_{yy}), \quad h_\times = \frac{2}{d}\ddot{I}_{xy}, \quad (5.19)$$

where  $I_{xx}$ ,  $I_{yy}$ , and  $I_{xy}$  are components of the quadrupole moment tensor

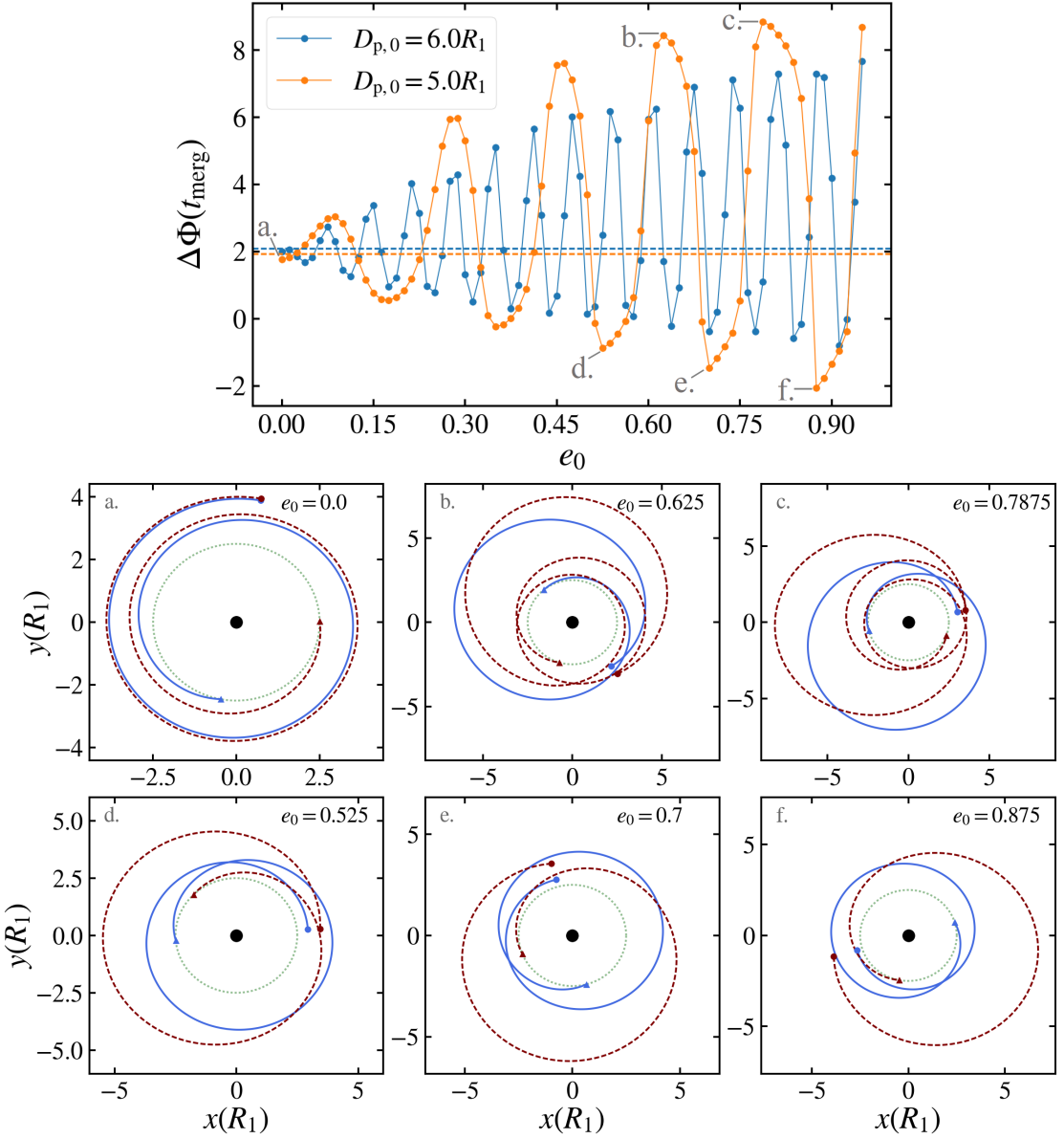


Figure 5.8: The upper panel is the same as in Fig. 5.7 with the orbital phase rather than the gravitational phase. The lower panels show the final few orbits for calculations with (blue solid lines) and without (red dashed lines) dynamical tides for binaries with  $D_{p,0} = 5.0R_1$  and values of  $e_0$  that maximize (b. and c.) or minimize (d., e., and f.)  $\Delta\Phi_{\text{merg}}$ . The dotted green circles indicate  $D = 2.5R_1$ .

(the  $xy$  coordinates are defined in the orbital plane), and  $d$  is the distance to the system. Neglecting the quadrupole moment contributions from the oscillation modes, we have

$$I_{xx} = \mu D^2 \cos^2 \Phi, \quad I_{yy} = \mu D^2 \sin^2 \Phi, \quad I_{xy} = 2\mu D^2 \sin 2\Phi. \quad (5.20)$$

The waveform is given by

$$h_+ = \frac{2\mu}{d} \left( \dot{D}^2 \cos 2\Phi + D\ddot{D} \cos 2\Phi - 4D\dot{D}\dot{\Phi} \sin 2\Phi - 2D^2\dot{\Phi}^2 \cos 2\Phi - D^2\ddot{\Phi} \sin 2\Phi \right), \quad (5.21)$$

$$h_\times = \frac{2\mu}{d} \left( \dot{D}^2 \sin 2\Phi + D\ddot{D} \sin 2\Phi + 4D\dot{D}\dot{\Phi} \cos 2\Phi - 2D^2\dot{\Phi}^2 \sin 2\Phi + D^2\ddot{\Phi} \cos 2\Phi \right). \quad (5.22)$$

We can combine  $h_+$  and  $h_\times$  to form a complex strain with amplitude  $A$  and phase  $\Psi$ ,

$$A e^{-i\Psi(t)} = h_+ - i h_\times. \quad (5.23)$$

Figure 5.5 shows the waveform that corresponds to the orbital evolution depicted in Fig. 5.4. The bottom panel shows the phase difference due to dynamical tides:

$$\Delta\Psi(t) = \Psi_{\text{Ntide}}(t) - \Psi_{\text{tide}}(t). \quad (5.24)$$

Note that  $\Delta\Psi(t) \sim 2\Delta\Phi(t)$ , as one would expect from the form of Eqs. (5.21) and (5.22). The spikes in  $\Delta\Psi(t)$  occur as the system passes through pericenter. In the final stages of orbital decay and circularization,  $\Delta\Psi$  quickly climbs. We label the value of  $\Delta\Psi$  when  $D = 2.5R_1$  as  $\Delta\Psi_{\text{merg}}$  (see the bottom panel of Fig. 5.5).

Because the orbit is initially very eccentric, the orbital frequency sweeps through many (of order 10's of) resonances with the f-mode throughout orbital decay. The resonances occur when  $\omega_\alpha = n\Omega_{\text{orb}}$  for integer  $n$  (see

Section 5.3). However, because of the rapid orbital decay and the large  $n$  values involved, we do not see discrete resonant excitation of the mode amplitude (see Appendix). The orbital phase  $\Phi$  does not suddenly increase when  $\omega_\alpha = n\Omega_{\text{orb}}$ <sup>1</sup>.

We now quantify how the tidal effects on the waveform depend on  $e_0$  and  $D_{p,0}$ . Fig. 5.6 shows  $\Delta t(N_p)$  (see the top panel of Fig. 5.4) as a function of the number of pericenter passages prior to merger,  $N_p$ , for two different values of  $D_{p,0}$  and a handful of values for  $e_0$ . In general, a large value of  $e_0$  can produce the largest timing shift for a given  $D_{p,0}$ . For some values of  $e_0$ ,  $\Delta t$  is negative, corresponding to a binary where the pericenter passage occurs closer to merger when tides are considered (see below). For a smaller  $D_{p,0}$ , the time advance can accumulate in fewer orbits. For example, for  $D_{p,0} = 5R_1$  and  $e_0 = 0.95$ ,  $\Delta t$  can reach 80 ms in seven orbits, while for the same  $e_0$  and  $D_p = 6R_1$ , more than sixteen orbits are required to reach the same  $\Delta t$ .

We can also examine how the cumulative phase shift just before merger  $\Delta\Psi_{\text{merg}}$  (see Fig. 5.5, lower panel) varies as a function of the initial eccentricity  $e_0$ . While  $\Delta t(N_p)$  mainly captures the effect of tides on orbital precession,  $\Delta\Psi_{\text{merg}}$  is a combination of the tidal influence on both the precession rate and the orbital decay rate. Fig. 5.7 shows that the excitation of the f-mode has the largest effect on systems that are highly eccentric and have small pericenter distances.

Note that systems with larger  $e_0$  do not fully circularize before  $D = 2.5R_1$ . As a result,  $\Delta\Psi_{\text{merg}}$  has a significant dependence on the orbital phase at merger. This effect is visible in the large oscillations in  $\Delta\Psi_{\text{merg}}$  as a function of  $e_0$ . Fig. 5.8 depicts the orbit calculations for systems at the extrema of

---

<sup>1</sup>This behavior is different from the circular orbit case, where resonance with a low-frequency g-mode or r-mode occurs when  $\omega_\alpha = 2\Omega_{\text{orb}}$  (see Xu and Lai [2017] and references therein).

the  $\Delta\Phi_{\text{merg}}$  vs.  $e_0$  curve to illustrate the reason for these oscillations. In general, dynamical tides remove energy from the binary orbit and enhance the rate of orbital decay. For a given  $\Phi(t)$ , the orbit-averaged separation (a similar concept to the semi-major axis) is always smaller for a calculation that includes dynamical tides than for one that does not. This is clearest in the circular case [see panel (a) of Fig. 5.8], where the binary separation is always slightly smaller in the calculation that includes tides. For eccentric binaries, the binary separation at merger ( $D = 2.5R_1$ ) can be significantly different from the orbit-averaged separation. Some binaries meet the condition for merger at pericenter and merge early at smaller  $\Phi(t)$  and wider orbit-averaged separations than  $2.5R_1$ . Others meet the merger condition at apocenter and merge late at larger  $\Phi(t)$ . The maxima (minima) in the oscillations of  $\Delta\Phi_{\text{merg}}$  vs.  $e_0$  occur when the calculation with tides results in merger at a relatively wide (tight) orbit while the calculation without tides leads to a merger at a tighter (wider) orbit. Panels (b) and (c) of Fig. 5.8 show calculations where  $\Delta\Phi_{\text{merg}}$  is maximized. Note that the final orbit with dynamical tides (blue solid line) is wider than the final orbit without dynamical tides (red dashed line) in these panels. Panels (d), (e), and (f) correspond to binaries where  $\Delta\Phi_{\text{merg}}$  is negative. For these systems, the final orbits are significantly wider for the calculations without dynamical tides than for those with tides included.

For small  $e_0$ , we can compare our  $\Delta\Psi_{\text{merg}}$  with the analytical result of the GW phase shift due to tides. From Eq. (66) of Lai et al. [1994b], the GW phase shift due to the tidal distortion of  $M_1$  (induced by  $M_2$ ) as the binary decays from a semi-major axis of  $a_i$  to  $a_f$  is

$$\Delta\Psi = \frac{3}{16}\kappa_n q_n \frac{R_1^5}{M_1^2 M_t^{1/2}} \left( a_f^{-5/2} - a_i^{-5/2} \right) \left( \frac{39}{4} + \frac{M_t}{M_2} \right), \quad (5.25)$$

where  $q_n = (1 - n/5)\kappa_n$ , and  $\kappa_n$  is defined in Eq. (8) of Lai et al. [1994b]<sup>2</sup>.

For a  $\Gamma = 2$  polytrope,  $q_n = 4\kappa_n/5$  and  $\kappa_n = 0.66$ . The term proportional to  $(M_t/M_2)$  in Eq. (5.25) is due to the gravitational emission of the tidally forced f-mode. Our calculations do not account for this effect. Thus, for comparison with our numerical results, we use

$$\Delta\Psi' = \frac{117}{64}\kappa_n q_n \frac{R_1^5}{M_1^2 M_t^{1/2}} (a_f^{-5/2} - a_i^{-5/2}), \quad (5.26)$$

which does not include GW emission associated with the mode. From Fig. 5.7, our results for small  $e_0$  are in agreement with the predicted value of  $\Delta\Psi_{\text{merg}}$  from Eq. (5.26). Note that, using Eq. 64 of Lai et al. [1994b],

$$\Omega_{\text{orb}} = \left(\frac{M_t}{a^3}\right)^{1/2} \left[1 + \frac{9}{4} \frac{\kappa_n q_n M_2}{M_1} \left(\frac{R_1}{a}\right)^5\right], \quad (5.27)$$

Eq. (5.25) is equivalent to

$$\frac{d\Psi}{d \ln f} = \frac{d\Psi_{\text{Ntide}}}{d \ln f} \left[1 - 3\kappa_n q_n \left(\frac{R_1}{a}\right)^5 \left(\frac{11M_2}{M_1} + \frac{M_t}{M_1}\right)\right], \quad (5.28)$$

where  $d\Psi_{\text{Ntide}}/d \ln f$  corresponds to the GW phase evolution without tidal effects. Equation (5.28) is the same as the expression derived in Flanagan and Hinderer [2008].

We have only presented results for an equal mass NS-NS binary, where tidal effects in both bodies contribute to the GW phase shift. In a NS-BH binary only the NS tidal response affects the GW phase shift. A NS-BH binary will have a larger mass ratio than a NS-NS binary. From Eq. (5.26), the GW phase shift from a coalescing circular binary is smaller for a system with a larger mass ratio. We expect that  $\Delta\Psi_{\text{merg}}$  for a NS-BH binary will exhibit similar oscillations with the initial orbital eccentricity as in Fig. 5.7, but with smaller amplitude and about a smaller value of  $\Delta\Phi(t_{\text{merg}})$ .

---

<sup>2</sup>The usual tidal Love number is given by  $k_2 = (3/2)\kappa_n q_n$ .

## 5.5 Discussion

We have demonstrated that dynamical tides (i.e. tidal excitations of NS f-modes) can have a significant effect on the orbits and therefore the GW signals from eccentric CO binaries with at least one NS. We have developed a model that couples the evolution of the NS f-mode with 2.5PN orbital evolution to track changes in the “f-mode+eccentric orbit” system as the orbit circularizes and moves toward coalescence. This model can be readily applied to a NS-NS binary or a BH-NS binary. The primary difference between the two types of binaries In general, the transfer of energy from the orbit to the f-mode speeds up the orbital decay and advances the phase of the GW signal. We have used our model to quantify how the f-mode excitation affects the timing of peaks in the GW signal as the binary moves toward coalescence for systems with a range of initial pericenter distances and eccentricities. We have found that systems with large eccentricities (for a given pericenter) may experience GW phase shifts due to tides that are nearly an order of magnitude larger than the phase shift produced by a circular merger (see Fig. 5.7).

Although the event rate of eccentric CO binary mergers with a NS is highly uncertain, such systems could offer a wealth of information on the equation of state of NSs. Observing these systems is complicated by fact that quasi-circular waveform templates cannot efficiently extract the inspiral of a highly eccentric CO binary Brown and Zimmerman [2010]. A matched-filtering search would require a reliable calculation of the GW signal throughout inspiral, merger, and ringdown. Alternative search methods have been developed in Coughlin et al. [2015], Tiwari et al. [2016], Lower et al. [2018]. Eccentric NS binary coalescence may be observable

with third generation detectors Papenfort et al. [2018], Chaurasia et al. [2018]. With some refinements, our model could be used to predict the timing of pericenter passages in eccentric NS binaries. To do this, our model would need to be modified to include the effects of NS spin, f-mode damping due to gravitational emission, and most importantly higher order PN effects. In particular, gravitational radiation associated with the tidally excited f-mode is coherent with the orbit, and can lead to a GW phase shift that is comparable to that from f-mode excitation (as computed in this paper). Therefore, our results provide a minimum expected phase shift due to dynamical tides in eccentric NS binaries.

# CHAPTER 6

## TIDAL EVOLUTION OF ECCENTRIC BINARIES DRIVEN BY CONVECTIVE TURBULENT VISCOSITY

Accepted for Publication in:

M. Vick and D.Lai. Tidal Evolution of Eccentric Binaries Driven by Convective Turbulent Viscosity. *MNRAS*, 2020.

### 6.1 Introduction

Tidal dissipation shapes a variety of astrophysical binaries, causing spin synchronization of the two bodies as well as orbital decay and circularization. For example, the evolution of a stellar binary toward a common envelope episode (CEE) is affected by tides. A CEE occurs when a binary system shares a gaseous envelope. The embedded system experiences drag forces that tighten the binary orbit [e.g. Paczynski, 1976, van den Heuvel, 1976]. Many astronomical transients are believed to originate from systems that have experienced a CEE [Belczynski et al., 2002a, Dominik et al., 2012, Belczynski et al., 2018]. Some transients may be directly associated with a CEE, e.g., recent work has suggested that luminous red novae may be caused by the ejection of a common envelope [Ivanova et al., 2013, MacLeod et al., 2017, Blagorodnova et al., 2017]. A CEE can also account for the formation of compact double neutron star or black hole binaries, whose ultimate coalescence is detectable with LIGO/Virgo [e.g. Bhattacharya and van den Heuvel, 1991, Belczynski et al., 2002b, Tauris and van den Heuvel, 2006, Dominik et al., 2012, Vigna-Gómez et al., 2018]. In many cases, the onset and outcome of a CEE may depend on the orbital

configuration of the binary when one component, a compact star, makes contact with the expanded convective envelope of the other component, a giant star. Because the pre-CEE binary can have a rather eccentric orbit, the strength of tidal dissipation in the convective envelope compared with the timescale for radius expansion of the giant star determines the orbit of the binary at the start of a CEE.

Tidal dissipation in a convective envelope can be also be important in binaries containing solar-type stars. Previous works have studied and compared different dissipation mechanisms within these stars. In the convective envelope, fundamental and inertial oscillation modes dissipate due to turbulent viscosity, while radiative diffusion operates in the stellar interior [e.g. Zahn, 1977, Goodman and Oh, 1997, Goodman and Dickson, 1998, Savonije and Witte, 2002, Ogilvie and Lin, 2007]. In some cases, internal gravity waves excited at the radiative-convective boundary grow in amplitude as they travel toward the center until non-linear wave-breaking dissipates the energy and angular momentum in the wave [Goodman and Dickson, 1998, Barker and Ogilvie, 2010, 2011, Chernov et al., 2013, Ivanov et al., 2013, Bolmont and Mathis, 2016, Weinberg et al., 2017, Sun et al., 2018]. This effect can drive rapid orbital decay. However, when the internal gravity waves do not achieve nonlinearity, turbulent viscosity in the convective envelope is often the dominant mechanism of tidal dissipation.

A large body of work has studied the dissipation of equilibrium tides in the convective envelope of a star. An analytical treatment was first developed by Zahn [1977], using an eddy viscosity  $\nu_0 \sim v_H l / 3$ , where  $l \sim H$  is the length-scale of the largest convective eddies and  $v_H \sim (F/\rho)^{1/3}$  is the convective velocity on scale  $H$  ( $H$  is the pressure scale height,  $F$  the

convective flux, and  $\rho$  the density). However, when the timescale of tidal forcing is shorter than the eddy turnover time,  $\tau_{\text{eddy}} = H/v_H$ , convective eddies cannot efficiently transport energy and momentum. Zahn [1989] proposed that, in this case, the viscosity should be reduced by a linear factor of  $(\omega\tau_{\text{eddy}})^{-1}$ , where  $\omega$  is the tidal forcing frequency. In contrast, Goldreich and Nicholson [1977] suggested that the viscosity reduction should scale with  $(\omega\tau_{\text{eddy}})^{-2}$ . Recently, numerical and analytical studies have supported a quadratic reduction factor [Penev and Sasselov, 2011, Penev et al., 2011, Ogilvie and Lesur, 2012, Duguid et al., 2019]. A few have even discovered negative viscosities at high forcing frequencies [Ogilvie and Lesur, 2012, Duguid et al., 2019].

While many previous studies have explored the effect of convective viscous dissipation on binaries in circular orbits, very few have considered the effect of frequency dependent viscosity reduction for highly eccentric binaries. A star on an eccentric orbit experiences multiple tidal forcing frequencies; the more eccentric the orbit, the wider the tidal frequency spectrum becomes. Ivanov and Papaloizou [2004b] studied how different prescriptions for viscosity reduction affect the orbital evolution of a binary with a fully convective primary (e.g. a low-mass star or planet). They found that when the viscosity reduction scales more steeply than  $(\omega\tau_{\text{eddy}})^{-1}$ , the orbital evolution of the system can change drastically.

In this paper, we study the effects of tidal dissipation due to convective turbulent viscosity in an eccentric binary. We consider both giant branch (GB) stars and solar-type stars, although our method can be applied to other types of stars with convective envelopes. In Section 6.2, we develop a general formalism for tidal evolution in an eccentric binary, accounting

for frequency dependent damping of tidally excited oscillations. We relate this formalism to the standard weak friction treatment of the equilibrium tide [Darwin, 1880, Alexander, 1973, Hut, 1981]. In Section 6.3 we introduce two stellar models (a GB model and a solar-type model) and discuss the effects of frequency dependent viscosity reduction in both. In Section 6.4 we present results for the tidal energy and angular momentum transfer rates for both stellar models as a function of the binary orbital parameters. In Section 6.5 we discuss an alternative (and simpler) calculation of the transfer rates in the case of highly eccentric ( $\gtrsim 0.8$ ) binaries before concluding in Section 6.6.

## 6.2 Tides and Dissipation in Eccentric Binaries: General Formalism

Consider a primary star with mass  $M_1$  and radius  $R_1$  in an orbit with semi-major axis  $a$  and eccentricity  $e$  about a secondary star,  $M_2$ . We study tidal dissipation in the convective envelope of the primary, neglecting the tide in the secondary.

In an inertial frame, the quadrupolar ( $l = 2$ ) tidal potential produced by  $M_2$  is

$$U(\mathbf{r}, t) = -GM_2 \sum_m \frac{W_{2m} r^2}{D^3} e^{-im\Phi(t)} Y_{2m}(\theta, \phi_i), \quad (6.1)$$

where  $\mathbf{r} = (r, \theta, \phi_i = \phi + \Omega_s t)$  is the position vector in spherical coordinates relative to the center of mass of the primary star, and the angle  $\phi$  is measured in the rotating frame of  $M_1$ , which rotates with frequency  $\Omega_s$ . Throughout this paper, we assume that the spin axis of the star is

aligned with the orbital angular momentum axis [see, e.g., Lai and Wu, 2006, for the gravitational potential of  $M_2$  if the spin axis and orbital axis are misaligned.] The time-varying binary separation is  $D(t)$ , and  $\Phi(t)$  is the orbital true anomaly. Only the  $m = 0, \pm 2$  terms are nonzero, with  $W_{20} = \sqrt{\pi/5}$  and  $W_{2\pm 2} = \sqrt{3\pi/10}$ . The potential can be decomposed into terms with frequencies that are integer multiples of the orbital frequency,  $\Omega = [G(M_1 + M_2)a^{-3}]^{1/2}$ . In the rotating frame of the primary, we have

$$U(\mathbf{r}, t) = - \sum_m \sum_{N=-\infty}^{\infty} U_{Nm} r^2 Y_{2m}(\theta, \phi) e^{-i\omega_{Nm}t}, \quad (6.2)$$

where

$$U_{Nm} \equiv \frac{GM_2}{a^3} W_{2m} F_{Nm}, \quad (6.3)$$

$$\omega_{Nm} \equiv N\Omega - m\Omega_s, \quad (6.4)$$

with  $F_{Nm}$  defined by the expansion

$$\left(\frac{a}{D}\right)^3 e^{-im\Phi(t)} = \sum_{N=-\infty}^{\infty} F_{Nm} e^{-iN\Omega t}, \quad (6.5)$$

and given by

$$F_{Nm} = \frac{1}{\pi} \int_0^\pi d\Psi \frac{\cos[N(\Psi - e \sin \Psi) - m\Phi(t)]}{(1 - e \cos \Psi)^2}, \quad (6.6)$$

where  $\Psi$  is the eccentric anomaly.

The linear response of  $M_1$  is specified by the Lagrangian displacement vector,  $\xi(\mathbf{r}, t)$ , which satisfies the equation of motion

$$\frac{\partial^2 \xi}{\partial t^2} + 2\boldsymbol{\Omega}_s \times \frac{\partial \xi}{\partial t} + \mathbf{C} \cdot \xi = -\nabla U, \quad (6.7)$$

in the rotating frame of the primary, where  $\mathbf{C}$  is a self-adjoint operator that contains the restoring forces acting on the perturbation. We can decompose the Lagrangian displacement into a sum of eigenmodes  $\xi_\alpha(\mathbf{r})$  of

frequency  $\omega_\alpha$  (where  $\alpha$  specifies the mode indices, which include the degree,  $l$ , and azimuthal index,  $m$ ) such that [Schenk et al., 2002, Lai and Wu, 2006]

$$\begin{bmatrix} \boldsymbol{\xi} \\ \partial\boldsymbol{\xi}/\partial t \end{bmatrix} = \sum_{\alpha} c_{\alpha}(t) \begin{bmatrix} \boldsymbol{\xi}_{\alpha}(\mathbf{r}) \\ -i\omega_{\alpha}\boldsymbol{\xi}_{\alpha}(\mathbf{r}) \end{bmatrix}, \quad (6.8)$$

where  $\omega_\alpha$  is the mode frequency in the rotating frame. Note that the above decomposition includes both positive and negative mode frequencies. We adopt the convention that the eigenmode oscillation has the form  $\boldsymbol{\xi}(\mathbf{r}, t) \propto e^{im\phi-i\omega_{\alpha}t}$  such that positive  $\omega_{\alpha}/m$  corresponds to a prograde mode. We use the normalization

$$\langle \boldsymbol{\xi}_{\alpha}, \boldsymbol{\xi}_{\alpha} \rangle \equiv \int d^3x \rho \boldsymbol{\xi}_{\alpha}^* \cdot \boldsymbol{\xi}_{\alpha} = M_1 R_1^2, \quad (6.9)$$

where  $\rho$  is the stellar density profile. With this phase space expansion, the modes satisfy the orthogonality relation  $\langle \boldsymbol{\xi}_{\alpha}, 2i\boldsymbol{\Omega}_s \times \boldsymbol{\xi}_{\beta} \rangle + (\omega_{\alpha} + \omega_{\beta}) \langle \boldsymbol{\xi}_{\alpha}, \boldsymbol{\xi}_{\beta} \rangle = 0$  for  $\alpha \neq \beta$ . We define

$$c_{\alpha}(t) = \sum_{N=-\infty}^{\infty} c_{\alpha N}(t), \quad (6.10)$$

and find [Lai and Wu, 2006, Fuller and Lai, 2012a]

$$\dot{c}_{\alpha N} + [i\omega_{\alpha} + \Gamma_{\alpha}(\omega_{Nm})] c_{\alpha N} = i \frac{U_{Nm} Q_{\alpha}}{2\epsilon_{\alpha}} e^{-i\omega_{Nm}t}, \quad (6.11)$$

where we have used

$$Q_{\alpha} = \langle \boldsymbol{\xi}_{\alpha}, \nabla(r^2 Y_{lm}) \rangle, \quad (6.12)$$

$$\epsilon_{\alpha} = \omega_{\alpha} + \langle \boldsymbol{\xi}_{\alpha}, i\boldsymbol{\Omega}_s \times \boldsymbol{\xi}_{\alpha} \rangle. \quad (6.13)$$

To the first order in the stellar rotation rate,  $\epsilon_{\alpha}$  is the eigenfrequency of a mode in the absence of rotation, provided  $\Omega_s \ll |\omega_{\alpha}|$ . The damping rate of the forced oscillation of mode  $\alpha$  at the forcing frequency  $\omega_{Nm}$  is denoted by

$\Gamma_\alpha(\omega_{Nm})$ . The solution to equation (6.11) is

$$c_{\alpha N}(t) = \frac{U_{Nm} Q_\alpha}{2\epsilon_\alpha} \frac{e^{-i\omega_{Nm} t}}{[\omega_\alpha - \omega_{Nm} - i\Gamma_\alpha(\omega_{Nm})]}, \quad (6.14)$$

On timescales much longer than the orbital period, the energy dissipation rate in the rotating frame is given by the sum over the response to multiple forcing frequencies for oscillation modes, i.e,

$$\dot{E} = \sum_{\alpha N} \dot{E}_{\alpha N}. \quad (6.15)$$

In this paper, we consider tidal dissipation due to viscosity in the stellar convection zone (see Section 6.3). For slow rotation ( $\Omega_s \ll |\omega_\alpha|$ ), the oscillation eigenmode is given by

$$\xi_\alpha(\mathbf{r}) = \xi_{ar}(\mathbf{r}) Y_{lm}(\theta, \phi) \mathbf{e}_r + \xi_{ah}(\mathbf{r}) r \nabla Y_{lm}(\theta, \phi), \quad (6.16)$$

where  $\xi_{ar}$  and  $\xi_{ah}$  are the radial and horizontal components of  $\xi_\alpha(\mathbf{r})$ . The viscous dissipation rate of mode  $\alpha$ , oscillating at the forcing frequency  $\omega_{Nm}$  with amplitude  $c_{\alpha N}$  is [see equation (5) of Sun et al. [2018]]

$$\begin{aligned} \dot{E}_{\alpha N} &= \frac{1}{2} \omega_{Nm}^2 |c_{\alpha N}|^2 \\ &\times \int_{r_{\text{conv}}}^{R_1} dr \, r^2 \rho v \left[ 4 \left( \frac{d\xi_{ar}}{dr} \right)^2 \right. \\ &+ 2l(l+1) \left( \frac{d\xi_{ah}}{dr} + \frac{\xi_{ar}}{r} - \frac{\xi_{ah}}{r} \right)^2 \\ &\left. + 2 \left( l(l+1) \frac{\xi_{ah}}{r} - 2 \frac{\xi_{ar}}{r} \right)^2 \right], \end{aligned} \quad (6.17)$$

where  $r_{\text{conv}}$  is the inner edge of the convective envelope, and  $v$  is the isotropic kinematic viscosity. Equation (6.17) assumes that the flow is approximately incompressible. We define the damping rate  $\gamma_\alpha(\omega_{Nm})$  as a relationship between  $\dot{E}_{\alpha N}$  and the kinetic energy of the mode such that

$$\dot{E}_{\alpha N} = 2\gamma_\alpha(\omega_{Nm}) \langle \dot{\xi}_{\alpha N}, \dot{\xi}_{\alpha N} \rangle = 2\gamma_\alpha(\omega_{Nm}) \omega_{Nm}^2 |c_{\alpha N}|^2 M_1 R_1^2, \quad (6.18)$$

with  $\xi_{\alpha N}(\mathbf{r}, t) \equiv c_{\alpha N}(t)\xi_\alpha(\mathbf{r})$ . Thus,

$$\begin{aligned}\gamma_\alpha(\omega_{Nm}) \equiv & \frac{1}{4} \int_{r_{\text{conv}}}^{R_1} dr r^2 \rho v \left[ 4 \left( \frac{d\xi_{\alpha r}}{dr} \right)^2 \right. \\ & + 2l(l+1) \left( \frac{d\xi_{\alpha h}}{dr} + \frac{\xi_{\alpha r}}{r} - \frac{\xi_{\alpha h}}{r} \right)^2 \\ & \left. + 2 \left( l(l+1) \frac{\xi_{\alpha h}}{r} - 2 \frac{\xi_{\alpha r}}{r} \right)^2 \right].\end{aligned}\quad (6.19)$$

The relationship between the two damping rates,  $\Gamma_\alpha(\omega_{Nm}) = \omega_{Nm}\gamma_\alpha(\omega_{Nm})/\epsilon_\alpha$ , is discussed in the Appendix. The total energy dissipation rate in the rotating frame is then given by the sum

$$\dot{E} = \frac{GM_2^2 R_1^5}{2a^6} \sum_{\alpha N} \left( \frac{Q_\alpha}{\bar{\epsilon}_\alpha} \right)^2 \frac{\gamma_\alpha(\omega_{Nm})(W_{2m}F_{Nm})^2 \omega_{Nm}^2}{(\omega_\alpha - \omega_{Nm})^2 + \Gamma_\alpha^2(\omega_{Nm})}. \quad (6.20)$$

In the above expression,  $Q_\alpha$  and  $\bar{\epsilon}_\alpha = \epsilon_\alpha(GM_1/R_1^3)^{-1/2}$  are dimensionless (i.e. they are in units where  $G = M_1 = R_1 = 1$ ). Note that if we restrict to modes with positive  $\omega_\alpha$  in the sum, we can combine terms with  $\omega_\alpha, m, N$  and  $-\omega_\alpha, -m, -N$ . The result is to multiply equation (6.20) by a factor of 2. We can calculate the tidal torque on the primary,  $T = \sum_{\alpha N} T_{\alpha N}$  using the relationship

$$T_{\alpha N} = \frac{m\dot{E}_{\alpha N}}{\omega_{Nm}}. \quad (6.21)$$

Then,

$$T = \sum_{\alpha N} T_{\alpha N} = T_0 \sum_{\alpha' N} \left( \frac{Q_\alpha}{\bar{\epsilon}_\alpha} \right)^2 \frac{m\gamma_\alpha(\omega_{Nm})(W_{2m}F_{Nm})^2 \omega_{Nm}}{(\omega_\alpha - \omega_{Nm})^2 + \Gamma_\alpha^2(\omega_{Nm})}, \quad (6.22)$$

where

$$T_0 \equiv \frac{GM_2^2 R_1^5}{a^6}, \quad (6.23)$$

and  $\sum_{\alpha'}$  implies that the sum is restricted to modes with  $\omega_\alpha > 0$ . The tidal energy transfer rate from the orbit to the primary in the inertial frame,  $\dot{E}_{\text{in}}$ , is related to  $\dot{E}$  and  $T$  via

$$\dot{E}_{\text{in}} = \dot{E} + \Omega_s T. \quad (6.24)$$

From equations (6.20)-(6.24), we find

$$\dot{E}_{\text{in}} = T_0 \Omega \sum_{\alpha'N} \left( \frac{Q_\alpha}{\bar{\epsilon}_\alpha} \right)^2 \frac{N\gamma_\alpha(\omega_{Nm})(W_{2m}F_{Nm})^2\omega_{Nm}}{(\omega_\alpha - \omega_{Nm})^2 + \Gamma_\alpha^2(\omega_{Nm})}. \quad (6.25)$$

Together, equations (6.22) and (6.25) govern the spin and orbital evolution of the binary (see Section 6.2.2). <sup>1</sup>

### 6.2.1 The Slow-Rotation and Weak Friction Limits

In the limit  $\Omega_s \ll \omega_\alpha$ ,  $\omega_\alpha \simeq \omega_{-\alpha} \simeq \epsilon_\alpha \simeq \epsilon_{-\alpha}$ . Assuming  $\omega_\alpha \gg |\omega_{Nm}|$  and  $\omega_\alpha \gg \Gamma_\alpha(\omega_{Nm})$ , equations (6.22) and (6.25) can be simplified to

$$T \simeq T_0 \sum_{\alpha'N} \left( \frac{Q_\alpha}{\bar{\omega}_\alpha} \right)^2 \frac{m\gamma_\alpha(\omega_{Nm})(W_{2m}F_{Nm})^2\omega_{Nm}}{\omega_\alpha^2}, \quad (6.26)$$

$$\dot{E}_{\text{in}} \simeq T_0 \Omega \sum_{\alpha'N} \left( \frac{Q_\alpha}{\bar{\omega}_\alpha} \right)^2 \frac{N\gamma_\alpha(\omega_{Nm})(W_{2m}F_{Nm})^2\omega_{Nm}}{\omega_\alpha^2}. \quad (6.27)$$

In the weak friction approximation [Darwin, 1880, Alexander, 1973, Hut, 1981], the damping rate  $\gamma_\alpha(\omega_{Nm}) = \gamma_\alpha$  is assumed to have no frequency dependence, and we expect equations (6.26) and (6.27) to reduce to the standard result from, e.g. Alexander [1973], Hut [1981]. To see this, we first identify the tidal Love number and lag time. The complex Love number associated with each forcing term ( $Nm$ ) is

$$\tilde{k}_2(\omega_{Nm}) = \left. \frac{[\delta\Phi(\mathbf{r}, t)]_{Nm}}{[U(\mathbf{r}, t)]_{Nm}} \right|_{r=R_1}, \quad (6.28)$$

where  $\delta\Phi(\mathbf{r}, t)$  is the potential from the perturbed density in the primary star. Using,

$$[\delta\Phi(\mathbf{r}, t)]_{Nm} = \sum_\alpha c_{\alpha N}(t) \delta\Phi_\alpha(\mathbf{r}), \quad (6.29)$$

---

<sup>1</sup>The derivation of equations (6.22) and (6.25) for the tidal torque and energy transfer rate differs from Ivanov and Papaloizou [2004b] in that we use a mode decomposition (equation 6.8) that is rigorously valid for rotating stars.

with the expansion in spherical harmonics (limited to  $l = 2$ )

$$\delta\Phi_\alpha(\mathbf{r})|_{r=R_1} = -\frac{4\pi}{5}\frac{GM_1}{R_1}Q_\alpha Y_{2m}(\theta, \phi), \quad (6.30)$$

we find that, for an f-mode oscillation in a slowly rotating body, the real part of the tidal Love number is

$$k_2 \simeq \frac{4\pi}{5} \left( \frac{Q_f}{\bar{\omega}_f} \right)^2, \quad (6.31)$$

where  $Q_f$  and  $\bar{\omega}_f = \omega_f(GM_1/R_1^3)^{-1/2}$  are the overlap integral and eigenfrequency of the  $l = 2$  f-mode for a non-rotating body. The tidal lag time can be defined as

$$\tau \equiv \frac{\gamma_f}{\omega_f^2}, \quad (6.32)$$

where  $\gamma_f$  is the damping rate of the  $l = 2$  f-mode oscillation calculated with equation (6.19) assuming that the kinematic viscosity is independent of the forcing frequency. The sum over oscillation modes in equations (6.22) and (6.25) is restricted to f-modes with  $m = -2, 0, 2$ . The tidal torque and energy transfer rate can then be written as

$$T = 3T_0 k_2 \tau \Omega \sum_{Nm} \frac{5}{12\pi} m (W_{2m} F_{Nm})^2 \frac{\omega_{Nm}}{\Omega}, \quad (6.33)$$

$$\dot{E}_{in} = 3T_0 k_2 \tau \Omega^2 \sum_{Nm} \frac{5}{12\pi} N (W_{2m} F_{Nm})^2 \frac{\omega_{Nm}}{\Omega}. \quad (6.34)$$

According to equations (22) and (23) of Storch and Lai [2014], we have

$$\sum_{Nm} \frac{5}{12\pi} m (W_{2m} F_{Nm})^2 \frac{\omega_{Nm}}{\Omega} = \frac{1}{(1-e^2)^6} \left[ f_2 - (1-e^2)^{3/2} f_5 \frac{\Omega_s}{\Omega} \right] \quad (6.35)$$

$$\sum_{Nm} \frac{5}{12\pi} N (W_{2m} F_{Nm})^2 \frac{\omega_{Nm}}{\Omega} = \frac{1}{(1-e^2)^{15/2}} \left[ f_1 - (1-e^2)^{3/2} f_2 \frac{\Omega_s}{\Omega} \right], \quad (6.36)$$

where  $f_1$ ,  $f_2$ , and  $f_5$  are functions of eccentricity defined in Hut [1981],

given by

$$f_1 = 1 + \frac{31}{2}e^2 + \frac{255}{8}e^4 + \frac{185}{16}e^6 + \frac{25}{64}e^8, \quad (6.37)$$

$$f_2 = 1 + \frac{15}{2}e^2 + \frac{45}{8}e^4 + \frac{5}{16}e^6, \quad (6.38)$$

$$f_5 = 1 + 3e^2 + \frac{3}{8}e^4. \quad (6.39)$$

This verifies that our formulation is equivalent to the weak friction model under the assumptions of slow rotation and frequency-independent viscous dissipation.

### 6.2.2 Orbital Evolution

We can combine the angular momentum and energy transfer rates to obtain the orbital evolution of the binary and spin evolution of the primary star driven by tidal dissipation. The rate of change of the orbital angular momentum is  $\dot{L} = -T$ , and the orbital energy dissipation rate is  $\dot{E}_{\text{orb}} = -\dot{E}_{\text{in}}$ . Using  $L = \mu\Omega a^2(1 - e^2)^{1/2}$  and  $E_{\text{orb}} = -\mu\Omega^2 a^2/2$  (with  $\mu$  the reduced mass of the binary), we find that

$$\frac{\dot{a}}{a} = -\frac{2}{\mu\Omega^2 a^2} \dot{E}_{\text{in}}, \quad (6.40)$$

$$\frac{\dot{\Omega}_s}{\Omega_s} = \frac{T}{I_1 \Omega_s}, \quad (6.41)$$

$$\frac{\dot{e}}{e} = \frac{1 - e^2}{e^2} \frac{1}{\mu\Omega a^2} \left[ \frac{T}{(1 - e^2)^{1/2}} - \frac{\dot{E}_{\text{in}}}{\Omega} \right], \quad (6.42)$$

where  $I_1 = kM_1R_1^2$  is the moment of inertia of the primary star.

To facilitate applications to different binary systems, we write  $T$  and  $\dot{E}_{\text{in}}$  in

the form

$$T = 3T_0 k_2 \tau \frac{\Omega}{(1 - e^2)^6} F_T(e, \Omega_s/\Omega, r_p/R_1), \quad (6.43)$$

$$\dot{E}_{\text{in}} = 3T_0 k_2 \tau \frac{\Omega^2}{(1 - e^2)^{15/2}} F_E(e, \Omega_s/\Omega, r_p/R_1), \quad (6.44)$$

where  $k_2$  and  $\tau$  are given by equations (6.31) and (6.32),  $r_p$  is the pericentre distance, and  $F_T$  and  $F_E$  are dimensionless functions that depend on  $e$ ,  $\Omega_s/\Omega$ ,  $r_p/R$ , and the structure of the star. Note that the semi-major axis evolution depends on  $F_E$  and the stellar spin on  $F_T$ . We also define the quantity

$$F_{\text{ecc}}(e, \Omega_s/\Omega, r_p/R_1) = \frac{1}{9} \frac{(1 - e^2)}{e^2} \left[ \frac{F_E}{(1 - e^2)} - F_T \right], \quad (6.45)$$

which characterizes the eccentricity evolution. In the weak friction limit,

$$F_T = f_2 - (1 - e^2)^{3/2} f_5 \frac{\Omega_s}{\Omega}, \quad (6.46)$$

$$F_E = f_1 - (1 - e^2)^{3/2} f_2 \frac{\Omega_s}{\Omega} \quad (6.47)$$

$$F_{\text{ecc}} = f_3 - (1 - e^2)^{3/2} f_4 \frac{11}{18} \frac{\Omega_s}{\Omega}, \quad (6.48)$$

where  $f_3$  and  $f_4$  are functions of the eccentricity defined in Hut [1981] and given by

$$f_3 = 1 + \frac{15}{4} e^2 + \frac{15}{8} e^4 + \frac{5}{64} e^6 \quad (6.49)$$

$$f_4 = 1 + \frac{3}{2} e^2 + \frac{1}{8} e^4. \quad (6.50)$$

For general binary systems (when the weak friction theory breaks down), we continue to use equations (6.43) and (6.44) to parameterize the angular momentum and energy transfer rates. By comparing equations (6.22) and

(6.25) to equations (6.43) and (6.44), we find

$$F_T(e, \Omega_s/\Omega, r_p/R_1) = \frac{5}{12\pi} \left( \frac{\bar{\omega}_f}{Q_f} \right)^2 \left( \frac{\omega_f^2}{\gamma_f \Omega} \right) (1 - e^2)^6 \\ \times \sum_{Nm} \left( \frac{Q_\alpha}{\bar{\epsilon}_\alpha} \right)^2 \frac{m(W_{2m} F_{Nm})^2 \omega_{Nm} \gamma_\alpha(\omega_{Nm})}{(\omega_\alpha - \omega_{Nm})^2 + \Gamma_\alpha^2(\omega_{Nm})}, \quad (6.51)$$

$$F_E(e, \Omega_s/\Omega, r_p/R_1) = \frac{5}{12\pi} \left( \frac{\bar{\omega}_f}{Q_f} \right)^2 \left( \frac{\omega_f^2}{\gamma_f \Omega} \right) (1 - e^2)^{15/2} \\ \times \sum_{Nm} \left( \frac{Q_\alpha}{\bar{\epsilon}_\alpha} \right)^2 \frac{N(W_{2m} F_{Nm})^2 \omega_{Nm} \gamma_\alpha(\omega_{Nm})}{(\omega_\alpha - \omega_{Nm})^2 + \Gamma_\alpha^2(\omega_{Nm})}, \quad (6.52)$$

$$F_{ecc}(e, \Omega_s/\Omega, r_p/R_1) = \frac{5}{108\pi} \left( \frac{\bar{\omega}_f}{Q_f} \right)^2 \left( \frac{\omega_f^2}{\gamma_f \Omega} \right) \frac{(1 - e^2)^{15/2}}{e^2} \\ \times \sum_{Nm} \left[ \left( N - \frac{m}{\sqrt{1 - e^2}} \right) \left( \frac{Q_\alpha}{\bar{\epsilon}_\alpha} \right)^2 \right. \\ \left. \times \frac{(W_{2m} F_{Nm})^2 \omega_{Nm} \gamma_\alpha(\omega_{Nm})}{(\omega_\alpha - \omega_{Nm})^2 + \Gamma_\alpha^2(\omega_{Nm})} \right]. \quad (6.53)$$

We can now write the orbital and spin evolution rates as

$$\frac{\dot{a}}{a} = -\frac{6}{t_d(1 - e^2)^{15/2}} F_E(e, \Omega_s/\Omega, r_p/R_1), \quad (6.54)$$

$$\frac{\dot{\Omega}_s}{\Omega_s} = \frac{3}{t_d(1 - e^2)^6} \left( \frac{\mu a^2 \Omega}{I_1 \Omega_s} \right) F_T(e, \Omega_s/\Omega, r_p/R_1), \quad (6.55)$$

$$\frac{\dot{e}}{e} = -\frac{27}{t_d(1 - e^2)^{13/2}} F_{ecc}(e, \Omega_s/\Omega, r_p/R_1), \quad (6.56)$$

where

$$t_d^{-1} \equiv \frac{T_0}{\mu a^2} k_2 \tau = \left( \frac{M_2}{M_1} \right) \left( \frac{M_1 + M_2}{M_1} \right) \left( \frac{R_1}{a} \right)^8 k_2 \frac{\gamma_f}{\bar{\omega}_f^2}. \quad (6.57)$$

### 6.3 Viscous Dissipation in Convective Envelopes and Stellar Models

The damping rate of a forced oscillation mode depends on the convective viscosity. The standard viscosity prescription is independent of the forcing

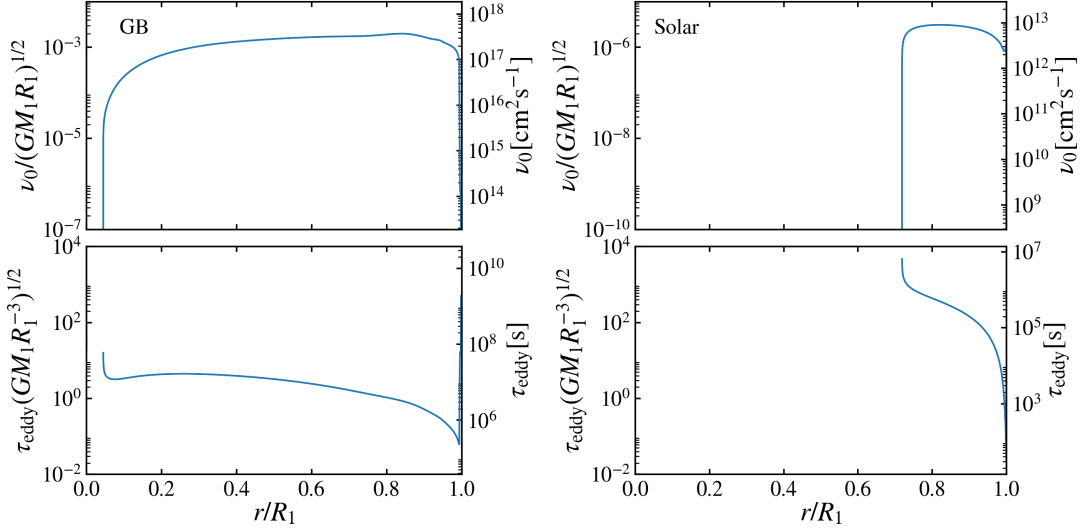


Figure 6.1: The standard (“unsuppressed”) turbulent viscosity  $\nu_0$  (top panels, see equation 6.58) and eddy turnover time  $\tau_{\text{eddy}} = H/v_H$  (bottom panels) in the convective envelopes of two MESA-generated stellar models. The left panels show a giant branch star with  $M_1 = 10M_\odot$  and  $R_1 = 379R_\odot$ , and the right panels show a solar-type star. In each panel, the left label shows  $\nu_0$  and  $\tau_{\text{eddy}}$  in dimensionless “stellar” units, while the right label shows the quantities in cgs units.

frequency and given by

$$\nu_0 = \frac{1}{3}Hv_H, \quad (6.58)$$

where  $H$  is the pressure scale height, and  $v_H \sim (F/\rho)^{1/3}$  is the convective velocity with  $F$  the convective flux. In Fig. 6.1, we show the viscosity and eddy turnover time  $\tau_{\text{eddy}} = H/v_H$  for two MESA-generated stellar models [Paxton et al., 2011], a  $10M_\odot$  giant branch (GB) star and a solar-type star.

When the eddy turnover time exceeds the tidal forcing period,  $\sim |\omega_{Nm}|^{-1}$ , convective eddies cannot transport momentum efficiently, and the turbulent viscosity is expected to be reduced. The correct prescription for viscosity reduction has been widely discussed in the literature [see Ogilvie, 2014, for a review]. We adopt a quadratic reduction, first suggested by Goldreich and Nicholson [1989] and confirmed in many recent studies [see

e.g. Duguid et al. [2019]],

$$\nu = \frac{1}{3} H \nu_H [1 + (\omega_{Nm} \tau_{\text{eddy}})^2]^{-1}. \quad (6.59)$$

Zahn [1977], Phinney [1992] and Verbunt and Phinney [1995] provided a simple estimate of the eccentricity circularization rate for nearly circular binary stars with convective envelopes based on the “unsuppressed” viscosity  $\nu_0$  (equation 6.58). To estimate the damping rate of the tidally forced f-mode (i.e. equilibrium tide), we assume  $\nu_0 \sim \text{constant}$  in the convective envelope. Then the integral in equation (6.19) can be approximated as

$$\gamma_{\text{est}} \sim \frac{M_{\text{env}}}{M_1} \left( \frac{\nu}{H^2} \right) \sim \frac{M_{\text{env}}}{M_1} \left( \frac{L}{M_{\text{env}} R_1^2} \right)^{1/3}, \quad (6.60)$$

where  $M_{\text{env}}$  is the mass of the convective region and we have used  $\nu_0 \sim H(F/\rho)^{1/3}$  and  $4\pi\rho H^3 \sim M_{\text{env}}$ . Using this estimate of the equilibrium tide dissipation rate, Phinney [1992] gave the following approximation to the eccentricity damping rate (see Eq. 6.57)

$$\frac{\dot{e}}{e} \approx -\gamma_{\text{est}} \left( \frac{M_2}{M_1} \right) \left( \frac{M_1 + M_2}{M_1} \right) \left( \frac{R_1}{a} \right)^8. \quad (6.61)$$

In Fig. 6.2, we compare  $\gamma(\omega_{Nm})$  calculated with equation (6.19) to  $\gamma_{\text{est}}$  for the MESA-generated GB and solar-type stellar models used to produce Fig. 6.1. We find that  $\gamma(\omega_{Nm} = 0) \sim \gamma_{\text{est}}$ . In stellar units,  $\gamma_{\text{est}} = 0.024(GM_1/R_1^3)^{1/2}$  for the GB model and  $\gamma_{\text{est}} = 9.5 \times 10^{-6}(GM_1/R_1^3)^{1/2}$  for the solar-type model, corresponding to  $\gamma_{\text{est}} = 0.20 \text{ yr}^{-1}$  and  $\gamma_{\text{est}} = 0.22 \text{ yr}^{-1}$  respectively. The eddy turnover time is generally larger in the solar-type model, so it is easier for the tidal forcing period to be comparable to  $\tau_{\text{eddy}}$  in the depths of the convective envelope. In consequence, viscosity reduction can have a very large effect on  $\gamma(\omega_{Nm})$  for the solar model, depending on  $\omega_{Nm}$ , and is less important for the GB model.

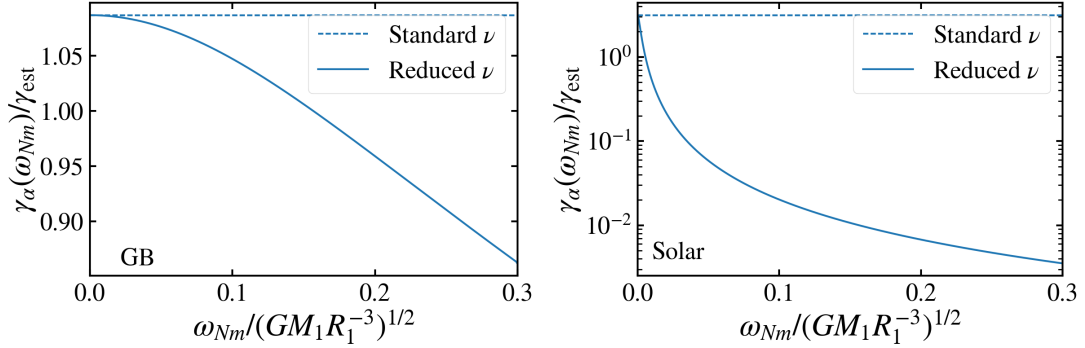


Figure 6.2: The stellar viscous damping rate (see equation 6.19) as a function of the forcing frequency  $\omega_{Nm}$  for the same MESA GB model (top panel) and solar model (bottom panel) used in Fig 6.1. The damping rates are scaled to  $\gamma_{\text{est}}$  (see equation 6.60). The dashed lines show the results for a standard (“un-suppressed”) viscosity  $\nu_0$  (equation 6.58), and the solid line is calculated with a quadratic viscosity reduction (see equation 6.59).

## 6.4 Sample Results

We have calculated  $F_T(e, \Omega_s/\Omega, r_p/R_1)$  and  $F_E(e, \Omega_s/\Omega, r_p/R_1)$  (defined in equations 6.43 and 6.44, see also equations 6.51-6.53) for the two stellar models introduced in Section 6.3. These dimensionless angular momentum and energy transfer rates control the synchronization rate of the primary star and the orbital evolution of the binary (see equations 6.54 - 6.56).

Typically, the timescale for the primary star to reach an equilibrium spin rate, or pseudosynchronous rate, is shorter than the timescale for orbital decay and circularization. This is clear from equations (6.54) - (6.56), where the spin evolution rate is faster than the orbital decay rate by a factor of order  $\sim \mu a^2 \Omega / I \Omega_s$ . For an eccentric orbit, the primary star can spin-up to pseudosynchronous rotation very quickly, and it is safe to assume that the star is rotating pseudosynchronously throughout orbital decay and circularization.

When a star rotates pseudosynchrounously, it experiences no net torque. Under the weak friction approximation, the dimensionless torque is given by equation (6.46), so the pseudosynchronous rate is

$$\Omega_{\text{ps}} = \frac{f_2}{(1 - e^2)^{3/2} f_5} \Omega = \frac{f_2}{(1 + e)^2 f_5} \Omega_p, \quad (6.62)$$

where

$$\Omega_p \equiv \left[ \frac{(1 + e)G(M_1 + M_2)}{r_p^3} \right]^{1/2} = \Omega \frac{(1 + e)^{1/2}}{(1 - e)^{3/2}}, \quad (6.63)$$

is the orbit frequency at pericenter [ $r_p = (1 - e)a$ ].

In realistic (MESA) stellar models, we use equation (6.51) to compute  $F_T$  for both the standard viscosity (equation 6.58) and the reduced viscosity (equation 6.59). Figure 6.3 displays the results for the GB stellar model and Fig. 6.4 for the solar model. Equilibrium spin (pseudosynchronous rotation) corresponds to  $F_T = 0$ . For the GB model, the pseudosynchronous value of  $\Omega_s$  can be nearly a factor of two larger than the predicted  $\Omega_{\text{ps}}$  from weak friction theory (equation 6.62). Additionally,  $F_T$  can be zero for multiple rotation rates, allowing for multiple spin equilibria (though not all of these are stable). This behavior was also noted and discussed in Storch and Lai [2014]. For the GB stellar model, the two viscosity prescriptions yield similar order of magnitudes for the values of  $F_T$ . This is unsurprising as the eddy timescale  $\tau_{\text{eddy}}$  is generally short throughout the convective envelope of the GB star, and the viscosity is never significantly reduced (see Fig. 6.2).

For the solar-type stellar model, the result of  $F_T$  with the reduced viscosity prescription is very different from either the weak friction approximation or the calculation that assumes standard (frequency-independent) viscosity (see Fig. 6.4). In general,  $|F_T|$  is 1-2 orders of magnitude smaller for

the reduced viscosity than for the standard viscosity. Additionally,  $F_T$  can cross zero for slower rotation rates of nearly half of  $\Omega_{ps}$  (equation 6.62) when the viscosity is reduced.

The functions  $F_E$  and  $F_{ecc}$  determine the orbital decay and circularization rates of the binary. Figure 6.5 displays  $F_E$  (left column) and  $F_{ecc}$  (right column) as a function of pericentre distance for the GB stellar model given a rotation rate of  $\Omega_s = 0.75\Omega_p$ , slightly below  $\Omega_{ps}$ . Each row corresponds to a different orbital eccentricity. The functions  $F_E(r_p/R_1)$  and  $F_{ecc}(r_p/R_1)$  have strong peaks that correspond to resonances between the mode frequencies,  $\omega_\alpha$ , and the forcing frequencies,  $\omega_{Nm}$ . For higher eccentricities ( $e \gtrsim 0.8$ ),  $F_{Nm}$  can be appreciable even for  $N$  of a few times larger than  $\Omega_p/\Omega = (1 + e)^{1/2}/(1 - e)^{3/2}$ . Thus many forcing frequencies contribute significantly to  $F_E$  and  $F_{ecc}$  and can dominate the sum near a resonance, as seen in the bottom row of Fig. 6.5. Importantly,  $F_E$  and  $F_{ecc}$  can be two orders of magnitude larger than the weak friction results (equations 6.47 and 6.48) for small  $r_p$  and high  $e$ . At larger pericentre distances,  $F_E$  and  $F_{ecc}$  agree with the weak friction results. For the GB stellar model, the choice of viscosity prescription does not have a significant effect on the calculated orbital decay and circularization rates, as expected due to the short eddy timescale in the convective zone.

Figure 6.6 shows  $F_E(r_p/R_1)$  and  $F_{ecc}(r_p/R_1)$  for the GB stellar model, as in Fig. 6.5, but for a larger spin rate of  $\Omega_s = 0.9\Omega_p$ . For some combinations of  $e$  and  $r_p$ ,  $\Omega_s = 0.9\Omega_p$  exceeds the pseudosynchronous rotation rate, giving rise to orbital expansion ( $F_E < 0$ , see equation 6.40). As an example, for  $e = 0.1$  (shown in the upper left panel of Fig. 6.6),  $F_E$  is negative for  $r_p/R_1 \gtrsim 2.5 - 3.5$  (depending on the viscosity prescription). Otherwise, there are no

qualitative differences between  $F_E(r_p/R_1)$  and  $F_{\text{ecc}}(r_p/R_1)$  for  $\Omega_s = 0.75\Omega_p$  and  $\Omega_s = 0.9\Omega_p$ .

The dimensionless orbital decay and circularization rates for the solar-type stellar model are shown in Fig. 6.7. For standard (frequency-independent)  $\nu$ ,  $F_E$  and  $F_{\text{ecc}}$  can be a few orders of magnitude larger than the weak friction results for small  $r_p$  and high  $e$  but agree with the weak friction results at larger  $r_p$ . Unlike for the GB model, the viscosity prescription dramatically affects the calculated  $F_E$  and  $F_{\text{ecc}}$ , evident in all panels of Fig. 6.7. Convective viscosity is inefficient in circularizing and shrinking the orbit because the eddy turnover time in the convection envelope is orders of magnitude longer than the pericentre passage time  $\Omega_p^{-1}$ . For a solar-type star, we expect orbital decay via convective dissipation to be a few orders of magnitude smaller than the weak friction prediction.

## 6.5 High-Eccentricity Limit: Alternative Calculation of Tidal Evolution

When the binary orbit is highly eccentric (with  $(1 - e) \ll 1$ ), oscillation modes in the primary star are excited at pericenter and subsequently damp as the mode oscillates freely throughout the rest of the orbit. In this regime, it is possible to calculate the tidal evolution in a different way [cf. Lai, 1997, Fuller and Lai, 2012a, Vick and Lai, 2018].

A key quantity is the tidal energy transfer to a stellar mode (labeled  $\alpha$ ) during the “first” pericenter passage (“first” means that there is no prior

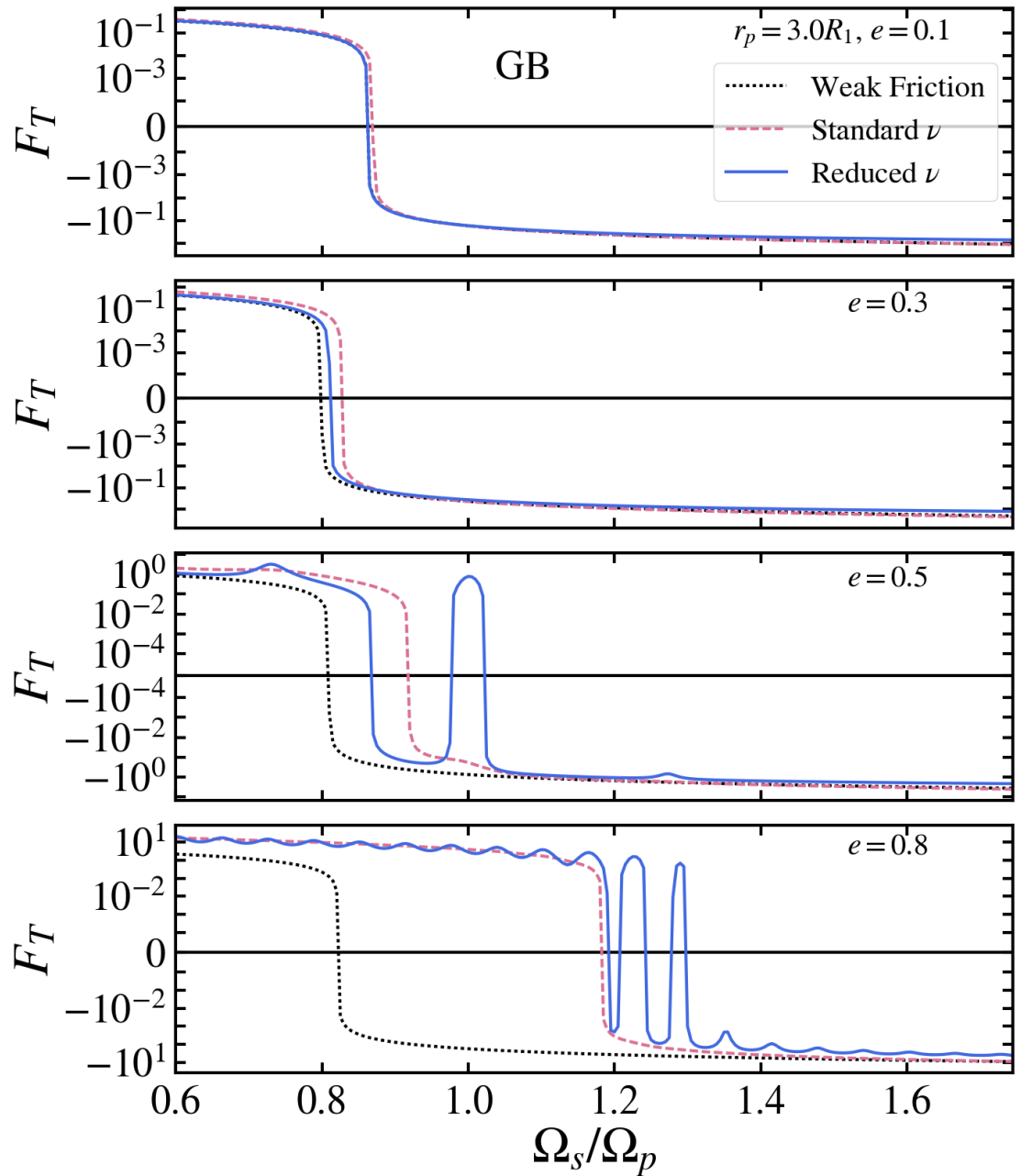


Figure 6.3:  $F_T(e, \Omega_s/\Omega, r_p/R_1)$  (equation 6.51) as a function of the rotation rate  $\Omega_s$  (in units of the pericentre frequency, equation 6.63) for a  $10 M_\odot$  GB stellar model depicted in Fig. 6.1. Results are shown for four different eccentricities, all with the same pericentre distance  $r_p = 3R_1$ . The dotted line is the weak friction result from equation (6.46). The (blue) solid line uses a reduced viscosity (equation 6.59) while the (red) dashed line uses the standard viscosity (equation 6.58). Pseudosynchronous rotation corresponds to  $F_T = 0$ .

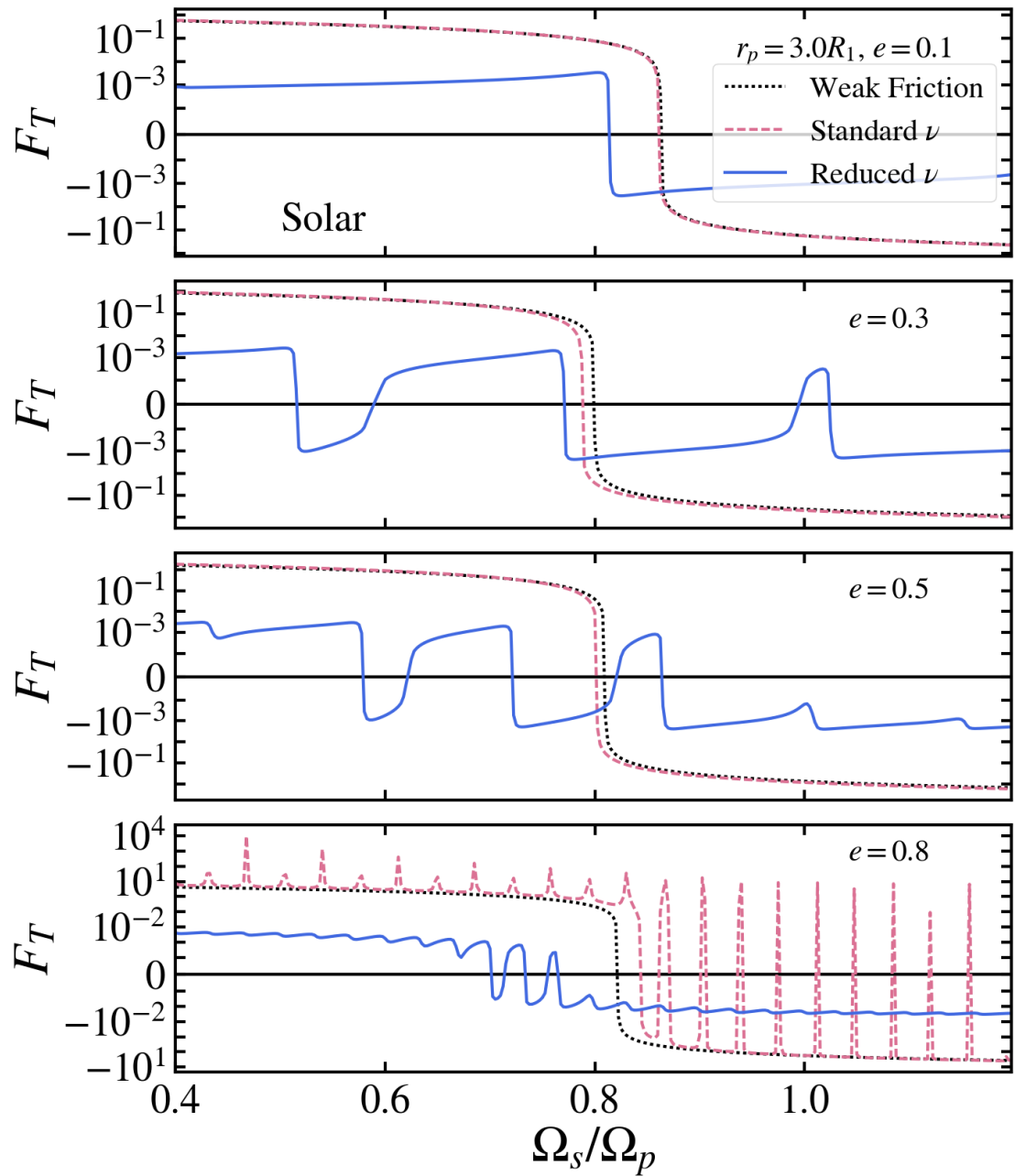


Figure 6.4: Same as Fig. 6.3 but for the solar-type stellar model depicted in Fig. 6.1.

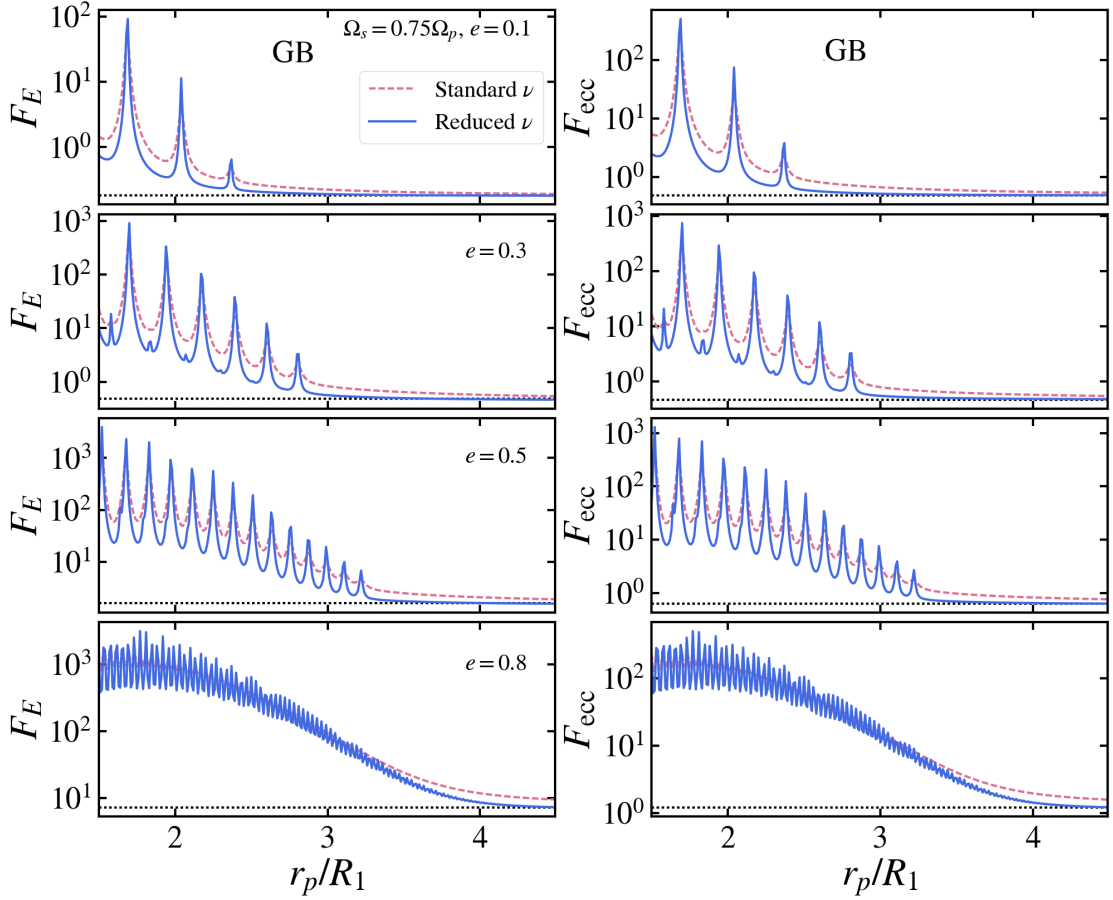


Figure 6.5:  $F_E(e, \Omega_s/\Omega, r_p/R_1)$  and  $F_{\text{ecc}}(e, \Omega_s/\Omega, r_p/R_1)$  (equations 6.52 and 6.53) as a function of the pericentre distance for the  $10 M_\odot$  GB stellar model depicted in Fig. 6.1. The stellar spin frequency is chosen to be  $0.75\Omega_p$ . The four pairs of panels show results for four eccentricities, as labeled. The dotted black lines correspond to the weak friction results (see equations 6.46 and 6.48). The solid lines are calculated with the reduced viscosity from equation (6.59) and the dashed lines with the frequency-independent viscosity from equation (6.58).

oscillation in the star). This can be computed as

$$\Delta E_{\text{in},\alpha} = 2\pi^2 \frac{GM_2^2 R_1^5}{r_p^6} \left( \frac{\sigma_\alpha}{\epsilon_\alpha} \right) |Q_\alpha K_{2m}|^2, \quad (6.64)$$

with

$$K_{2m} = \frac{W_{2m}}{2\pi} \int_{-P/2}^{P/2} dt \left( \frac{r_p}{D} \right)^3 e^{i\sigma_\alpha t - im\Phi(t)}, \quad (6.65)$$

where  $r_p = a(1 - e)$ ,  $Q_\alpha$  and  $\epsilon_\alpha$  are given by equations (6.12) and (6.13), and  $\sigma_\alpha = \omega_\alpha + m\Omega_s$  is the mode frequency in the inertial frame. Under

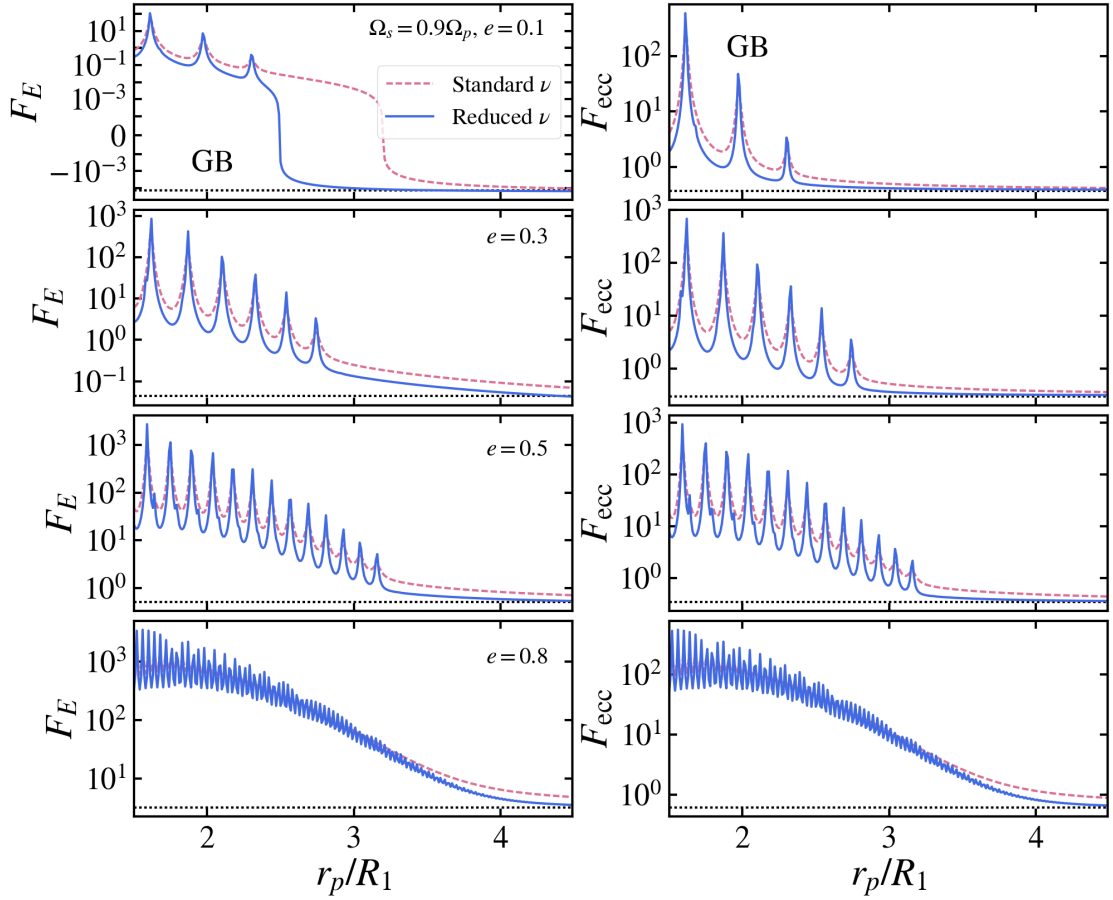


Figure 6.6: Same as Fig. 6.5 except the stellar spin frequency is chosen to be  $0.9\Omega_p$ .

the condition that  $\sigma_\alpha/\Omega_p \gtrsim$  a few, the integral  $K_{2m}$  can be approximated with expressions provided in Appendix C of Lai [1997]. Note that equation (6.64) includes contributions from both the  $\omega_\alpha, m$  and the physically identical  $-\omega_{-\alpha}, -m$  terms. The total energy transfer in a single pericentre passage is given by the restricted sum over positive-frequency modes,

$$\Delta E_{\text{in}} = \sum_{\alpha'} \Delta E_{\text{in},\alpha}.$$

When the mode damping time  $\Gamma_\alpha^{-1} = \Gamma_\alpha^{-1}(\omega_\alpha)$  is less than the orbital period,

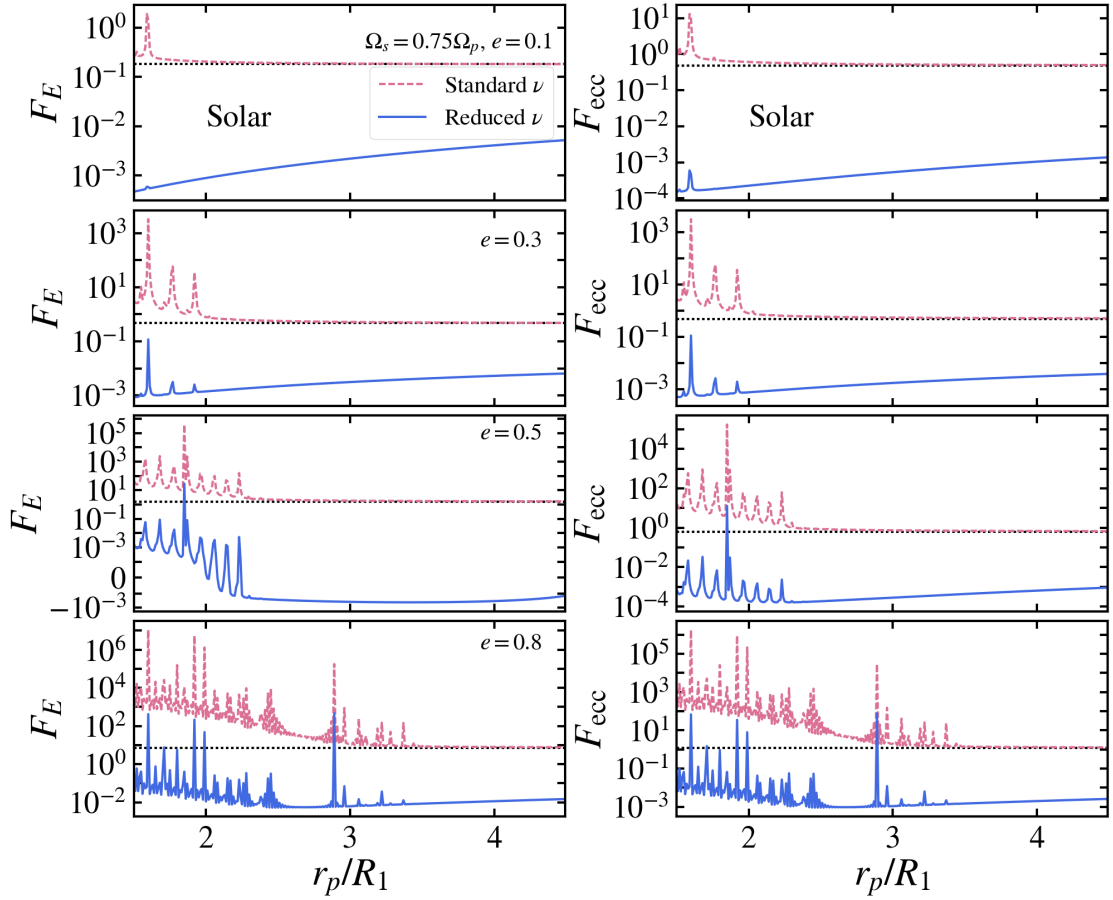


Figure 6.7: Same as Fig. 6.5 but for the solar-type stellar model.

i.e.,  $\Gamma_\alpha^{-1} \lesssim P$ , the orbital energy decay rate is simply given by

$$\dot{E}_{\text{orb}} \simeq - \sum_{\alpha'} \frac{\Delta E_{\text{in},\alpha}}{P}. \quad (6.66)$$

On the other hand, when  $\Gamma_\alpha^{-1} \gtrsim P$ , the orbital decay rate is [Lai, 1997, Vick and Lai, 2018]

$$\dot{E}_{\text{orb}} = - \sum_{\alpha'} \dot{E}_{\text{in},\alpha} \simeq -2 \sum_{\alpha'} \Gamma_\alpha E_{\text{ss},\alpha} = -2 \sum_{\alpha'} \gamma_\alpha(\omega_\alpha) \frac{\omega_\alpha}{\epsilon_\alpha} E_{\text{ss},\alpha}. \quad (6.67)$$

Note that the mode damping rate  $\Gamma_\alpha = \Gamma_\alpha(\omega_\alpha)$  is related to  $\gamma_\alpha = \gamma_\alpha(\omega_\alpha)$  (see Fig. 6.2) by  $\Gamma_\alpha = \omega_\alpha \gamma_\alpha / \epsilon_\alpha$  (see Appendix). The steady-state mode energy

$E_{ss,\alpha}$  is given by [Lai, 1997, Fuller and Lai, 2012a]

$$E_{ss,\alpha} = \frac{\Delta E_{in,\alpha}}{2 [\cosh(\Gamma_\alpha P) - \cos(\sigma_\alpha P)]}. \quad (6.68)$$

For a single freely oscillating mode, the tidal torque is related to the energy transfer rate in the inertial frame via

$$T_\alpha = \frac{m}{\sigma_\alpha} \dot{E}_{in,\alpha}. \quad (6.69)$$

For  $\Gamma_\alpha P \ll 1$  [and thus  $\cosh(\Gamma_\alpha P) \simeq 1$ ], equation (6.68) implies that a resonance occurs when  $\sigma_\alpha P$  is an integer multiple of  $2\pi$ . This resonance condition is the same as  $\omega_\alpha = N\Omega - m\Omega_s = \omega_{Nm}$  (see equations 6.22 and 6.25).

As in Section 6.2, we define the dimensionless torque and energy dissipation rates  $F_T$  and  $F_E$  that are related to  $T$  and  $\dot{E}_{in}$  by equations (6.43) and (6.44) respectively. When  $\Gamma_\alpha P \lesssim 1$ , we have

$$F_T = \frac{5\pi}{6} \left( \frac{\bar{\omega}_f}{Q_f} \right)^2 \left( \frac{\omega_f^2}{\gamma_f \Omega} \right) (1+e)^6 \sum_{\alpha'} \left( \frac{\gamma_\alpha \omega_\alpha}{\epsilon_\alpha^2} \right) \frac{m |Q_\alpha K_{2m}|^2}{[\cosh(\Gamma_\alpha P) - \cos(\sigma_\alpha P)]} \quad (6.70)$$

$$F_E = \frac{5\pi}{6} \left( \frac{\bar{\omega}_f}{Q_f} \right)^2 \left( \frac{\omega_f^2}{\gamma_f \Omega} \right) (1+e)^{15/2} (1-e)^{3/2} \sum_{\alpha'} \left( \frac{\gamma_\alpha \omega_\alpha}{\epsilon_\alpha^2} \right) \left( \frac{\sigma_\alpha}{\Omega} \right) \frac{|Q_\alpha K_{2m}|^2}{[\cosh(\Gamma_\alpha P) - \cos(\sigma_\alpha P)]}. \quad (6.71)$$

When  $\Gamma_\alpha P \gtrsim 1$ , and energy transfer at pericenter is dissipated within a single orbit, we use

$$F_T = \frac{5}{12} \left( \frac{\bar{\omega}_f}{Q_f} \right)^2 \left( \frac{\omega_f^2}{\gamma_f \Omega} \right) (1+e)^6 \sum_{\alpha'} m \left( \frac{\Omega}{\epsilon_\alpha} \right) |Q_\alpha K_{2m}|^2 \quad (6.72)$$

$$F_E = \frac{5}{12} \left( \frac{\bar{\omega}_f}{Q_f} \right)^2 \left( \frac{\omega_f^2}{\gamma_f \Omega} \right) (1+e)^{15/2} (1-e)^{3/2} \sum_{\alpha'} \left( \frac{\sigma_\alpha}{\epsilon_\alpha} \right) |Q_\alpha K_{2m}|^2. \quad (6.73)$$

A key assumption of the above formulation of tidal evolution is that the damping of the free mode oscillations, away from pericentre, dominates the tidal dissipation rate. This is true at small  $r_p$  and large eccentricity. However, as  $r_p$  increases, damping of forced oscillations during pericentre

passages becomes important. To illustrate this point, we carry out time-dependent calculation of the “mode + orbit” system for an equal-mass binary with a non-rotating solar-type primary star. The secondary is treated as a point mass. Figure 6.8 shows the evolution of the energy in  $l = 2$  f-mode oscillations, the orbital energy, and the total energy (the sum of the mode and orbital energies), for (initial) eccentricity  $e = 0.85$  and two different pericentre distances ( $r_p = 2.5R_1$  in the left panel and  $r_p = 5.5R_1$  right panel). The coupled evolution of the mode amplitudes and the orbit was executed by combining equation (6.11) of Section 6.2 for the time evolution of the mode amplitude and equations (6) and (7) of Vick and Lai [2019a] for the orbital evolution (with all general relativity terms set to zero). Expressions for the mode energy and orbital energy are provided in equations (12) and (13) of Vick and Lai [2019a]. For  $r_p = 2.5R_1$ , the binary is in the regime where the damping of free mode oscillations dominates the energy dissipation. In the left panel of Fig. 6.8, we see that the total energy does not change significantly during pericentre passages, and the mode energy decays as the oscillations damp away from pericentre. In the right panel, for  $r_p = 5.5R_1$ , the dissipation of forced oscillations at pericentre dominates the energy dissipation, and the total energy of the system decreases sharply during each pericentre passage.

We can identify the transition between the two dissipation regimes by comparing  $\Delta E_{\text{diss},p}$ , the amount of energy dissipated during a single pericentre passage, with  $\Delta E_{\text{diss,np}}$ , the energy dissipated during the rest of the orbit. For simplicity, let us assume a single mode is dominant. We can estimate  $\Delta E_{\text{diss},p}$  as  $\gamma_a(\Omega_p)E_k/\Omega_p$ , (see equation D.4), where  $\Omega_p$  is the orbital frequency at pericentre (equation 6.63), and  $E_k$  is the kinetic energy

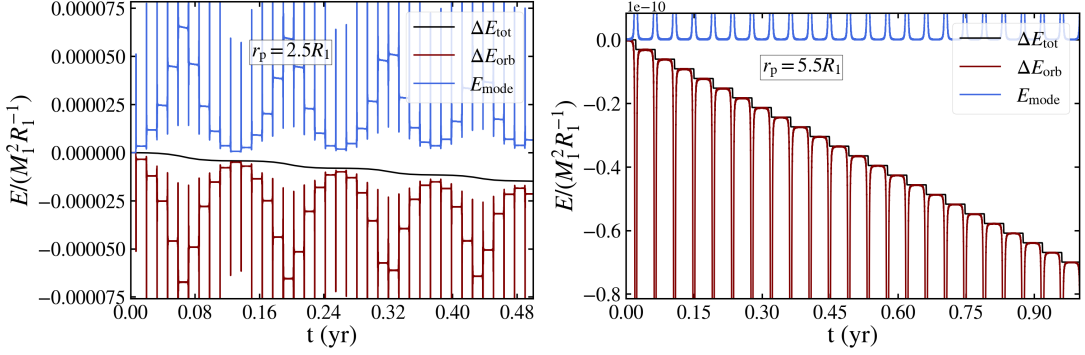


Figure 6.8: The evolution of the mode energy  $E_{\text{mode}}$  (a sum of the energies in the  $l = 2, m = -2, 0, 2$  f-modes), orbital energy,  $\Delta E_{\text{orb}} = E_{\text{orb}} - E_{\text{orb},0}$ , and total energy  $\Delta E_{\text{tot}} = E_{\text{tot}} - E_{\text{tot},0} = E_{\text{mode}} + \Delta E_{\text{orb}}$  in units where  $G = M_1 = R_1 = 1$  for a binary with the solar-type stellar model, a mass ratio of  $M_2/M_1 = 1$ , and an initial eccentricity  $e = 0.85$ . The strong peaks and valleys correspond to pericentre passages. In the left panel (with the initial pericentre distance  $r_p = 2.5R_1$ ), the total energy changes smoothly, and does not show sudden changes at pericentre; for such small  $r_p$ , the dissipation of forced oscillations near pericentre is negligible, and the mode energy visibly decays throughout the rest of the orbit. In the right panel (with larger  $r_p = 5.5R_1$ ), sharp changes in the total energy at pericentre account for majority of energy dissipation in the binary.

in the oscillations at pericentre, given by  $E_k \sim k_2 M_1 (R_1 \epsilon_p)^2 \Omega_p^2 / \bar{\omega}_f^2$ , with  $\epsilon_p = M_2 R_1^3 / (M_1 r_p^3)$ . Then,

$$\Delta E_{\text{diss,p}} \sim \gamma_\alpha(\Omega_p) \Omega_p M_1 R_1^2 \left( \frac{k_2}{\bar{\omega}_f^2} \right) \left( \frac{M_2}{M_1} \right)^2 \left( \frac{R_1}{r_p} \right)^6. \quad (6.74)$$

The energy dissipated in a single orbit away from pericentre is

$$\Delta E_{\text{diss,np}} \sim \min[1, \Gamma_\alpha(\omega_\alpha) P] \Delta E_{\text{in},\alpha}, \quad (6.75)$$

where we have neglected resonances (which occur at  $\sigma_\alpha = N\Omega$ ), and  $\Delta E_{\text{in},\alpha}$  is given by equation (6.64). In Fig. 6.9, we compare equations (6.74) and (6.75) for both the GB and solar-type stellar models assuming the standard (frequency-independent) viscosity. We find that  $E_{\text{diss,p}} \gtrsim E_{\text{diss,np}}$  (i.e. tidal energy dissipation occurs primarily during the pericentre passage) when  $r_p \gtrsim 3.7R_1$  for the GB star and  $r_p \gtrsim 3R_1$  for the solar-type star. Therefore,

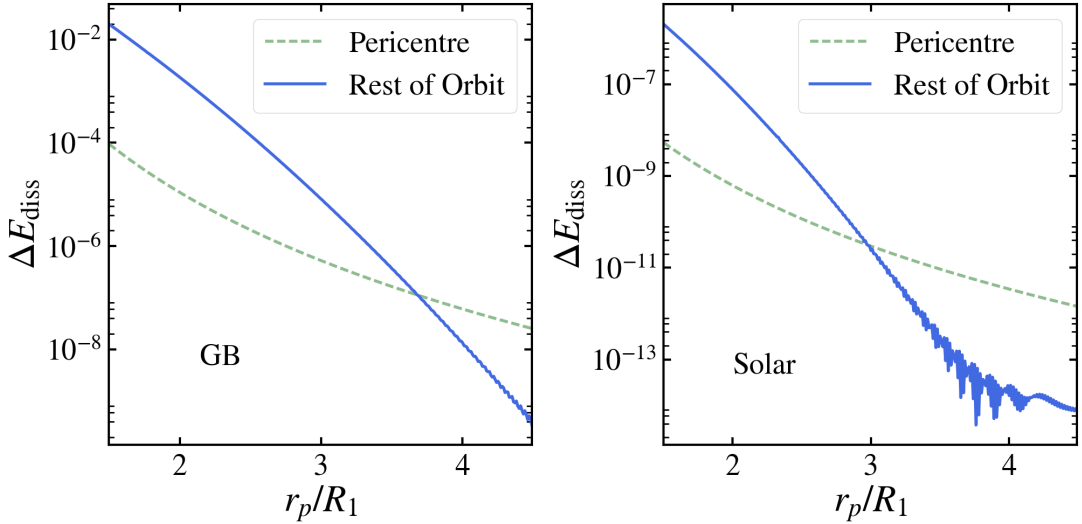


Figure 6.9: The energy dissipation in a single orbit near pericentre (equation 6.74) and over the rest of the orbit (equation 6.75) for a highly eccentric binary as a function of  $r_p/R_1$  for the GB stellar model (left panel) and the solar-type model (right panel) assuming the standard (frequency-independent) viscosity. The orbital eccentricity is  $e = 0.85$  and the stellar rotation rate is  $\Omega_s = 0.75\Omega_p$ .

equations (6.70)-(6.73) are only accurate for small  $r_p$  and we expect deviation from the results of Section 6.4 when  $r_p \gtrsim 3R_1$ .

In Figs. 6.10 and 6.11, we show the dimensionless energy transfer rate for a highly eccentric binary (equation 6.71) as a function of  $r_p/R_1$  and compare with the general expression from equation (6.52). For the GB model, the mode damping time,  $\Gamma^{-1}$ , is shorter than the orbital period for the parameters covered in Fig. 6.10 [ $\Gamma_\alpha^{-1} = 4.5 \text{ yr} \times (\omega_\alpha/\epsilon_\alpha)$  using the standard viscosity while the orbital period is  $P = 12.8 \text{ yr} \times (M_1/M_t)^{1/2}(r_p/R_1)^{3/2}$  for the chosen eccentricity of  $e = 0.85$  and total mass  $M_t = M_1 + M_2$ ]. Therefore  $F_E$  is given by equation (6.73), and the solid lines in the left and right panels are identical. For  $r_p \lesssim 3R_1$ , the general expression for  $F_E$  (equation 6.52) agrees with the high-eccentricity calculation (ignoring peaks due to resonances between a mode and a component of the tidal forcing). Note that

the derivation of equation (6.52) assumes that the mode damping rate is longer than an orbital period, so the high-eccentricity calculation (equation 6.73) should be more accurate in this regime. For  $r_p \gtrsim 3R_1$ , the high-eccentricity expression no longer agrees with equation (6.52) and the weak friction result, as expected, because dissipation near the pericentre, where the oscillation modes are strongly forced, becomes the dominant contributor to the energy and angular momentum transfer rates.

Figure 6.11 displays  $F_E$  for the solar-type stellar model. Here, the viscous damping time,  $\Gamma_\alpha(\omega_\alpha)^{-1}$ , is much longer than the orbital period [ $\Gamma_\alpha^{-1} = 1.5 \text{ yr} \times (\omega_\alpha/\epsilon_\alpha)$  using the standard viscosity and  $P = 4.7 \times 10^{-3} \text{ yr} \times (M_1/M_t)^{1/2} (r_p/R_1)^{3/2}$  for  $e = 0.85$ ], so equation (6.71) is appropriate for the high-eccentricity regime. The function  $F_E(r_p/R_1)$  has strong peaks that correspond to resonances between the orbital frequency and the mode frequency in the inertial frame. From Fig. 6.11, we see that the high-eccentricity calculation agrees well with the general calculation from equation (6.52) at small  $r_p$  for both the standard (left panel) and the reduced (right panel) viscosity. As with the GB model, the high-eccentricity prescription under-predicts the dissipation rates for larger  $r_p$  because it does not include mode damping near the pericentre.

## 6.6 Summary and Discussion

We have developed a general formalism for calculating the orbital decay and circularization rates as well as the spin synchronization rate of a star with a convective envelope in an eccentric binary. Our formalism allows for frequency-dependent turbulent viscosity reduction, which is impor-

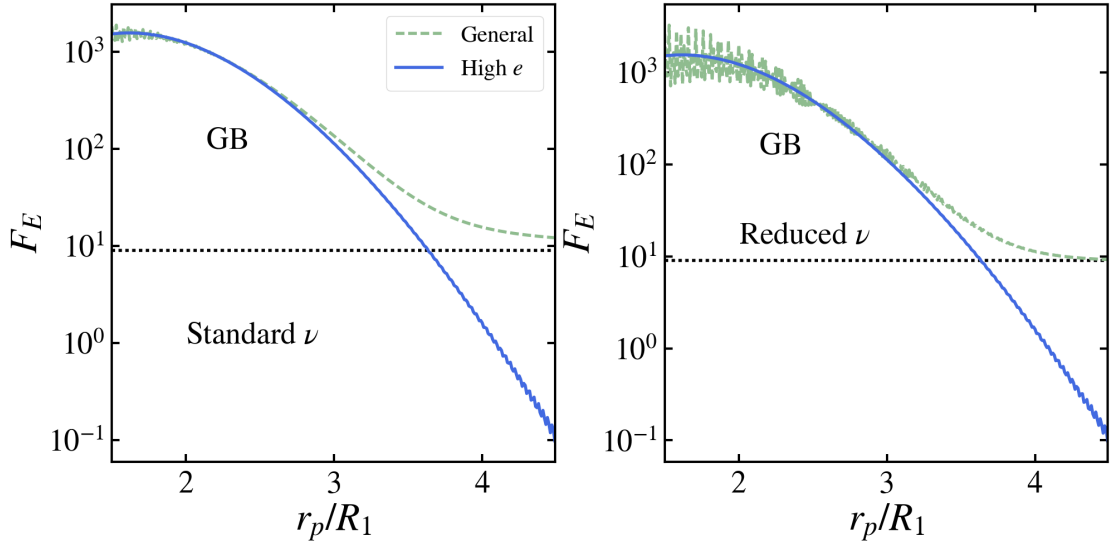


Figure 6.10: The dimensionless tidal energy transfer rate  $F_E(e, \Omega_s/\Omega, r_p/R_1)$  (equations 6.52) vs the pericentre distance for the  $10 M_\odot$  GB stellar model. The orbital eccentricity is  $e = 0.85$  and the stellar rotation rate is  $\Omega_s = 0.75\Omega_p$ . The left panel is calculated with the standard (frequency-independent) viscosity and the right panel with the reduced viscosity from equation (6.59). The solid lines are obtained using the high-eccentricity expression (equations 6.71 and 6.73), and the dashed green lines are obtained using the general expression (equation 6.52). The dotted black lines correspond to the weak friction result (equation 6.47).

tant in the convective envelope when the eddy turnover time is longer than the tidal forcing period. The most general results are summarized in equations (6.51)-(6.57). In the slow-rotation limit, and assuming that the mode frequency is much larger than the forcing frequencies, and that the damping time is independent of the forcing frequency, these general expressions reduce to the well-known weak friction results.

In Section 6.4, we calculated the dimensionless orbital decay, circularization and spin evolution rates for both GB and solar-type stellar models. We found that the pseudosynchronous rotation rate of the star can be almost a factor of two faster than the weak tidal friction prediction for a GB star (Fig. 6.3) and a factor of a few slower for a solar-type star (Fig. 6.4). We

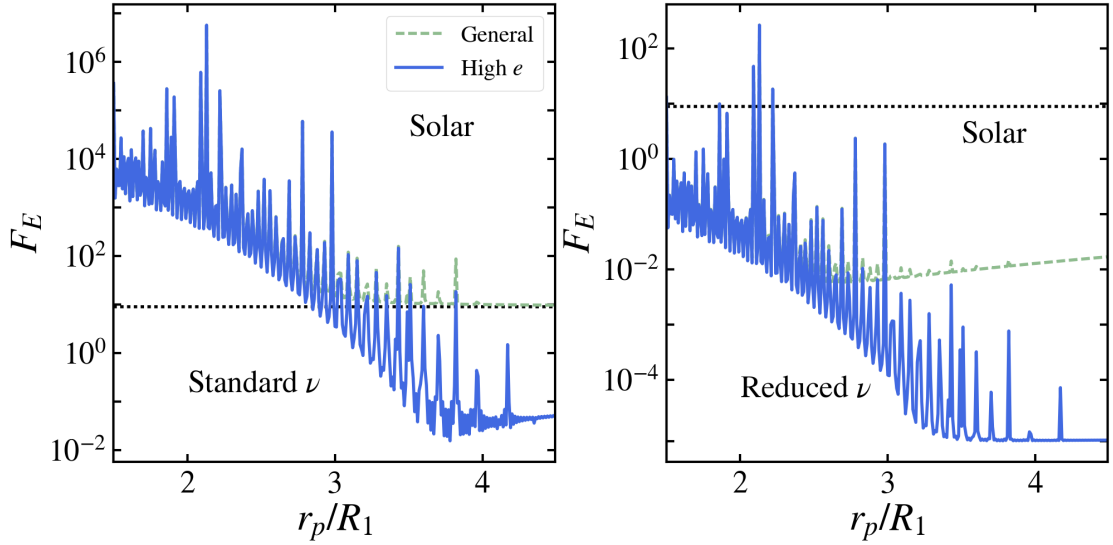


Figure 6.11: Same as Fig. 6.10 but for the solar-type stellar model. Note that in both panels, the high-eccentricity result (equation 6.71) is in near perfect agreement with the general expression (equation 6.52) for small  $r_p$ .

also found that, at small pericentre distances and high eccentricities, the orbital decay and circularization rates can be a few orders of magnitude larger than the prediction from weak tidal friction for an GB star (where the eddy turnover time is fast enough that viscosity reduction is negligible) and a few orders of magnitude smaller for a solar-type star due to viscosity reduction (see Figs. 6.5, 6.6, and 6.7).

Lastly, in Section 6.5 we presented a simpler calculation of the dissipation rates for highly eccentric orbits that only requires a sum over oscillation modes (rather than a sum over both the oscillation modes and many forcing frequencies). The key results are summarized in equations (6.70)-(6.73) (in conjunction with equations 6.43 and 6.44). This approach neglects dissipation near pericenter and is valid for  $r_p \lesssim 3R_1$ .

Our results are relevant to understanding populations of binary systems with evolved stars [e.g. Shporer et al., 2016], and those with solar-type

stars, such as some of the Kepler Heartbeat stars [Price-Whelan and Goodman, 2018] and systems containing close-in giant planets. Our general equations can be used to track the spin and orbital evolution of a star in a binary system to answer questions such as how often binary systems will retain eccentricity at the onset of a common envelope phase and to reassess the importance of turbulent viscosity in the host star in the orbital decay of a giant planet.

One intriguing behavior that we did not discuss in this paper is resonance-locking. In this scenario, a system encounters a resonance between the frequency of a stellar oscillation mode and the orbital frequency. As the stellar spin and orbit (and perhaps the stellar structure) evolve, the mode frequency and orbital frequency change in lock-step, maintaining the resonance [Witte and Savonije, 1999, Fuller and Lai, 2012a]. Ivanov and Papaloizou [2004b] identified the possibility of a similar behavior where significant viscosity reduction in the primary could cause an eccentric binary to evolve through multiple resonances between the primary star's rotation rate and the orbital frequency. Orbital decay is significantly enhanced while a resonance persists (see Figs. 6.5, 6.6, and 6.7). In some binary stellar systems, resonance-locking may set the timescale for orbital decay.

CHAPTER 7

**TIDAL DISSIPATION IMPACT ON THE ECCENTRIC ONSET OF  
COMMON ENVELOPE PHASES IN MASSIVE BINARY STAR  
SYSTEMS**

## 7.1 Introduction

Common envelope phases occur in binary systems when one star evolves and grows in radius such that it impinges on the orbit of its companion. As the two stellar cores become subsumed within a shared envelope, they spiral closer under the influence of drag forces [van den Heuvel, 1976]. Thus, common envelope phases represent a brief but transformative episode in the evolution of many binary or multiple stellar systems [see, for example, the excellent reviews of Iben and Livio, 1993, Taam and Sandquist, 2000, Ivanova et al., 2013, De Marco and Izzard, 2017]. In transforming wide binaries into much more compact ones, common envelope phases are thought to be a crucial element in the assembly of compact binaries that merge and produce gravitational wave sources [e.g. Taam and Sandquist, 2000, Belczynski et al., 2002b, Kalogera et al., 2007, Belczynski et al., 2008, Dominik et al., 2012, Ivanova et al., 2013].

As recent work has focused on the common envelope phases that may lead to the formation of merging compact object binaries, it has become clear that some of the details of massive-star common envelope phases may be different from those in the previously-emphasized lower-mass systems [as described in the reviews of Taam and Sandquist, 2000, Ivanova et al., 2013]. In particular Kruckow et al. [2016] and Klencki et al. [2020] have studied pre-common envelope massive star structures, with a focus on de-

termining the binding energy of their envelopes, and Vigna-Gómez et al. [2020] performed a binary population synthesis study of all the common envelope phases that lead to eventual merging double neutron star systems within the COMPAS suite [Stevenson et al., 2017, Vigna-Gómez et al., 2018].

This focus on massive-star evolution in close binaries has revealed the significance of tidal interactions in shaping these objects [e.g. Kushnir et al., 2016]. In particular, in pre-common envelope systems, as the giant star evolves and grows in radius, there will be a period of time during which strong tides are active followed by eventual Roche-lobe overflow (RLO). In the massive-star progenitors of merging compact objects, it is not clear that tides will have sufficient time to act to always synchronize and circularize a system to the classic Roche-lobe geometry prior to RLO [Vigna-Gómez et al., 2020]. This paper applies new, more sophisticated models of tidal dissipation in giant star convective envelopes to study the impact of pre-common envelope tidal evolution. Our results, therefore, are of critical importance as the initial conditions for a subsequent common envelope or mass-transferring interaction.

There are two tidal dissipation mechanisms that can be important in a massive giant star with a radiative core and convective envelope. The first is turbulent viscosity, where the shearing of tidally driven fluid oscillations (fundamental and inertial modes) in the envelope is dissipated as heat [e.g. Zahn, 1977, Goodman and Oh, 1997, Ogilvie and Lin, 2007]. The other is radiative diffusion in the stellar interior [e.g. Goodman and Dickson, 1998, Savonije and Witte, 2002]. This second mechanism is most important when gravity waves are excited at the radiative-convective boundary and

grow in amplitude as they propagate inward. Eventually non-linear wave-braking dissipates all of the energy and angular momentum carried by the ingoing gravity wave [Goodman and Dickson, 1998, Barker and Ogilvie, 2010, 2011, Fuller and Lai, 2012b, Chernov et al., 2013, Ivanov et al., 2013, Bolmont and Mathis, 2016, Weinberg et al., 2017, Sun et al., 2018]. However, when the gravity waves do not become nonlinear, dissipation in the convective envelope drives orbital decay.

A large body of work has focused on orbital circularization and decay due to tidal dissipation in the convective envelope of a star of a close binary. An analytical treatment for tidal dissipation via turbulent viscosity was first developed by Zahn [1977]. Verbunt and Phinney [1995] presented a similar expression for the tidal circularization timescale for nearly circular binaries. The weak friction approximation [Hut, 1981] can be used more broadly to study the tidal evolution of binaries with any eccentricity [as in Hurley et al., 2002]. This model assumes that the star is tidally deformed into a static shape that lags behind the equipotential surface — an approximation that holds when the tidal forcing frequency,  $\omega$ , is much lower than the dynamical frequency of the star  $\sim (GM_1/R_1^3)^{-1/2}$  (for a star with mass  $M_1$  and radius  $R_1$ ). The model also assumes that turbulent viscosity is equally effective at dissipating energy for all tidal forcing frequencies. In reality, the turbulent viscosity is reduced when the timescale for tidal forcing  $\sim \omega^{-1}$  is shorter than the turnover time for the largest convective eddies in the star  $\tau_{\text{eddy}}$ . Two conflicting scaling laws have been suggested for the form of the viscosity reduction. Zahn [1989] proposed the linear reduction  $1/(1 + \omega\tau_{\text{eddy}})$ , while Goldreich and Nicholson [1977] favored  $1/[1 + (\omega\tau_{\text{eddy}})^2]$ . The latter is the standard result for a damped

harmonic oscillator with frequency  $\omega$  and damping time  $\tau_{\text{eddy}}$ . Recently, numerical and analytical studies have generally supported a quadratic reduction factor [Penev and Sasselov, 2011, Penev et al., 2011, Ogilvie and Lesur, 2012, Duguid et al., 2019]. Though numerical simulations from Vidal and Barker [2020] suggest that both scaling relations may be correct in different regimes of the tidal forcing frequency.

Vick and Lai [2019b] developed a general formalism for tidal evolution in an eccentric binary. Their treatment is accurate at close separations where  $\omega$  begins to approach  $(GM_1/R_1^3)^{-1/2}$  and accounts for frequency dependent damping of tidally-driven oscillations. It also recovers the standard results of the weak friction approximation for binaries with larger separations. Vick and Lai [2019b] demonstrated that, for a giant star in a close binary, viscosity reduction typically is not important. However, the rate of tidal circularization can be orders of magnitude faster than predicted by the weak friction approximation for highly eccentric binaries where the ratio of the pericentre distance  $r_p$  to stellar radius is  $\sim$  a few.

In this paper, we study the coupled role of stellar evolution and tidal dissipation in shaping pre-common envelope systems by applying the tidal theory in Vick and Lai [2019b]. In Section 7.2, we introduce the tools that we use to tackle this problem — MESA generated stellar evolution models [Paxton et al., 2011] and the formalism from Vick and Lai [2019a] — and discuss how we couple the two. In Section 7.3, we present and categorize the outcomes of concurrent stellar evolution and tidal orbital circularization. We focus on the orbital eccentricity and the primary star rotation rate at the onset of RLO. We also explore how tidal dissipation affects the distribution of those properties at the onset of binary mass transfer given an

initial distribution of orbital parameters when the primary star leaves the main sequence. We discuss the limitations and significance of our results in Section 7.4, and we summarize and conclude in Section 7.5.

## 7.2 Theory of Tidal Dissipation in Eccentric Binaries

In order to understand the coupled role of stellar evolution and tidal dissipation we need: (i) a time-dependent model of the structure of the massive star after it has left the main sequence; (ii) an understanding of how the timescale for tidal dissipation changes with the stellar structure; and (iii) a framework for calculating the tidal energy and angular momentum transfer rates given the current orbit and tidal dissipation rate.

The weak friction model [Alexander, 1973, Hut, 1981] is commonly used to describe equilibrium tidal interactions. In this model, the gravitational potential of a companion raises a tidal bulge on the primary star. When the binary orbit is eccentric or the primary is not synchronously rotating, the bulge lags behind the axis connecting the two bodies. The magnitude of the lag angle depends on the rate at which the star can dissipate the energy in tidally excited fluid motion. This picture of a static tidal bulge relies on the assumption that the timescale for strong tidal interactions in the binary is longer than the dynamical response time of the star.

When the primary star evolves off of the main sequence, the binary separation is large compared to the stellar radius, and tidal interactions are weak. However, as the stellar radius expands, the primary experiences a stronger tidal potential from its companion. Additionally, the timescale for strong tidal interactions in the binary (roughly the duration of a pericen-

tre passage) begins to approach the dynamical time of a giant star. Under these conditions, the standard weak friction model of tides is no longer accurate, and can severely underestimate the strength of tidal interactions. We use the theory of dissipation in a giant star in an eccentric orbit developed in Vick and Lai [2019b] to study how stellar evolution and tidal dissipation jointly shape the orbital evolution of the binary.

### 7.2.1 Stellar Models

We have used version 11701 of the MESA stellar evolution code to calculate the structural evolution of  $10M_{\odot}$  and  $15M_{\odot}$  stars from the end of the main sequence to carbon depletion [Paxton et al., 2011]. We assumed an initial metallicity of  $Z = Z_{\odot} = 0.0142$  [Asplund et al., 2009], and used the “Dutch” wind scheme. The inlist to reproduce our calculations is available at the MESA Marketplace ([http://cococubed.asu.edu/mesa\\_market/inlists.html](http://cococubed.asu.edu/mesa_market/inlists.html)). The result is a suite of stellar profiles at different time stamps in the star’s evolution. The time interval between profiles ranges from 10 years (during periods of rapid radius expansion) to  $5 \times 10^5$  years when the stellar structure is relatively static.

At each timestep, we used the code GYRE to calculate the eigenfrequency and mode profile of the stellar  $l = 2$  f-mode for a given MESA model (assuming no rotation) [Townsend and Teitler, 2013]. We implemented a vacuum outer boundary and a zero radial displacement inner boundary. For models with a convective envelope, the transition between the core and envelope was used as the location of the inner boundary. We used

the condition on the convective velocity  $v_c(r) > 10^3$  cm/s to identify  $r_c$ , the start of the envelope. For models from earlier in the star's evolution, before the development of deep convection, we chose an inner boundary just outside of the composition transition from predominantly hydrogen to predominantly helium.

### 7.2.2 Calculation of the Tidal Dissipation Rate in a Giant Star

As the primary  $M_1$  transitions to core helium burning, the star develops a deep convective envelope. Within this outer region, turbulent viscosity can dissipate tidally excited fluid motion, sapping energy and angular momentum from the orbit.

#### Order of Magnitude Calculation

A simple estimate of the tidal circularization time for a nearly-circular binary is provided in, e.g. Zahn [1977], Phinney [1992]; and Verbunt and Phinney [1995]. Assuming that the viscosity in the convective envelope is a constant value  $\nu_0$ , we can estimate the damping rate of a tidally forced oscillation as,

$$\gamma_{\text{est}} \sim \frac{M_{\text{env}}}{M_1} \left( \frac{\nu_0}{H^2} \right) \sim \frac{M_{\text{env}}}{M_1} \left( \frac{L}{M_{\text{env}} R_1^2} \right)^{1/3}, \quad (7.1)$$

where  $H$  is the pressure scale-height (and the length-scale of the largest convective eddies),  $M_{\text{env}}$  is the mass of the envelope, and  $L$  is the convective luminosity. We have used  $\nu_0 \sim H(L/4\pi\rho R_1^2)^{1/3}$  and  $M_{\text{env}} \sim 4\pi\rho H^3$ , where  $\rho$  is the average density in the convective envelope. For a nearly circular

orbit, this damping rate is related to the binary circularization time  $\tau_{\text{circ}}$  via,

$$t_{\text{circ}} \equiv \left| \frac{\dot{e}}{e} \right| \sim \frac{1}{\gamma_{\text{est}}} \left( \frac{M_1}{M_2} \right) \left( \frac{M_1}{M_t} \right) \left( \frac{a}{R_1} \right)^8, \quad (7.2)$$

with  $M_2$  the mass of the companion,  $M_t = M_1 + M_2$  and semi-major axis  $a$  [see Phinney, 1992].

With a given stellar profile, we can also calculate the damping time for a forced oscillation more precisely. The response of  $M_1$  to the tidal potential of  $M_2$  will be dominated by the quadrupolar  $l = 2$  terms (if the binary is sufficiently separated). When the turnover time for the largest convective eddies is shorter than the timescale for tidal forcing, the viscosity in the envelope is not reduced, and the damping rate is independent of the forcing frequency ( $\omega = 2\Omega - 2\Omega_s$  in a circular orbit). In a red giant star, the eddy turnover time in the convective envelope is typically short relative to the tidal forcing period, and this condition is satisfied while  $\omega \ll (GM_1R_1^{-3})^{1/2}$  [see the top panel of Fig. 2 in Vick and Lai, 2019b].

### Weak Friction Approximation and Nearly Circular Orbits

When the viscous damping rate in the envelope is independent of the tidal forcing frequency, the tidal dissipation rate can be framed in terms of the stellar tidal Love number and lag time. If the tidal forcing period is much longer than the dynamical time of the star, this treatment is equivalent to the weak friction approximation. For an  $l = 2$  f-mode oscillation in a slowly rotating body, the real part of the tidal Love number is,

$$k_2 \simeq \frac{4\pi}{5} \left( \frac{Q_f}{\bar{\omega}_f} \right)^2, \quad (7.3)$$

where  $Q_f$  is an overlap integral defined in equation (38) of Press and Teukolsky [1977], normalized such that  $G = M_1 = R_1 = 1$ , and  $\omega_f \equiv \bar{\omega}_f (GM_1/R_1^3)^{1/2}$  is the f-mode frequency. The tidal lag time is given by,

$$\tau \equiv \frac{\gamma_f}{\omega_f^2}, \quad (7.4)$$

with  $\gamma_f$  the damping rate of the  $l = 2$  f-mode due to turbulent viscosity. Assuming that the flow is incompressible, the viscous damping rate is given by,

$$\begin{aligned} \gamma_f \equiv & \frac{1}{4} \int_{r_c}^{R_1} dr r^2 \rho(r) v(r) \left[ 4 \left( \frac{d\xi_r}{dr} \right)^2 \right. \\ & + 2l(l+1) \left( \frac{d\xi_h}{dr} + \frac{\xi_r}{r} - \frac{\xi_h}{r} \right)^2 \\ & \left. + 2 \left( l(l+1) \frac{\xi_h}{r} - 2 \frac{\xi_r}{r} \right)^2 \right], \end{aligned} \quad (7.5)$$

where  $\xi_r$  and  $\xi_h$  are the radial and horizontal Lagrangian displacement vectors for the  $l = 2$  f-mode [Landau and Lifshitz, 1959, Sun et al., 2018, Vick and Lai, 2019b].

Under the condition that the tidal forcing frequency  $\omega \ll \omega_f$ , we can express the circularization rate for a synchronously rotating star in a nearly circular binary as, [Darwin, 1880, Alexander, 1973, Hut, 1981]

$$\frac{\dot{e}}{e} = -\frac{21}{2} k_2 \tau \Omega^2 \frac{M_2}{M_1} \left( \frac{R_1}{a} \right)^5, \quad (7.6)$$

where  $\Omega = (GM_t/a^3)^{1/2}$  is the orbital frequency. By comparing equation (7.6) to equation (7.2), We find that the effective damping rate from tidal dissipation is,

$$\gamma_{\text{eff}} \equiv \frac{21}{2} k_2 \tau \left( \frac{GM_1}{R_1^3} \right). \quad (7.7)$$

## Theory of Tides and Dissipation in an eccentric binary

Vick and Lai [2019a] developed a general formalism for the treatment of tidal dissipation in the convective envelope of a star in an eccentric binary. Here, we summarize the key results.

The quadrupolar tidal potential experienced by the primary star  $M_1$  from the companion  $M_2$  can be decomposed into a sum over many forcing frequencies,

$$\omega_{Nm} \equiv N\Omega - m\Omega_s, \quad (7.8)$$

where  $N$  is an integer. In the rotating frame of the primary, the potential is given by

$$U(\mathbf{r}, t) = - \sum_m \sum_{N=-\infty}^{\infty} U_{Nm} r^2 Y_{2m}(\theta, \phi) e^{-i\omega_{Nm} t}, \quad (7.9)$$

where  $\mathbf{r} = (r, \theta, \phi)$  is the position vector in spherical coordinates relative to the center of mass of the primary star, and the angle  $\phi$  is measured in the rotating frame of  $M_1$ . Throughout the paper, we assume that the spin-axis of  $M_1$  is aligned with the orbital angular momentum axis. We define

$$U_{Nm} \equiv \frac{GM_2}{a^3} W_{2m} F_{Nm} \quad (7.10)$$

with  $F_{Nm}$  given by

$$F_{Nm} = \frac{1}{\pi} \int_0^\pi d\Psi \frac{\cos[N(\Psi - e \sin \Psi) - m\Phi(t)]}{(1 - e \cos \Psi)^2}. \quad (7.11)$$

Only the  $m = 0, \pm 2$  terms are nonzero, with  $W_{20} = \sqrt{\pi/5}$  and  $W_{2\pm 2} = \sqrt{3\pi/10}$ .

The tidal response of  $M_1$  is a weighted sum of the response to each frequency term in the tidal potential. Vick and Lai [2019b] derived general expressions for the tidal torque and energy transfer rate (see their equations 26 and 27). For a giant star, the tidal forcing time is often longer than

the eddy turnover time, and viscosity reduction is negligible. We therefore approximate the f-mode dissipation rate as the frequency-independent  $\gamma_f$  from equation (7.5), and obtain the tidal energy transfer rate in the inertial frame and the tidal torque:

$$T = T_0 \sum_{mN} \left( \frac{Q_f}{\bar{\epsilon}_f} \right)^2 \frac{m \gamma_f (W_{2m} F_{Nm})^2 \omega_{Nm}}{(\omega_f - \omega_{Nm})^2 + \Gamma_f^2(\omega_{Nm})}, \quad (7.12)$$

$$\dot{E}_{in} = T_0 \Omega \sum_{mN} \left( \frac{Q_f}{\bar{\epsilon}_f} \right)^2 \frac{N \gamma_f (W_{2m} F_{Nm})^2 \omega_{Nm}}{(\omega_f - \omega_{Nm})^2 + \Gamma_f^2(\omega_{Nm})}, \quad (7.13)$$

where  $\epsilon = \bar{\epsilon}(GM_1/R_1^3)^{1/2}$  is defined in equation (13) of Vick and Lai [2019b], and  $\Gamma_f = \gamma_f \omega_{Nm}/\epsilon_f$ . For convenience, equations (7.12) and (7.13) can be rewritten in the form

$$T = 3T_0 k_2 \tau \frac{\Omega}{(1 - e^2)^6} F_T(e, \Omega_s/\Omega, r_p/R_1), \quad (7.14)$$

$$\dot{E}_{in} = 3T_0 k_2 \tau \frac{\Omega^2}{(1 - e^2)^{15/2}} F_E(e, \Omega_s/\Omega, r_p/R_1), \quad (7.15)$$

with dimensionless

$$F_T(e, \Omega_s/\Omega, r_p/R_1) = \frac{5}{12\pi} \left( \frac{\bar{\omega}_f}{Q_f} \right)^2 \left( \frac{\omega_f^2}{\gamma_f \Omega} \right) (1 - e^2)^6 \times \sum_{Nm} \left( \frac{Q_f}{\bar{\epsilon}_f} \right)^2 \frac{m (W_{2m} F_{Nm})^2 \omega_{Nm} \gamma_f}{(\omega_f - \omega_{Nm})^2 + \Gamma_f^2(\omega_{Nm})}, \quad (7.16)$$

$$F_E(e, \Omega_s/\Omega, r_p/R_1) = \frac{5}{12\pi} \left( \frac{\bar{\omega}_f}{Q_f} \right)^2 \left( \frac{\omega_f^2}{\gamma_f \Omega} \right) (1 - e^2)^{15/2} \times \sum_{Nm} \left( \frac{Q_f}{\bar{\epsilon}_f} \right)^2 \frac{N (W_{2m} F_{Nm})^2 \omega_{Nm} \gamma_f}{(\omega_f - \omega_{Nm})^2 + \Gamma_f^2(\omega_{Nm})}. \quad (7.17)$$

In the weak friction limit,  $F_T$  and  $F_E$  become the standard

$$F_{T,WF} = f_2 - (1 - e^2)^{3/2} f_5 \frac{\Omega_s}{\Omega}, \quad (7.18)$$

$$F_{E,WF} = f_1 - (1 - e^2)^{3/2} f_2 \frac{\Omega_s}{\Omega}, \quad (7.19)$$

where  $f_1$ ,  $f_2$ , and  $f_5$  are functions of eccentricity defined in Hut [1981]. However, for highly eccentric orbits with small pericentre distances  $r_p$ , the

dimensionless torque and energy transfer rate can be much larger than the weak friction calculation suggests [see Fig. 5 of Vick and Lai, 2019b].

### 7.2.3 Coupling the Stellar and Orbital Evolution

In order to couple the stellar evolution and orbital evolution, we use the stellar oscillation code GYRE to calculate the properties of the f-mode (i.e.  $\gamma_f$ ,  $\bar{\omega}_f$ ,  $\bar{\epsilon}_f$ , and  $Q_f$ ). We then use spline interpolation to obtain the stellar mass, radius, and mode properties as a function of time.

The time evolution of  $a$ ,  $e$ , and  $\Omega_s$  is given by the following equations:

$$\frac{\dot{a}}{a} = \left. \frac{\dot{a}}{a} \right|_{\text{Tides}} + \left. \frac{\dot{a}}{a} \right|_{\text{Wind}} \quad (7.20)$$

$$\frac{\dot{\Omega}_s}{\Omega_s} = \left. \frac{\dot{\Omega}_s}{\Omega_s} \right|_{\text{Tides}} - \frac{\dot{I}}{I}, \quad (7.21)$$

$$\frac{\dot{e}}{e} = \left. \frac{\dot{e}}{e} \right|_{\text{Tides}}, \quad (7.22)$$

where  $I = \eta M_1 R_1^2$  is the moment of inertia of the primary, and the time evolution of  $\eta$ ,  $M_1$ , and  $R_1$  is taken from the MESA stellar models. The tidal energy transfer and torque can be combined to determine the tidal contributions to the orbital evolution,

$$\left. \frac{\dot{a}}{a} \right|_{\text{Tides}} = -\frac{6}{t_d(1-e^2)^{15/2}} F_E(e, \Omega_s/\Omega, r_p/R_1), \quad (7.23)$$

$$\left. \frac{\dot{\Omega}_s}{\Omega_s} \right|_{\text{Tides}} = \frac{3}{t_d(1-e^2)^6} \left( \frac{\mu a^2 \Omega}{I \Omega_s} \right) F_T(e, \Omega_s/\Omega, r_p/R_1), \quad (7.24)$$

$$\left. \frac{\dot{e}}{e} \right|_{\text{Tides}} = -\frac{27}{t_d(1-e^2)^{13/2}} F_{\text{ecc}}(e, \Omega_s/\Omega, r_p/R_1), \quad (7.25)$$

where  $\mu = M_1 M_2 / M_t$  is the reduced mass of the binary and,

$$t_d^{-1} \equiv \frac{T_0}{\mu a^2} k_2 \tau = \left( \frac{M_2}{M_1} \right) \left( \frac{M_1 + M_2}{M_1} \right) \left( \frac{R_1}{a} \right)^8 k_2 \frac{\gamma_f}{\bar{\omega}_f^2}. \quad (7.26)$$

We have combined  $F_E$  and  $F_T$  to characterize the eccentricity evolution via,

$$F_{\text{ecc}} = \frac{1}{9} \frac{(1-e^2)}{e^2} \left[ \frac{F_E}{(1-e^2)} - F_T \right]. \quad (7.27)$$

We assume isotropic wind mass loss, such that the wind-driven secular time evolution of the semi-major axis is,

$$\left. \frac{\dot{a}}{a} \right|_{\text{Wind}} = - \frac{\dot{M}_1}{M_t}, \quad (7.28)$$

and the eccentricity is unchanged. We define the circularization time of the binary as,

$$t_{\text{circ}} \equiv \left| \frac{e}{\dot{e}} \right|. \quad (7.29)$$

As the binary circularizes, the tidal torque will cause the star to spin up to the pseudosynchronous rotation rate, where the star experiences no net torque. In the weak friction approximation, the pseudosynchronous rotation rate is given by,

$$\Omega_{\text{ps}} = \frac{f_2}{f_5(1-e^2)^{3/2}} \Omega, \quad (7.30)$$

For a highly eccentric orbit, the true pseudosynchronous rotation rate, where  $\dot{\Omega}_s$  is zero, can occur at slightly faster rotation rates than given by equation (7.30) [Vick and Lai, 2019b]. In a circular orbit,  $f_2$  and  $f_5$  are 1, and the synchronous rotation rate is the orbital frequency.

When the binary is sufficiently close, mass transfer will become important, and equations (7.23) - (7.25) will no longer capture the orbital evolution. The onset of mass transfer occurs when the primary is Roche-lobe filling. A precise calculation of the Roche radius depends on both the stellar spin and orbital eccentricity [e.g. Sepinsky et al., 2007a]. For simplicity, we use a common approximation adapted from Eggleton [1983],

$$r_{\text{Roche}} = r_p \frac{0.49q^{2/3}}{0.6q^{2/3} + \ln(1+q^{1/3})}, \quad (7.31)$$

where  $r_p$  is the pericentre distance and  $q = M_1/M_2$  is the mass ratio. For a binary with a companion of mass  $M_2 = 1.4M_\odot$ , the primary fills its Roche-lobe when  $r_p \approx 1.8R_1$  for  $M_1 = 10M_\odot$  and when  $r_p \approx 1.7R_1$  for  $M_1 = 15M_\odot$ .

## 7.3 Results

### 7.3.1 Tidal Dissipation Rate as a Function of Stellar Evolution

We have used the MESA-generated stellar models introduced in Section 7.2.3 to understand the tidal dissipation timescale of a star after it leaves the main sequence.

Figure 7.1 displays changes in the stellar radius and structure of the  $10 M_\odot$  and  $15 M_\odot$  stellar models as they evolve from core hydrogen burning to carbon depletion (at which point the collapse of the core is imminent). The top panel shows that the bulk of the radius evolution occurs in two bursts. On the giant branch, the radius expands by a factor of  $\sim 40$  for the  $10 M_\odot$  model and  $\sim 60$  for the  $15 M_\odot$  model. As the radius expands, the structure of the star changes significantly. The middle panels of Fig. 7.1 show that the stars develop deep convective envelopes during the first episode of radius expansion. Once the envelope has developed, turbulent viscosity in the envelope is the most efficient mechanism for tidal dissipation in the star. The bottom panels of Fig. 7.1 display the damping rate from viscous dissipation, calculated via equation (7.7). This calculation assumes a significant convection zone within the star, and likely does not capture the tidal dissipation rate of the star before the envelope begins to

develop. We can compare the more precise calculation of  $\gamma_{\text{eff}}$  with the convenient estimate from Zahn [1975], Phinney [1992], Verbunt and Phinney [1995] provided in equation (7.1), and find that, while  $\gamma_{\text{eff}}$  is smaller than  $\gamma_{\text{est}}$ , they agree within a factor of a few.

For many binaries, the timing of when deep convection of the outer envelope develops in the primary will determine whether tides can play an important role in circularizing the orbit before the onset of RLO. Before the convective envelope forms, tidal dissipation cannot circularize the orbit efficiently because the timescale for viscous dissipation is longer than the stellar evolution timescale. Figure 7.2 provides a zoom-in of the first episode of radius expansion in Fig. 7.1. The vertical black lines indicate the development of a significant convective envelope with  $M_{\text{env}} > 0.1M_1$ . For the  $10 M_\odot$  ( $15 M_\odot$ ) stellar model, this criterion is met when the radius has expanded by a factor of  $\sim 18$  ( $\sim 26$ ). Following helium ignition in the core, the stellar radius will further expand to  $\sim 43$  ( $\sim 66$ ) times its value at the end of the main sequence over the course of about  $2 \times 10^5$  yrs ( $2 \times 10^4$  yrs).

### 7.3.2 Tidal Circularization Timescale and the Binary Orbit

The tidal circularization timescale depends not only on the stellar structure, but also the binary orbital parameters and the spin rate of the primary. Figure 7.3 shows the tidal circularization time  $t_{\text{circ}}$  (see equations 7.25 and 7.29) as a function of the orbital eccentricity for a variety of pericentre values. The timescale is calculated for a non-rotating  $10 M_\odot$  primary that has already ascended the giant branch and developed deep convection in a binary with a  $1.4 M_\odot$  companion. We have used  $\gamma_{\text{eff}} = 0.4 \text{ yr}^{-1}$ , and

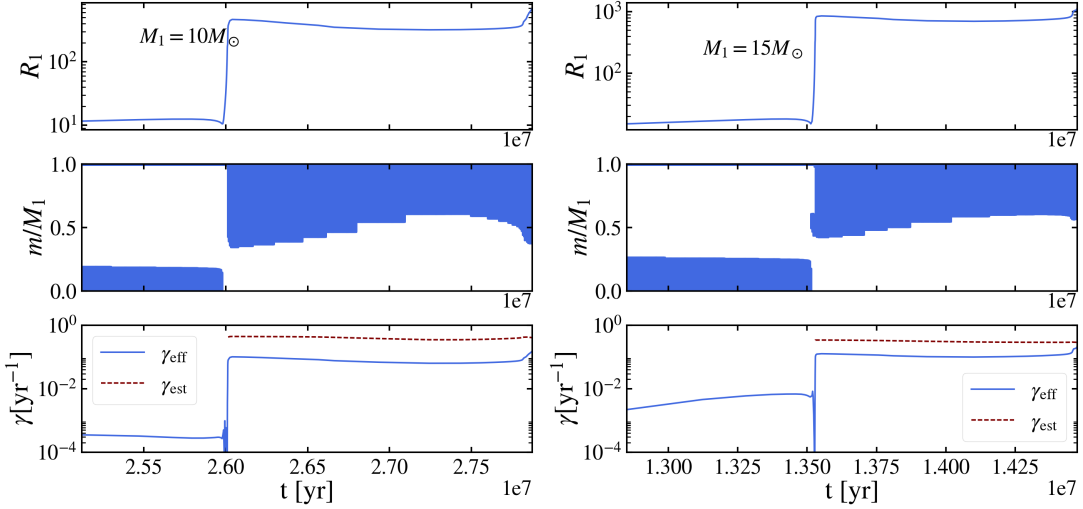


Figure 7.1: The evolution of the stellar structure and the effective tidal damping rate (from viscous dissipation in the convective envelope) for a  $M_1 = 10M_\odot$  (left) and  $M_1 = 15M_\odot$  (right) MESA-generated stellar model. The top panels show the evolution of the radius. The middle panels illustrate the convective regions in the stars. The bottom panels show the tidal damping rates for the stellar models calculated with equation (7.7) and compared with an estimate from equation (7.1).

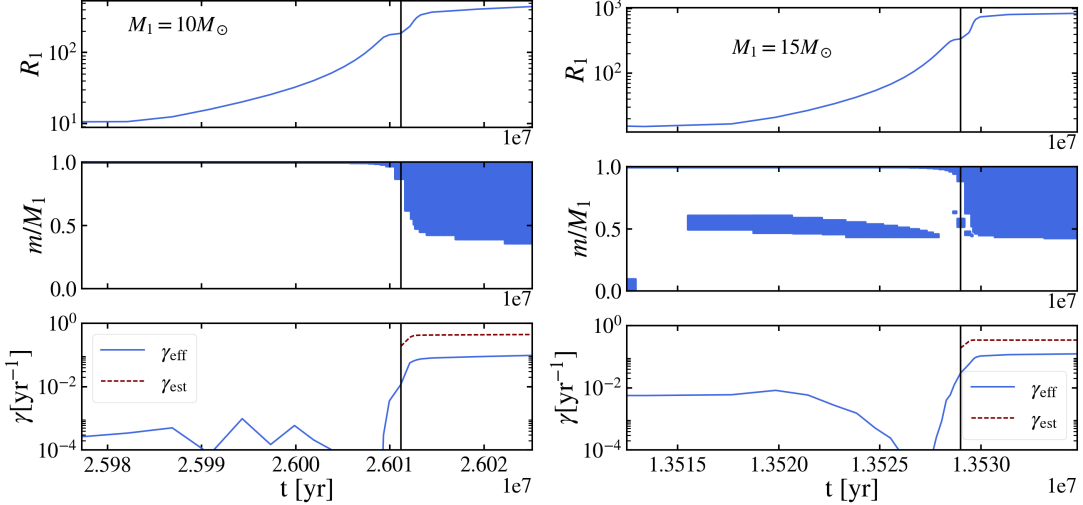


Figure 7.2: The same as Fig. 7.1 but zoomed-in on the first episode of radius expansion. The vertical black lines mark the development of a convective envelope with  $M_{\text{env}} > 0.1M_1$ . The viscous dissipation rates shown in the bottom panel likely do not capture tidal dissipation to the left of the black line before the development of the envelope.

set the f-mode frequency and damping rate to  $\omega_f = 1.75(GM_1/R_1^3)^{1/2}$  and  $\gamma_f = 0.04(GM_1/R_1^3)^{1/2}$ .

The circularization time depends very strongly on  $r_p/R$ , and is orders of magnitude shorter for tighter binaries. This timescale is also shortest for small orbital eccentricities. In Fig. 7.3, the circularization timescales for the two smallest pericentre distances,  $r_p/R_1 = 1.5$  and  $r_p/R_1 = 2.0$ , have a complicated dependence on the orbital eccentricity. This arises due to enhanced tidal dissipation at resonances between the orbital period and the f-mode frequency in the inertial frame.

Figure 7.3 also displays the standard weak friction calculation of the circularization timescale  $t_{\text{circ},WF}$  in the top panel (dashed lines). The bottom panel shows the ratio of  $t_{\text{circ}}$  to  $t_{\text{circ},WF}$ . The weak friction timescale is given by equation (7.25), but calculated with the dimensionless functions  $F_{T,WF}$  and  $F_{E,WF}$  from equations (7.18) and (7.19). The weak friction approximation is valid when the dominant tidal forcing frequency, of order the pericenter frequency  $\Omega_p = \Omega(1 + e)^{1/2}/(1 - e)^{3/2}$ , is much slower than the f-mode frequency, which is of order  $(GM_1/R_1^3)^{1/2}$ . At large  $r_p/R_1$  and small eccentricity, where  $\Omega_p \ll (GM_1/R_1^3)^{1/2}$ , the two timescales  $t_{\text{circ}}$  and  $t_{\text{circ},WF}$  are in good agreement. However, for larger  $e$  and smaller  $r_p$  the weak friction calculation overestimates the circularization timescale by a few orders of magnitude.

As the radius of the primary expands,  $r_p/R_1$  rapidly decreases. Figure 7.4 shows  $t_{\text{circ}}$  for the  $10 M_\odot$  stellar model assuming a fixed orbit with  $e = 0.8$  and a given pericentre distances ( $r_p = 1.9, 3.8$ , or  $5.7$  au), and a non-rotating but evolving primary. The convective envelope does not develop until a little after  $2.6 \times 10^7$  yrs (indicated with a dotted black line in Fig. 7.4).

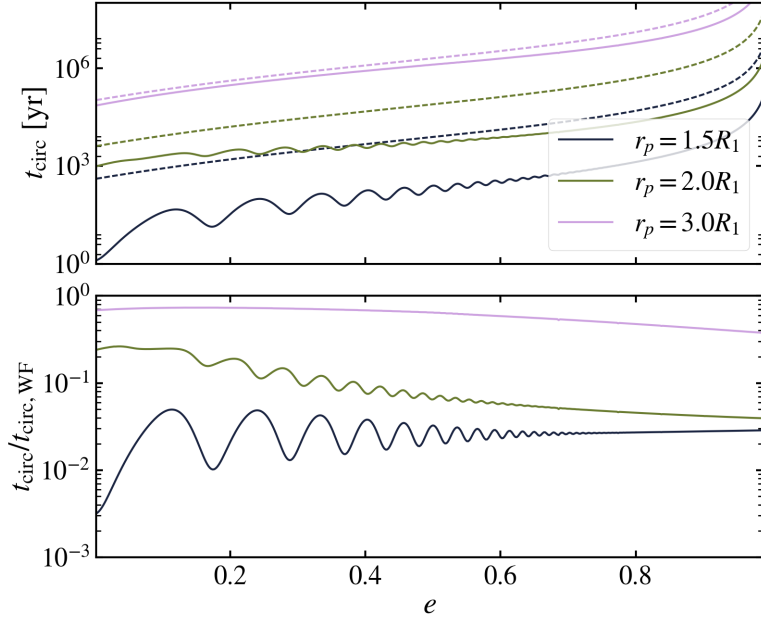


Figure 7.3: Circularization timescale ( $|e/\dot{e}|$ ) at a variety of pericenter distances for a binary with a  $1.4M_\odot$  companion as a function of eccentricity. The timescales were calculated assuming ... (essentially using the values for the giant star after the radius has expanded the first time). Dashed lines show the weak friction timescales. The bottom panel shows the ratio of the timescale to the weak friction timescale. As  $r_p$  increases, the ratio asymptotes to 1.

The dashed black red in the bottom panel is the Roche limit. The small black diamond indicates the onset of RLO for the  $r_p = 1.9$  au binary. In this system, the star reaches  $r_{\text{Roche}}$  within  $\sim 2 \times 10^3$  years of developing a convective envelope. This timescale is faster than  $t_{\text{circ}}$  for the binary (before crossing the red dashed line). Although the tidal circularization time is shortest for small  $r_p/R$ , tight binaries also have the shortest timescales for reaching RLO. Systems where  $r_p$  is too small will not have time to tidally circularize before the primary grows to  $r_{\text{Roche}}$ .

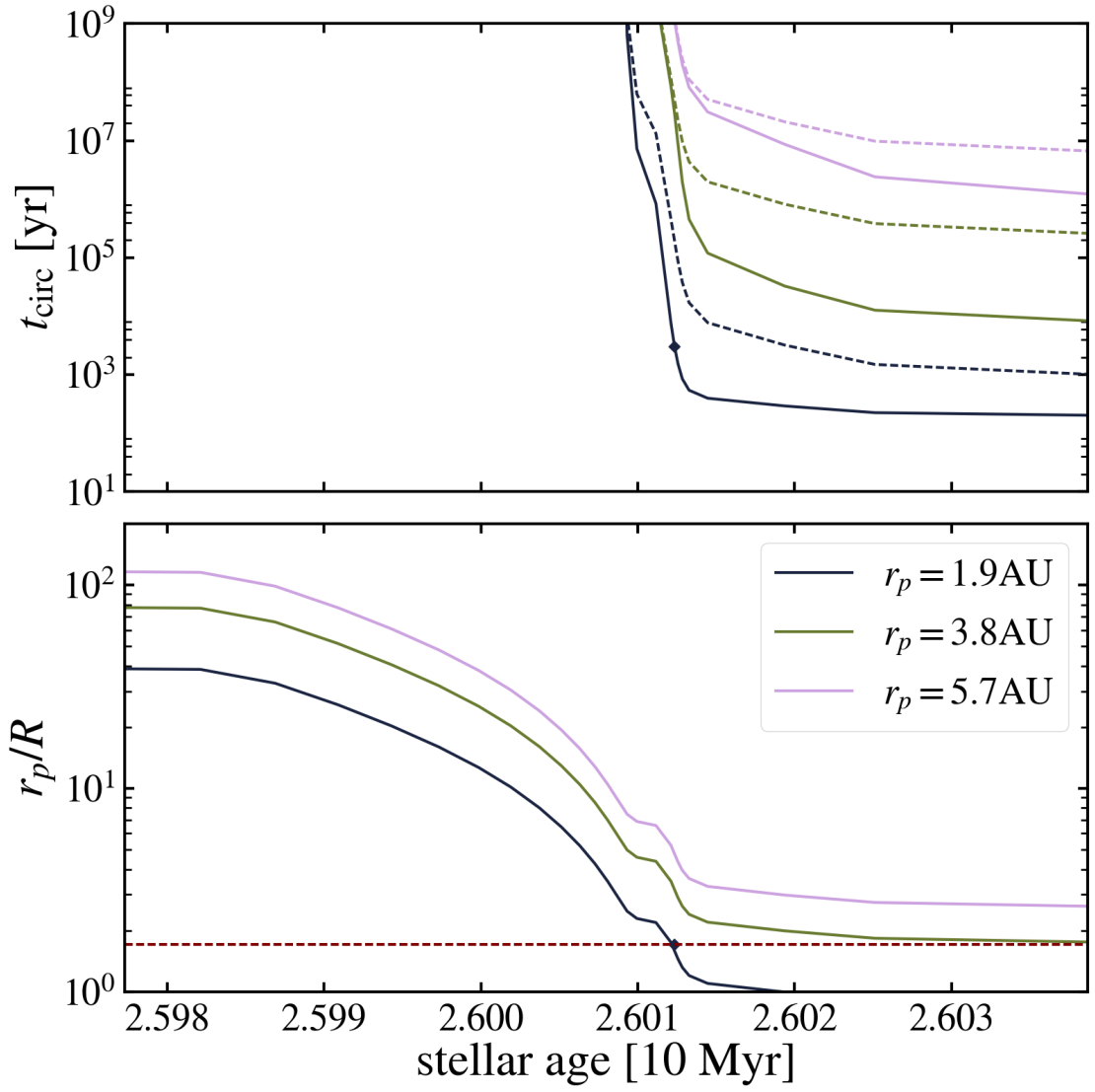


Figure 7.4: Top panel: The circularization timescale ( $\tau_{\text{circ}} = |e/\dot{e}|$ ) for a binary with  $M = 10M_\odot$  primary, a  $1.4M_\odot$  companion, and initial eccentricity  $e_0 = 0.8$ . The solid line shows the timescale calculated via equations (7.25) and (7.29), and dashed lines of the same color show the weak friction result for comparison. The black dotted line indicates when the convective envelope develops ( $M_{\text{env}} > 0.1M_1$ ). This calculation considers only changes in the stellar structure and radius. Bottom panel: The pericentre distance in units of the evolving stellar radius. The horizontal red dashed line is the condition for RLO.

### 7.3.3 Outcomes of Coupled Stellar and Orbital Evolution

Next, we present the results of coupled stellar and orbital evolution for binaries using the 10 and  $15 M_{\odot}$  stellar models and the method described in Section 7.2.3. Figure 7.5 highlights three possible outcomes of coupled orbital and stellar evolution. These are:

1. a binary that does not circularize before reaching the Roche-radius;
2. a binary that is tidally circularized before the primary evolves to  $R_1 = r_{\text{Roche}}$ ; and
3. a system that is too wide to undergo RLO.

In each case, the initial orbital eccentricity is  $e_0 = 0.8$  and the initial stellar rotation period is 1 day. The three different values of the initial pericentre separation  $r_{p,0}$  are the same as those used in Fig. 7.4.

For the smallest value of  $r_{p,0}$  the orbit does not circularize before the star grows to  $R_1 = r_{\text{Roche}}$ . There is not enough time between the development of the convective envelope and reaching the Roche radius for tidal dissipation in the envelope to circularize the orbit. The black diamonds in Fig. 7.5 mark the binary parameters and stellar rotation rate when  $R_1 = r_{\text{Roche}}$ . At this point the semi-major axis and eccentricity are essentially unchanged, while the rotation rate has slowed to conserve the spin angular momentum of the star as the radius expands.

In the intermediate case where  $e_0 = 0.8$  and  $r_{p,0} = 70R_{1,0}$ , the orbit circularizes significantly as the primary climbs the giant branch. The orbit continues circularizing when the primary ascends the asymptotic branch. In this case, the binary is nearly circular when  $R_1 = r_{\text{Roche}}$ . The rotation period of the primary is slightly longer than the predicted pseudosynchronous

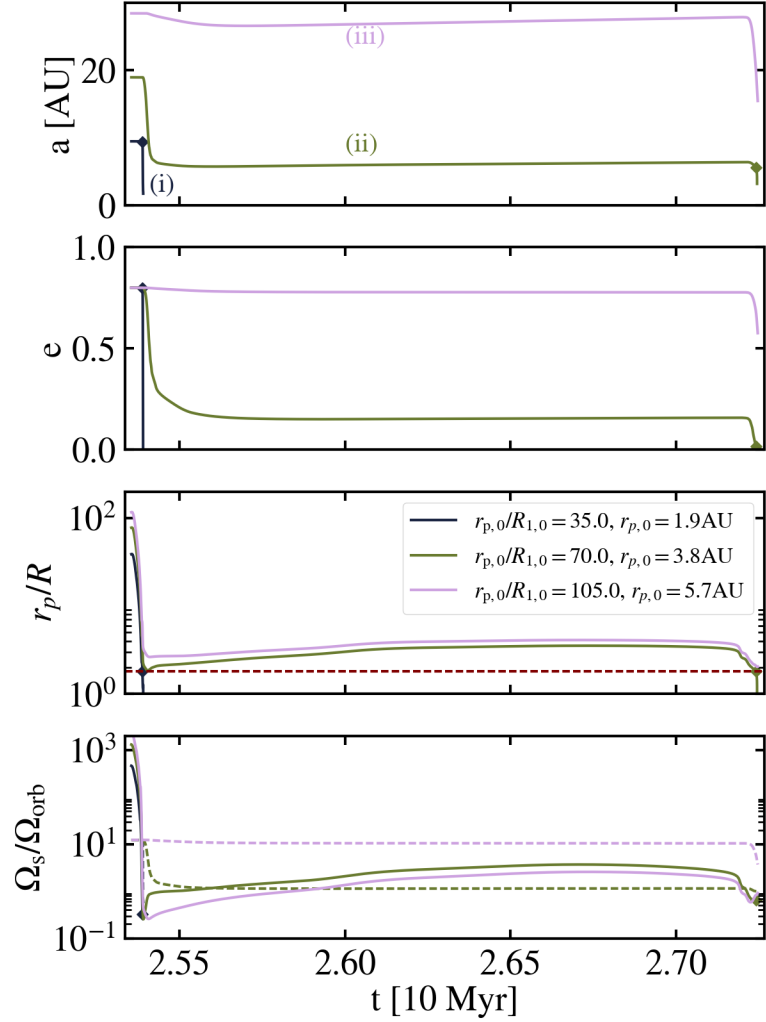


Figure 7.5: The orbital evolution of binary with a  $10M_\odot$  primary star, initial eccentricity  $e_0 = 0.8$ , and the same initial pericentre values  $r_{p,0}$  as in Fig. 7.4. The cases are numbered according to the outcomes listed at the start of Section 7.3.3. The top two panels are  $a$  and  $e$ . The third panel is  $r_p/R_1$ , with the Roche radius  $r_p = r_{\text{Roche}}$  indicated by the red dashed line. The bottom panel shows the rotation period of the star (solid lines) and the weak friction pseudosynchronous rotation rate from equation (7.30) (dashed lines). The diamonds in each panel indicate when a given binary reaches the criterion for RLO.

rate from the weak friction theory. As the star expands, its rotation slows down. This effect is in competition with the tidal torque, which acts to spin up the convective envelope. The resulting stellar rotation rate at  $R_1 = r_{\text{Roche}}$  is  $\sim 1.5$  times slower than the orbital frequency (which is the expected pseudosynchronous rotation rate for a nearly circular orbit).

In the final case, displayed as a pink line in Fig. 7.5, the initial pericentre distance is quite large. The binary cannot reach the criterion for RLO within the lifetime of the primary star. If we take the Roche radius as a hard limit for mass transfer, this binary is too widely separated to undergo a common envelope episode.

With an understanding of the main categories of outcome, we can survey results from a range of orbital configurations. Figures 7.6 and 7.7 display the binary eccentricity at the onset of RLO,  $e_{\text{Roche}}$ , for a variety of ‘initial’ orbital parameters when the primary star evolves off of the main sequence. We have assumed that stellar rotation period at this point is 1 day, but found that altering the initial spin has a negligible effect on  $e_{\text{Roche}}$ . For the  $10 M_{\odot}$  stellar model, binaries with  $r_{p,0} \lesssim 3$  AU on the main sequence do not circularize before reaching the Roche radius. The same is true of binaries with  $r_{p,0} \lesssim 6$  AU for the  $15 M_{\odot}$  stellar model. The orbital evolution of these binaries looks something like the black line from Fig. 7.5. Though the timescale for tidal circularization can become very short as the stellar radius expands, it is still longer than the time between when the primary develops a convective envelope and when the radius grows to the Roche limit. In some cases, the star cannot even develop a convective envelope before mass transfer begins (systems below the white dashed line in Figs. 7.6 and 7.7). These binaries retain their initial eccentricity from

before the primary leaves the main sequence.

In contrast, many binaries with an initial separation greater than  $\sim 4$  AU for a  $10 M_\odot$  primary or  $\sim 7$  AU for  $M_1 = 15 M_\odot$  circularize completely before RLO begins. In these binaries, the timescale between the onset of deep convection in the primary and radius growth to  $R_1 = r_{\text{Roche}}$  is longer than the tidal circularization timescale. The green line in Fig. 7.5 is an example of a system in this category.

Some binaries with large pericentre distances and high eccentricities will never undergo RLO. In Figs. 7.6 and 7.7, these systems lie above the solid black lines. They have the longest timescales for tidal circularization.

Figures 7.6 and 7.7 also display the rotation rate of the primary at the Roche radius as a fraction of the pseudosynchronous rotation rate (see equation 7.30). Before the primary develops a convective envelope, tides are inefficient at transferring angular momentum between the orbit and the star. The spin angular momentum of the star is effectively conserved, so the stellar rotation rate slows as the radius expands. For the  $10 M_\odot$  ( $15 M_\odot$ ) stellar model, in a binary with  $r_{p,0} \lesssim 3$  AU (6 AU) the stellar rotation rate at the Roche radius is given by  $\Omega_s = (k_0 M_{1,0} R_{1,0}^2) \Omega_{s,0} / (k M_1 R_1^2)$ , where the 0 subscript indicates the value when the star leaves the main sequence. When the star develops a convective envelope, its structure changes significantly as does the moment of inertia constant  $k$ . This change accounts for the sharp transition in the stellar rotation rate across the white dashed line in the right panels of Figs. 7.6 and 7.7. Both Figs. 7.6 and 7.7 show a light green curve in  $e_0$  and  $r_{p,0}$  below the black line that separates wide binaries (though this feature is far more obvious in Fig. 7.6). Systems above this ridge are nearly pseudosynchronous at the onset of

RLO. Below the ridge, the primary star grows to the Roche radius while on the giant branch. Above, the primary reaches  $R_1 = r_{\text{Roche}}$  on the asymptotic branch.

When  $r_{p,0}$  is slightly larger, tidal dissipation can alter the orbit before  $R_1 = r_{\text{Roche}}$ , and the tidal torque spins up the star to a rotation rate of order the orbital frequency. Note that this effect acts in opposition to the radius expansion, which decreases the stellar spin rate.

### 7.3.4 Tidal Circularization and the Eccentricity Distribution of pre-Common Envelope Stellar Binaries

We use the results from the Section 7.3.3 to understand how tidal dissipation should affect the distribution of binary eccentricities and stellar rotation rates at the Roche radius.

For simplicity, we begin with a thermal distribution in eccentricity and a loguniform distribution in semi-major axis (i.e.  $\sqrt{e}$  is drawn uniformly from  $[0, 1]$  and  $\log_{10}(a)$  from  $[-1, 3]$  au). We then reject any set of initial conditions with an eccentricity and pericentre outside of the range spanned by the grid of results in Figs. 7.6 and 7.7. This provides an initial distribution of  $r_{p,0}$  and  $e$  within the ranges  $7.5R_{1,0} < r_{p,0} < 122.5R_{1,0}$  and  $0.025 < e < 0.925$ . The initial eccentricity distribution is shown as the blue line in Fig. 7.8. We then group the initial orbital parameters into bins of width 0.05 in eccentricity and  $5R_{1,0}$  in pericentre distance that correspond to the grid in Figs. 7.6 and 7.7. We use the corresponding value of  $e_{\text{Roche}}$  for each bin in Figs. 7.6 or 7.7 to create a distribution of eccentricities at the Roche radius. Binaries that never reach RLO are removed from both

the initial eccentricity distribution and the Roche radius distribution. The resulting cumulative distribution functions for the two stellar models are shown as the light pink lines in Fig. 7.8. The dark red line shows the contribution to the eccentricity distribution from binaries where  $r_{p,0}$  is too small for the primary to develop a convective envelope before  $R_1 = r_{\text{Roche}}$ .

For both the  $10 M_\odot$  and  $15 M_\odot$  stellar models, the distribution of  $e_{\text{Roche}}$  is shifted toward lower eccentricities. For our choice of initial distribution of binary properties,  $e_{\text{Roche}} < 0.1$  for  $\sim 13\%$  of systems that reach RLO for the  $10 M_\odot$  star ( $\sim 4\%$  for the  $15 M_\odot$  star). However, higher values of  $e_{\text{Roche}}$  still contribute significantly to the distribution. This is consistent with the fact that many binaries will not have time to circularize before reaching the RLO criterion.

In Fig. 7.9, we provide the distribution of rotation rates for binaries that have circularized ( $e_{\text{Roche}} < 0.01$ ) before the primary reaches the Roche radius. This distribution was obtained in the same way as for  $e_{\text{Roche}}$  but by using results for  $\Omega_s$  rather than the orbital eccentricity. In the top row, we assume an initial stellar rotation period of  $P_{s,0} = 1$  day when the star leaves the main sequence. In the bottom row,  $P_{s,0} = 10$  days. Note that almost all systems are rotating subsynchronously (i.e.  $\Omega_s/\Omega_{\text{orb}} < 1$ ) at  $r_p = r_{\text{Roche}}$ . This is true regardless of the initial rotation period of the star. The subsynchronous rotation rates can be explained by competition between the tidal torque spinning up the star, and stellar expansion spinning the star down. Our results suggest that many giant stars may be rotating more slowly than expected at the onset of binary mass transfer.

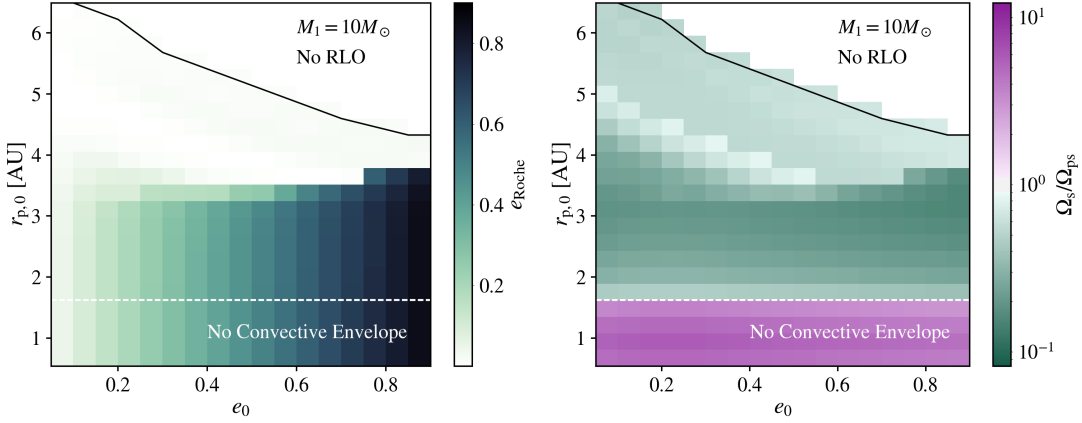


Figure 7.6: Left: Eccentricity at the Roche radius for a  $10M_{\odot}$  primary star with a  $1.4 M_{\odot}$  companion ( $r_p = 1.8R_1$ ). Right: The ratio of the stellar rotation rate  $\Omega_s$  to the weak friction pseudosynchronous rate  $\Omega_{ps}$  (see equation 7.30). Systems above the solid black line are too wide to merge within the lifetime of the primary star. Below the dashed white line,  $r_{p,0}$  is too small for the star to develop a convective envelope before  $r_p = r_{Roche}$ .

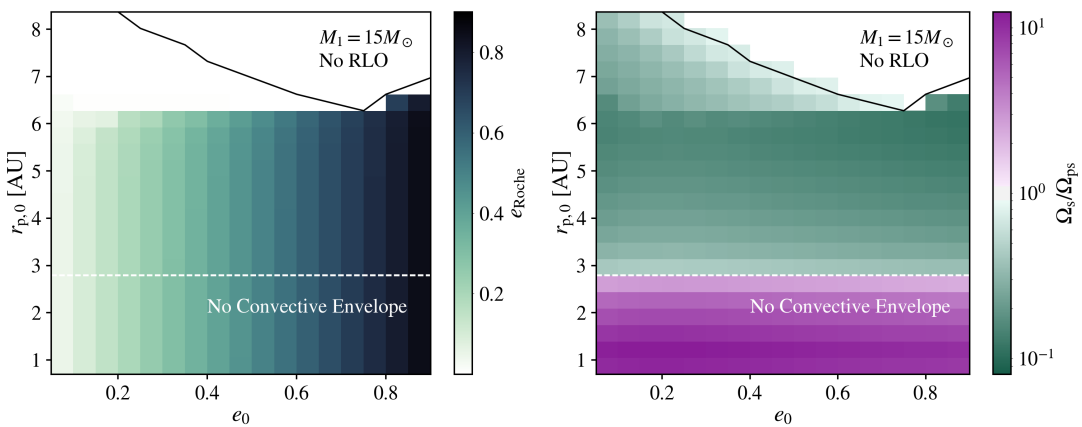


Figure 7.7: Same as in Fig. 7.6 but for the  $15M_{\odot}$  stellar model.

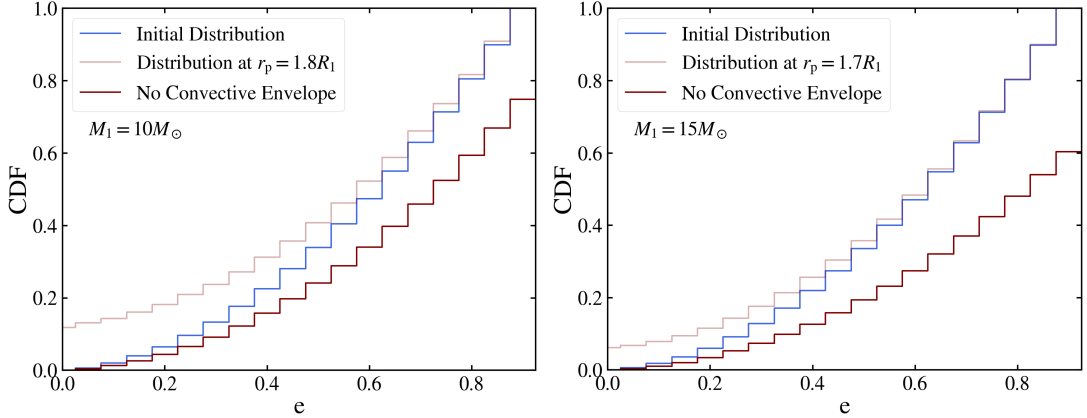


Figure 7.8: The cumulative distribution function of the binary eccentricities at the Roche radius for the  $10M_{\odot}$  stellar model (left) and  $15M_{\odot}$  stellar model (right) given a thermal initial eccentricity distribution. The light pink line is the eccentricity distribution of binaries for which  $r_{\text{Roche}}$  is smaller than the stellar radius at which the star develops a convective envelope ( $M_{\text{env}} > 0.1M_1$ ).

## 7.4 Discussion

Next we discuss some caveats associated with our analysis and the implications of our results for common envelope phases and their outcomes.

### 7.4.1 Possible Limitations

Throughout this paper, we focus on dissipation through turbulent viscosity in the convective envelope. In particular we use a linear treatment, and consider only the dissipation of the tidally excited  $l = 2$  fundamental mode. This formalism is most accurate when the binary separation is larger than a few times the stellar radius and when the primary star is slowly rotating. As the binary separation decreases, higher degree fundamental modes contribute more and more significantly to the tidal response of the star. When the binary orbital period is resonant with a fundamen-

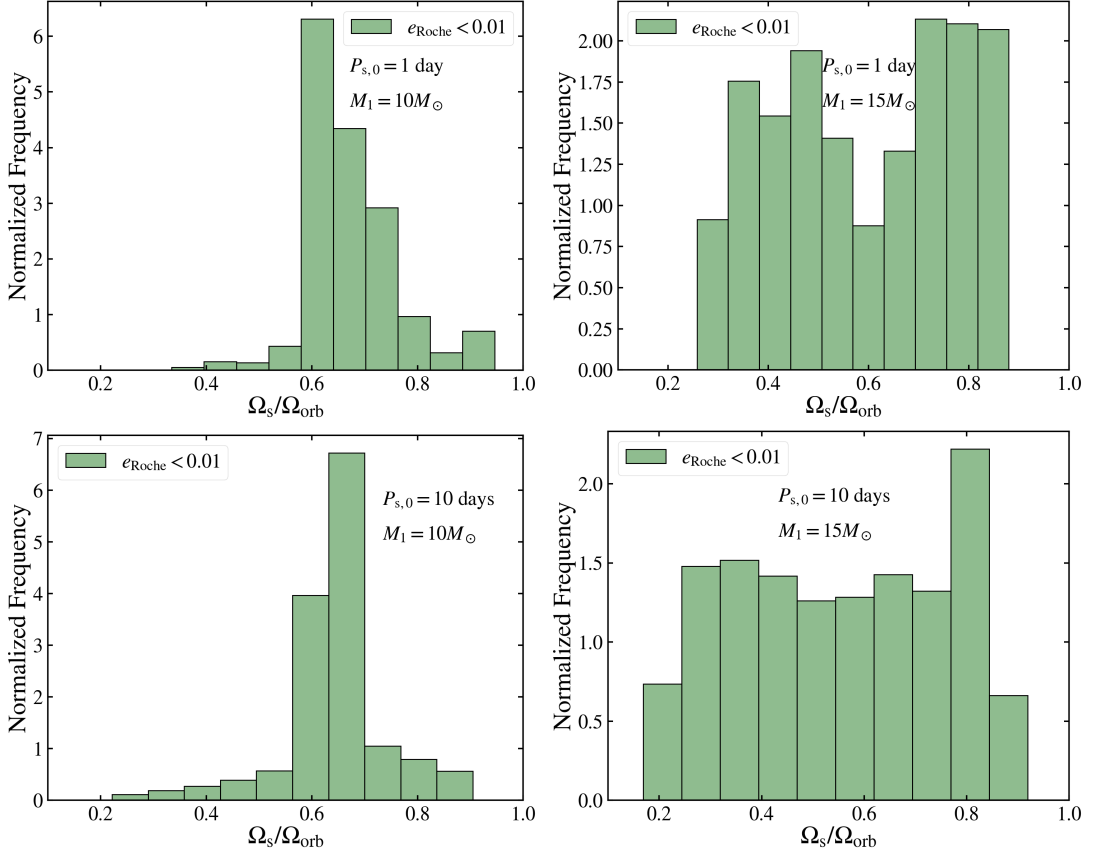


Figure 7.9: Histograms of the rotation rate as a fraction of the orbital frequency for systems with an eccentricity at the Roche radius of  $e_{\text{Roche}} < 0.01$ . The left and right panels show the rotation rate for the  $M_1 = 10 M_\odot$  and  $M_1 = 15 M_\odot$  stellar models respectively. The top and bottom panels show results for an initial rotation period of 1 day and 10 days respectively.

tal mode period, these higher degree oscillations can dominate the tidal response of the star [MacLeod et al., 2019], resulting in enhanced tidal dissipation. Including f-modes with higher  $l$  in our calculation would likely decrease the tidal circularization time at small orbital separations.

We have not included the contribution from inertial modes in our study of tidal dissipation in a giant star. Inertial modes are restored by the Coriolis force, and can be excited at smaller tidal forcing frequencies. In a circular orbit, the forcing frequency is  $2\Omega - 2\Omega_s$ . We expect that giant stars will

be slowly rotating after expanding, and for many systems, inertial waves will not contribute significantly to tidal dissipation [e.g. Ogilvie and Lin, 2007]. In cases where the tidal synchronization time is short enough that the primary is spun-up close to  $\Omega_s \sim \Omega$ , the presence of inertial waves may result in enhanced dissipation.

We have also ignored radiative diffusion within the core. Dissipation within the core is most important when ingoing gravity waves excited at the radiative-convective boundary can damp within a group velocity travel time to the center and back. In this ‘traveling wave’ regime, the dissipation rate is given by the luminosity of the ingoing wave. The calculation of the tidal torque from gravity waves in the radiative core was first carried out by Goodman and Dickson [1998] and later re-expressed in Kushnir et al. [2017]. The form of the tidal torque in Kushnir et al. [2017] reveals a strong dependence on the radius of the core/envelope boundary,  $r_c$ . The strength of the torque scales as  $(r_c/R_1)^9$ , where  $R_1$  is the radius of the star. In the massive giant stars that we are considering,  $r_c/R_1 \sim$  a few percent after the convective envelope has fully developed. In consequence, the tidal dissipation rate from damped internal gravity waves is negligible compared to dissipation in the envelope.

Lastly, when the binary has reached RLO, the magnitude of the tidal distortion can be of order  $\sim 10\%$  the size of the object (depending on the eccentricity), and we assume that mass loss takes over as the primary driver of subsequent orbital evolution. Under these conditions, our formalism is not expected to remain accurate. However, tidal dissipation may continue to play a large role in circularising the binary. As the binary separation continues to decrease, the interaction between the two bodies will only

become much stronger. For instance, in Fig. 7.5, when we extend our calculation beyond the Roche limit for the small separation case (the black line), the orbit fully circularizes before  $r_p = R_1$ . Eventually, the tidal distortion of the primary can no longer be treated as a perturbation, and tidally excited oscillations will likely damp non-linearly through, e.g., coupling between multiple oscillation modes. In cases where the donor star is not synchronously rotating, the strong distortion of the primary may have an interesting effect on mass transfer [e.g. as seen in the simulations of oscillating stars in MacLeod et al., 2019].

#### 7.4.2 Implications for Common Envelope Phases

Traditionally, we have imagined that common envelope phases largely result from unstable RLO in circular orbits [e.g. for recent examples of simulations of the onset of common envelope phases in circular orbits, see Ricker and Taam, 2008, 2012, Nandez et al., 2014, Nandez and Ivanova, 2016, Iaconi et al., 2017, MacLeod et al., 2018a,b, MacLeod and Loeb, 2020a,b]. This assumption is likely motivated by the fact that many near-contact binaries are largely circular, and by the simplicity associated with the circular-orbit limit. Further, circularized orbits are likely in common envelope systems involving lower-mass giants [e.g. Ivanova et al., 2013, Nandez et al., 2014], because the stellar evolution timescale is slow compared to the tidal dissipation timescale, which scales relatively weakly with stellar mass (as indicated, for example, by Equation (7.1)). The population synthesis models of Vigna-Gómez et al. [2020] and the more detailed analysis of this work, however, indicate that in many systems involving massive donors with lower-mass companions, the orbit does not circular-

ize prior to the onset of mass exchange.

This conclusion has several implications for the subsequent evolution of the system. Critically, the dynamics of eccentric mass transfer in binary systems are an area of very active study, including analytic predictions [Sepinsky et al., 2007b, 2009, 2010, Dosopoulou and Kalogera, 2016a,b, Dosopoulou et al., 2017, Hamers and Dosopoulou, 2019] and gas dynamical modeling [Church et al., 2009, Lajoie and Sills, 2011a,b, Staff et al., 2016, Bobrick et al., 2017]. In particular, the mass lost from the donor each peripase passage, and the angular momentum imparted to it determine the orbital evolution. It remains unclear whether systems will be expected to circularize following the onset of mass removal from the donor, or remain eccentric as the interaction proceeds. Because of these modifications in mass and angular momentum exchange, it is very likely that the binary eccentricity will affect the subsequent stability of mass exchange and thus determine whether or not the binary will undergo a common envelope phase.

The outcomes of common envelope phases may depend on the initial dynamics and eccentricity of the orbit in ways that are not yet clear. One hydrodynamic study of a common envelope phase with an eccentric onset has been carried out by Staff et al. [2016]. In these models, the binary typically consisted of a  $3.05M_{\odot}$  asymptotic giant branch donor interacting with a  $1.7M_{\odot}$  point-mass accretor, implying a mass ratio of approximately 0.55. The peripase was chosen such that the donor lost on the order of 10% of its own mass in the first passage, which had eccentricities varying between 0.33 and 0.7 across the models considered. Staff et al. [2016] found that after 2-3 passages, the donor's envelope had inflated sufficiently and

the eccentricity had decreased such that the accretor particle did not leave the donor’s envelope. After this point, Staff et al. [2016] argued that the ensuing common envelope phase carries qualitative similarity to models of common envelope phases that are initialized in circular orbits. Finally, Staff et al. [2016] noted that they are not able to estimate how eccentricity affects the final separation of their common envelope models, because it is limited by spatial resolution in their simulations.

It is worth noting that many simulations of common envelope phases that are initialized with circular orbits develop eccentricity as the objects plunge together [for some recent examples, see Ohlmann et al., 2016, Chamandy et al., 2018, Prust and Chang, 2019]. This may be due to artificial initial conditions in which the accretor is placed in a non-equilibrium configuration near the surface of the donor [see Figure 4 of Iaconi et al., 2017, for example]. However, the subsequent behavior that is observed is that this eccentricity is either maintained or is slow to dissipate as the orbital separation tightens [e.g. Figure 1 of Ohlmann et al., 2016]. At the simplest level, the details of these dynamics have to do with the relative drag forces at periapse and apoapse, which depend on the density profile of the common envelope as well as the relative velocities determined by the eccentric orbit.

These previous simulation results are suggestive that some eccentricity may be maintained by a common envelope system as it coalesces. In subsequent phases, as the orbital tightening slows, previous modeling suggests that remaining eccentricity may be reduced. The implications of this eccentricity for the orbital inspiral dynamics may lie largely in the way that the eccentric orbit impinges upon and modifies the structure of the

common envelope. This will be particularly true if an accretion disk forms around the accretor following each periapse passage [Staff et al., 2016], which might supply energetic feedback to the surroundings via a disk wind or jet [Shishkin and Soker, 2020]. The extreme case of this scenario, outlined by Shishkin and Soker [2020] is that the envelope is continuously removed and the objects never fully immerse into a shared envelope. Even in less extreme scenarios, as the objects spiral through a modified envelope structure we might expect variations in the resultant dynamics and common envelope outcome [e.g. as discussed in the context of drag forces by Chamandy et al., 2019].

The answers to many of these questions surrounding the importance of eccentricity in common envelope phase dynamics await future, more systematic study. Our present results indicate, however, that the eccentric onset of common envelope phases involving massive star donors may be the norm, rather than a special case.

#### **7.4.3 Implications for the Formation of Gravitational-Wave Mergers**

The LIGO and VIRGO network of gravitational wave detectors have demonstrated that long-positied mergers of binary black holes and neutron stars occur with remarkable frequency in the local universe [LIGO Scientific Collaboration and Virgo Collaboration, 2017, 2019]. While there are many conclusions to draw from this new abundance of empirical data, one of the remaining uncertainties is how these populations of stellar remnants are assembled into tight orbits. For both black hole and, especially,

neutron star systems, common envelope phases are one of the key possible assembly channels [as discussed by, e.g. van den Heuvel and De Loore, 1973, Paczynski, 1976, Webbink, 1984, van den Heuvel and Taam, 1984, Iben and Livio, 1993, Tauris, 1994, Belczynski et al., 2002a, Kalogera et al., 2007, Belczynski et al., 2008, Dominik et al., 2012, Ivanova et al., 2013]. Black holes have other plausible assembly channels, including dynamical captures in hierarchical multiple stars or dense clusters [e.g. Thompson, 2011, Pejcha et al., 2013, Naoz et al., 2013, Naoz and Fabrycky, 2014, Antognini et al., 2014, Samsing et al., 2014, Morscher et al., 2015, Breivik et al., 2016, Rodriguez et al., 2016a,b, Antonini et al., 2016], isolated evolution in initially-close binaries [Mandel and de Mink, 2016, de Mink and Mandel, 2016], or perhaps most realistically, a combination of cluster dynamics and binary stellar evolution [e.g. Mapelli and Zampieri, 2014, Ziosi et al., 2014, Giacobbo et al., 2018, Mapelli and Giacobbo, 2018, Mapelli et al., 2019, Spera et al., 2019, Di Carlo et al., 2019].

Enriching our understanding of the gravitational-wave source population with an understanding of their evolutionary history requires more detailed study of their assembly channels. Recently, Belczynski et al. [2018] have compared estimated rates for double neutron star systems in particular from these various channels [also see the excellent review double neutron star assembly of Tauris et al., 2017]. In particular, population models of binary neutron star mergers due to common envelope phases have trouble reproducing the currently estimated merger rate [LIGO Scientific Collaboration and Virgo Collaboration, 2017, 2019] on the basis of the GW170817 merger [Belczynski et al., 2018, Vigna-Gómez et al., 2018, Mapelli and Giacobbo, 2018, Andrews and Mandel, 2019, Andrews et al.,

2020]. This alone indicates that more detailed work is needed to understand these sources evolutionary history.

In our modeling of tidal evolution, we have focused on pre-common envelope binary parameter combinations relevant to the evolutionary history of eventual double neutron star systems, as studied by Vigna-Gómez et al. [2020]. In modeling the interaction of giant stars with  $1.4M_{\odot}$  companion is representative of the evolutionary state following the first supernova in the binary system, after the formation of the first neutron star. The ensuing common envelope phase is thought to be crucial to the assembly of double neutron star systems into tight orbits (for a helpful evolutionary schematic see the cartoons of Vigna-Gómez et al. [2020]’s or Belczynski et al. [2018]’s Figure 1). Our findings demonstrate that the majority of these systems will not circularize prior to the onset of these common envelope phases. Thus, within the current models, the typical common envelope phase that leads to a binary neutron star often begins eccentric.

The expected impact of pre-common envelope eccentricity on these common envelope phases remains uncertain, as we have discussed in the previous Section. It is, however, clear that these phases merit further study, with attention to the ways in which pre-common envelope eccentricity may affect the post-common envelope system that emerges. These results could then be applied to next-generation binary population models to study the statistical impacts on the merging compact object rate and population.

## 7.5 Summary & Conclusion

In this paper, we have studied how coupled stellar evolution and tidal dissipation affect the orbital parameters of binaries with a primary star that has left the main sequence and a compact companion. These systems may undergo subsequent mass transfer or common envelope phases, and eventually form compact object binaries that produce a gravitational wave signal as they merge. Although we define a more general methodology, we have focused our analysis on systems similar to those that undergo common envelope phases leading to the formation of merging double neutron stars [Vigna-Gómez et al., 2020].

Our analysis was performed by coupling models of evolving giant star primaries with the orbital evolution of the binary, as described in Section 7.2. We generated two stellar models with MESA (one  $10M_{\odot}$  and one  $15M_{\odot}$ ) to describe the stellar radius and viscous damping rates as functions of time as the primary star develops a convective envelope (see Section 7.2.2 and Figs. 7.1 and 7.2). We assumed a  $1.4M_{\odot}$  non-tidal companion, representative of a neutron star. We then used the orbital evolution equations (7.23 - 7.25) and the time-dependent stellar structure to calculate the binary  $a$  and  $e$  and the stellar spin rate  $\Omega_s$  on the way to RLO. This model is accurate even in the limits of close pericentre distances and highly eccentric orbits, in which cases the weak friction tidal model that is typically applied underestimates the strength of dissipation [Vick and Lai [2019b] and Fig. 3]. Our main findings are:

- 1) We identify three main outcomes of the coupled stellar and orbital evolution, which are highlighted in Fig. 7.5:

- i) The binary does not circularize before the primary overflows its Roche lobe ( $R_1 = r_{\text{Roche}}$ );
- ii) The binary completely circularizes before the onset of RLO; or
- iii) The binary is too wide to undergo RLO.

The initial properties of the binary orbital configuration largely determine which of these outcomes arises.

- 2) We find that orbital eccentricity at RLO depends very sensitively on the initial pericentre distance (as defined by the initial orbital parameters,  $r_{p,0}$  and  $e_0$ , before the primary leaves that main sequence). For the  $10M_\odot$  ( $15M_\odot$ ) primaries interacting with  $1.4M_\odot$  companions, systems with  $r_{p,0} \lesssim 3$  AU (6 AU) retained their initial eccentricity at the onset of RLO (Section 7.3.3 and Figs. 7.6 and 7.7).
- 3) For  $10M_\odot$  ( $15M_\odot$ ) plus  $1.4M_\odot$  binaries that eventually overflow their Roche lobes, given an initially thermal eccentricity distribution and a loguniform semimajor axis distribution, for systems within the ranges of  $r_{p,0}$  and  $e_0$  in Fig. 7.6 (Fig. 7.7), 75% (63%) overflow their Roche lobes before a convective envelope develops, at eccentricity similar to their initial eccentricity, 12% (33%) develop a convective envelope but overflow their Roche lobes at  $e > 0.1$ , and 13% (4%) develop a convective envelope and circularize prior to RLO at  $e < 0.1$  (see also Fig. 7.8).
- 4) For systems that do not develop a convective envelope prior to RLO, tidal dissipation has little effect on the stellar spin, and these donors are likely to spin at a rate similar to their initial rotation rate at the end of the main sequence (Figs. 7.6 and 7.7). For systems that do develop a convective envelope prior to RLO, stellar spin slows significantly

due to structural changes in the star. In general, the spin rate at RLO correlates with the degree of tidal circularization. For systems that do not circularize, tides do not have a significant effect on the stellar spin rate; these systems rotate significantly subsynchronously at RLO (Figs. 7.6 and 7.7). In binaries that do tidally circularize, the stellar rotation period approaches synchronicity, but remains longer than the orbital period, typically by a factor of approximately 1.25 to 4 because tidal dissipation and stellar evolution are acting at similar rates (Figs. 7.6, 7.7, and 7.9).

Our results suggest that a detailed analysis of the interaction of tides and stellar evolution is needed in systems containing evolving massive stars because the evolutionary (for example radius growth) timescale is similar to the tidal dissipation timescale. Our modeling further indicates the critical importance of the phases just prior to RLO, when tides are at their strongest. In this regime our model, which sums over energy deposition into individual modes, predicts dissipation rates up to  $10^2$  times greater than that of the more-typically applied weak friction model. However, as we have discussed in Section 7.4.1, non-linear tidal oscillations in this regime may lead to additional dissipation just prior to (or even following) RLO.

Despite these uncertainties, our analysis reveals that it is likely that many systems that undergo common envelope phases involving massive donor stars do so with initially eccentric orbits at the time of RLO [Vigna-Gómez et al., 2020]. These eccentric interactions remain poorly understood [though see Staff et al., 2016]. Our results may seem in tension with the population synthesis of Hurley et al. [2002] which coupled weak tidal

friction and binary evolution, and found that most binaries will tidally circularize before RLO. However, our investigation differs from theirs in that we focus on the case of massive stars that reach the Roche radius during a phase of rapid radius expansion. Our understanding of how common envelope phases operate in massive binaries will certainly benefit from more detailed consideration of the tidal evolution that precedes them.

## CHAPTER 8

### FUTURE WORK

One of the primary questions raised by the high-e migration theory of hot Jupiter formation is whether the planet can survive such extreme tidal heating. In my previous work (Chapter 4), I ignored the effect of tidal heating on the giant planet structure and luminosity. The planet’s response to heating is a natural area for follow-up investigation.

A giant planet’s response to heating depends sensitively on the location of heat deposition [e.g. Komacek and Youdin, 2017]. If most of the dissipation occurs near the surface of the planet, the planet may efficiently radiate away additional heat without undergoing significant structural change. However if heat is deposited at a greater depth, the planet radius will expand, leaving the planet vulnerable to being tidally shredded.

I intend to use a combination of both analytical and numerical methods to better understand the location of tidal heating. An analysis of non-linear energy dissipation mechanisms in giant planets, such as coupling between multiple oscillation modes, would give insight into the depth of heating. Another possible tool is hydrodynamic simulations using, e.g., Athena ++ [Stone et al., 2020] to examine where heat is deposited when resonantly forced oscillations dissipate nonlinearly. (See Fig. 8.1 for an example of the simulation of a tidally forced oscillation with Athena ++.)

However, even without precise knowledge of the location of energy dissipation in a giant planet, studies of non-linear dissipation in other contexts [e.g. Kumar and Goodman, 1996, Kastaun et al., 2010] suggest that most heating should occur near the surface of the planet, where the amplitude of tidally excited oscillations is largest. With this in mind, the stellar

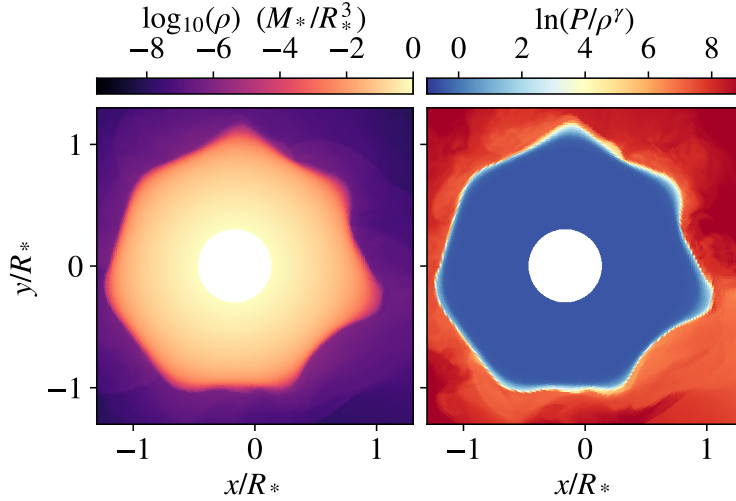


Figure 8.1: Slices through a three dimensional hydrodynamic simulation in which a fundamental oscillatory mode in a giant star model is resonantly driven to nonlinear amplitude by a tidal perturber. The left panel shows oscillatory waves in the density panel, the right shows specific entropy. Deviations from the star’s originally isentropic interior show localized heating near the object’s surface. This hydrodynamic model was performed in spherical polar coordinates surrounding the stellar center using the Eulerian hydrodynamic code Athena++.

evolution code, MESA [Paxton et al., 2011], could be used to explore the response of a giant planet to uniform tidal heating that extends to various depths. The result of this study would be a prescription for how the planet radius, luminosity, and fundamental mode properties evolve with time as a function of the heating rate, initial planet radius, and the depth of heating.

These MESA-generated heating curves could be used to couple the structural evolution of the planet with the model for dynamical tides developed in Chapters 3 and 4. The dynamical tide model is implemented as an iterative map, where once per orbit, the semi-major axis, eccentricity, planet rotation rate, and planet oscillation amplitudes are updated in accordance

with energy transfer due to dynamical tides at pericenter. When the oscillation amplitudes become too large, energy is dissipated non-linearly, and tidal heating occurs. This map could be adapted to model the planet structure and orbit consistently as the planet is tidally heated and the orbit decays. The result of this work would be a robust answer to whether a giant planet can survive chaotic tidal migration, and a set of predictions for observational signatures of this process, such as brightening of the giant planet or an unusual planet rotation rate.

## APPENDIX A

### APPENDIX FOR CHAPTER 2

For large  $\eta$  and  $e$  it is often necessary to calculate the Hansen coefficient  $F_{Nm}$ , for  $N \gg 1$  to accurately determine the tidal energy and angular momentum transfer rates. For illustration, consider a system with  $\eta = 20$ ,  $e = 0.95$  and  $\Omega_s = 0$ . The largest  $\omega$  included in our calculations is  $\omega \sim 0.1 (GM/R^3)^{1/2}$  because gravity waves with larger  $\omega$  will not propagate in the WD (see Section 2.4). Therefore, the largest  $N$  that appears in equations (2.34)-(2.36) is given by

$$N_{\max} = \left\lfloor 0.1 \left( \frac{1-e}{\eta} \right)^{3/2} \right\rfloor. \quad (\text{A.1})$$

For the system described above,  $N_{\max} = 800$ . Note that although  $F_{Nm}$  decreases with increasing  $N$ , the dimensionless tidal torque  $\hat{F}(\omega)$  increases very steeply with  $\omega$ . These two effects can balance each other so that terms with large  $N$  contribute significantly to the tidal transfer rates, equations (2.34)-(2.36).

In order to calculate  $F_{Nm}$  for large  $N$  and  $e$ , it is useful to find an approximation. These Hansen coefficients are calculated by integrating over an oscillatory term [see equation (2.28)]. When  $N$  is large, there are many oscillations over the interval of integration, so numerical integration is inefficient and, unless handled carefully, inaccurate. We therefore treat the  $F_{Nm}$  as a continuous function,  $F_m(N)$  and fit this function with the form:

$$F_m(N) = \alpha N^\beta \exp(-\gamma N). \quad (\text{A.2})$$

This form is motivated by approximations for the parabolic case ( $e=1$ ) in Press and Teukolsky [1977] and Lai [1997].

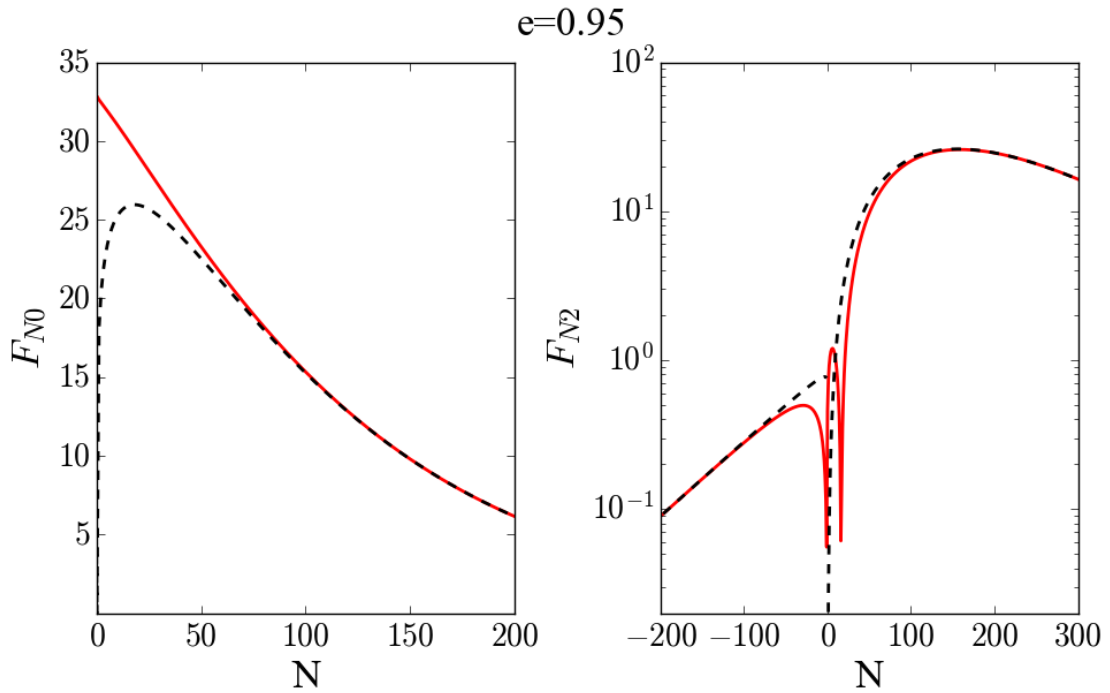


Figure A.1: The Hansen coefficients  $F_{Nm}$  in solid red and an approximation of the form equation (A.2) in dashed black. Both panels use  $e = 0.95$ . The left panel shows results for  $m = 0$  while the right panel shows results for  $m = 2$ . From the symmetry of the Hansen coefficients,  $F_{N2} = F_{-N-2}$ . For large  $N$ , the approximation is accurate to 0.01%.

Fig. A.1 shows a comparison between  $F_{Nm}$  and the approximation  $F_m(N)$  for  $e = 0.95$ . With that eccentricity,

$$\begin{aligned} F_0(N) &\approx 18.3 N^{0.186} \exp(-0.0103 N), \\ F_2(N) &\approx 0.024 N^{1.73} \exp(-0.0111 N), \\ F_{-2}(N) &\approx 0.766 N^{0.040} \exp(-0.0118 N). \end{aligned} \tag{A.3}$$

For large  $e$  the approximation is accurate to within 0.01%.

APPENDIX B  
APPENDIX FOR CHAPTER 3

## B.1 Physical Justification for the Iterative Map

We present a brief derivation of the iterative map based on the hydrodynamics of forced stellar oscillations in binaries. We consider the tidally-excited oscillations of the primary body (mass  $M$  and radius  $R$ ) by the companion of mass  $M'$ . The gravitational potential produced by  $M'$  reads

$$U(\mathbf{r}, t) = -GM' \sum_{lm} \frac{W_{lm} r^l}{D^{l+1}} e^{-im\Phi(t)} Y_{lm}(\theta, \phi), \quad (\text{B.1})$$

where  $\mathbf{r} = (r, \theta, \phi)$  is the position vector (in spherical coordinates) relative to the centre of mass of  $M$ ,  $D(t)$  is the binary separation and  $\Phi$  is the orbital true anomaly. The dominant quadrupole terms have  $l = |m| = 2$  and  $m = 0$ , for which  $W_{2\pm 2} = (3\pi/10)^{1/2}$  and  $W_{20} = (\pi/5)^{1/2}$ . For simplicity, we neglect stellar rotation [see Schenk et al. [2002], Lai and Wu [2006]]. To linear order, the response of star  $M$  to the tidal forcing frequency is specified by the Lagrangian displacement  $\xi(\mathbf{r}, t)$ . A free oscillation mode of frequency  $\omega_\alpha$  has the form  $\xi_\alpha(\mathbf{r}, t) = \xi_\alpha(\mathbf{r}) e^{-i\omega_\alpha t} \propto e^{im\phi - i\omega_\alpha t}$ . We carry out phase-space expansion of  $\xi(\mathbf{r}, t)$  in terms of the eigenmodes Schenk et al. [2002]:

$$\begin{bmatrix} \xi \\ \partial\xi/\partial t \end{bmatrix} = \sum_\alpha c_\alpha(t) \begin{bmatrix} \xi_\alpha(\mathbf{r}) \\ -i\omega_\alpha \xi_\alpha(\mathbf{r}) \end{bmatrix}. \quad (\text{B.2})$$

The linear fluid dynamics equations for the forced stellar oscillations then reduce to the evolution equation for the mode amplitude  $c_\alpha(t)$  [Lai and Wu, 2006]:

$$\dot{c}_\alpha + (i\omega_\alpha + \gamma_\alpha)c_\alpha = \frac{iGM'W_{lm}Q_\alpha}{2\omega_\alpha D^{l+1}} e^{-im\Phi(t)}, \quad (\text{B.3})$$

where  $\gamma_\alpha$  is the mode (amplitude) damping rate, and

$$Q_\alpha = \frac{1}{M^{1/2} R^{(l-1)}} \int d^3x \rho \xi_\alpha^\star \cdot \nabla(r^l Y_{lm}) \quad (\text{B.4})$$

is the dimensionless tidal overlap integral. The eigenmode is normalized according to  $\int d^3x \rho(\mathbf{r}) |\xi_\alpha(\mathbf{r})|^2 = 1$ , which implies that  $\xi$  has units of  $M^{-1/2}$ .

The general solution to equation (B.3) is

$$c_\alpha = e^{-(i\omega_\alpha + \gamma_\alpha)t} \int_{t_0}^t \frac{iGM'W_{lm}Q_\alpha}{2\omega_\alpha D^{l+1}} e^{(i\omega_\alpha + \gamma_\alpha)t' - im\Phi(t')} dt'. \quad (\text{B.5})$$

For eccentric binaries, we can write this as a sum over multiple pericentre passages. To do so, let  $t_k$  be the time of the  $k$ -th apocentre passage. [Note that, for the moment, this use of  $k$  differs from the meaning used in equations (3.1)-(3.5), where it is used to describe the number of pericentre passages]. We can relate  $t_k$  to  $t_{k-1}$  via

$$t_k = t_{k-1} + \frac{1}{2}(P_{k-1} + P_k). \quad (\text{B.6})$$

Now define

$$\Delta c_\alpha = \int_{-P_{k-1}/2}^{P_k/2} \frac{iGM'W_{lm}Q_\alpha}{2\omega_\alpha D^{l+1}} e^{(i\omega_\alpha + \gamma_\alpha)t' - im\Phi(t')} dt'. \quad (\text{B.7})$$

This is the change in mode amplitude during a pericentre passage, and it is approximately constant for any  $k$  provided the orbit is very eccentric and the pericentre distance  $r_{\text{peri}}$  remains constant (see the main text for discussion). We can then write  $c_\alpha$  at time  $t_k$  simply as

$$c_{\alpha,k} = e^{-(i\omega_\alpha + \gamma_\alpha)t_k} \Delta c_\alpha \sum_{j=1}^k e^{(i\omega_\alpha + \gamma_\alpha)(t_{j-1} + P_{j-1}/2)}. \quad (\text{B.8})$$

We can reorganize equation (B.8) into an iterative form

$$c_{\alpha,k} = c_{\alpha,k-1} e^{-(i\omega_\alpha + \gamma_\alpha)(P_{k-1} + P_k)/2} + e^{-(i\omega_\alpha + \gamma_\alpha)P_k/2} \Delta c_\alpha. \quad (\text{B.9})$$

We now shift the index  $k$  to count pericentre passages rather than apocentre passages by defining

$$a_{\alpha,k} = \sqrt{2}\omega_\alpha c_{\alpha,k} e^{-i\omega P_k/2}/|E_{B,0}|, \quad (\text{B.10})$$

where we have also re-normalized the mode amplitude so that the scaled mode energy (in units of  $|E_{B,0}|$ ) is  $\tilde{E}_{\alpha,k} = |a_{\alpha,k}|^2$ . (Note the mode energy is given by  $E_{\alpha,k} = 2\omega_\alpha^2|c_{\alpha,k}|^2$ .) Equation (B.9) then reduces to

$$a_{\alpha,k} = (a_{\alpha,k-1} + \Delta a_\alpha) e^{-(i\omega_\alpha + \gamma_\alpha)P_k}, \quad (\text{B.11})$$

where  $\Delta a_\alpha = \sqrt{2}\omega_\alpha \Delta c_\alpha / |E_{B,0}|$ .

Using equation (B.7), we can write  $\Delta E_{\alpha,1}$  explicitly in terms of orbital parameters and mode properties:

$$\Delta E_{\alpha,1} = |E_{B,0}|(\Delta a_\alpha)^2 = \frac{GM'^2}{R} \left( \frac{R}{r_{\text{peri}}} \right)^{2(l+1)} T(\eta, \omega_\alpha / \Omega_{\text{peri}}, e), \quad (\text{B.12})$$

where the dimensionless function  $T$  is given by

$$T = 2\pi^2 Q_\alpha^2 K_{lm}^2. \quad (\text{B.13})$$

Ignoring the negligible effect of mode damping at pericentre, we have

$$K_{lm} = \frac{W_{lm}}{2\pi} \left( \frac{GM}{R^3} \right)^{1/2} \int_{-P/2}^{P/2} dt' \left( \frac{r_{\text{peri}}}{D} \right)^{l+1} e^{i\omega_\alpha t' - im\Phi(t')}. \quad (\text{B.14})$$

The energy transfer for a parabolic passage ( $e \rightarrow 1$ ) was first derived in Press and Teukolsky [1977]. Equations (B.12)-(B.14), which apply to eccentric orbits as well, were presented in Lai [1997] [see equations (22)-(23)] and in Fuller and Lai [2012a] [see equation (14)-(15); note that in equation (15),  $R$  should be replaced by  $D_p$ .]

Note that the integral in equation (B.14) is difficult to calculate accurately and efficiently because the mode frequency is typically orders of magnitude larger than the orbital frequency. However, for parabolic orbits,  $K_{lm}$

can be evaluated in the limit  $\omega_\alpha/\Omega_{\text{peri}} \gg 1$  [Lai, 1997]. For example, for  $l = 2, m = 2$ ,

$$K_{22} = \frac{2z^{3/2}\eta^{3/2}e^{-2z/3}}{\sqrt{15}} \left(1 - \frac{\sqrt{\pi}}{4\sqrt{z}} + \dots\right), \quad (\text{B.15})$$

where

$$z \equiv \sqrt{2}\omega_\alpha/\Omega_{\text{peri}}. \quad (\text{B.16})$$

This expansion approximates  $K_{lm}$  to within a few percent for  $(1 - e) \ll 1$  and  $z \gtrsim 3$ . For typical f-mode frequencies, the latter condition is satisfied for  $\eta \gtrsim$  a few.

## B.2 Non-dissipative Systems

### B.2.1 Maximum Mode Energy for Non-Chaotic Systems

In the oscillatory and resonant regimes, the mode energy  $\tilde{E}_k \ll 1$ , and the iterative map given by equation (3.19) can be rewritten:

$$z_{k+1} \simeq 1 + z_k e^{-i\hat{P}_0 + i|\Delta\hat{P}_1||z_k|^2}, \quad (\text{B.17})$$

where  $z_k \equiv a_{k-}/\Delta a = a_{k-1}/\Delta a + 1$ .

**Oscillatory Regime:** When  $|\delta\hat{P}_0| = |\hat{P}_0 - 2\pi N| \gg |\Delta\hat{P}_1||z_k|^2$ , the map simplifies to

$$z_{k+1} \simeq 1 + z_k e^{-i\hat{P}_0}. \quad (\text{B.18})$$

This yields the solution (for  $z_1 = 1$ )

$$z_k \simeq \frac{1 - e^{-ik\hat{P}_0}}{1 - e^{-i\hat{P}_0}}, \quad (\text{B.19})$$

which is equivalent to equation (3.16). The validity of this oscillatory solution requires  $|\delta\hat{P}_0| \gg |\Delta\hat{P}_1|/(1 - \cos \hat{P}_0)$  or  $|\delta\hat{P}_0|^3 \gg |\Delta\hat{P}_1|$ .

**Resonant Regime:** When  $|\delta\hat{P}_0|^3 \ll |\Delta\hat{P}_1|$ , the system is in the resonant regime, and the map becomes

$$z_{k+1} - z_k \simeq 1 + i|\Delta\hat{P}_1||z_k|^2 z_k. \quad (\text{B.20})$$

For  $k \gg 1$ , we can approximate the mode amplitude as a continuous function of  $k$ , and the above equation reduces to

$$\frac{dz}{dk} \simeq 1 + i|\Delta\hat{P}_1||z|^2 z. \quad (\text{B.21})$$

Now we express  $z$  explicitly in terms of an amplitude  $A$  and phase  $\theta$ :

$$z = A e^{i\theta}. \quad (\text{B.22})$$

Equation (B.21) can be rewritten as two differential equations:

$$\frac{dA}{dk} \simeq \cos \theta, \quad (\text{B.23})$$

$$\frac{d\theta}{dk} \simeq \frac{1}{A} (|\Delta\hat{P}_1|A^3 - \sin \theta). \quad (\text{B.24})$$

We combine these to examine how the amplitude varies with the phase:

$$\frac{dA}{d\theta} = \frac{A \cos \theta}{(|\Delta\hat{P}_1|A^3 - \sin \theta)}. \quad (\text{B.25})$$

To solve the above equation, we use the substitutions

$$u = |\Delta\hat{P}_1|A^3, \quad v = \sin \theta. \quad (\text{B.26})$$

Equation (B.25) then simplifies to

$$\frac{du}{dv} = \frac{3u}{u-v}. \quad (\text{B.27})$$

For the initial condition  $u = v = 0$ , which corresponds to  $a_0 = 0$ , the solution is simply  $u = 4v$ , or

$$A = \left( \frac{4 \sin \theta}{|\Delta\hat{P}_1|} \right)^{1/3}, \quad (\text{B.28})$$

which has the maximum value  $(4/|\Delta\hat{P}_1|)^{1/3}$ . The maximum mode energy for a system near resonance is therefore

$$\tilde{E}_{\text{res}} \equiv \tilde{E}_{k,\text{max}} = (\Delta a)^2 \left( \frac{4}{|\Delta\hat{P}_1|} \right)^{2/3} \simeq \frac{2^{7/3}}{3} \frac{|\Delta\hat{P}_1|^{1/3}}{\hat{P}_0}. \quad (\text{B.29})$$

We can use the above result to approximate the shape that the mode amplitude traces in the complex plane over many orbits. Our numerical calculation (see Fig. 3.3) shows that the mode amplitude as a function of its phase can be described by

$$\left| \frac{a_k}{\Delta a} + 0.5 \right| \simeq \left( \frac{4 \sin \theta}{|\Delta\hat{P}_1|} \right)^{1/3}, \quad (\text{B.30})$$

where  $\theta$  is the phase of  $a_k/\Delta a + 0.5$ . This is similar to equation (B.28) except for a shift along the real axis. For  $|\Delta\hat{P}_1| \ll 1$ , this approximation performs very well, as seen in Fig. 3.3.

## B.2.2 Resonant Timescale

The mode of a non-dissipative system near resonance evolves periodically, repeatedly tracing out a closed shape in the complex amplitude plane. We define  $t_{\text{res}}$  as the period of the resonant oscillations. To calculate this timescale, we use equations (B.23) and (B.28) to find

$$\frac{d\theta}{dk} \simeq \left( \frac{|\Delta\hat{P}_1|}{4} \right)^{1/3} 3(\sin \theta)^{2/3}. \quad (\text{B.31})$$

Integrating the above differential equation from  $\theta = 0$  to  $\theta = \pi$  gives

$$t_{\text{res}} \simeq 3.85 P |\Delta\hat{P}_1|^{-1/3}, \quad (\text{B.32})$$

where  $P$  is the orbital period associated with the resonance. In order of magnitude, the number of orbits necessary to reach the maximum mode amplitude  $|a_{\text{res}}| \sim |\Delta\hat{P}_1|^{-1/3} \Delta a$  is simply  $|a_{\text{res}}|/\Delta a$ .

### B.2.3 Maximum Mode Energy for Chaotic Systems

As discussed in the main text, the mode energy of a chaotic system initially grows stochastically with an expected value of  $\langle \tilde{E}_k \rangle \sim \Delta \tilde{E}_1 k$  [see equation (3.24) and Fig. 3.5], but cannot exceed a maximum value,  $\tilde{E}_{\max}$ . As the mode energy increases, the change in the orbital period between pericentre passages,  $\Delta \hat{P}_k$ , decreases [see equation (3.25)]. The maximum mode energy is approximately set by  $|\Delta \hat{P}_k| \sim 1$ , and is given by equation (3.26).

This condition is related to that found in Mardling [1995a,b], where the maximum mode energy is set by a “chaos boundary” that separates orbital parameters that produce chaotic behaviour from those that produce oscillatory behaviour. The location of the boundary depends on the current mode amplitude. The iterative map in this paper demonstrates that such boundaries are determined by the size of  $|\Delta \hat{P}_k|$ , which depends on  $\Delta a$  and  $a_{k-1}$  [see equation (3.25)]. Both the onset of chaotic behaviour and the maximum mode energy are set by conditions on  $|\Delta \hat{P}_k|$  (where  $k = 1$  when considering the onset). It follows that both conditions are related to “chaos boundaries”, as observed by Mardling [1995a,b].

In reality, the dependence of  $\tilde{E}_{\max}$  on  $\hat{P}_0$  and  $|\Delta \hat{P}_1|$  is more complicated than the power law trend from equation (3.26). Figures B.1 and B.2 show “jumps” and “drops” in  $\tilde{E}_{\max}$  at some values of  $\hat{P}_0$  and  $|\Delta \hat{P}_1|$ . To understand this step-like behaviour, we note that the maximum mode energy for a non-dissipative system is associated with the minimum (dimensionless) orbital period by

$$\hat{P}_{\min} = \hat{P}_0 \left( \frac{1}{1 + \tilde{E}_{\max}} \right)^{3/2}. \quad (\text{B.33})$$

We have found that for a chaotic system, as  $|\Delta \hat{P}_k|$  decreases toward unity, the orbital period tends to evolve away from resonances with the stellar

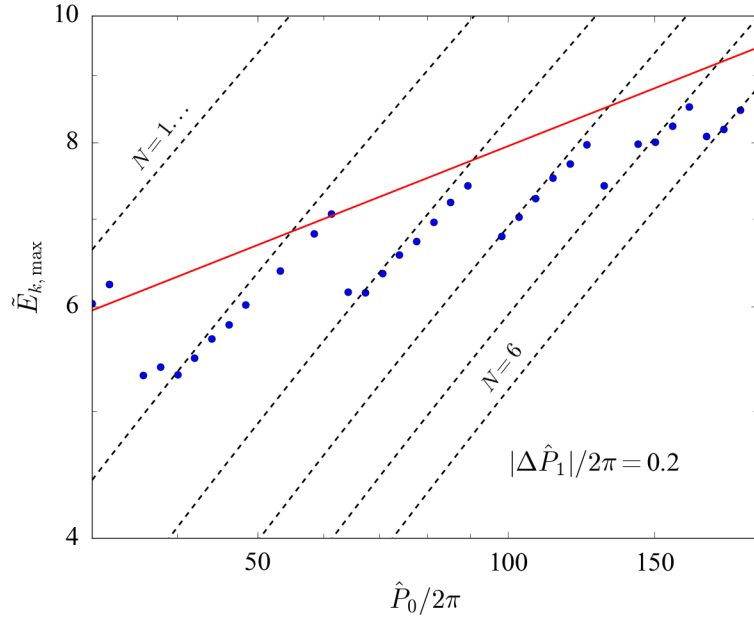


Figure B.1: Numerical results for  $\tilde{E}_{\max}$  (blue dots) after  $3 \times 10^6$  orbits for chaotic systems with  $|\Delta\tilde{P}_1|/2\pi = 0.2$ . The red line is  $1.5(\hat{P}_0|\Delta\hat{P}_1|)^{1/4}$  [see equation (3.26)]. The dotted lines are from equation (B.34) with different values of  $N$ .

mode and to linger directly between them. This behaviour can be understood from the fact that, for a system near resonance, the shifts in mode amplitude during pericentre tend to add over successive passages, pushing the system away from the resonance. Imposing  $\hat{P}_{\min} \simeq 2\pi(N + 1/2)$  yields

$$\tilde{E}_{\max} \simeq \left[ \frac{\hat{P}_0}{2\pi(N + 1/2)} \right]^{2/3} - 1. \quad (\text{B.34})$$

Equation (B.34) is in good agreement with results shown in Figs. B.1 and B.2. We see that the jumps in  $\tilde{E}_{\max}$  correspond to changes in  $N$ . Combining equation (B.34) with the broader trend of equation (3.26) captures the main features of how  $\tilde{E}_{\max}$  depends on  $\hat{P}_0$  and  $|\Delta\hat{P}_1|$  for chaotic systems.

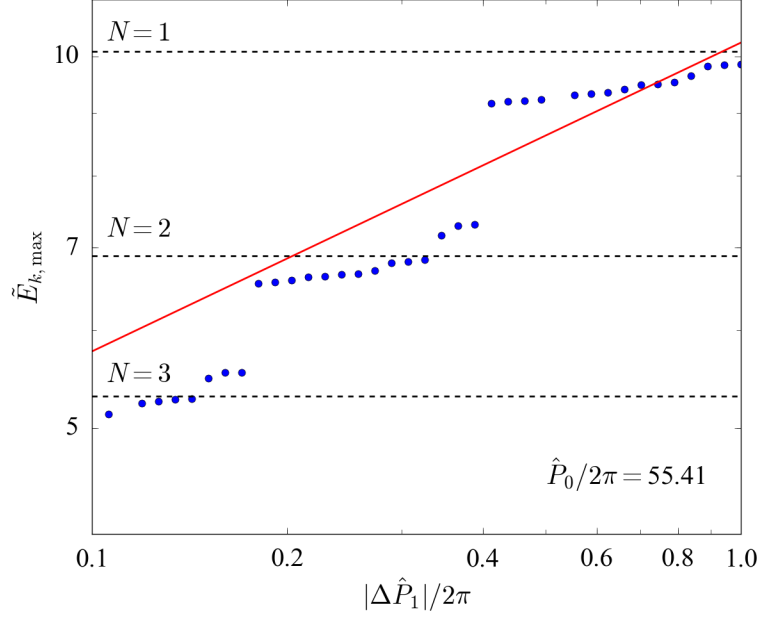


Figure B.2: Numerical results for  $\tilde{E}_{\max}$  (blue dots) after  $3 \times 10^6$  orbits for chaotic systems with  $\hat{P}_0/2\pi = 55.41$ . The red line is  $1.5(\hat{P}_0|\Delta\hat{P}_1|)^{1/4}$  [see equation (3.26)]. The dotted lines are from equation (B.34 with different values of  $N$ ).

### B.3 G-mode Properties of Stellar Models

One application of our model is the tidal capture of main-sequence stars by compact objects, including massive black holes. We use the stellar evolution code, MESA [Paxton et al., 2011], and the non-adiabatic pulsation code, GYRE [Townsend and Teitler, 2013], to determine the properties of g-modes in the radiative envelope of stars between  $2$  and  $10M_\odot$ . The characteristic damping times of modes are found using the imaginative part of the mode frequency. These values are generally in good agreement with a quasi-adiabatic approximation that assumes radiative damping. Figure B.3 shows the computed damping rates for three stellar models. For the  $2M_\odot$  model, the damping rate only varies by a factor of a few for the relevant g-modes. For the  $10M_\odot$  model (and other models with

$10M_{\odot} \leq M \leq 20M_{\odot}$ ), the damping rates are much smaller for higher frequency modes.

The amount of energy transferred to a mode (labelled  $\alpha$ ) in the “first” pericentre passage  $\Delta E_{\alpha,1}$  (i.e., when the oscillation amplitude is zero before the passage) depends on the stellar structure and mode properties. We use the method of Press and Teukolsky [1977] to calculate  $\Delta E_{\alpha,1}$ . The quasi-steady-state mode dissipation rate from equation (3.30) is of order  $\gamma_{\alpha}\Delta E_{\alpha,1}$ . Figure B.4 shows an example of the calculated  $\Delta E_{\alpha,1}$  and the energy dissipation rates for systems with different stellar properties and  $\eta = 3$ . We find that stars with  $M \lesssim 5M_{\odot}$  tend to have a single low-order g-mode with large  $\tilde{\Delta E}_{\alpha,1}$  that dominates the energy transfer rate. To represent a system with a dominant mode, we choose the  $\omega$  and  $\gamma$  ratios between modes from the  $2M_{\odot}$  model and the  $\tilde{E}_{\alpha,1}$  ratio for  $\eta = 3$ . More massive stars ( $M \gtrsim M_{\odot}$ ) have a number of g-modes that contribute roughly equally to the energy transfer rate. To represent a system where multiple modes are important for energy transfer, we choose the  $\omega$  and  $\gamma$  ratios between modes from the  $10M_{\odot}$  model and the  $\tilde{E}_{\alpha,1}$  ratio for  $\eta = 3$ .

The orbital parameter  $\eta = (r_{\text{peri}}/R)(M/M_t)^{1/3}$  (where  $r_{\text{peri}}$  is the pericentre distance) also strongly affects  $\Delta E_{\alpha,1}$ , though the dependence on  $e$  is negligible for highly eccentric orbits. For larger  $\eta$ , the orbital frequency at pericentre is smaller, and higher-order g-modes contribute more to tidal energy transfer, as illustrated in Fig. B.5.

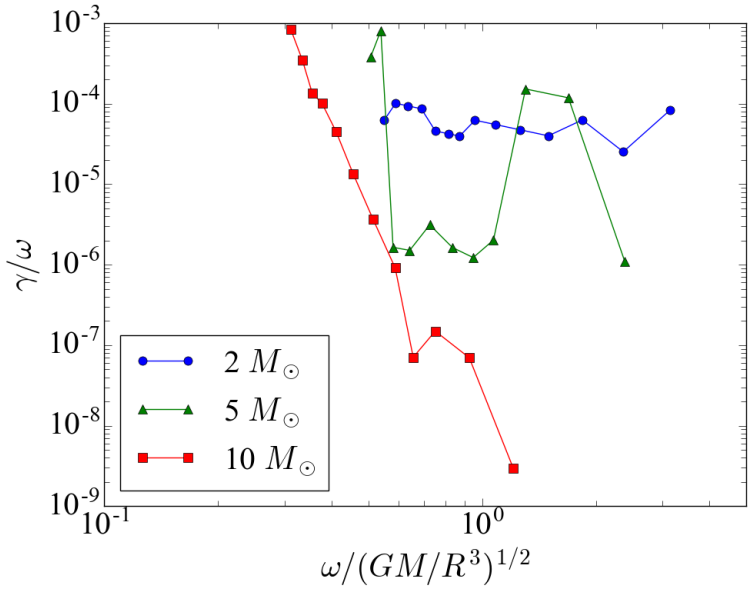


Figure B.3: Numerical results for the g-mode frequencies ( $\omega$ ) and damping rates ( $\gamma$ ) of three MESA stellar models analysed with the non-adiabatic stellar pulsation code, GYRE. The dip in  $\gamma/\omega$  for the  $5M_\odot$  model is typical for models in the mass range  $4 - 8M_\odot$ .

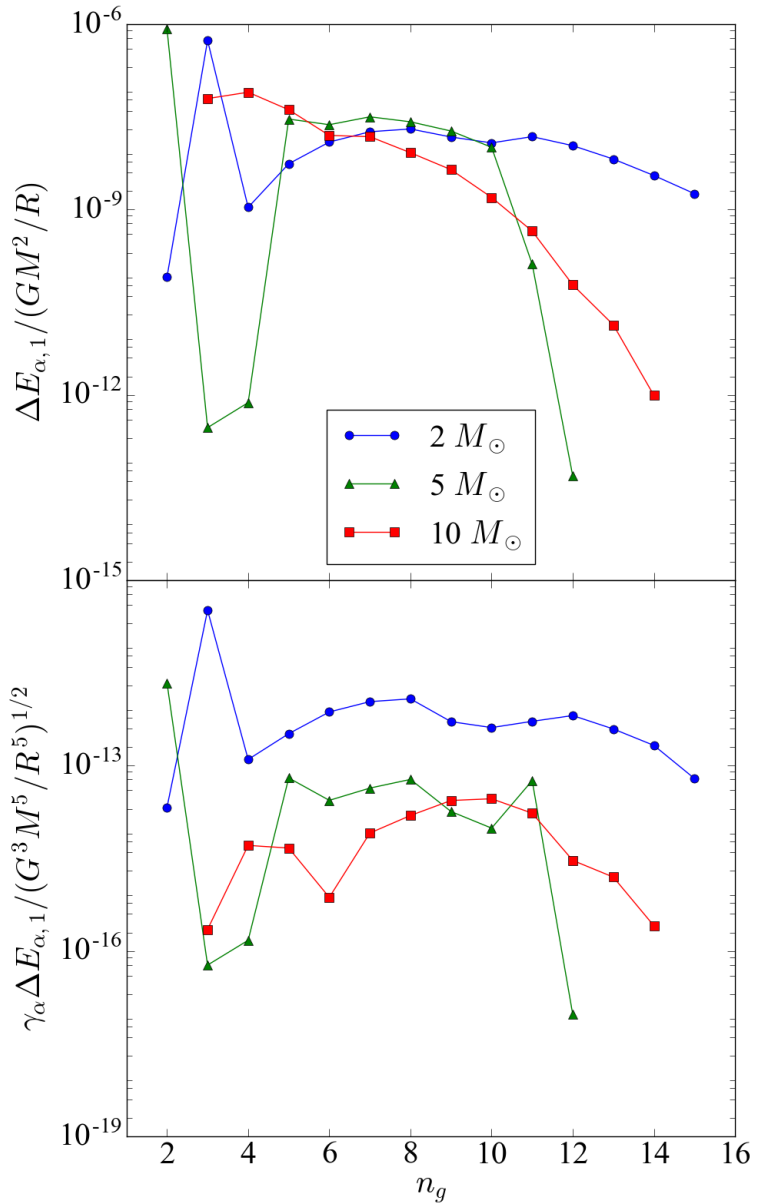


Figure B.4: Numerical results for  $\Delta E_{\alpha,1}$  and  $\gamma_{\alpha} \Delta E_{\alpha,1}$  vs.  $n_g$  (the radial mode number) for three MESA stellar models analysed with the non-adiabatic stellar pulsation code, GYRE. The energy transfer  $\Delta E_{\alpha,1}$  is calculated assuming  $\eta = 3$  and  $e = 0.95$ .

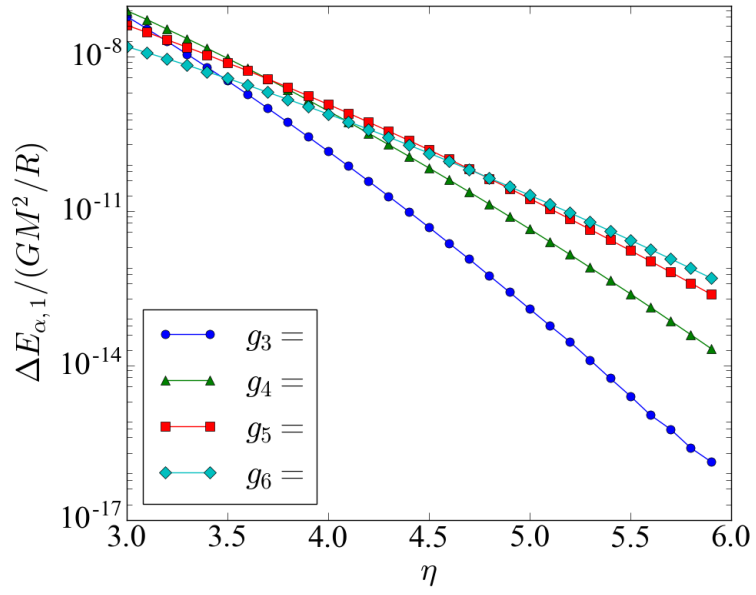


Figure B.5: Numerical results for  $\Delta E_{\alpha,1}$  for four g-modes of the  $10M_{\odot}$  stellar model as a function of  $\eta$ . For larger  $\eta$ , higher order g-modes receive more energy at pericentre than lower-order g-modes.

APPENDIX C  
APPENDIX FOR CHAPTER 5

### C.1 Orbital decay through f-mode resonances

As the eccentric binary orbit decays due to gravitational radiation, the orbital frequency  $\Omega_{\text{orb}}$  encounters resonances with the f-mode frequency  $\omega_\alpha$  such that

$$\omega_\alpha = n\Omega_{\text{orb}}, \quad (\text{C.1})$$

with integer  $n$  (see also Section 5.3). When the orbital frequency sweeps through a resonance slowly (over the course of multiple orbits), the NS mode energy can increase significantly, resulting in enhanced orbital decay and a phase shift in the gravitational waveform. This phase shift has been calculated for a variety of NS models and oscillation modes in the case of a circular orbit [e.g. Lai, 1994, Shibata, 1994, Reisenegger and Goldreich, 1994, Ho and Lai, 1999, Lai and Wu, 2006, Yu and Weinberg, 2017a,b, Andersson and Ho, 2018, Xu and Lai, 2017], and recently was considered for the low eccentricity case ( $e \ll 1$ ) near the  $\omega_\alpha = 3\Omega_{\text{orb}}$  resonance Yang [2019]. We generalize this calculation to higher-order resonances and arbitrary eccentricities, and show that these resonances generally produce a small GW phase shift.

When the orbital decay due to gravitational radiation occurs on a much longer timescale than an orbital period, we can approximate the gravitational potential produced by  $M_2$  on  $M_1$  (Eq. 5.1) as a sum of multiple forcing frequencies,  $n\Omega_{\text{orb}}$ , with positive integer  $n$ . We neglect PN effects (other than gravitational radiation) in this analysis. The time evolution of

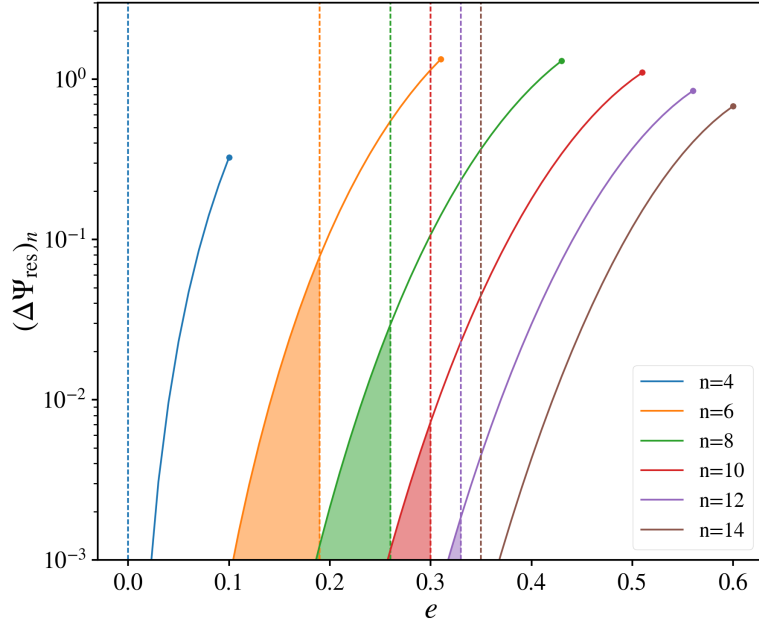


Figure C.1: The GW phase shift  $(\Delta\Psi_{\text{res}})_n = 2(\Delta\Phi_{\text{res}})_n$  (see Eq. C.10) due to mode-orbit resonance ( $\omega_\alpha = n\Omega_{\text{orb}}$  with positive integer  $n$ ) as a function of the orbital eccentricity at the resonance. The results are for the  $l = m = 2$  f-mode of a  $\Gamma = 2$  polytropic NS model with  $M_1 = 1.4 M_\odot$  and  $R_1 = 10$  km in an equal mass binary. The dashed lines indicate  $\delta N_{\text{res}} = 1$  (see Eq. C.12). The results for  $(\Delta\Psi_{\text{res}})_n$  (solid lines) are valid when  $\delta N_{\text{res}} > 1$ , in the shaded region to the left of the dashed lines. The maximum displayed  $e$  for each value of  $n$  corresponds to the condition that the pericenter distance  $D_p$  exceeds  $2.5R_1$ .

the mode amplitude  $c_\alpha$  satisfies [e.g. Fuller and Lai, 2012a, Vick et al., 2017]

$$\dot{c}_\alpha + i\omega_\alpha c_\alpha = \frac{iM_2 W_{lm} Q_\alpha}{2\omega_\alpha a^{l+1}} \sum_n F_{mn} \exp \left[ -i \int^t dt' n\Omega_{\text{orb}}(t') \right], \quad (\text{C.2})$$

where  $a$  is the Newtonian semi-major axis, and

$$F_{mn} = \frac{1}{\pi} \int_0^\pi \frac{\cos[n(E - e \sin E) - m\Phi(t)]}{(1 - e \cos E)^2} dE, \quad (\text{C.3})$$

with  $E$  the eccentric anomaly and

$$\cos \Phi(t) = \frac{\cos E - e}{1 - e \cos E}. \quad (\text{C.4})$$

Note that  $G = M_1 = R_1 = 1$  in Eq. (C.2). Solving for  $c_\alpha(t)$  yields

$$c_\alpha e^{i\omega_\alpha t} = \sum_n F_{mn} \int dt \frac{iM_2 W_{lm} Q_\alpha}{2\omega_\alpha a^{l+1}} e^{i[\omega_\alpha t - \int^t dt' n\Omega_{\text{orb}}(t')]} \quad (\text{C.5})$$

As  $\Omega_{\text{orb}}$  increases due to orbital decay, large changes in the mode amplitude can occur when the orbit sweeps through a resonance with the mode frequency.

If the orbital decay is sufficiently slow, the mode amplitude after an encounter with the resonance  $\omega_\alpha = n\Omega_{\text{orb}}$  can be evaluated using the stationary phase approximation, giving

$$|c_\alpha| \simeq \frac{iM_2 W_{lm} Q_\alpha F_{mn}}{2\omega_\alpha a_n^{l+1}} \left( \frac{2\pi}{n\dot{\Omega}_{\text{orb},n}} \right)^{1/2}, \quad (\text{C.6})$$

with  $a_n$  and  $\dot{\Omega}_{\text{orb},n}$  evaluated at the resonance. The change in the mode energy is  $(\Delta E_{\text{res}})_n = 2\omega_\alpha^2 |c_\alpha|^2$ . The associated change in the orbital phase due to the resonance is given by Lai [1994]

$$(\Delta\Phi_{\text{res}})_n \simeq - \left( \Omega_{\text{orb}} t_D \frac{\Delta E_{\text{res}}}{|E_{\text{orb}}|} \right)_n, \quad (\text{C.7})$$

where  $E_{\text{orb}} = -M_1 M_2 / 2a$  is the orbital energy, and  $t_D = |a/\dot{a}|$  is the orbital decay time due to gravitational radiation. Using (see Eq. 5.6 of Peters [1964])

$$\frac{\dot{\Omega}_{\text{orb}}}{\Omega_{\text{orb}}} = \frac{3}{2t_D} = \frac{96}{5} \frac{M_1^3 q (1+q)}{a^4} \mathcal{F}(e), \quad (\text{C.8})$$

where  $q = M_2/M_1$ , and

$$\mathcal{F}(e) \equiv \frac{1}{(1-e^2)^{7/2}} \left( 1 + \frac{73}{24} e^2 + \frac{37}{96} e^4 \right), \quad (\text{C.9})$$

we find

$$(\Delta\Phi_{\text{res}})_n \simeq \frac{-25\pi}{3 \times 2^9} \left( \frac{R_1}{M_1} \right)^5 \frac{n}{\bar{\omega}_\alpha^2 q (1+q)} \left[ \frac{W_{2m} Q_\alpha F_{mn}}{\mathcal{F}(e)} \right]^2, \quad (\text{C.10})$$

where  $\bar{\omega} = \omega/(M_1 R_1^{-3})^{1/2}$ , and  $e$  is the eccentricity at resonance. The phase shift in the gravitational waveform is  $(\Delta\Psi_{\text{res}})_n \simeq 2(\Delta\Phi_{\text{res}})_n$ .

Equations (C.6), (C.7) and (C.10) are valid only when the orbital decay is sufficiently slow. From Eq. (C.6), we see that the change in the mode

amplitude corresponds to the rate of change of the mode amplitude at resonance multiplied by the duration of the resonance,

$$\delta t_{\text{res}} \equiv \left( \frac{2\pi}{n\dot{\Omega}_{\text{orb},n}} \right)^{1/2}. \quad (\text{C.11})$$

The number of orbital cycles during which resonance occurs is

$$\delta N_{\text{res}} = \frac{\Omega_{\text{orb},n}}{2\pi} \delta t_{\text{res}} = \left[ \frac{5}{192\pi} \left( \frac{R_1}{M_1} \right)^{5/2} \frac{(1+q)^{1/3}}{q} \frac{n^{2/3}}{\bar{\omega}_\alpha^{5/3} \mathcal{F}(e)} \right]^{1/2}. \quad (\text{C.12})$$

Resonance is significant only when  $\delta N_{\text{res}} \gtrsim 1$ . When  $\delta N_{\text{res}} \lesssim 1$ , the orbit moves through the resonance too quickly to strongly excite the oscillation.

We calculate  $(\Delta\Psi_{\text{res}})_n$  for the f-mode of a  $\Gamma = 2$  polytropic NS model with  $M_1 = 1.4 M_\odot$  and  $R_1 = 10$  km over a large range of  $n$  and  $e$  and display the results in Fig. C.1. For NS binaries that satisfy  $\delta N_{\text{res}} \gtrsim 1$ , we find that  $(\Delta\Psi_{\text{res}})_n$  is always less than 0.1. We conclude that for eccentric NS binaries, f-mode resonances do not contribute significantly to the tidally generated phase shift. This finding is consistent with our numerical integrations in Section 5.4, which did not exhibit sudden increases in the mode energy corresponding to mode-orbit resonances.

APPENDIX D  
APPENDIX FOR CHAPTER 6

## D.1 The Relationship between Damping Rates

We have assumed that viscous dissipation is solely responsible for the damping of oscillation modes. In equation (6.19), we defined the damping rate  $\gamma_\alpha(\omega_{Nm})$  by relating the viscous dissipation rate of mode  $\alpha$  oscillating at the frequency  $\omega_{Nm}$  to the kinetic energy of the mode. However, this damping rate is different from  $\Gamma_\alpha(\omega_{Nm})$  (see equation 6.11), which relates the energy dissipation rate to the total energy of the mode. Here, we derive the relationship between the two damping rates.

The total dissipation rate in the rotating frame is equal to the tidal energy transfer rate in the same frame, given by

$$\dot{E} = \int d^3x \rho \frac{\partial \boldsymbol{\xi}^*}{\partial t} \cdot (-\nabla U). \quad (\text{D.1})$$

Decomposed into a sum over oscillation modes and forcing frequencies (see equations 6.2, 6.8, and 6.10), this is

$$\dot{E} = \int d^3x \rho \sum_{\alpha N} \sum_{N'm'} \dot{c}_{\alpha N}^* U_{N'm'} e^{-i\omega_{N'm'} t} \boldsymbol{\xi}_\alpha^*(\mathbf{r}) \cdot \nabla(r^2 Y_{2m'}). \quad (\text{D.2})$$

Using equations (6.4),(6.12), and (6.14), and averaging over time, the energy dissipation rate is

$$\begin{aligned} \dot{E} &= M_1 R_1^2 \sum_{\alpha N} \frac{\omega_{Nm}}{2\epsilon_\alpha} \frac{(U_{Nm} Q_\alpha)^2 \Gamma_\alpha(\omega_{Nm})}{[(\omega_\alpha - \omega_{Nm})^2 + \Gamma_\alpha^2(\omega_{Nm})]} \\ &= 2M_1 R_1^2 \sum_{\alpha N} \Gamma_\alpha(\omega_{Nm}) \omega_{Nm} \epsilon_\alpha |c_{\alpha N}|^2. \end{aligned} \quad (\text{D.3})$$

The above implies that the energy dissipation rate associated with each mode and forcing frequency  $\omega_{Nm}$  is

$$\dot{E}_{\alpha N} = 2\Gamma_\alpha(\omega_{Nm}) \omega_{Nm} \epsilon_\alpha |c_{\alpha N}|^2 M_1 R_1^2. \quad (\text{D.4})$$

By comparing equations (6.19) and (D.4), we obtain a relationship between  $\gamma_\alpha(\omega_{Nm})$  and  $\Gamma_\alpha(\omega_{Nm})$ :

$$\Gamma_\alpha(\omega_{Nm}) = \gamma_\alpha(\omega_{Nm}) \frac{\omega_{Nm}}{\epsilon_\alpha}. \quad (\text{D.5})$$

Similarly, for a freely oscillating mode,  $\Gamma_\alpha(\omega_\alpha) = \gamma_\alpha(\omega_\alpha)\omega_\alpha/\epsilon_\alpha$ .

## BIBLIOGRAPHY

- B. P. Abbott, R. Abbott, T. D. Abbott, S. Abraham, F. Acernese, K. Ackley, C. Adams, R. X. Adhikari, LIGO Scientific Collaboration, and Virgo Collaboration. GWTC-1: A Gravitational-Wave Transient Catalog of Compact Binary Mergers Observed by LIGO and Virgo during the First and Second Observing Runs. *Physical Review X*, 9(3):031040, July 2019. doi: 10.1103/PhysRevX.9.031040.
- Helmut A. Abt. Observed Orbital Eccentricities. *ApJ*, 629(1):507–511, August 2005. doi: 10.1086/431207.
- Helmut A. Abt. Observed Orbital Eccentricities. II. Late-Type Stars. *ApJ*, 651(2):1151–1154, November 2006. doi: 10.1086/507457.
- Helmut A. Abt and Chayan Boonyarak. Tidal Effects in Binaries of Various Periods. *ApJ*, 616(1):562–566, November 2004. doi: 10.1086/423795.
- S. Albrecht, J. N. Winn, J. A. Johnson, A. W. Howard, G. W. Marcy, R. P. Butler, P. Arriagada, J. D. Crane, S. A. Shectman, I. B. Thompson, T. Hirano, G. Bakos, and J. D. Hartman. Obliquities of Hot Jupiter Host Stars: Evidence for Tidal Interactions and Primordial Misalignments. *ApJ*, 757: 18, September 2012. doi: 10.1088/0004-637X/757/1/18.
- M. E. Alexander. The Weak Friction Approximation and Tidal Evolution in Close Binary Systems. *Astrophys. and Space Sci.*, 23(2):459–510, Aug 1973. doi: 10.1007/BF00645172.
- K. R. Anderson and D. Lai. Moderately Eccentric Warm Jupiters from Secular Interactions with Exterior Companions. *ArXiv e-prints*, May 2017.

K. R. Anderson, N. I. Storch, and D. Lai. Formation and stellar spin-orbit misalignment of hot Jupiters from Lidov-Kozai oscillations in stellar binaries. *MNRAS*, 456:3671–3701, March 2016. doi: 10.1093/mnras/stv2906.

Nils Andersson and Wynn C. G. Ho. Using gravitational-wave data to constrain dynamical tides in neutron star binaries. *Phys. Rev. D.*, 97(2):023016, Jan 2018. doi: 10.1103/PhysRevD.97.023016.

Jeff J. Andrews and Ilya Mandel. Double Neutron Star Populations and Formation Channels. *ApJL*, 880(1):L8, July 2019. doi: 10.3847/2041-8213/ab2ed1.

Jeff J. Andrews, Katelyn Breivik, Chris Pankow, Daniel J. D’Orazio, and Mohammad Taher Safarzadeh. LISA and the Existence of a Fast-merging Double Neutron Star Formation Channel. *ApJL*, 892(1):L9, March 2020. doi: 10.3847/2041-8213/ab5b9a.

Joe M. Antognini, Benjamin J. Shappee, Todd A. Thompson, and Pau Amaro-Seoane. Rapid eccentricity oscillations and the mergers of compact objects in hierarchical triples. *MNRAS*, 439(1):1079–1091, March 2014. doi: 10.1093/mnras/stu039.

F. Antonini, A. S. Hamers, and Y. Lithwick. Dynamical Constraints on the Origin of Hot and Warm Jupiters with Close Friends. *Astron. Journal*, 152:174, December 2016. doi: 10.3847/0004-6256/152/6/174.

F. Antonini, S. Toonen, and A. S. Hamers. Binary Black Hole Mergers from Field Triples: Properties, Rates, and the Impact of Stellar Evolution. *ApJ*, 841:77, June 2017. doi: 10.3847/1538-4357/aa6f5e.

Fabio Antonini and Hagai B. Perets. Secular Evolution of Compact Binaries near Massive Black Holes: Gravitational Wave Sources and Other Exotica. *ApJ*, 757(1):27, Sep 2012. doi: 10.1088/0004-637X/757/1/27.

Martin Asplund, Nicolas Grevesse, A. Jacques Sauval, and Pat Scott. The Chemical Composition of the Sun. *Annual Review of Astron. and Astrophys.*, 47(1):481–522, September 2009. doi: 10.1146/annurev.astro.46.060407.145222.

A. J. Barker and G. I. Ogilvie. On the tidal evolution of Hot Jupiters on inclined orbits. *MNRAS*, 395:2268–2287, June 2009. doi: 10.1111/j.1365-2966.2009.14694.x.

A. J. Barker and G. I. Ogilvie. On internal wave breaking and tidal dissipation near the centre of a solar-type star. *MNRAS*, 404:1849–1868, June 2010. doi: 10.1111/j.1365-2966.2010.16400.x.

A. J. Barker and G. I. Ogilvie. Stability analysis of a tidally excited internal gravity wave near the centre of a solar-type star. *MNRAS*, 417:745–761, October 2011. doi: 10.1111/j.1365-2966.2011.19322.x.

K. Batygin, P. H. Bodenheimer, and G. P. Laughlin. In Situ Formation and Dynamical Evolution of Hot Jupiter Systems. *ApJ*, 829:114, October 2016. doi: 10.3847/0004-637X/829/2/114.

T. W. Baumgarte, G. B. Cook, M. A. Scheel, S. L. Shapiro, and S. A. Teukolsky. General relativistic models of binary neutron stars in quasiequilibrium. *Phys. Rev. D.*, 57(12):7299–7311, Jun 1998. doi: 10.1103/PhysRevD.57.7299.

C. Beaugé and D. Nesvorný. Multiple-planet Scattering and the Origin of Hot Jupiters. *ApJ*, 751:119, June 2012. doi: 10.1088/0004-637X/751/2/119.

P. G. Beck, K. Hambleton, J. Vos, T. Kallinger, S. Bloemen, A. Tkachenko, R. A. García, R. H. Østensen, C. Aerts, D. W. Kurtz, J. De Ridder, S. Hekker, K. Pavlovski, S. Mathur, K. De Smedt, A. Derekas, E. Corsaro, B. Mosser, H. Van Winckel, D. Huber, P. Degroote, G. R. Davies, A. Prša, J. Debosscher, Y. Elsworth, P. Nemeth, L. Siess, V. S. Schmid, P. I. Pápics, B. L. de Vries, A. J. van Marle, P. Marcos-Arenal, and A. Lobel. Pulsating red giant stars in eccentric binary systems discovered from Kepler space-based photometry. A sample study and the analysis of KIC 5006817. *Astron. and Astrophys.*, 564:A36, April 2014. doi: 10.1051/0004-6361/201322477.

K. Belczynski, M. Dominik, T. Bulik, R. O’Shaughnessy, C. Fryer, and D. E. Holz. The Effect of Metallicity on the Detection Prospects for Gravitational Waves. *ApJL*, 715:L138–L141, June 2010. doi: 10.1088/2041-8205/715/2/L138.

K. Belczynski, D. E. Holz, T. Bulik, and R. O’Shaughnessy. The first gravitational-wave source from the isolated evolution of two stars in the 40-100 solar mass range. *Nature*, 534:512–515, June 2016. doi: 10.1038/nature18322.

K. Belczynski, A. Askar, M. Arca-Sedda, M. Chruslinska, M. Donnari, M. Giersz, M. Benacquista, R. Spurzem, D. Jin, G. Wiktorowicz, and D. Belloni. The origin of the first neutron star - neutron star

merger. *Astron. and Astrophys.*, 615:A91, Jul 2018. doi: 10.1051/0004-6361/201732428.

Krzysztof Belczynski, Tomasz Bulik, and Bronislaw Rudak. Study of Gamma-Ray Burst Binary Progenitors. *ApJ*, 571(1):394–412, May 2002a. doi: 10.1086/339860.

Krzysztof Belczynski, Vassiliki Kalogera, and Tomasz Bulik. A Comprehensive Study of Binary Compact Objects as Gravitational Wave Sources: Evolutionary Channels, Rates, and Physical Properties. *ApJ*, 572(1):407–431, Jun 2002b. doi: 10.1086/340304.

Krzysztof Belczynski, Vassiliki Kalogera, Frederic A. Rasio, Ronald E. Taam, Andreas Zezas, Tomasz Bulik, Thomas J. Maccarone, and Natalia Ivanova. Compact Object Modeling with the StarTrack Population Synthesis Code. *ApJS*, 174(1):223–260, January 2008. doi: 10.1086/521026.

D. Bhattacharya and E. P. J. van den Heuvel. Formation and evolution of binary and millisecond radio pulsars. *Physics Reports*, 203(1-2):1–124, Jan 1991. doi: 10.1016/0370-1573(91)90064-S.

L. Bildsten and C. Cutler. Tidal interactions of inspiraling compact binaries. *ApJ*, 400:175–180, November 1992. doi: 10.1086/171983.

Taylor Binnington and Eric Poisson. Relativistic theory of tidal Love numbers. *Phys. Rev. D.*, 80(8):084018, Oct 2009. doi: 10.1103/PhysRevD.80.084018.

N. Blagorodnova, R. Kotak, J. Polshaw, M. M. Kasliwal, Y. Cao, A. M. Cody, G. B. Doran, N. Elias-Rosa, M. Fraser, C. Fremling, C. Gonzalez-Fernandez, J. Harmanen, J. Jencson, E. Kankare, R. P. Kudritzki, S. R.

Kulkarni, E. Magnier, I. Manulis, F. J. Masci, S. Mattila, P. Nugent, P. Ochner, A. Pastorello, T. Reynolds, K. Smith, J. Sollerman, F. Taddia, G. Terreran, L. Tomasella, M. Turatto, P. M. Vreeswijk, P. Wozniak, and S. Zaggia. Common Envelope Ejection for a Luminous Red Nova in M101. *ApJ*, 834(2):107, Jan 2017. doi: 10.3847/1538-4357/834/2/107.

Luc Blanchet. Gravitational Radiation from Post-Newtonian Sources and Inspiralling Compact Binaries. *Living Reviews in Relativity*, 17(1):2, Feb 2014. doi: 10.12942/lrr-2014-2.

J. S. Bloom, D. Giannios, B. D. Metzger, S. B. Cenko, D. A. Perley, N. R. Butler, N. R. Tanvir, A. J. Levan, P. T. O'Brien, L. E. Strubbe, F. De Colle, E. Ramirez-Ruiz, W. H. Lee, S. Nayakshin, E. Quataert, A. R. King, A. Cucchiara, J. Guillochon, G. C. Bower, A. S. Fruchter, A. N. Morgan, and A. J. van der Horst. A Possible Relativistic Jetted Outburst from a Massive Black Hole Fed by a Tidally Disrupted Star. *Science*, 333:203, July 2011. doi: 10.1126/science.1207150.

Alexey Bobrick, Melvyn B. Davies, and Ross P. Church. Mass transfer in white dwarf-neutron star binaries. *MNRAS*, 467(3):3556–3575, May 2017. doi: 10.1093/mnras/stx312.

A. C. Boley, A. P. Granados Contreras, and B. Gladman. The In Situ Formation of Giant Planets at Short Orbital Periods. *ApJL*, 817:L17, February 2016. doi: 10.3847/2041-8205/817/2/L17.

Emeline Bolmont and Stéphane Mathis. Effect of the rotation and tidal dissipation history of stars on the evolution of close-in planets. *Celestial Mechanics and Dynamical Astronomy*, 126(1-3):275–296, Nov 2016. doi: 10.1007/s10569-016-9690-3.

Katelyn Breivik, Carl L. Rodriguez, Shane L. Larson, Vassiliki Kalogera, and Frederic A. Rasio. Distinguishing between Formation Channels for Binary Black Holes with LISA. *ApJL*, 830(1):L18, October 2016. doi: 10.3847/2041-8205/830/1/L18.

Duncan A. Brown and Peter J. Zimmerman. Effect of eccentricity on searches for gravitational waves from coalescing compact binaries in ground-based detectors. *Phys. Rev. D.*, 81(2):024007, Jan 2010. doi: 10.1103/PhysRevD.81.024007.

M. L. Bryan, H. A. Knutson, A. W. Howard, H. Ngo, K. Batygin, J. R. Crepp, B. J. Fulton, S. Hinkley, H. Isaacson, J. A. Johnson, G. W. Marcy, and J. T. Wright. Statistics of Long Period Gas Giant Planets in Known Planetary Systems. *ApJ*, 821:89, April 2016. doi: 10.3847/0004-637X/821/2/89.

J. Burkart, E. Quataert, P. Arras, and N. N. Weinberg. Tidal asteroseismology: Kepler's KOI-54. *MNRAS*, 421:983–1006, April 2012. doi: 10.1111/j.1365-2966.2011.20344.x.

D. N. Burrows, J. A. Kennea, G. Ghisellini, V. Mangano, B. Zhang, K. L. Page, M. Eracleous, P. Romano, T. Sakamoto, A. D. Falcone, J. P. Osborne, S. Campana, A. P. Beardmore, A. A. Breeveld, M. M. Chester, R. Corbet, S. Covino, J. R. Cummings, P. D'Avanzo, V. D'Elia, P. Esposito, P. A. Evans, D. Fugazza, J. M. Gelbord, K. Hiroi, S. T. Holland, K. Y. Huang, M. Im, G. Israel, Y. Jeon, Y.-B. Jeon, H. D. Jun, N. Kawai, J. H. Kim, H. A. Krimm, F. E. Marshall, P. Mészáros, H. Negoro, N. Omodei, W.-K. Park, J. S. Perkins, M. Sugizaki, H.-I. Sung, G. Tagliaferri, E. Troja, Y. Ueda, Y. Urata, R. Usui, L. A. Antonelli,

S. D. Barthelmy, G. Cusumano, P. Giommi, A. Melandri, M. Perri, J. L. Racusin, B. Sbarufatti, M. H. Siegel, and N. Gehrels. Relativistic jet activity from the tidal disruption of a star by a massive black hole. *Nature*, 476:421–424, August 2011. doi: 10.1038/nature10374.

Luke Chamandy, Adam Frank, Eric G. Blackman, Jonathan Carroll-Nellenback, Baowei Liu, Yisheng Tu, Jason Nordhaus, Zhuo Chen, and Bo Peng. Accretion in common envelope evolution. *MNRAS*, 480(2): 1898–1911, October 2018. doi: 10.1093/mnras/sty1950.

Luke Chamandy, Eric G. Blackman, Adam Frank, Jonathan Carroll-Nellenback, Yangyuxin Zou, and Yisheng Tu. How drag force evolves in global common envelope simulations. *MNRAS*, 490(3):3727–3739, December 2019. doi: 10.1093/mnras/stz2813.

S. Chatterjee, E. B. Ford, S. Matsumura, and F. A. Rasio. Dynamical Outcomes of Planet-Planet Scattering. *ApJ*, 686:580-602, October 2008. doi: 10.1086/590227.

S. V. Chaurasia, T. Dietrich, N. K. Johnson-McDaniel, M. Ujevic, W. Tichy, and B. Brügmann. Gravitational waves and mass ejecta from binary neutron star mergers: Effect of large eccentricities. *Phys. Rev. D.*, 98(10): 104005, November 2018. doi: 10.1103/PhysRevD.98.104005.

R. M. Cheng and T. Bogdanović. Tidal disruption of a star in the Schwarzschild spacetime: Relativistic effects in the return rate of debris. *Phys. Rev. D*, 90(6):064020, September 2014. doi: 10.1103/PhysRevD.90.064020.

R. M. Cheng and C. R. Evans. Relativistic effects in the tidal interaction

between a white dwarf and a massive black hole in Fermi normal coordinates. *Phys. Rev. D*, 87(10):104010, May 2013. doi: 10.1103/PhysRevD.87.104010.

S. V. Chernov, J. C. B. Papaloizou, and P. B. Ivanov. Dynamical tides excited in rotating stars of different masses and ages and the formation of close in orbits. *MNRAS*, 434(2):1079–1097, Sep 2013. doi: 10.1093/mnras/stt1042.

C. Chirenti, R. Gold, and M. C. Miller. Gravitational Waves from F-modes Excited by the Inspiral of Highly Eccentric Neutron Star Binaries. *ApJ*, 837:67, March 2017. doi: 10.3847/1538-4357/aa5ebb.

Ross P. Church, Johann Dischler, Melvyn B. Davies, Christopher. A. Tout, Tim Adams, and Martin E. Beer. Mass transfer in eccentric binaries: the new oil-on-water smoothed particle hydrodynamics technique. *MNRAS*, 395(2):1127–1134, May 2009. doi: 10.1111/j.1365-2966.2009.14619.x.

A. C. M. Correia, G. Boué, and J. Laskar. Pumping the Eccentricity of Exoplanets by Tidal Effect. *ApJL*, 744:L23, January 2012. doi: 10.1088/2041-8205/744/2/L23.

M. Coughlin, P. Meyers, E. Thrane, J. Luo, and N. Christensen. Detectability of eccentric compact binary coalescences with advanced gravitational-wave detectors. *Phys. Rev. D.*, 91(6):063004, Mar 2015. doi: 10.1103/PhysRevD.91.063004.

Thibault Damour and Alessandro Nagar. Relativistic tidal properties of

neutron stars. *Phys. Rev. D.*, 80(8):084035, Oct 2009. doi: 10.1103/PhysRevD.80.084035.

G. H. Darwin. On the Secular Changes in the Elements of the Orbit of a Satellite Revolving about a Tidally Distorted Planet. *Philosophical Transactions of the Royal Society of London Series I*, 171:713–891, Jan 1880.

R. I. Dawson and J. A. Johnson. Origins of Hot Jupiters. *Annual Review of Astron. and Astrophys.*, 56:175–221, September 2018. doi: 10.1146/annurev-astro-081817-051853.

R. I. Dawson, R. A. Murray-Clay, and J. A. Johnson. The Photoeccentric Effect and Proto-hot Jupiters. III. A Paucity of Proto-hot Jupiters on Super-eccentric Orbits. *ApJ*, 798:66, January 2015. doi: 10.1088/0004-637X/798/2/66.

F. De Colle, J. Guillochon, J. Naiman, and E. Ramirez-Ruiz. The Dynamics, Appearance, and Demographics of Relativistic Jets Triggered by Tidal Disruption of Stars in Quiescent Supermassive Black Holes. *ApJ*, 760: 103, December 2012. doi: 10.1088/0004-637X/760/2/103.

Orsola De Marco and Robert G. Izzard. Dawes Review 6: The Impact of Companions on Stellar Evolution. *Publications of the Astronomical Society of Australia*, 34:e001, January 2017. doi: 10.1017/pasa.2016.52.

S. E. de Mink and I. Mandel. The chemically homogeneous evolutionary channel for binary black hole mergers: rates and properties of gravitational-wave events detectable by advanced LIGO. *MNRAS*, 460 (4):3545–3553, August 2016. doi: 10.1093/mnras/stw1219.

Ugo N. Di Carlo, Nicola Giacobbo, Michela Mapelli, Mario Pasquato, Mario Spera, Long Wang, and Francesco Haardt. Merging black holes in young star clusters. *MNRAS*, 487(2):2947–2960, August 2019. doi: 10.1093/mnras/stz1453.

M. Dominik, K. Belczynski, C. Fryer, D. E. Holz, E. Berti, T. Bulik, I. Mandel, and R. O’Shaughnessy. Double Compact Objects. II. Cosmological Merger Rates. *ApJ*, 779:72, December 2013. doi: 10.1088/0004-637X/779/1/72.

M. Dominik, E. Berti, R. O’Shaughnessy, I. Mandel, K. Belczynski, C. Fryer, D. E. Holz, T. Bulik, and F. Pannarale. Double Compact Objects III: Gravitational-wave Detection Rates. *ApJ*, 806:263, June 2015. doi: 10.1088/0004-637X/806/2/263.

Michal Dominik, Krzysztof Belczynski, Christopher Fryer, Daniel E. Holz, Emanuele Berti, Tomasz Bulik, Ilya Mandel, and Richard O’Shaughnessy. Double Compact Objects. I. The Significance of the Common Envelope on Merger Rates. *ApJ*, 759(1):52, Nov 2012. doi: 10.1088/0004-637X/759/1/52.

Fani Dosopoulou and Vicky Kalogera. Orbital Evolution of Mass-transferring Eccentric Binary Systems. I. Phase-dependent Evolution. *ApJ*, 825(1):70, July 2016a. doi: 10.3847/0004-637X/825/1/70.

Fani Dosopoulou and Vicky Kalogera. Orbital Evolution of Mass-transferring Eccentric Binary Systems. II. Secular Evolution. *ApJ*, 825(1):71, July 2016b. doi: 10.3847/0004-637X/825/1/71.

Fani Dosopoulou, Smadar Naoz, and Vassiliki Kalogera. Roche-lobe Over-

flow in Eccentric Planet-Star Systems. *ApJ*, 844(1):12, July 2017. doi: 10.3847/1538-4357/aa7a05.

Craig D. Duguid, Adrian J. Barker, and C. A. Jones. Tidal flows with convection: frequency-dependence of the effective viscosity and evidence for anti-dissipation. *MNRAS*, page 2514, Oct 2019. doi: 10.1093/mnras/stz2899.

W. E. East. Gravitational Waves from the Collision of Tidally Disrupted Stars with Massive Black Holes. *ApJ*, 795:135, November 2014. doi: 10.1088/0004-637X/795/2/135.

W. E. East, F. Pretorius, and B. C. Stephens. Eccentric black hole-neutron star mergers: Effects of black hole spin and equation of state. *Phys. Rev. D.*, 85(12):124009, June 2012. doi: 10.1103/PhysRevD.85.124009.

P. P. Eggleton. Approximations to the radii of Roche lobes. *ApJ*, 268:368–369, May 1983. doi: 10.1086/160960.

A. C. Fabian, J. E. Pringle, and M. J. Rees. Tidal capture formation of binary systems and X-ray sources in globular clusters. *MNRAS*, 172:15p–18p, August 1975. doi: 10.1093/mnras/172.1.15P.

D. Fabrycky and S. Tremaine. Shrinking Binary and Planetary Orbits by Kozai Cycles with Tidal Friction. *ApJ*, 669:1298–1315, November 2007. doi: 10.1086/521702.

V. Ferrari, L. Gualtieri, and A. Maselli. Tidal interaction in compact binaries: A post-Newtonian affine framework. *Phys. Rev. D.*, 85(4):044045, Feb 2012. doi: 10.1103/PhysRevD.85.044045.

- É. É. Flanagan and T. Hinderer. Constraining neutron-star tidal Love numbers with gravitational-wave detectors. *Phys. Rev. D*, 77(2):021502, January 2008. doi: 10.1103/PhysRevD.77.021502.
- F. Fressin, G. Torres, D. Charbonneau, S. T. Bryson, J. Christiansen, C. D. Dressing, J. M. Jenkins, L. M. Walkowicz, and N. M. Batalha. The False Positive Rate of Kepler and the Occurrence of Planets. *ApJ*, 766:81, April 2013. doi: 10.1088/0004-637X/766/2/81.
- J. Fuller. Pre-supernova outbursts via wave heating in massive stars - I. Red supergiants. *MNRAS*, 470:1642–1656, September 2017. doi: 10.1093/mnras/stx1314.
- J. Fuller and D. Lai. *MNRAS*, 412:1331–1340, 2011.
- J. Fuller and D. Lai. Dynamical tides in eccentric binaries and tidally excited stellar pulsations in Kepler KOI-54. *MNRAS*, 420:3126–3138, March 2012a. doi: 10.1111/j.1365-2966.2011.20237.x.
- J. Fuller and D. Lai. Dynamical tides in compact white dwarf binaries: tidal synchronization and dissipation. *MNRAS*, 421:426–445, March 2012b. doi: 10.1111/j.1365-2966.2011.20320.x.
- J. Fuller and D. Lai. Tidal Novae in Compact Binary White Dwarfs. *ApJL*, 756:L17, September 2012c. doi: 10.1088/2041-8205/756/1/L17.
- J. Fuller and D. Lai. Dynamical tides in compact white dwarf binaries: helium core white dwarfs, tidal heating and observational signatures. *MNRAS*, 430:274–287, March 2013. doi: 10.1093/mnras/sts606.
- J. Fuller and D. Lai. Dynamical tides in compact white dwarf binaries:

influence of rotation. *MNRAS*, 444:3488–3500, November 2014. doi: 10.1093/mnras/stu1698.

Nicola Giacobbo, Michela Mapelli, and Mario Spera. Merging black hole binaries: the effects of progenitor’s metallicity, mass-loss rate and Eddington factor. *MNRAS*, 474(3):2959–2974, March 2018. doi: 10.1093/mnras/stx2933.

D. Giannios and B. D. Metzger. Radio transients from stellar tidal disruption by massive black holes. *MNRAS*, 416:2102–2107, September 2011. doi: 10.1111/j.1365-2966.2011.19188.x.

R. Gold, S. Bernuzzi, M. Thierfelder, B. Brügmann, and F. Pretorius. Eccentric binary neutron star mergers. *Phys. Rev. D.*, 86(12):121501, December 2012. doi: 10.1103/PhysRevD.86.121501.

P. Goldreich and P. D. Nicholson. Turbulent Viscosity and Jupiter’s Tidal Q. *Icarus*, 30(2):301–304, Feb 1977. doi: 10.1016/0019-1035(77)90163-4.

P. Goldreich and P. D. Nicholson. Tidal friction in early-type stars. *ApJ*, 342:1079–1084, July 1989. doi: 10.1086/167665.

J. Goodman and E. S. Dickson. Dynamical Tide in Solar-Type Binaries. *ApJ*, 507:938–944, November 1998. doi: 10.1086/306348.

Jeremy Goodman and Siang Peng Oh. Fast Tides in Slow Stars: The Efficiency of Eddy Viscosity. *ApJ*, 486(1):403–412, Sep 1997. doi: 10.1086/304505.

J. Guillochon. Catalog of possible tidal disruption events, 2016. URL <https://astrocrash.net/resources/tde-catalogue/>.

J. Guillochon, E. Ramirez-Ruiz, and D. Lin. Consequences of the Ejection and Disruption of Giant Planets. *ApJ*, 732:74, May 2011. doi: 10.1088/0004-637X/732/2/74.

T. Guillot. THE INTERIORS OF GIANT PLANETS: Models and Outstanding Questions. *Annual Review of Earth and Planetary Sciences*, 33:493–530, January 2005. doi: 10.1146/annurev.earth.32.101802.120325.

A. S. Hamers and S. F. Portegies Zwart. Secular dynamics of hierarchical multiple systems composed of nested binaries, with an arbitrary number of bodies and arbitrary hierarchical structure. First applications to multiplanet and multistar systems. *MNRAS*, 459:2827–2874, July 2016. doi: 10.1093/mnras/stw784.

Adrian S. Hamers and Fani Dosopoulou. An Analytic Model for Mass Transfer in Binaries with Arbitrary Eccentricity, with Applications to Triple-star Systems. *ApJ*, 872(2):119, February 2019. doi: 10.3847/1538-4357/ab001d.

Brad M. S. Hansen. Calibration of Equilibrium Tide Theory for Extrasolar Planet Systems. *ApJ*, 723(1):285–299, November 2010. doi: 10.1088/0004-637X/723/1/285.

G. Hébrard, F. Bouchy, F. Pont, B. Loeillet, M. Rabus, X. Bonfils, C. Moutou, I. Boisse, X. Delfosse, M. Desort, A. Eggenberger, D. Ehrenreich, T. Forveille, A.-M. Lagrange, C. Lovis, M. Mayor, F. Pepe, C. Perrier, D. Queloz, N. C. Santos, D. Ségransan, S. Udry, and A. Vidal-Madjar. Misaligned spin-orbit in the XO-3 planetary system? *Astron. and Astrophys.*, 488:763–770, September 2008. doi: 10.1051/0004-6361:200810056.

G. Hébrard, J.-M. Désert, R. F. Díaz, I. Boisse, F. Bouchy, A. Lecavelier Des Etangs, C. Moutou, D. Ehrenreich, L. Arnold, X. Bonfils, X. Delfosse, M. Desert, A. Eggenberger, T. Forveille, J. Gregorio, A.-M. Lagrange, C. Lovis, F. Pepe, C. Perrier, F. Pont, D. Queloz, A. Santerne, N. C. Santos, D. Ségransan, D. K. Sing, S. Udry, and A. Vidal-Madjar. Observation of the full 12-hour-long transit of the exoplanet HD 80606b. Warm-Spitzer photometry and SOPHIE spectroscopy. *Astron. and Astrophys.*, 516:A95, June 2010. doi: 10.1051/0004-6361/201014327.

J. G. Hills. Possible power source of Seyfert galaxies and QSOs. *Nature*, 254:295–298, March 1975. doi: 10.1038/254295a0.

W. C. G. Ho and D. Lai. Resonant tidal excitations of rotating neutron stars in coalescing binaries. *MNRAS*, 308:153–166, September 1999. doi: 10.1046/j.1365-8711.1999.02703.x.

C. Huang, Y. Wu, and A. H. M. J. Triaud. Warm Jupiters Are Less Lonely than Hot Jupiters: Close Neighbors. *ApJ*, 825:98, July 2016. doi: 10.3847/0004-637X/825/2/98.

Jarrod R. Hurley, Christopher A. Tout, and Onno R. Pols. Evolution of binary stars and the effect of tides on binary populations. *MNRAS*, 329 (4):897–928, February 2002. doi: 10.1046/j.1365-8711.2002.05038.x.

P. Hut. Tidal evolution in close binary systems. *Astron. and Astrophys.*, 99: 126–140, Jun 1981.

Roberto Iaconi, Thomas Reichardt, Jan Staff, Orsola De Marco, Jean-Claude Passy, Daniel Price, James Wurster, and Falk Herwig. The effect of a wider initial separation on common envelope binary inter-

action simulations. *MNRAS*, 464(4):4028–4044, February 2017. doi: 10.1093/mnras/stw2377.

Jr. Iben, Icko and Mario Livio. Common Envelopes in Binary Star Evolution. *Publications of the Astronomical Society of the Pacific*, 105:1373, December 1993. doi: 10.1086/133321.

K. Ioka, K. Hotokezaka, and T. Piran. Are Ultra-long Gamma-Ray Bursts Caused by Blue Supergiant Collapsars, Newborn Magnetars, or White Dwarf Tidal Disruption Events? *ApJ*, 833:110, December 2016. doi: 10.3847/1538-4357/833/1/110.

P. B. Ivanov and J. C. B. Papaloizou. On the tidal interaction of massive extrasolar planets on highly eccentric orbits. *MNRAS*, 347:437–453, January 2004a. doi: 10.1111/j.1365-2966.2004.07238.x.

P. B. Ivanov and J. C. B. Papaloizou. On equilibrium tides in fully convective planets and stars. *MNRAS*, 353(4):1161–1175, Oct 2004b. doi: 10.1111/j.1365-2966.2004.08136.x.

P. B. Ivanov and J. C. B. Papaloizou. Dynamic tides in rotating objects: orbital circularization of extrasolar planets for realistic planet models. *MNRAS*, 376:682–704, April 2007a. doi: 10.1111/j.1365-2966.2007.11463.x.

P. B. Ivanov and J. C. B. Papaloizou. Orbital circularisation of white dwarfs and the formation of gravitational radiation sources in star clusters containing an intermediate mass black hole. *Astron. and Astrophys.*, 476: 121–135, December 2007b. doi: 10.1051/0004-6361:20077105.

P. B. Ivanov and J. C. B. Papaloizou. Close encounters of a rotating star with planets in parabolic orbits of varying inclination and the formation of hot Jupiters. *Celestial Mechanics and Dynamical Astronomy*, 111:51–82, October 2011. doi: 10.1007/s10569-011-9367-x.

P. B. Ivanov, J. C. B. Papaloizou, and S. V. Chernov. A unified normal mode approach to dynamic tides and its application to rotating Sun-like stars. *MNRAS*, 432(3):2339–2365, Jul 2013. doi: 10.1093/mnras/stt595.

N. Ivanova, S. Justham, X. Chen, O. De Marco, C. L. Fryer, E. Gaburov, H. Ge, E. Glebbeek, Z. Han, X. D. Li, G. Lu, T. Marsh, P. Podsiadlowski, A. Potter, N. Soker, R. Taam, T. M. Tauris, E. P. J. van den Heuvel, and R. F. Webbink. Common envelope evolution: where we stand and how we can move forward. *Astron. and Astrophys. Rev.*, 21:59, Feb 2013. doi: 10.1007/s00159-013-0059-2.

M. Jurić and S. Tremaine. Dynamical Origin of Extrasolar Planet Eccentricity Distribution. *ApJ*, 686:603–620, October 2008. doi: 10.1086/590047.

V. Kalogera, K. Belczynski, C. Kim, R. O’Shaughnessy, and B. Willems. Formation of double compact objects. *Physics Reports*, 442(1-6):75–108, April 2007. doi: 10.1016/j.physrep.2007.02.008.

W. Kastaun et al. *PRD*, 82(10):104036, 2010.

B. Katz and S. Dong. The rate of WD-WD head-on collisions may be as high as the SNe Ia rate. *ArXiv e-prints*, November 2012.

Lawrence E. Kidder, Clifford M. Will, and Alan G. Wiseman. Spin effects in the inspiral of coalescing compact binaries. *Phys. Rev. D.*, 47(10):R4183–R4187, May 1993. doi: 10.1103/PhysRevD.47.R4183.

B. Kirk, K. Conroy, A. Prša, M. Abdul-Masih, A. Kochoska, G. Matijević, K. Hambleton, T. Barclay, S. Bloemen, T. Boyajian, L. R. Doyle, B. J. Fulton, A. J. Hoekstra, K. Jek, S. R. Kane, V. Kostov, D. Latham, T. Mazeh, J. A. Orosz, J. Pepper, B. Quarles, D. Ragozzine, A. Shporer, J. Southworth, K. Stassun, S. E. Thompson, W. F. Welsh, E. Agol, A. Derekas, J. Devor, D. Fischer, G. Green, J. Gropp, T. Jacobs, C. Johnston, D. M. LaCourse, K. Saetre, H. Schwengeler, J. Toczyski, G. Werner, M. Garrett, J. Gore, A. O. Martinez, I. Spitzer, J. Stevick, P. C. Thomadis, E. H. Vrijmoet, M. Yenawine, N. Batalha, and W. Borucki. Kepler Eclipsing Binary Stars. VII. The Catalog of Eclipsing Binaries Found in the Entire Kepler Data Set. *Astron. Journal*, 151:68, March 2016. doi: 10.3847/0004-6256/151/3/68.

Jakub Klencki, Gijs Nelemans, Alina G. Istrate, and Onno Pols. Massive donors in interacting binaries: effect of metallicity. *arXiv e-prints*, art. arXiv:2004.00628, April 2020.

W. Kley and R. P. Nelson. Planet-Disk Interaction and Orbital Evolution. *Annual Review of Astron. and Astrophys.*, 50:211–249, September 2012. doi: 10.1146/annurev-astro-081811-125523.

H. A. Knutson, B. J. Fulton, B. T. Montet, M. Kao, H. Ngo, A. W. Howard, J. R. Crepp, S. Hinkley, G. Á. Bakos, K. Batygin, J. A. Johnson, T. D. Morton, and P. S. Muirhead. Friends of Hot Jupiters. I. A Radial Velocity Search for Massive, Long-period Companions to Close-in Gas Giant Planets. *ApJ*, 785:126, April 2014. doi: 10.1088/0004-637X/785/2/126.

C. S. Kochanek. The dynamical evolution of tidal capture binaries. *ApJ*, 385:604–620, February 1992. doi: 10.1086/170966.

Thaddeus D. Komacek and Andrew N. Youdin. Structure and Evolution of Internally Heated Hot Jupiters. *ApJ*, 844(2):94, August 2017. doi: 10.3847/1538-4357/aa7b75.

Y. Kozai. Secular perturbations of asteroids with high inclination and eccentricity. *Astron. Journal*, 67:591, November 1962. doi: 10.1086/108790.

J. H. Krolik and T. Piran. Jets from Tidal Disruptions of Stars by Black Holes. *ApJ*, 749:92, April 2012. doi: 10.1088/0004-637X/749/1/92.

M. U. Kruckow, T. M. Tauris, N. Langer, D. Szécsi, P. Marchant, and Ph. Podsiadlowski. Common-envelope ejection in massive binary stars. Implications for the progenitors of GW150914 and GW151226. *Astronomy and Astrophysics*, 596:A58, November 2016. doi: 10.1051/0004-6361/201629420.

P. Kumar and J. Goodman. Nonlinear Damping of Oscillations in Tidal-Capture Binaries. *ApJ*, 466:946, August 1996. doi: 10.1086/177565.

D. Kushnir, B. Katz, S. Dong, E. Livne, and R. Fernández. Head-on Collisions of White Dwarfs in Triple Systems Could Explain Type Ia Supernovae. *ApJL*, 778:L37, December 2013. doi: 10.1088/2041-8205/778/2/L37.

Doron Kushnir, Matias Zaldarriaga, Juna A. Kollmeier, and Roni Waldman. GW150914: spin-based constraints on the merger time of the progenitor system. *MNRAS*, 462(1):844–849, October 2016. doi: 10.1093/mnras/stw1684.

Doron Kushnir, Matias Zaldarriaga, Juna A. Kollmeier, and Roni Wald-

- man. Dynamical tides reexpressed. *MNRAS*, 467(2):2146–2149, May 2017. doi: 10.1093/mnras/stx255.
- D. Lai. Resonant Oscillations and Tidal Heating in Coalescing Binary Neutron Stars. *MNRAS*, 270:611, October 1994. doi: 10.1093/mnras/270.3.611.
- D. Lai. Orbital Decay of the PSR J0045-7319 Binary System: Age of Radio Pulsar and Initial Spin of Neutron Star. *ApJL*, 466:L35, July 1996a. doi: 10.1086/310166.
- D. Lai. Orbital Decay of the PSR J0045-7319 Binary System: Age of Radio Pulsar and Initial Spin of Neutron Star. *ApJL*, 466:L35, July 1996b. doi: 10.1086/310166.
- D. Lai. Dynamical Tides in Rotating Binary Stars. *ApJ*, 490:847–862, December 1997.
- D. Lai and A. G. Wiseman. Innermost stable circular orbit of inspiraling neutron-star binaries: Tidal effects, post-Newtonian effects, and the neutron-star equation of state. *Phys. Rev. D.*, 54:3958–3964, September 1996. doi: 10.1103/PhysRevD.54.3958.
- D. Lai and Y. Wu. Resonant tidal excitations of inertial modes in coalescing neutron star binaries. *Phys. Rev. D*, 74(2):024007, July 2006. doi: 10.1103/PhysRevD.74.024007.
- D. Lai, F. A. Rasio, and S. L. Shapiro. Hydrodynamics of rotating stars and close binary interactions: Compressible ellipsoid models. *ApJ*, 437: 742–769, December 1994a. doi: 10.1086/175036.

D. Lai, F. A. Rasio, and S. L. Shapiro. Hydrodynamic instability and coalescence of binary neutron stars. *ApJ*, 420:811–829, January 1994b. doi: 10.1086/173606.

Charles-Philippe Lajoie and Alison Sills. Mass Transfer in Binary Stars Using Smoothed Particle Hydrodynamics. I. Numerical Method. *ApJ*, 726(2):66, January 2011a. doi: 10.1088/0004-637X/726/2/66.

Charles-Philippe Lajoie and Alison Sills. Mass Transfer in Binary Stars Using Smoothed Particle Hydrodynamics. II. Eccentric Binaries. *ApJ*, 726(2):67, January 2011b. doi: 10.1088/0004-637X/726/2/67.

Lev Davidovich Landau and E. M. Lifshitz. *Fluid mechanics*. 1959.

H. M. Lee and J. P. Ostriker. Cross sections for tidal capture binary formation and stellar merger. *ApJ*, 310:176–188, November 1986. doi: 10.1086/164674.

A. J. Levan, N. R. Tanvir, R. L. C. Starling, K. Wiersema, K. L. Page, D. A. Perley, S. Schulze, G. A. Wynn, R. Chornock, J. Hjorth, S. B. Cenko, A. S. Fruchter, P. T. O’Brien, G. C. Brown, R. L. Tunnicliffe, D. Malesani, P. Jakobsson, D. Watson, E. Berger, D. Bersier, B. E. Cobb, S. Covino, A. Cucchiara, A. de Ugarte Postigo, D. B. Fox, A. Gal-Yam, P. Goldoni, J. Gorosabel, L. Kaper, T. Krühler, R. Karjalainen, J. P. Osborne, E. Pian, R. Sánchez-Ramírez, B. Schmidt, I. Skillen, G. Tagliaferri, C. Thöne, O. Vaduvescu, R. A. M. J. Wijers, and B. A. Zauderer. A New Population of Ultra-long Duration Gamma-Ray Bursts. *ApJ*, 781:13, January 2014. doi: 10.1088/0004-637X/781/1/13.

G. Li and A. Loeb. Accumulated tidal heating of stars over multiple peri-

centre passages near SgrA\*. *MNRAS*, 429:3040–3046, March 2013. doi: 10.1093/mnras/sts567.

M. L. Lidov. The evolution of orbits of artificial satellites of planets under the action of gravitational perturbations of external bodies. *Planet. Space Sci.*, 9:719–759, October 1962. doi: 10.1016/0032-0633(62)90129-0.

LIGO Scientific Collaboration and Virgo Collaboration. GW170817: Observation of Gravitational Waves from a Binary Neutron Star Inspiral. *Physical Review Letters*, 119(16):161101, October 2017. doi: 10.1103/PhysRevLett.119.161101.

LIGO Scientific Collaboration and Virgo Collaboration. GWTC-1: A Gravitational-Wave Transient Catalog of Compact Binary Mergers Observed by LIGO and Virgo during the First and Second Observing Runs. *Physical Review X*, 9(3):031040, July 2019. doi: 10.1103/PhysRevX.9.031040.

D. N. C. Lin, P. Bodenheimer, and D. C. Richardson. Orbital migration of the planetary companion of 51 Pegasi to its present location. *Nature*, 380: 606–607, April 1996. doi: 10.1038/380606a0.

Craig W. Lincoln and Clifford M. Will. Coalescing binary systems of compact objects to (post)<sup>5/2</sup>-Newtonian order: Late-time evolution and gravitational-radiation emission. *Phys. Rev. D.*, 42(4):1123–1143, Aug 1990. doi: 10.1103/PhysRevD.42.1123.

V. M. Lipunov, K. A. Postnov, and M. E. Prokhorov. Black holes and gravitational waves: Possibilities for simultaneous detection using first-

generation laser interferometers. *Astronomy Letters*, 23:492–497, July 1997.

V. M. Lipunov, V. Kornilov, E. Gorbovskoy, D. A. H. Buckley, N. Tiurina, P. Balanutsa, A. Kuznetsov, J. Greiner, V. Vladimirov, D. Vlasenko, V. Chazov, D. Kuvshinov, A. Gabovich, S. B. Potter, A. Kniazev, S. Crawford, R. Rebolo Lopez, M. Serra-Ricart, G. Israelián, N. Lodieu, O. Gress, N. Budnev, K. Ivanov, V. Poleschuk, S. Yazev, A. Tlatov, V. Senik, V. Yurkov, D. Dormidontov, A. Parkhomenko, Y. Sergienko, R. Podesta, H. Levato, C. Lopez, C. Saffe, F. Podesta, and C. Mallamaci. First gravitational-wave burst GW150914: MASTER optical follow-up observations. *MNRAS*, 465:3656–3667, March 2017. doi: 10.1093/mnras/stw2669.

Y. Lithwick and Y. Wu. Secular chaos and its application to Mercury, hot Jupiters, and the organization of planetary systems. *Proceedings of the National Academy of Science*, 111:12610–12615, September 2014. doi: 10.1073/pnas.1308261110.

B. Liu and D. Lai. Black Hole and Neutron Star Binary Mergers in Triple Systems: Merger Fraction and Spin-Orbit Misalignment. *ApJ*, 863:68, August 2018. doi: 10.3847/1538-4357/aad09f.

B. Liu, D. J. Muñoz, and D. Lai. Suppression of extreme orbital evolution in triple systems with short-range forces. *MNRAS*, 447:747–764, February 2015. doi: 10.1093/mnras/stu2396.

Bin Liu and Dong Lai. Enhanced black hole mergers in binary-binary interactions. *MNRAS*, 483(3):4060–4069, Mar 2019. doi: 10.1093/mnras/sty3432.

Bin Liu, Dong Lai, and Yi-Han Wang. Black Hole and Neutron Star Binary Mergers in Triple Systems: II. Merger Eccentricity and Spin-Orbit Misalignment. *arXiv e-prints*, art. arXiv:1905.00427, May 2019.

Nicholas Loutrel, Samuel Liebersbach, Nicolás Yunes, and Neil Cornish. The eccentric behavior of inspiralling compact binaries. *Classical and Quantum Gravity*, 36(2):025004, Jan 2019. doi: 10.1088/1361-6382/aaf2a9.

Marcus E. Lower, Eric Thrane, Paul D. Lasky, and Rory Smith. Measuring eccentricity in binary black hole inspirals with gravitational waves. *Phys. Rev. D.*, 98(8):083028, Oct 2018. doi: 10.1103/PhysRevD.98.083028.

J.-P. Luminet and B. Pichon. Tidal pinching of white dwarfs. *Astron. and Astrophys.*, 209:103–110, January 1989.

John C. Lurie, Karl Vyhmeister, Suzanne L. Hawley, Jamel Adilia, Andrea Chen, James R. A. Davenport, Mario Jurić, Michael Puig-Holzman, and Kolby L. Weisenburger. Tidal Synchronization and Differential Rotation of Kepler Eclipsing Binaries. *Astronomical Journal*, 154(6):250, December 2017. doi: 10.3847/1538-3881/aa974d.

M. MacLeod, J. Goldstein, E. Ramirez-Ruiz, J. Guillochon, and J. Samsing. Illuminating Massive Black Holes with White Dwarfs: Orbital Dynamics and High-energy Transients from Tidal Interactions. *ApJ*, 794:9, October 2014. doi: 10.1088/0004-637X/794/1/9.

M. MacLeod, J. Guillochon, E. Ramirez-Ruiz, D. Kasen, and S. Rosswog. Optical Thermonuclear Transients from Tidal Compression of White

Dwarfs as Tracers of the Low End of the Massive Black Hole Mass Function. *ApJ*, 819:3, March 2016. doi: 10.3847/0004-637X/819/1/3.

Morgan MacLeod and Abraham Loeb. Runaway Coalescence of Pre-common-envelope Stellar Binaries. *ApJ*, 893(2):106, April 2020a. doi: 10.3847/1538-4357/ab822e.

Morgan MacLeod and Abraham Loeb. Pre-common-envelope Mass Loss from Coalescing Binary Systems. *ApJ*, 895(1):29, May 2020b. doi: 10.3847/1538-4357/ab89b6.

Morgan MacLeod, Phillip Macias, Enrico Ramirez-Ruiz, Jonathan Grindlay, Aldo Batta, and Gabriela Montes. Lessons from the Onset of a Common Envelope Episode: the Remarkable M31 2015 Luminous Red Nova Outburst. *ApJ*, 835(2):282, Feb 2017. doi: 10.3847/1538-4357/835/2/282.

Morgan MacLeod, Eve C. Ostriker, and James M. Stone. Runaway Coalescence at the Onset of Common Envelope Episodes. *ApJ*, 863(1):5, August 2018a. doi: 10.3847/1538-4357/aacf08.

Morgan MacLeod, Eve C. Ostriker, and James M. Stone. Bound Outflows, Unbound Ejecta, and the Shaping of Bipolar Remnants during Stellar Coalescence. *ApJ*, 868(2):136, December 2018b. doi: 10.3847/1538-4357/aae9eb.

Morgan MacLeod, Michelle Vick, Dong Lai, and James M. Stone. Polygram Stars: Resonant Tidal Excitation of Fundamental Oscillation Modes in Asynchronous Stellar Coalescence. *ApJ*, 877(1):28, May 2019. doi: 10.3847/1538-4357/ab184c.

Ilya Mandel and Selma E. de Mink. Merging binary black holes formed through chemically homogeneous evolution in short-period stellar binaries. *MNRAS*, 458(3):2634–2647, May 2016. doi: 10.1093/mnras/stw379.

Michela Mapelli and Nicola Giacobbo. The cosmic merger rate of neutron stars and black holes. *MNRAS*, 479(4):4391–4398, October 2018. doi: 10.1093/mnras/sty1613.

Michela Mapelli and Luca Zampieri. Roche-lobe Overflow Systems Powered by Black Holes in Young Star Clusters: The Importance of Dynamical Exchanges. *ApJ*, 794(1):7, October 2014. doi: 10.1088/0004-637X/794/1/7.

Michela Mapelli, Nicola Giacobbo, Filippo Santoliquido, and Maria Celeste Artale. The properties of merging black holes and neutron stars across cosmic time. *MNRAS*, 487(1):2–13, July 2019. doi: 10.1093/mnras/stz1150.

G. Marcy, R. P. Butler, D. Fischer, S. Vogt, J. T. Wright, C. G. Tinney, and H. R. A. Jones. Observed Properties of Exoplanets: Masses, Orbits, and Metallicities. *Progress of Theoretical Physics Supplement*, 158:24–42, 2005. doi: 10.1143/PTPS.158.24.

R. A. Mardling. The Role of Chaos in the Circularization of Tidal Capture Binaries. I. The Chaos Boundary. *ApJ*, 450:722, September 1995a. doi: 10.1086/176178.

R. A. Mardling. The Role of Chaos in the Circularization of Tidal Capture Binaries. II. Long-Time Evolution. *ApJ*, 450:732, September 1995b. doi: 10.1086/176179.

- R. A. Mardling and S. J. Aarseth. Tidal interactions in star cluster simulations. *MNRAS*, 321:398–420, March 2001. doi: 10.1046/j.1365-8711.2001.03974.x.
- M. C. Miller and D. P. Hamilton. Four-Body Effects in Globular Cluster Black Hole Coalescence. *ApJ*, 576:894–898, September 2002. doi: 10.1086/341788.
- M. C. Miller and V. M. Lauburg. Mergers of Stellar-Mass Black Holes in Nuclear Star Clusters. *ApJ*, 692:917–923, February 2009. doi: 10.1088/0004-637X/692/1/917.
- Meagan Morscher, Bharath Pappabiraman, Carl Rodriguez, Frederic A. Rasio, and Stefan Umbreit. The Dynamical Evolution of Stellar Black Holes in Globular Clusters. *ApJ*, 800(1):9, February 2015. doi: 10.1088/0004-637X/800/1/9.
- D. J. Muñoz, D. Lai, and B. Liu. The formation efficiency of close-in planets via Lidov-Kozai migration: analytic calculations. *MNRAS*, 460:1086–1093, July 2016. doi: 10.1093/mnras/stw983.
- C. D. Murray and S.F. Dermott. *Solar System Dynamics*. Cambridge Univ. Press, Cambridge, 2000.
- M. Nagasawa, S. Ida, and T. Bessho. Formation of Hot Planets by a Combination of Planet Scattering, Tidal Circularization, and the Kozai Mechanism. *ApJ*, 678:498-508, May 2008. doi: 10.1086/529369.
- J. L. A. Nandez and N. Ivanova. Common envelope events with low-mass giants: understanding the energy budget. *MNRAS*, 460(4):3992–4002, August 2016. doi: 10.1093/mnras/stw1266.

- J. L. A. Nandez, N. Ivanova, and Jr. Lombardi, J. C. V1309 Sco—Understanding a Merger. *ApJ*, 786(1):39, May 2014. doi: 10.1088/0004-637X/786/1/39.
- S. Naoz. The Eccentric Kozai-Lidov Effect and Its Applications. *Annual Review of Astron. and Astrophys.*, 54:441–489, September 2016. doi: 10.1146/annurev-astro-081915-023315.
- S. Naoz, W. M. Farr, and F. A. Rasio. On the Formation of Hot Jupiters in Stellar Binaries. *ApJL*, 754:L36, August 2012. doi: 10.1088/2041-8205/754/2/L36.
- Smadar Naoz and Daniel C. Fabrycky. Mergers and Obliquities in Stellar Triples. *ApJ*, 793(2):137, October 2014. doi: 10.1088/0004-637X/793/2/137.
- Smadar Naoz, Will M. Farr, Yoram Lithwick, Frederic A. Rasio, and Jean Teyssandier. Secular dynamics in hierarchical three-body systems. *MNRAS*, 431(3):2155–2171, May 2013. doi: 10.1093/mnras/stt302.
- N. Narita, B. Sato, T. Hirano, and M. Tamura. First Evidence of a Retrograde Orbit of a Transiting Exoplanet HAT-P-7b. *Publications of the Astronomical Society of Japan*, 61:L35–L40, October 2009. doi: 10.1093/pasj/61.5.L35.
- H. Ngo, H. A. Knutson, S. Hinkley, J. R. Crepp, E. B. Bechter, K. Batygin, A. W. Howard, J. A. Johnson, T. D. Morton, and P. S. Muirhead. Friends of Hot Jupiters. II. No Correspondence between Hot-jupiter Spin-Orbit Misalignment and the Incidence of Directly Imaged Stellar Companions. *ApJ*, 800:138, February 2015. doi: 10.1088/0004-637X/800/2/138.

Christopher E. O'Connor and Bradley M. S. Hansen. Constraining planetary migration and tidal dissipation with coeval hot Jupiters. *MNRAS*, 477(1):175–189, June 2018. doi: 10.1093/mnras/sty645.

G. I. Ogilvie and D. N. C. Lin. Tidal Dissipation in Rotating Solar-Type Stars. *ApJ*, 661:1180–1191, June 2007. doi: 10.1086/515435.

Gordon I. Ogilvie. Tidal Dissipation in Stars and Giant Planets. *Annual Review of Astron. and Astrophys.*, 52:171–210, Aug 2014. doi: 10.1146/annurev-astro-081913-035941.

Gordon I. Ogilvie and Geoffroy Lesur. On the interaction between tides and convection. *MNRAS*, 422(3):1975–1987, May 2012. doi: 10.1111/j.1365-2966.2012.20630.x.

Sebastian T. Ohlmann, Friedrich K. Röpke, Rüdiger Pakmor, and Volker Springel. Hydrodynamic Moving-mesh Simulations of the Common Envelope Phase in Binary Stellar Systems. *ApJL*, 816(1):L9, January 2016. doi: 10.3847/2041-8205/816/1/L9.

R. M. O’Leary, B. Kocsis, and A. Loeb. Gravitational waves from scattering of stellar-mass black holes in galactic nuclei. *MNRAS*, 395:2127–2146, June 2009. doi: 10.1111/j.1365-2966.2009.14653.x.

B. Paczynski. Common Envelope Binaries. In Peter Eggleton, Simon Mitton, and John Whelan, editors, *Structure and Evolution of Close Binary Systems*, volume 73 of *IAU Symposium*, page 75, Jan 1976.

L. J. Papenfort, R. Gold, and L. Rezzolla. Dynamical ejecta and nucleosynthetic yields from eccentric binary neutron-star mergers. *Phys. Rev. D.*, 98(10):104028, November 2018. doi: 10.1103/PhysRevD.98.104028.

A. Parisi and R. Sturani. Gravitational waves from neutron star excitations in a binary inspiral. *Phys. Rev. D.*, 97(4):043015, February 2018. doi: 10.1103/PhysRevD.97.043015.

Kishore C. Patra, Joshua N. Winn, Matthew J. Holman, Michael Gillon, Artem Burdanov, Emmanuel Jehin, Laetitia Delrez, Francisco J. Pozuelos, Khalid Barkaoui, Zouhair Benkhaldoun, Norio Narita, Akihiko Fukui, Nobuhiko Kusakabe, Kiyoie Kawauchi, Yuka Terada, L. G. Bouma, Nevin N. Weinberg, and Madelyn Broome. The Continuing Search for Evidence of Tidal Orbital Decay of Hot Jupiters. *Astronomical Journal*, 159(4):150, April 2020. doi: 10.3847/1538-3881/ab7374.

B. Paxton, L. Bildsten, A. Dotter, F. Herwig, P. Lesaffre, and F. Timmes. Modules for Experiments in Stellar Astrophysics (MESA). *Astrophysical Journal Supplement*, 192:3, January 2011. doi: 10.1088/0067-0049/192/1/3.

Ondřej Pejcha, Joe M. Antognini, Benjamin J. Shappee, and Todd A. Thompson. Greatly enhanced eccentricity oscillations in quadruple systems composed of two binaries: implications for stars, planets and transients. *MNRAS*, 435(2):943–951, October 2013. doi: 10.1093/mnras/stt1281.

Kaloyan Penev and Dimitar Sasselov. Tidal Evolution of Close-in Extrasolar Planets: High Stellar Q from New Theoretical Models. *ApJ*, 731(1):67, Apr 2011. doi: 10.1088/0004-637X/731/1/67.

Kaloyan Penev, Joseph Barranco, and Dimitar Sasselov. Three-dimensional Spectral Simulations of Anelastic Turbulent Convection. *ApJ*, 734(2):118, Jun 2011. doi: 10.1088/0004-637X/734/2/118.

- A. J. Penner, N. Andersson, L. Samuelsson, I. Hawke, and D. I. Jones. Tidal deformations of neutron stars: The role of stratification and elasticity. *Phys. Rev. D.*, 84(10):103006, Nov 2011. doi: 10.1103/PhysRevD.84.103006.
- P. C. Peters. Gravitational radiation and the motion of two point masses. *Phys. Rev.*, 136, 1964.
- C. Petrovich. Steady-state Planet Migration by the Kozai-Lidov Mechanism in Stellar Binaries. *ApJ*, 799:27, January 2015a. doi: 10.1088/0004-637X/799/1/27.
- C. Petrovich. Hot Jupiters from Coplanar High-eccentricity Migration. *ApJ*, 805:75, May 2015b. doi: 10.1088/0004-637X/805/1/75.
- C. Petrovich and S. Tremaine. Warm Jupiters from Secular Planet-Planet Interactions. *ApJ*, 829:132, October 2016. doi: 10.3847/0004-637X/829/2/132.
- E. S. Phinney. Pulsars as Probes of Newtonian Dynamical Systems. *Philosophical Transactions of the Royal Society of London Series A*, 341(1660):39–75, Oct 1992. doi: 10.1098/rsta.1992.0084.
- P. Podsiadlowski, S. Rappaport, and Z. Han. On the formation and evolution of black hole binaries. *MNRAS*, 341:385–404, May 2003. doi: 10.1046/j.1365-8711.2003.06464.x.
- S. F. Portegies Zwart and S. L. W. McMillan. Black Hole Mergers in the Universe. *ApJL*, 528:L17–L20, January 2000. doi: 10.1086/312422.
- W. H. Press and S. A. Teukolsky. On formation of close binaries by two-body tidal capture. *ApJ*, 213:183–192, April 1977. doi: 10.1086/155143.

Adrian M. Price-Whelan and Jeremy Goodman. Binary Companions of Evolved Stars in APOGEE DR14: Orbital Circularization. *ApJ*, 867(1):5, Nov 2018. doi: 10.3847/1538-4357/aae264.

Logan J. Prust and Philip Chang. Common envelope evolution on a moving mesh. *MNRAS*, 486(4):5809–5818, July 2019. doi: 10.1093/mnras/stz1219.

D. Raghavan, H. A. McAlister, T. J. Henry, D. W. Latham, G. W. Marcy, B. D. Mason, D. R. Gies, R. J. White, and T. A. ten Brummelaar. A Survey of Stellar Families: Multiplicity of Solar-type Stars. *ApJS*, 190:1–42, September 2010. doi: 10.1088/0067-0049/190/1/1.

F. A. Rasio and E. B. Ford. Dynamical instabilities and the formation of extrasolar planetary systems. *Science*, 274:954–956, November 1996. doi: 10.1126/science.274.5289.954.

M. J. Rees. Tidal disruption of stars by black holes of 10 to the 6th-10 to the 8th solar masses in nearby galaxies. *Nature*, 333:523–528, June 1988. doi: 10.1038/333523a0.

A. Reisenegger and P. Goldreich. Excitation of neutron star normal modes during binary inspiral. *ApJ*, 426:688–691, May 1994. doi: 10.1086/174105.

Paul M. Ricker and Ronald E. Taam. The Interaction of Stellar Objects within a Common Envelope. *ApJL*, 672(1):L41, January 2008. doi: 10.1086/526343.

Paul M. Ricker and Ronald E. Taam. An AMR Study of the Common-

envelope Phase of Binary Evolution. *ApJ*, 746(1):74, February 2012. doi: 10.1088/0004-637X/746/1/74.

C. L. Rodriguez, M. Morscher, B. Pattabiraman, S. Chatterjee, C.-J. Haster, and F. A. Rasio. Binary Black Hole Mergers from Globular Clusters: Implications for Advanced LIGO. *Physical Review Letters*, 115(5):051101, July 2015. doi: 10.1103/PhysRevLett.115.051101.

Carl L. Rodriguez, Sourav Chatterjee, and Frederic A. Rasio. Binary black hole mergers from globular clusters: Masses, merger rates, and the impact of stellar evolution. *Phys. Review D*, 93(8):084029, April 2016a. doi: 10.1103/PhysRevD.93.084029.

Carl L. Rodriguez, Carl-Johan Haster, Sourav Chatterjee, Vicky Kalogera, and Frederic A. Rasio. Dynamical Formation of the GW150914 Binary Black Hole. *ApJL*, 824(1):L8, June 2016b. doi: 10.3847/2041-8205/824/1/L8.

S. Rosswog, E. Ramirez-Ruiz, and W. R. Hix. Atypical Thermonuclear Supernovae from Tidally Crushed White Dwarfs. *ApJ*, 679:1385-1389, June 2008a. doi: 10.1086/528738.

S. Rosswog, E. Ramirez-Ruiz, W. R. Hix, and M. Dan. Simulating black hole white dwarf encounters. *Computer Physics Communications*, 179: 184–189, July 2008b. doi: 10.1016/j.cpc.2008.01.031.

S. Rosswog, E. Ramirez-Ruiz, and W. R. Hix. Tidal Disruption and Ignition of White Dwarfs by Moderately Massive Black Holes. *ApJ*, 695:404–419, April 2009. doi: 10.1088/0004-637X/695/1/404.

- J. Samsing. Eccentric black hole mergers forming in globular clusters. *Phys. Rev. D.*, 97(10):103014, May 2018. doi: 10.1103/PhysRevD.97.103014.
- J. Samsing, M. MacLeod, and E. Ramirez-Ruiz. The Formation of Eccentric Compact Binary Inspirals and the Role of Gravitational Wave Emission in Binary-Single Stellar Encounters. *ApJ*, 784:71, March 2014. doi: 10.1088/0004-637X/784/1/71.
- A. Santerne, C. Moutou, M. Tsantaki, F. Bouchy, G. Hébrard, V. Adibekyan, J.-M. Almenara, L. Amard, S. C. C. Barros, I. Boisse, A. S. Bonomo, G. Bruno, B. Courcol, M. Deleuil, O. Demangeon, R. F. Díaz, T. Guillot, M. Havel, G. Montagnier, A. S. Rajpurohit, J. Rey, and N. C. Santos. SOPHIE velocimetry of Kepler transit candidates. XVII. The physical properties of giant exoplanets within 400 days of period. *Astron. and Astrophys.*, 587:A64, March 2016. doi: 10.1051/0004-6361/201527329.
- G. J. Savonije and M. G. Witte. Tidal interaction of a rotating 1 vec {M\_sun} star with a binary companion. *Astron. and Astrophys.*, 386:211–221, Apr 2002. doi: 10.1051/0004-6361:20020237.
- A. K. Schenk, P. Arras, É. Flanagan, S. A. Teukolsky, and I. Wasserman. Nonlinear mode coupling in rotating stars and the r-mode instability in neutron stars. *Phys. Rev. D*, 65(2):024001, January 2002. doi: 10.1103/PhysRevD.65.024001.
- J. F. Sepinsky, B. Willems, and V. Kalogera. Equipotential Surfaces and Lagrangian Points in Nonsynchronous, Eccentric Binary and Planetary Systems. *ApJ*, 660(2):1624–1635, May 2007a. doi: 10.1086/513736.

J. F. Sepinsky, B. Willems, V. Kalogera, and F. A. Rasio. Interacting Binaries with Eccentric Orbits: Secular Orbital Evolution Due to Conservative Mass Transfer. *ApJ*, 667(2):1170–1184, October 2007b. doi: 10.1086/520911.

J. F. Sepinsky, B. Willems, V. Kalogera, and F. A. Rasio. Interacting Binaries with Eccentric Orbits. II. Secular Orbital Evolution due to Non-conservative Mass Transfer. *ApJ*, 702(2):1387–1392, September 2009. doi: 10.1088/0004-637X/702/2/1387.

J. F. Sepinsky, B. Willems, V. Kalogera, and F. A. Rasio. Interacting Binaries with Eccentric Orbits. III. Orbital Evolution due to Direct Impact and Self-Accretion. *ApJ*, 724(1):546–558, November 2010. doi: 10.1088/0004-637X/724/1/546.

A. Sesana, A. Vecchio, M. Eracleous, and S. Sigurdsson. Observing white dwarfs orbiting massive black holes in the gravitational wave and electro-magnetic window. *MNRAS*, 391:718–726, December 2008. doi: 10.1111/j.1365-2966.2008.13904.x.

R. V. Shcherbakov, A. Pe'er, C. S. Reynolds, R. Haas, T. Bode, and P. Laguna. GRB060218 as a Tidal Disruption of a White Dwarf by an Intermediate-mass Black Hole. *ApJ*, 769:85, June 2013. doi: 10.1088/0004-637X/769/2/85.

Masaru Shibata. Gravitational waves by compact star orbiting around rotating supermassive black holes. *Phys. Rev. D.*, 50(10):6297–6311, Nov 1994. doi: 10.1103/PhysRevD.50.6297.

Dmitry Shishkin and Noam Soker. Eccentric grazing envelope evo-

lution towards type IIb supernova progenitors. *arXiv e-prints*, art. arXiv:2003.14096, March 2020.

Avi Shporer, Jim Fuller, Howard Isaacson, Kelly Hambleton, Susan E. Thompson, Andrej Prša, Donald W. Kurtz, Andrew W. Howard, and Ryan M. O’Leary. Radial Velocity Monitoring of Kepler Heartbeat Stars. *ApJ*, 829(1):34, Sep 2016. doi: 10.3847/0004-637X/829/1/34.

Kedron Silsbee and Scott Tremaine. Lidov-Kozai Cycles with Gravitational Radiation: Merging Black Holes in Isolated Triple Systems. *ApJ*, 836(1):39, Feb 2017. doi: 10.3847/1538-4357/aa5729.

A. Socrates, B. Katz, S. Dong, and S. Tremaine. Super-eccentric Migrating Jupiters. *ApJ*, 750:106, May 2012. doi: 10.1088/0004-637X/750/2/106.

Mario Spera, Michela Mapelli, Nicola Giacobbo, Alessandro A. Trani, Alessandro Bressan, and Guglielmo Costa. Merging black hole binaries with the SEVN code. *MNRAS*, 485(1):889–907, May 2019. doi: 10.1093/mnras/stz359.

Jan E. Staff, Orsola De Marco, Daniel Macdonald, Pablo Galaviz, Jean-Claude Passy, Roberto Iaconi, and Mordecai-Mark Mac Low. Hydrodynamic simulations of the interaction between an AGB star and a main-sequence companion in eccentric orbits. *MNRAS*, 455(4):3511–3525, February 2016. doi: 10.1093/mnras/stv2548.

Simon Stevenson, Alejandro Vigna-Gómez, Ilya Mandel, Jim W. Barrett, Coenraad J. Neijssel, David Perkins, and Selma E. de Mink. Formation of the first three gravitational-wave observations through isolated

binary evolution. *Nature Communications*, 8:14906, April 2017. doi: 10.1038/ncomms14906.

James M. Stone, Kengo Tomida, Christopher J. White, and Kyle G. Felker. The Athena++ Adaptive Mesh Refinement Framework: Design and Magnetohydrodynamic Solvers. *arXiv e-prints*, art. arXiv:2005.06651, May 2020.

N. C. Stone and B. D. Metzger. Rates of stellar tidal disruption as probes of the supermassive black hole mass function. *MNRAS*, 455:859–883, January 2016. doi: 10.1093/mnras/stv2281.

N. C. Stone, A. H. W. Küpper, and J. P. Ostriker. Formation of massive black holes in galactic nuclei: runaway tidal encounters. *MNRAS*, 467: 4180–4199, June 2017. doi: 10.1093/mnras/stx097.

N. I. Storch, D. Lai, and K. R. Anderson. Dynamics of stellar spin driven by planets undergoing Lidov-Kozai migration: paths to spin-orbit misalignment. *MNRAS*, 465:3927–3942, March 2017. doi: 10.1093/mnras/stw3018.

Natalia I. Storch and Dong Lai. Viscoelastic tidal dissipation in giant planets and formation of hot Jupiters through high-eccentricity migration. *MNRAS*, 438(2):1526–1534, Feb 2014. doi: 10.1093/mnras/stt2292.

M. Sun, P. Arras, N. N. Weinberg, N. W. Troup, and S. R. Majewski. Orbital decay in binaries containing post-main-sequence stars. *MNRAS*, 481(3): 4077–4092, Dec 2018. doi: 10.1093/mnras/sty2464.

Ronald E. Taam and Eric L. Sandquist. Common Envelope Evolution of

Massive Binary Stars. *Annual Review of Astron. and Astrophys.*, 38:113–141, January 2000. doi: 10.1146/annurev.astro.38.1.113.

T. M. Tauris. Binary evolution and formation of binary millisecond pulsars. *Proceedings of the Astronomical Society of Australia*, 11(1):82, April 1994.

T. M. Tauris and E. P. J. van den Heuvel. *Formation and evolution of compact stellar X-ray sources*, volume 39, pages 623–665. 2006.

T. M. Tauris, M. Kramer, P. C. C. Freire, N. Wex, H. T. Janka, N. Langer, Ph. Podsiadlowski, E. Bozzo, S. Chaty, M. U. Kruckow, E. P. J. van den Heuvel, J. Antoniadis, R. P. Breton, and D. J. Champion. Formation of Double Neutron Star Systems. *ApJ*, 846(2):170, September 2017. doi: 10.3847/1538-4357/aa7e89.

E. Tejeda, E. Gaftron, and S. Rosswog. Tidal disruptions by rotating black holes: relativistic hydrodynamics with Newtonian codes. *ArXiv e-prints*, January 2017.

I. Tews, J. Margueron, and S. Reddy. Critical examination of constraints on the equation of state of dense matter obtained from GW170817. *Phys. Rev. C*, 98(4):045804, Oct 2018. doi: 10.1103/PhysRevC.98.045804.

Jean Teyssandier, Dong Lai, and Michelle Vick. Formation of hot Jupiters through secular chaos and dynamical tides. *MNRAS*, 486(2):2265–2280, June 2019. doi: 10.1093/mnras/stz1011.

The LIGO Scientific Collaboration, the Virgo Collaboration, B. P. Abbott, R. Abbott, T. D. Abbott, S. Abraham, F. Acernese, K. Ackley, C. Adams,

R. X. Adhikari, and et al. GWTC-1: A Gravitational-Wave Transient Catalog of Compact Binary Mergers Observed by LIGO and Virgo during the First and Second Observing Runs. *arXiv e-prints*, November 2018.

S. E. Thompson, M. Everett, F. Mullally, T. Barclay, S. B. Howell, M. Still, J. Rowe, J. L. Christiansen, D. W. Kurtz, K. Hambleton, J. D. Twicken, K. A. Ibrahim, and B. D. Clarke. A Class of Eccentric Binaries with Dynamic Tidal Distortions Discovered with Kepler. *ApJ*, 753:86, July 2012. doi: 10.1088/0004-637X/753/1/86.

Todd A. Thompson. Accelerating Compact Object Mergers in Triple Systems with the Kozai Resonance: A Mechanism for “Prompt” Type Ia Supernovae, Gamma-Ray Bursts, and Other Exotica. *ApJ*, 741(2):82, November 2011. doi: 10.1088/0004-637X/741/2/82.

V. Tiwari, S. Klimenko, N. Christensen, E. A. Huerta, S. R. P. Mohapatra, A. Gopakumar, M. Haney, P. Ajith, S. T. McWilliams, G. Vedovato, M. Drago, F. Salemi, G. A. Prodi, C. Lazzaro, S. Tiwari, G. Mitselmakher, and F. Da Silva. Proposed search for the detection of gravitational waves from eccentric binary black holes. *Phys. Rev. D.*, 93(4):043007, Feb 2016. doi: 10.1103/PhysRevD.93.043007.

R. H. D. Townsend and S. A. Teitler. GYRE: an open-source stellar oscillation code based on a new Magnus Multiple Shooting scheme. *MNRAS*, 435:3406–3418, November 2013. doi: 10.1093/mnras/stt1533.

A. H. M. J. Triaud, A. Collier Cameron, D. Queloz, D. R. Anderson, M. Gillon, L. Hebb, C. Hellier, B. Loeillet, P. F. L. Maxted, M. Mayor, F. Pepe, D. Pollacco, D. Ségransan, B. Smalley, S. Udry, R. G. West, and

P. J. Wheatley. Spin-orbit angle measurements for six southern transiting planets. New insights into the dynamical origins of hot Jupiters. *Astron. and Astrophys.*, 524:A25, December 2010. doi: 10.1051/0004-6361/201014525.

W. Unno, Y. Osaki, H. Ando, H. Saio, and H. Shibahashi. *Nonradial Oscillations of Stars*. 1989.

Kōji Uryū, François Limousin, John L. Friedman, Eric Gourgoulhon, and Masaru Shibata. Nonconformally flat initial data for binary compact objects. *Phys. Rev. D.*, 80(12):124004, Dec 2009. doi: 10.1103/PhysRevD.80.124004.

E. P. J. van den Heuvel. Late Stages of Close Binary Systems. In Peter Eggleton, Simon Mitton, and John Whelan, editors, *Structure and Evolution of Close Binary Systems*, volume 73 of *IAU Symposium*, page 35, Jan 1976.

E. P. J. van den Heuvel and C. De Loore. The nature of X-ray binaries III. Evolution of massive close binaries with one collapsed component - with a possible application to Cygnus X-3. *Astronomy and Astrophysics*, 25:387, June 1973.

E. P. J. van den Heuvel and R. E. Taam. Two types of binary radio pulsars with different evolutionary histories. *Nature*, 309(5965):235–237, May 1984. doi: 10.1038/309235a0.

S. van Velzen, G. E. Anderson, N. C. Stone, M. Fraser, T. Wevers, B. D. Metzger, P. G. Jonker, A. J. van der Horst, T. D. Staley, A. J. Mendez, J. C. A. Miller-Jones, S. T. Hodgkin, H. C. Campbell, and R. P. Fender. A radio jet

from the optical and x-ray bright stellar tidal disruption flare ASASSN-14li. *Science*, 351:62–65, January 2016. doi: 10.1126/science.aad1182.

F. Verbunt and E. S. Phinney. Tidal circularization and the eccentricity of binaries containing giant stars. *Astron. and Astrophys.*, 296:709, Apr 1995.

M. Vick, D. Lai, and J. Fuller. Tidal dissipation and evolution of white dwarfs around massive black holes: an eccentric path to tidal disruption. *MNRAS*, 468:2296–2310, June 2017. doi: 10.1093/mnras/stx539.

Michelle Vick and Dong Lai. Dynamical tides in highly eccentric binaries: chaos, dissipation, and quasi-steady state. *MNRAS*, 476(1):482–495, May 2018. doi: 10.1093/mnras/sty225.

Michelle Vick and Dong Lai. Tidal effects in eccentric coalescing neutron star binaries. *Phys. Rev. D*, 100(6):063001, Sep 2019a. doi: 10.1103/PhysRevD.100.063001.

Michelle Vick and Dong Lai. Tidal Evolution of Eccentric Binaries Driven by Convective Turbulent Viscosity. *arXiv e-prints*, art. arXiv:1912.04892, December 2019b.

Jérémie Vidal and Adrian J. Barker. Turbulent Viscosity Acting on the Equilibrium Tidal Flow in Convective Stars. *ApJL*, 888(2):L31, January 2020. doi: 10.3847/2041-8213/ab6219.

Alejandro Vigna-Gómez, Coenraad J. Neijssel, Simon Stevenson, Jim W. Barrett, Krzysztof Belczynski, Stephen Justham, Selma E. de Mink, Bernhard Müller, Philipp Podsiadlowski, Mathieu Renzo, Dorottya Szécsi, and Ilya Mandel. On the formation history of Galactic double neu-

tron stars. *MNRAS*, 481(3):4009–4029, Dec 2018. doi: 10.1093/mnras/sty2463.

Alejandro Vigna-Gómez, Morgan MacLeod, Coenraad J. Neijssel, Floor S. Broekgaarden, Stephen Justham, George Howitt, Selma E. de Mink, and Ilya Mand el. Common-Envelope Episodes that lead to Double Neutron Star formation. *arXiv e-prints*, art. arXiv:2001.09829, January 2020.

J. Wang, D. A. Fischer, E. P. Horch, and J.-W. Xie. Influence of Stellar Multiplicity On Planet Formation. III. Adaptive Optics Imaging of Kepler Stars With Gas Giant Planets. *ApJ*, 806:248, June 2015. doi: 10.1088/0004-637X/806/2/248.

R. F. Webbink. Double white dwarfs as progenitors of R Coronae Borealis stars and type I supernovae. *ApJ*, 277:355–360, February 1984. doi: 10.1086/161701.

Nevin N. Weinberg, Meng Sun, Phil Arras, and Reed Essick. Tidal Dissipation in WASP-12. *ApJL*, 849(1):L11, Nov 2017. doi: 10.3847/2041-8213/aa9113.

W. F. Welsh, J. A. Orosz, C. Aerts, T. M. Brown, E. Brugamyer, W. D. Cochran, R. L. Gilliland, J. A. Guzik, D. W. Kurtz, D. W. Latham, G. W. Marcy, S. N. Quinn, W. Zima, C. Allen, N. M. Batalha, S. Bryson, L. A. Buchhave, D. A. Caldwell, T. N. Gautier, III, S. B. Howell, K. Kinemuchi, K. A. Ibrahim, H. Isaacson, J. M. Jenkins, A. Prsa, M. Still, R. Street, B. Wohler, D. G. Koch, and W. J. Borucki. KOI-54: The Kepler Discovery of Tidally Excited Pulsations and Brightenings in a Highly Eccentric Binary. *ApJS*, 197:4, November 2011. doi: 10.1088/0067-0049/197/1/4.

- L. Wen. On the Eccentricity Distribution of Coalescing Black Hole Binaries Driven by the Kozai Mechanism in Globular Clusters. *ApJ*, 598:419–430, November 2003. doi: 10.1086/378794.
- J. N. Winn and D. C. Fabrycky. The Occurrence and Architecture of Exo-planetary Systems. *Annual Review of Astron. and Astrophys.*, 53:409–447, August 2015. doi: 10.1146/annurev-astro-082214-122246.
- J. N. Winn, J. A. Johnson, S. Albrecht, A. W. Howard, G. W. Marcy, I. J. Crossfield, and M. J. Holman. HAT-P-7: A Retrograde or Polar Orbit, and a Third Body. *ApjL*, 703:L99–L103, October 2009. doi: 10.1088/0004-637X/703/2/L99.
- M. G. Witte and G. J. Savonije. Tidal evolution of eccentric orbits in massive binary systems. A study of resonance locking. *Astron. and Astrophys.*, 350:129–147, October 1999.
- J. T. Wright, G. W. Marcy, A. W. Howard, J. A. Johnson, T. D. Morton, and D. A. Fischer. The Frequency of Hot Jupiters Orbiting nearby Solar-type Stars. *ApJ*, 753:160, July 2012. doi: 10.1088/0004-637X/753/2/160.
- Y. Wu. Diffusive Tidal Evolution for Migrating hot Jupiters. *ArXiv e-prints*, October 2017.
- Y. Wu. Diffusive Tidal Evolution for Migrating Hot Jupiters. *Astron. Journal*, 155:118, March 2018. doi: 10.3847/1538-3881/aaa970.
- Y. Wu and Y. Lithwick. Secular Chaos and the Production of Hot Jupiters. *ApJ*, 735:109, July 2011. doi: 10.1088/0004-637X/735/2/109.
- Y. Wu and N. Murray. Planet Migration and Binary Companions: The Case of HD 80606b. *ApJ*, 589:605–614, May 2003. doi: 10.1086/374598.

Yanqin Wu. Origin of Tidal Dissipation in Jupiter. I. Properties of Inertial Modes. *ApJ*, 635(1):674–687, December 2005. doi: 10.1086/497354.

W. Xu and D. Lai. Resonant tidal excitation of oscillation modes in merging binary neutron stars: Inertial-gravity modes. *Phys. Rev. D*, 96(8):083005, October 2017. doi: 10.1103/PhysRevD.96.083005.

H. Yang, W. E. East, V. Paschalidis, F. Pretorius, and R. F. P. Mendes. Evolution of highly eccentric binary neutron stars including tidal effects. *Phys. Rev. D.*, 98(4):044007, August 2018. doi: 10.1103/PhysRevD.98.044007.

Huan Yang. Inspiralizing eccentric binary neutron stars: orbital motion and tidal resonance. *arXiv e-prints*, art. arXiv:1904.11089, Apr 2019.

Samuel W. Yee, Joshua N. Winn, Heather A. Knutson, Kishore C. Patra, Shreyas Vissapragada, Michael M. Zhang, Matthew J. Holman, Avi Shporer, and Jason T. Wright. The Orbit of WASP-12b Is Decaying. *ApJL*, 888(1):L5, January 2020. doi: 10.3847/2041-8213/ab5c16.

Hang Yu and Nevin N. Weinberg. Resonant tidal excitation of superfluid neutron stars in coalescing binaries. *MNRAS*, 464(3):2622–2637, Jan 2017a. doi: 10.1093/mnras/stw2552.

Hang Yu and Nevin N. Weinberg. Dynamical tides in coalescing superfluid neutron star binaries with hyperon cores and their detectability with third-generation gravitational-wave detectors. *MNRAS*, 470(1):350–360, Sep 2017b. doi: 10.1093/mnras/stx1188.

J.-P. Zahn. The dynamical tide in close binaries. *Astron. and Astrophys.*, 41:329–344, July 1975.

J. P. Zahn. Reprint of 1977A&amp;A....57..383Z. Tidal friction in close binary stars. *Astron. and Astrophys.*, 500:121–132, May 1977.

J. P. Zahn. Tidal evolution of close binary stars. I - Revisiting the theory of the equilibrium tide. *Astron. and Astrophys.*, 220(1-2):112–116, Aug 1989.

I. Zalamea, K. Menou, and A. M. Beloborodov. White dwarfs stripped by massive black holes: sources of coincident gravitational and electromagnetic radiation. *MNRAS*, 409:L25–L29, November 2010. doi: 10.1111/j.1745-3933.2010.00930.x.

Brunetto Marco Ziosi, Michela Mapelli, Marica Branchesi, and Giuseppe Tormen. Dynamics of stellar black holes in young star clusters with different metallicities - II. Black hole-black hole binaries. *MNRAS*, 441(4):3703–3717, July 2014. doi: 10.1093/mnras/stu824.